NONLINEAR ROBUST FRAMEWORK FOR REAL-TIME HYBRID SIMULATION OF STRUCTURAL SYSTEMS: DESIGN, IMPLEMENTATION, AND VALIDATION

A Dissertation

Submitted to the Faculty

of

Purdue University

by

Amin Maghareh

In Partial Fulfillment of the

Requirements for the Degree

of

Doctor of Philosophy

August 2017

Purdue University

West Lafayette, Indiana

To my family, whose love and support made this work possible

ACKNOWLEDGMENTS

First, I would like to express my sincere gratitude and appreciation for my advisor, Prof. Shirley J. Dyke. Her guidance, support and advice through my tenure as a PhD student were vital to my success. She is an exceptional mentor and scholar, and I consider myself very lucky to have been her student.

I would like to thank my committee members, Dr. Arun Prakash, Dr. Julio Ramirez, Dr. Richard Christenson and Dr. Jeffrey Rhoads. They shared their valuable time with me and allowed me to discuss many issues I encountered during my PhD years. I am grateful for their support and advice in my research.

I would like to thank my fellow graduate students at the Intelligent Infrastructure Systems Laboratory at Purdue University, especially Daniel Gomez, Christian Silva, Ge(Gaby) Ou, and Ali Ozdagli.

Financial support for my PhD research was provided from the NSF under grant CNS-1136075. In addition, I would like to express my appreciation to the support for the development of the novel CIRST instrument made possible through the NSF MRI Program under grant CNS-1028668 and the School of Mechanical Engineering at Purdue University.

TABLE OF CONTENTS

Page

Page

LIST OF TABLES

LIST OF FIGURES

Figure Page

Figure Page

Figure Page

Figure Page

Figure Page

Figure Page

ABBREVIATIONS

CBF	Concentrically-braced Frame
CSI	Control-structure Interaction
DAC	Digital-to-analog Converter
DDE	Delay Differential Equation
DSS	Dynamically Substructured System
EFT	Effective Force Testing
HS	Hybrid Simulation
PGA	Peak Ground Acceleration
PPI	Predictive Performance Indicator
PSI	Predictive Stability Indicator
LVDT	Linear Variable Displacement Transducer
MDOF	Multi-degree-of-freedom
MR	Magnetorheological
MRF	Moment Resisting Frame
NEES	Network for Earthquake Engineering Simulation
NDDE	Neutral Delay Differential Equation
RDDE	Retarded Delay Differential Equation
RT-HPC	Real-time High Performance Computing
RTHS	Real-time Hybrid Simulation
SDOF	Single-degree-of-freedom
SMC	Sliding Mode Control
SRCSys	Self-tuning Robust Control System
TET	Targeted Energy Transfer
USGS	United States Geological Survey

vRTHS	Virtual Real-time Hybrid Simulation
ZOH	Zero Order Hold

ABSTRACT

Maghareh, Amin Ph.D., Purdue University, August 2017. Nonlinear Robust Framework for Real-time Hybrid Simulation of Structural Systems: Design, Implementation, and Validation. Major Professor: Shirley J. Dyke.

Real-time hybrid simulation (RTHS) is a cyber-physical, time-efficient and cost-effective technique that integrates physical testing with computational simulation to offer powerful methods to examine structural behavior and seismic resilience at multiple scales. To enforce interface conditions between computational and physical substructures, usually, servo-hydraulic actuators serve as transfer system. In implementation of any RTHS, global stability and performance must be given appropriate attention. In this dissertation, the overarching research objective is to establish and validate a systematic approach to design a safe, stable and accurate RTHS considering the significance of partitioning configuration, transfer system dynamics, nonlinearity and uncertainty in the physical substructure.

Transfer and sensing systems introduce de-synchronization at the interface. These added dynamics in the feedback loop can result in instabilities and losses in performance. In RTHS, each partitioning choice has a different set of stability requirements and as the partitioning choice becomes more complex, set of stability requirements can become extremely narrow. Thus, predictive indicators are developed which provide a relatively easy and useful method to examine various partitioning choices. To enhance understanding of transfer system dynamics, a nonlinear dynamical model is proposed for a servo-hydraulic actuator coupled with a nonlinear physical specimen. The nonlinear dynamical model is transformed into controllable canonical form for further tracking control purposes. Based on the dynamical model, a high-precision nonlinear control system is developed to achieve the interface conditions.

Self-tuning Robust Control System is a multi-layer nonlinear control system designed to accommodate extensive performance variations in the physical substructure due to structural component failure, complexity, and nonstationary behavior.

1. INTRODUCTION

1.1 Motivation

The resilience of our communities to all manner of disturbances will depend on the steps that researchers take today to reduce vulnerability tomorrow. Like many other countries, the U.S. faces multiple natural hazards that endanger its safety, economic well-being and security. These natural hazards include acute disasters such as earthquake and tsunami, and slow-onset natural disasters such as climate change. Here, vulnerability does not only depend on exposure to disturbances, which can affect society, but also depends on policies and decisions made before, during and after an incident. A fundamental step towards achieving the goal of resilient communities is advancing our knowledge of structural/infrastructure systems and their associated risks.

Structural engineers are charged with understanding risk and resilience to natural disasters, generating the knowledge and innovations, and developing systematic decision-making frameworks that will best serve society in mitigating the impacts of natural hazards. Seismic events are a major source of catastrophic natural disasters, often leading to loss of human life, civil structures and infrastructures. The 2014 U.S. seismic hazard map generated by the United States Geological Survey (USGS) is provided in Figure 1.1. As civil structures evolve to meet the needs of future generations, there is an increasing demand to address ongoing challenges such as demonstrating the effectiveness of performance-based seismic design, considering soil-structure interaction, utilizing new materials and techniques capable of reducing seismic impact, and improving retrofitting strategies [1]. These challenges justify the need for calibrating computational models and verifying the new design guidelines and mitigation

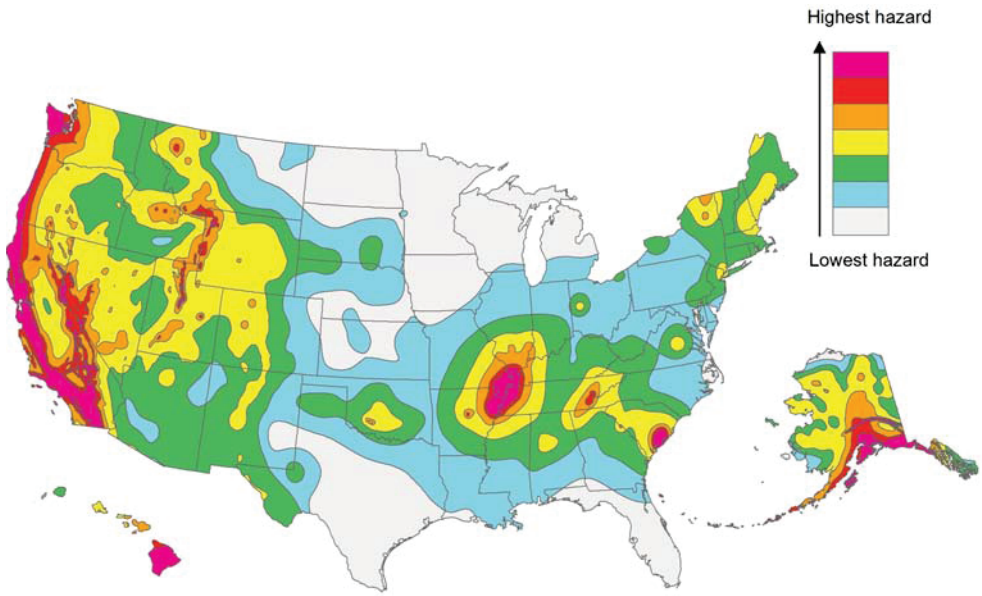

Fig. 1.1. 2014 hazard map (PGA 2% in 50 years), courtesy of USGS.

techniques through extending and evolving our experimental capabilities in a more *time-efficient* and *cost-effective* manner.

1.2 Experimental Dynamic Testing

Currently, there exist three main experimental methods to evaluate structural behavior in the presence of dynamic loads, (1) shake table testing, (2) quasi-static testing, and (3) hybrid simulation [2].

Shake table testing enables researchers to achieve realistic conditions and evaluate critical issues such as collapse mechanisms, component failures, acceleration amplifications, residual displacements and post-earthquake capacities [3]. In the seismic evaluation of civil structures using shake table testing, a researcher needs to know the actuator's required peak velocity (directly related to the oil flow rate provided by the pumping system and servo-valve), rated capacity of the actuator, maximum stroke, and actuator frequency bandwidth [4]. To design a test, considering these well-defined parameters, there is usually no stability concern, and the results are re-

liable. However, as the size of the payload increases, for instance testing full-scale large civil structures, there is greater likelihood of interactions between the structure and shake table, and thus testing will require advanced control techniques. In addition, since very few shake tables in the world are capable of testing full-scale large structures and those experiments may be prohibitively expensive, shake table testing is usually limited to prototypes, limited in payload, and often conducted for critical parts of a structure at the component level [5].

Quasi-static testing is another experimental technique in which the structure (or structural component) under investigation is subject to a predefined displacement history at a slow rate. One of the most important advantages of the quasi-static testing compared to the shake table testing is that it does not require dynamic loading even though it is an experimental technique for evaluating the dynamic performance of structures. Since quasi-static loading actuators are larger than typical dynamic actuators in laboratories due to cost, the quasi-static technique enables researchers to conduct large- or full-scale experiments and closely observe the performance of the structure under investigation [6]. Currently, this technique is usually applied to study the hysteretic and cyclic behavior of structural components subject to seismic loading [7]. While quasi-static testing can be implemented on large civil structures, it has two major drawbacks, it requires a predefined displacement history [8], and it does not preserve rate-dependence while evaluating the dynamic performance of structures.

Hybrid simulation (HS) is a cost-effective experimental technique used to evaluate the dynamic performance of large civil structures. In hybrid simulation, the structure under investigation (i.e., *reference structure*) is partitioned into two substructures, (i) a *physical* (a.k.a., experimental) substructure, which usually includes the structure's more complex components, and (ii) a *computational* (a.k.a., numerical) substructure, which usually includes the well-understood components. Coupling between the two substructures is achieved by enforcing equilibrium and compatibility at the interface (*interface conditions*) [9]. One of the critical assumptions for

conducting HS is that the effect of loading rate on the interaction force of the computational substructure is insignificant. This critical assumption has been validated for some structural materials, such as reinforced concrete and steel under certain conditions [6, 10]. However, with the introduction of new structural components and devices with rate-dependent behavior for seismic protection (e.g., rubber bearings, viscous dampers, friction dampers, sloshing dampers, magneto-rheological dampers, and electro-rheological dampers), conventional quasi-static testing and hybrid simulation are unable to effectively evaluate the dynamic performance of rate-dependent structural components [6]. Therefore, the need to examine the dynamic performance of rate-dependent structural components leads researchers to conduct fast hybrid simulation and *real-time hybrid simulation*.

Real-time hybrid simulation (RTHS) is a cyber-physical, *time-efficient* and *cost-effective* technique that integrates physical testing with computational simulation to offer powerful methods to examine structural behavior and seismic resilience at multiple scales. In RTHS, similar to HS, the interface interaction between the substructures is enforced by a transfer system. The transfer system needs to be controlled such that the interface conditions are executed in real-time [11].

Since 1969, hybrid simulation has been constantly evolving as a powerful experimental method for examining structural and infrastructure behavior subject to extreme dynamic loading. The timeline of hybrid simulation is shown in Figure 1.2. Hybrid simulation found its way into structural engineering with Hakuno et al. [12] who used HS to conduct a dynamic destructive test of a cantilever beam using an online system consisting of an analog computer and an electro-magnetic actuator. In 1981, application of online computer-controlled testing was developed so that computational substructures can be combined with a physical experiment to simulate the seismic response of the reference system [13]. In 1983, Takanashi and Ohi conducted a continuous computer-actuator on-line system to evaluate the seismic response of steel structures [14]. In the late 80s, researchers shown that results of HS and shake table tests are comparable if experimental errors are effectively mitigated in con-

ducting HS [15, 16]. In 1992, Nakashima et al. conducted the first real-time pseudo dynamic testing [6]. In the late 90s, Diming et al. conducted real-time earthquake simulation studies of large scale structures using effective force testing (EFT) [17]. In the U.S., geographically distributed HS was first carried out as part of the NEES efforts for advanced earthquake engineering experiment and simulation [18]. Later in 2005, Mosqueda et al. conducted a geographically-distributed hybrid simulation allowing the seismic evaluation of complex structural systems by enabling simultaneous testing of multiple large-scale physical substructures [2]. This work was later extended to implementation of geographically distributed hybrid simulation in hard real-time to evaluate the performance of magneto-rheological dampers for seismic hazard mitigation [19].

1.3 Objective and Contribution

In this dissertation, the main focus is developing a methodology for the design of RTHS experiments based on sound engineering principles. Most of the past experiments conducted using RTHS have been based on trial and error. In other words, a research team selects a structure, partitions the structure into physical and computational components, and hopes that a transfer system controller can be designed to enable the testing to proceed. Little thought was given in advance to the quality in

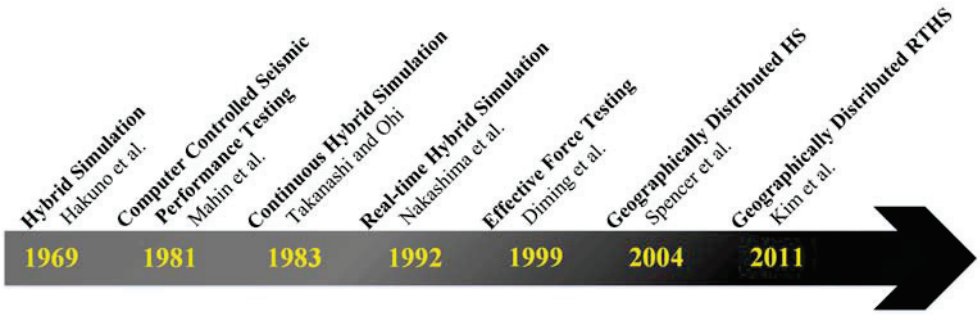

Fig. 1.2. Hybrid simulation timeline.

terms of reproducing the actual global behavior or the potential for instabilities in the experimental feedback loop.

In RTHS, transfer and sensing systems introduce de-synchronization at the interface, including frequency-independent time-delay (caused by communication delay, A/D conversion, and computation delay) and frequency-dependent time-lag (caused by transfer system dynamics and limitations). These added dynamics in the feedback loop can result in instabilities and losses in performance. Thus, in this dissertation, the overarching research objective is to establish and validate a systematic approach to design a safe, stable and accurate real-time hybrid simulation considering the significance of partitioning configuration, transfer system dynamics, nonlinearity and uncertainty in the physical substructure. Figure 1.3 presents a summary of the approach established and validated in this dissertation.

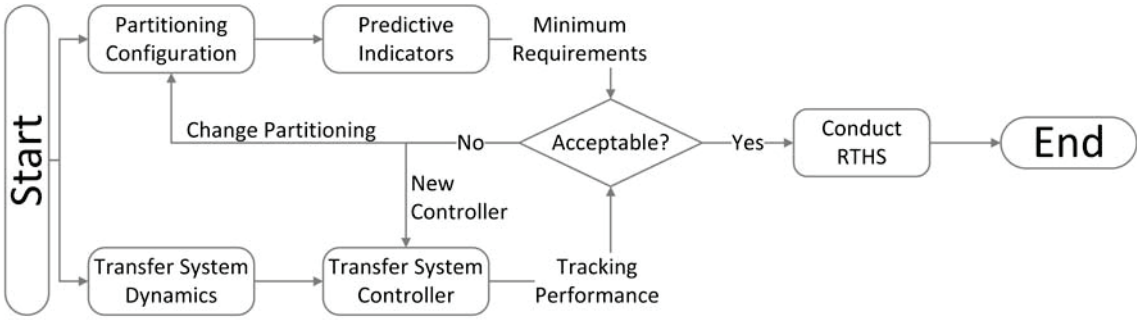

Fig. 1.3. Configuring a successful RTHS.

In this dissertation, initial efforts have been directed toward establishing *predictive stability* and *performance indicators* (PSI and PPI) to be used to configure an RTHS experiment. PPI and PSI enable researchers to assess the sensitivity of an RTHS configuration to de-synchronization at the interface. In addition, for verification of this approach, PSI has been applied to small- and large-scale, single- and multi-degree of freedom RTHS experiments to conduct a stability analysis of various partitioning configurations.

In addition, a control strategy is developed that is effective for nonlinear control plants (i.e., transfer system coupled with a nonlinear physical substructure) with high uncertainty to extend the scope of RTHS to a broader set of applications. Thus far, RTHS has mainly been applied when the physical substructure is represented as a time-invariant known system. Ultimately, RTHS will be most useful when the physical substructure is quite general, for instance an unknown time-varying nonlinear system, or even including component failure. For successful implementation of RTHS, neglecting the dynamics of hydraulic transfer system generally results either in system instability or sub-optimal performance. Thus, a nonlinear dynamical model is developed and described in *controllable canonical form* to capture the dynamics of the hydraulic control plant. The importance of considering this model in RTHS is twofold: (1) to design an effective controller/compensator to enhance the performance and stability of the hydraulic actuator(s) for linear and nonlinear substructures; and (2) to design a partitioning configuration with a suitable physical substructure in which the transfer system limited ability to apply forces in certain situations has minimal impact on the global response of the simulation. The nonlinear dynamical model has been verified in a number of experimental case studies.

Based on the hydraulic control plant, a high-precision nonlinear control system is developed to achieve the interface conditions. *Self-tuning Robust Control System* (SRCSys) is a multi-layer nonlinear control system designed to accommodate extensive performance variations in the physical substructure due to failure, complexity, and nonstationary behavior. SRCSys has been verified for rate-dependent, time-varying and amplitude-dependent physical specimens.

1.4 Scope of Work

In execution of real-time hybrid simulation, stability and accuracy are the main challenges. In this dissertation, *successful RTHS* refers to the case in which the partitioned system captures the essential dynamics of the reference structure subjected

to dynamic loading. However, it should be noted that a trivial case in which the physical substructure is significantly small in comparison to the computational substructure may be successful, but not an interesting and challenging choice to study. Stability and accuracy in RTHS are mainly a function of five conditions, (1) *overall dynamics of the reference structure*, (2) *fidelity of the computational substructure*, (3) *integration scheme and time increment*, (4) *partitioning configuration*, and (5) *execution of interface conditions*. In other words, instability and inaccuracy stem from three different sources, computational model idealization (*fidelity of the computational substructure*), numerical integration (*integration scheme and time increment*), and experimental errors (*overall dynamics of the reference structure*, *partitioning configuration*, and *execution of interface conditions*).

Chapter 2 discusses the significance of condition (1): overall dynamics of the reference structure, and condition (4): partitioning configuration on stability and accuracy in RTHS. In this chapter, first a virtual time delay framework is demonstrated in which the sensitivity of a partitioning choice to interface de-synchronization can be examined prior to adopting a transfer system control strategy. Due to this virtual time delay framework, PSI is obtained analytically and it is independent of transfer system and controller dynamics, providing a relatively easy and useful method to examine many partitioning choices. Later, predictive stability and performance indicators are established for use with single degree-of-freedom linear and weakly nonlinear systems. These indicators allow researchers to quantitatively examine the impact of partitioning choices on stability and performance, and to assess the sensitivity of an RTHS configuration to de-synchronization at the interface. In the second half of Chapter 2, PSI is extended to any linear multi-degree-of-freedom (MDOF) system. Here, a novel matrix method is adopted to convert a delay differential equation to a generalized eigenvalue problem using a set of vectorization mappings, and then to analytically solve the delay differential equations in a computationally efficient way. In this chapter, multiple illustrative examples are provided to demonstrate and

validate the significance of PSI and PPI in conducting successful RTHS. Chapter 2 has been published in [20–24].

Chapters 3 and 4 are mainly focused on condition (5): execution of interface conditions. In Chapter 3, a nonlinear dynamical model for a servo-hydraulic actuator coupled with a nonlinear physical specimen is developed. Later in this chapter, the nonlinear dynamical model is transformed into controllable canonical form for further tracking control purposes in the proceeding chapter. A parametric identification method has been developed and validated for identifying the hydraulic transfer system parameters including analog controller, servo-valve and hydraulic actuator. In addition, in a series of experiments, the controllable canonical model is numerically and experimentally validated for a servo-hydraulic actuator coupled with nonlinear physical specimens. For this purpose, a nonlinear device is designed and fabricated to exhibit various nonlinear force-displacement profiles as functions of its initial condition and the type of materials used as replaceable coupons. Chapter 3 has been published in [25].

In Chapter 4, the model developed for hydraulic control plant in Chapter 3 is used to develop a high-precision multi-layer nonlinear control system: *Self-tuning Robust Control System (SRCSys)*, which accommodates extensive performance variations and uncertainties in the physical substructure. SRCSys consists of two layers: robustness and adaptation. The layer of robustness will synthesize a nonlinear control law such that the closed-loop dynamics withstand extensive parametric and non-parametric uncertainties. Sliding mode control (SMC) is employed as the control scheme in this layer. Further, adaptation law is designed to reduce parametric uncertainties through run-time, slow and controlled learning of the physical plant based on measured performance.

In conducting a successful RTHS, condition (2): fidelity of the computational substructure, and condition (3): integration scheme and time increment are two significant elements that are not covered in this dissertation. In the computational substructure, modeling error arises from any discrepancies between the response of

the actual (or real) portion modeled as computational substructure and the response acquired from the computational model. An existing challenge in RTHS is that due to the strict hard real-time constraints, large computational models cannot readily be used. In RTHS, the time required to solve a computationally demanding model could certainly be much greater than the maximum time interval required to ensure stability and performance for the transfer system control strategy. Therefore, low-order or mid-order computational models, which usually do not require such large integration time are adopted by researchers. Idealized models that are limited in their ability to represent the underlying dynamics of the computational substructure may not be suited to the purpose intended for the simulation. To overcome this challenge, two approaches are available: real-time high-performance computing (RT-HPC) [26, 27] and multi-rate real-time hybrid simulation (mr-RTHS) [28]. In RTHS, explicit or implicit integration schemes are utilized to solve the computational model representing a portion of the reference structure. A very significant characteristic of explicit methods, which makes them more attractive for conducting RTHS, is that with explicit approaches all the numerical computations are processed in a consistent predictable amount of time. Using explicit schemes, the next state of the structure is computed merely based on the current state and the input.

2. RTHS: STABILITY AND PERFORMANCE

RTHS is a complex cyber-physical technique that couples computational simulation with physical experiments in a way that enables low-cost and efficient testing of rate-dependent specimens. In the implementation of any RTHS, global stability and performance (accuracy) must be given appropriate attention. Stability and accuracy of RTHS are mainly a function of five conditions, (1) overall dynamics of the reference structure, (2) fidelity of the computational substructure, (3) integration scheme and time increment, (4) partitioning configuration, and (5) execution of interface conditions. Several researchers have investigated the impact of these entities on stability and accuracy of simulations [29–35].

Errors occur in RTHS from three different sources, model idealization, numerical integration, and experimental errors. Modeling error arises from any discrepancies between the response of the actual (or real) portion modeled as computational substructure and the response acquired from its model. In RTHS, explicit or implicit integration schemes are utilized to solve the idealized computational substructure. A significant characteristic of the explicit methods, which makes it more attractive for conducting RTHS, is that with this approach all the computations are processed in a consistent predictable amount of time. Using explicit schemes, the next state of the numerical model is computed merely based on the current state and the input(s). In RTHS, the fact that in the explicit schemes the actuator command is computed without prior knowledge of the system's response can be a major source of computational error. Depending upon which integration scheme is adopted, stability and accuracy issues may be limiting factors [2]. Moreover, in the implementation of RTHS with more complex reference structures (particularly, the computational substructure), parallel computing has become increasingly important due to the advances in multiprocessor systems and high computational demand in the computational substructure. In

an attempt to address this issue, Li, *et al.* designed, implemented and evaluated a practical real-time platform that efficiently runs sporadic parallel task sets with implicit deadlines [36]. Finally, in RTHS, there are a number of experimental sources of error which can be categorized as epistemic and aleatoric errors. Sources of epistemic errors are systematic, such as transfer system dynamics, computational delays, communication delays, and sensor dynamics and miscalibration. However, sources of aleatoric errors are random, such as measurement noise and random truncations in the analog-to-digital (AD) conversions of signals.

RTHS performance (or stability) indicators can be divided into three categories, (i) indicators computed prior to an experiment (pre-experiment) to enable to predict the susceptibility of an RTHS configuration to any systematic or random sources of error, (ii) indicators computed during the experiment (online) to evaluate the quality of RTHS responses and detect unacceptable results in run-time, and (iii) indicators computed after the experiment (post-experiment) to assess the quality of RTHS responses with respect to reference responses.

Pre-experiment indicators are necessary for users to predict the accuracy of RTHS responses, to develop the minimum requirements with respect to any user-defined acceptance criterion, and to assist researchers in enhancing the stability and performance of RTHS responses more effectively. A number of researchers have developed different techniques to determine the impact of systematic errors on the overall performance of the system. To name a couple, Horiuchi, *et al.* have developed an effective viscous damping for a linear elastic specimen and a constant feedback delay [37] and Mosqueda, *et al.* estimated the effective damping ratio of a SDOF RTHS with a constant time delay [31]. Later, an online (run-time) energy indicator, hybrid simulation error monitors (HSEM), was developed to assess the quality of RTHS responses [30,31]. In these studies, Mosqueda, *et al.* investigated the impact of experimental errors on linear and nonlinear seismic responses of structures using HSEM. Moreover, this indicator also serves as a basis for an RTHS safety system to cease the simulation, examine source of error, and possibly correct the issue. Finally, towards

RTHS data analysis process and in the presence of reference responses, researchers have been using a number of time-based or frequency-based indicators to assess the quality of RTHS responses [38, 39].

In this chapter, predictive (pre-experiment) stability and performance indicators are discussed for use with SDOF and MDOF systems. The objective of this chapter is threefold, (i) to develop an RTHS stability switch criterion, (ii) to establish quantitative measures to assess the sensitivity of an RTHS configuration to de-synchronization at the interface, and (iii) to develop an RTHS design guideline associated with minimum requirements for transfer system control and sampling frequency. A set of delay differential equations (DDEs) is developed as virtual framework for predictive indicators. These indicators allow researchers to configure an RTHS, to examine the impact of partitioning choices on stability and performance. The main parameters investigated in this chapter are, (1) structural characteristics of the reference structure (e.g., natural frequency, damping ratio, and structural nonlinearity), (2) partitioning parameters, and (3) transfer system time delay associated with the feedback force signal. The predictive and stability indicators are developed in a way to be reconcilable with each other. Finally, through a number of illustrative examples, the PPI and PSI are demonstrated and validated for SDOF and MDOF systems.

2.1 Transfer System

In RTHS, transfer system is used to apply the interface conditions between the computational and physical substructures. Depending on how the reference structure is partitioned into computational and physical substructures, hydraulic actuator(s) and/or shake table are used as transfer system. The general formulation for linear RTHS method and substructuring techniques are provided by Shao *et al.,* [40].

De-synchronization at the cyber-physical interface is a major source of system instability in RTHS. A typical real-time hybrid simulation framework, see Figure 2.1, includes: (i) a computational model capable of being executed in real-time, (ii) a

transfer system control strategy to obtain an accurate tracking of desired trajectory at the interface, (iii) a sensing system, and (iv) a physical substructure.

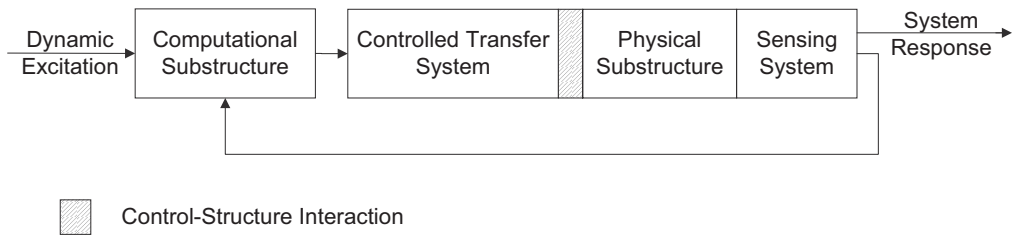

Fig. 2.1. Block diagram of a partitioned structural system for RTHS implementation.

To implement RTHS, a reference structure can be partitioned in many different ways depending on the nature and objective of the experiment. To meet the necessary interface conditions, the hydraulic actuator and the physical substructure are physically coupled through either a load frame/reaction wall or a shake table [40].

For instance, Figure 2.2(a) displays a nonlinear oscillator attached to a three-story structure while the entire structural system is subjected to ground excitation. One possible way to partition the reference structure into computational and physical substructures is presented in Figure 2.3. In this configuration, the first two stories are modeled as computational substructure and the model is executed using a real-time operating platform. The top story and the nonlinear oscillator are mounted on a shake table driven by a controlled hydraulic actuator to enforce the interface conditions.

In another example, a magneto-rheological damper (i.e., a semiactive control device) is attached to the first story of a three-story structure subjected to ground excitation, see Figure 2.2(b). A possible configuration in which the reference structure is partitioned into computational and physical substructures is shown in Figure 2.4.

In RTHS, system instability is a significant safety concern and it may damage physical specimens and/or transfer system. Also, system instability causes some researchers to avoid using RTHS due the level of complexity in comparison with other

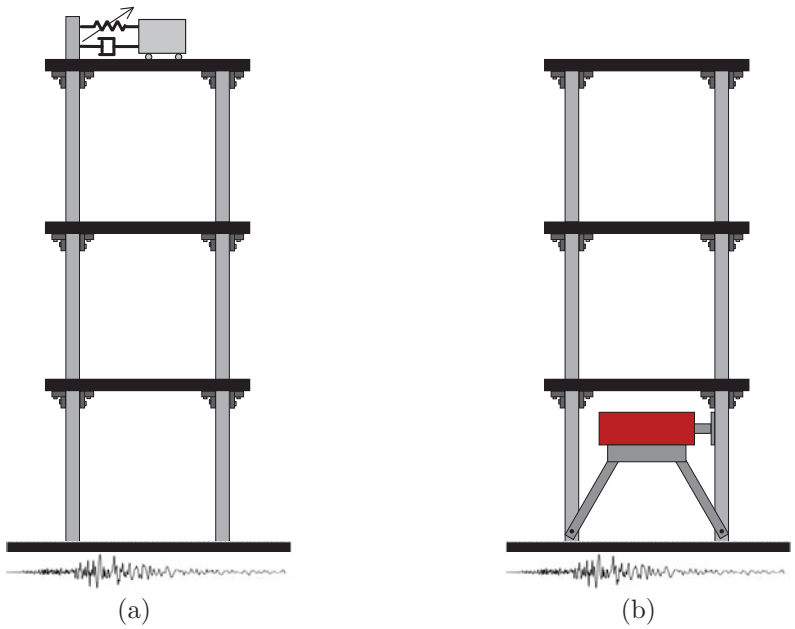

Fig. 2.2. A primary structural system attached to (a) nonlinear oscillator (b) magneto-rheological damper.

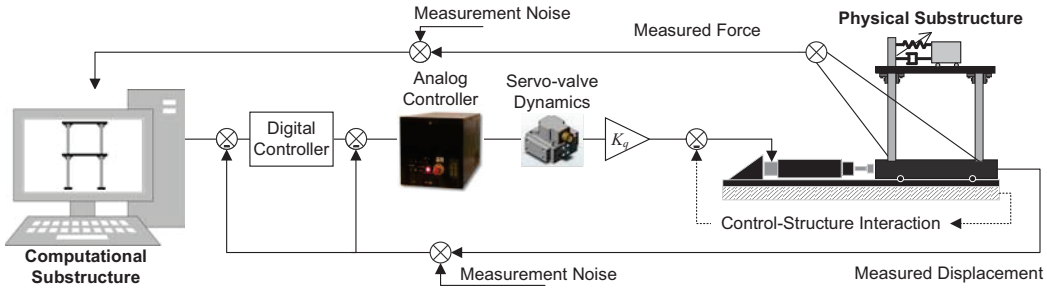

Fig. 2.3. Schematic diagram of real-time hybrid simulation for Figure 2.2(a).

alternatives. There are various transfer system parameters impacting the stability (and performance) of RTHS. These parameters include physical limitations of the available components (e.g., actuator speed, servo-valve speed, oil-column resonance, etc.) and user choices (e.g., analog controller's parameters, digital control strategy, etc.). To conduct a successful RTHS, it is absolutely necessary for a user to have

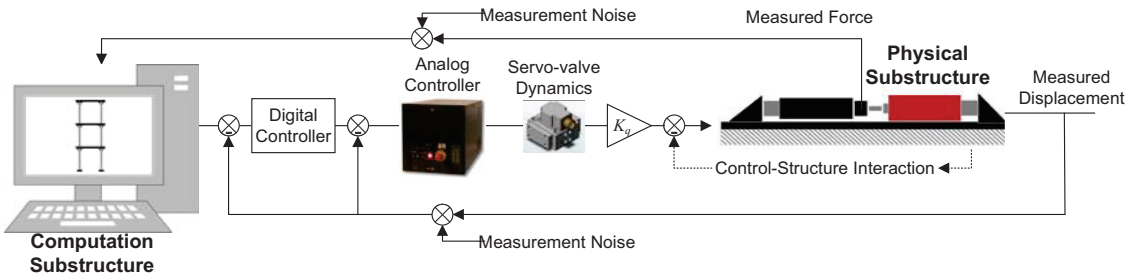

Fig. 2.4. Schematic diagram of real-time hybrid simulation for Figure 2.2(b).

a good understanding of these parameters and limitations. The transfer and sensing systems introduce de-synchronization at the interface which can be categorized into two groups: frequency-independent time delay (caused by communication delay, analog-to-digital and digital-to analog conversions, and computation delay) and frequency-dependent time lag (caused by transfer dynamics and limitations) into the system. In addition, it has been demonstrated that the dynamical characteristics of the physical substructure impact the transfer system performance due to control-structure-interaction [41].

2.1.1 Control-structure Interaction in RTHS

In this section, control-structure interaction and its effect in implementation of RTHS is discussed while a hydraulic actuator is considered as transfer system. In the case of a hydraulic actuator, a coupling is present between the actuator and physical specimen [41] where in the case of RTHS, the physical specimen is the physical substructure. Currently, RTHS is being implemented for complex MDOF systems in which control of multiple actuators are required. These multiple actuators are intrinsically coupled through the physical substructure. This phenomenon imposes certain challenges and considerations in transfer system control for implementing of a successful test.

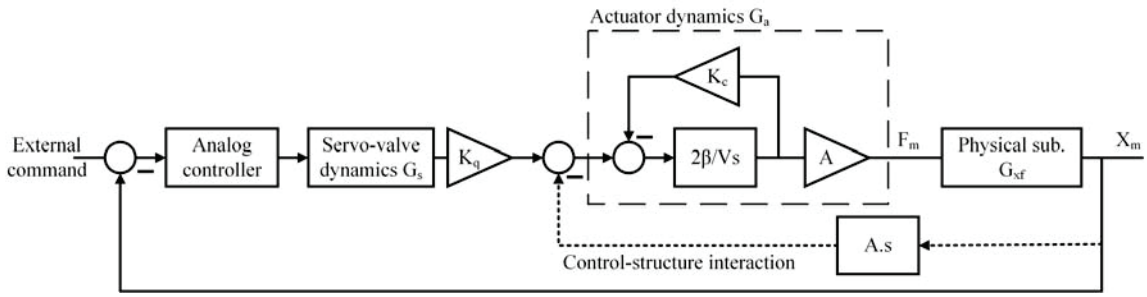

Fig. 2.5. Transfer system coupled with physical substructure.

In displacement control RTHS, an external command (command displacement) drives the transfer system attached to the physical substructure, see Figure 2.5. The hydraulic actuator is a part of the transfer system which is driven by valve input command and generates the force applied to the physical substructure. A block diagram representation of an open-loop actuator model is provided in Figure 2.6. For RTHS and in the case of a hydraulic actuator attached to a physical substructure, a velocity feedback exists between the actuator and the valve input. In [42], the fluid flow rate in an actuator is linearized about the origin. Figure 2.6 is obtained based on the linearized equation of hydraulic flow rate in the actuator, which is

$$\dot{f} = \frac{2\beta}{V}(AK_q i - K_c f - A^2 \dot{x}) \tag{2.1}$$

where f, β, V, A, K_q, i, K_c, and x are actuator force, bulk modulus of the fluid, half the volume of hydraulic actuator, piston area, valve flow gain, valve input, leakage coefficient, and actuator displacement, respectively. Due to CSI, the dynamics of the physical substructure directly impact the characteristics of the transfer system. Moreover, when the physical substructure undergoes structural changes or is replaced by a new substructure, the overall dynamics (and performance) of the transfer system will change through CSI and therefore, a new transfer system controller is required.

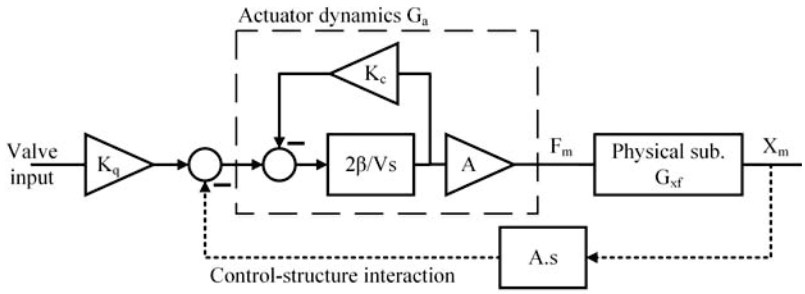

Fig. 2.6. Actuator dynamics coupled with physical substructure.

With a simple rearrangement in the block diagram shown in Figure 2.6, Figure 2.7(a) can be obtained. In this representation, actuator transfer function can be written as

$$G_a = \frac{A}{\frac{V}{2\beta}s + K_c} \tag{2.2}$$

and,

$$K_q G_a = \frac{AK_q}{\frac{V}{2\beta}s + K_c} = \frac{\frac{AK_q}{K_c}}{\frac{V}{2\beta K_c}s + 1} \tag{2.3}$$

Next, all the parameters are lumped into three new parameters [41]: a_1, a_2, and a_3,

$$a_1 = \frac{2\beta K_q A}{V}; a_2 = \frac{2\beta A^2}{V}; a_3 = \frac{2\beta K_c}{V} \tag{2.4}$$

and Equation 2.3 becomes

$$K_q G_a = \frac{\frac{a_1}{a_3}}{\frac{1}{a_3}s + 1} = \frac{a_1}{s + a_3} \tag{2.5}$$

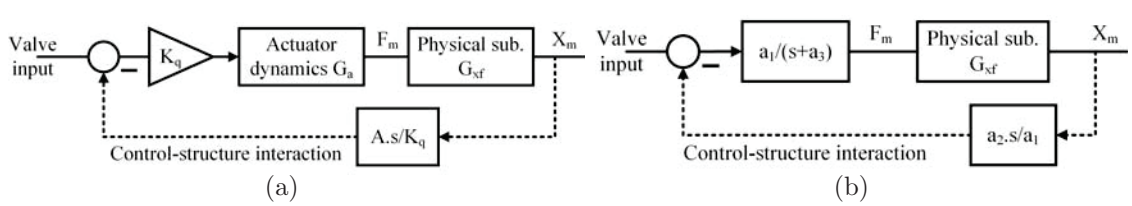

Fig. 2.7. Equivalent actuator dynamics coupled with physical substructure.

The fact that a change in the structural properties of the physical substructure will change the dynamics of the transfer system, imposes a challenge for studying the impact of partitioning choice on the global stability and performance of an RTHS system. Thus, in the next section, a virtual framework is proposed in which the sensitivity of a partitioning choice to interface de-synchronization will be studied independent of transfer system dynamics. Later, the results obtained from this framework will be investigated and validated.

2.1.2 Virtual Framework for Predictive Indicators

The governing equation of a general reference structure can be expressed as

$$[M]\ddot{X}(t) + [C]\dot{X}(t) + R(X) = -[M]\Gamma\ddot{x}_g(t) \tag{2.6}$$

where $[M]$, $[C]$, $R(X)$, Γ, $X(t)$, and $\ddot{x}_g(t)$ are the structure's mass matrix, damping matrix, restoring force vector, influence vector, displacement vector, and ground acceleration, respectively. The reference structure is partitioned into computational and physical substructures

$$\{[M], [C], R(X)\} = \{[M_p], [C_p], R_p(X)\} + \{[M_n], [C_n], R_n(X)\} \tag{2.7}$$

where p and n indices refer to the physical and computational substructures. The governing equation of the computational substructure can be expressed as

$$[M_n]\ddot{X}(t) + [C_n]\dot{X}(t) + R_n(X) = -[M]\Gamma\ddot{x}_g(t) - F_{fb}(t) \tag{2.8}$$

where $F_{fb}(t)$ is the interaction force (or feedback force) vector measured in the physical substructure and used as a feedback signal into the computational substructure. In an ideal case, $F_{fb}(t)$ can be defined as

$$F_{fb}(t) = [M_p]\ddot{X}(t) + [C_p]\dot{X}(t) + R_p(X) \tag{2.9}$$

Combining Equations (2.8) and (2.9) yields the governing equation of the reference structure in Equation (2.6). However, the ideal case requires perfect tracking control

over the transfer system, no measurement noise, no time delay, and that all the interface conditions are satisfied perfectly. Due to transfer system control limitations and computational/communication time delay, the governing equation of an RTHS system becomes

$$[M_n]\ddot{X}(t)+[C_n]\dot{X}(t)+R_n(X) = -[M]\Gamma\ddot{x}_g(t)-T\{\sum a_i F_{fb}(t-\tau_i), \sum b_i \dot{F}_{fb}(t-\tau_i), \ldots\} \tag{2.10}$$

where $T\{\ldots\}$ is an operator representing the effect of transfer system dynamics and $F_{fb}(t-\tau)$ indicates time delay in the interaction force signal.

In RTHS, sources of time lags (frequency dependent) and time delays (frequency independent) can be classified into three major categories, (1) communication delays, (2) computational delays, and (3) transfer system dynamics. No matter which transfer system control (or compensation) strategy is adopted, there is always a frequency-dependent phase shift between the desired displacement and transfer system displacement which is referred as time lag (or system dynamics). Time delay and system dynamics are two different concepts which are sometimes used interchangeably. Figure 2.8 demonstrates a general distributed RTHS architecture with multiple physical and computational substructures. In addition, the presence of the communication and computational delays and transfer system dynamics are shown.

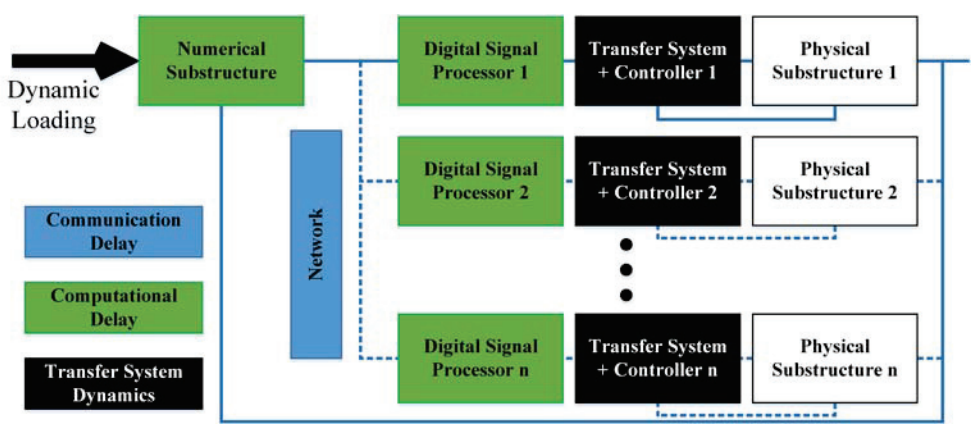

Fig. 2.8. General distributed RTHS architecture.

2.1.3 Communication Delay

To implement RTHS, there is a continuous exchange of information between the computational and physical components. In RTHS, communication delays vary from almost negligible for an RTHS using a single processor (no network) to more than a hundred milliseconds for geographically-distributed testing. Geographically-distributed RTHS presents a challenge in which the required communication over the internet results in random delays [2]. Thus, communication delays become especially significant when conducting geographically-distributed RTHS [7]. A simple representation of time delay is provided in Figure 2.9.

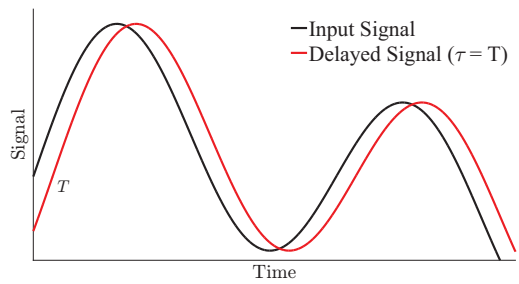

Fig. 2.9. Communication time delay.

2.1.4 Computational Delay

In RTHS, integration schemes are implemented to solve the discretized governing equation of the computational substructure. Stability and performance issues are limiting factors which determine the maximum permissible computational time and therefore, the largest natural frequency of the computational model in a linear case. All the computations are executed on processors and then the command signal is implemented using a digital-to-analog converter (DAC). One of the most common DAC methods is zero-order hold (ZOH) shown in Figure 2.10. In this method, the

signal is held constant during the integration time-step. The transfer function of the ZOH method can be expressed as

$$H_{ZOH}(s) = \frac{1 - e^{-sT}}{sT} \tag{2.11}$$

where $s \in \mathbb{C}$ is the Laplace variable and T is the integration time-step. By applying the Tylor expansion, $H_{ZOH}(s)$ can be written as

$$H_{ZOH}(s) = \frac{1 - (1 - sT + (sT)^2/2 + o(T^3))}{sT} = 1 - \frac{sT}{2} + o(T^2) \tag{2.12}$$

For a relatively small integration time-step, Equation (2.12) can be approximated with

$$H_{ZOH}(s) = 1 - \frac{sT}{2} + o(T^2) \approx e^{-sT/2} \tag{2.13}$$

Thus, the effect of the ZOH conversion on the signal is approximately equal to that of a time delay of $T/2 = (2f_s)^{-1}$ where f_s is the sampling frequency in Hz.

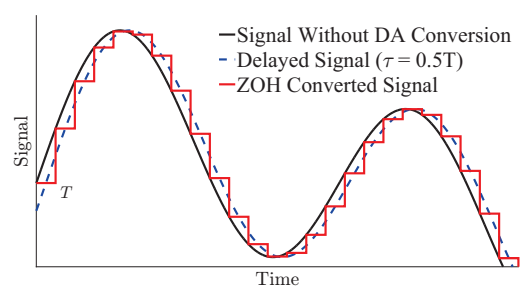

Fig. 2.10. Computational time delay.

2.1.5 Transfer System Dynamics (or Time Lag)

Regardless of the transfer system control strategy, there is always a time lag between the desired displacement and the response of transfer system. Furthermore, due to the effects of CSI, the dynamics of a hydraulic actuator and the plant are coupled through a natural velocity feedback, see Figure 2.11. So, the time lag is caused by both actuator dynamics and the attached specimen [41]. However, for most cases, the

contribution of actuator dynamics is dominating [43] and within the seismic frequency bandwidth, experimental studies have demonstrated that a linearized actuator model can capture the essential dynamics of the transfer system [33]. Typically, for a SDOF

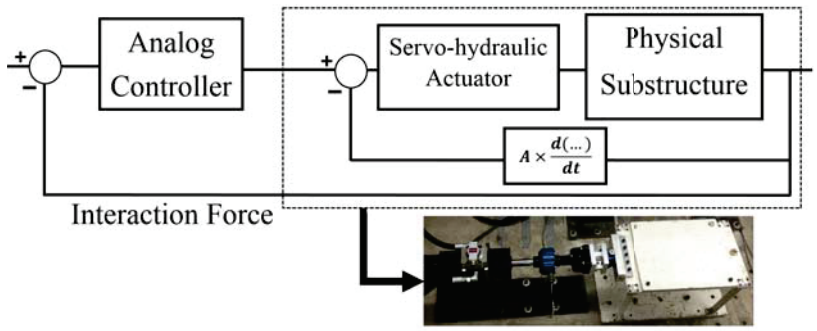

Fig. 2.11. Control-structure interaction.

RTHS, the natural frequency of the attached specimen in RTHS is large compared to the seismic frequency bandwidth. Therefore, the phase of the actuator frequency response function can be approximated as linear and modeled as a pure time delay [7].

2.1.6 Virtual Framework for Predictive Indicators

Time delay and system dynamics are two different concepts which are sometimes used interchangeably. To delineate the difference, this section compares the dynamics of a servo-hydraulic actuator model with a time delay system in the frequency domain. A time delay system, and a linear system dynamics can be mathematically expressed as

$$x(t) = u(t - \tau) \tag{2.14a}$$

$$x^{(n)}(t) + \ldots + a_0 x(t) = b_m u^{(m)}(t) + \ldots + b_1 u(t) + b_0 \tag{2.14b}$$

where $u(t)$, $x(t)$ and τ are system input, system output and time delay value, respectively. A very common type of transfer system in RTHS is a controlled servo-hydraulic actuator. For a more realistic comparison, a servo-hydraulic actuator shown in Fig-

ure 2.12, was identified at the Intelligent Infrastructure System Lab (*IISL*) at Purdue University. The identified dynamics of the servo-hydraulic actuator is given by

$$\frac{x_{msd}(s)}{x_{cmd}(s)} = \frac{2.382 \times 10^9}{s^4 + 485.5s^3 + 1.317 \times 10^5 s^2 + 3.182 \times 10^7 s + 2.382 \times 10^9} \tag{2.15}$$

Figure 2.13 provides the frequency responses of the servo-hydraulic actuator and a pure time delay system.

Clearly, over a relatively low frequency bandwidth, the dynamics of pure time delay and transfer system are quite similar. In RTHS, the frequency bandwidth of interest is the seismic frequency bandwidth and it is restricted to relatively low frequency bandwidth. Therefore, over the seismic frequency bandwidth, the dynamic interaction of a transfer system and the physical substructure can be modeled with a constant time delay [35, 44]. Here, Equation (2.10) is replaced by Equations (2.16a) and (2.16b) in which the communication delay, computational delay, and transfer system dynamics are all lumped into a single time delay (τ) which acts upon the interaction force signal.

$$[M_n]\ddot{x}(t) + [C_n]\dot{x}(t) + R_n(x) = -[M]\Gamma\ddot{x}_g(t) - F_{fb}(t-\tau) \tag{2.16a}$$

$$F_{fb}(t) = [M_p]\ddot{x}(t) + [C_p]\dot{x}(t) + R_p(x) \tag{2.16b}$$

As predictive (or pre-experiment) indicators for conducting successful and safe RTHS, predictive stability indicator is initially discussed for single-degree-of-freedom systems. In the virtual framework for predictive indicators, a virtual time delay is applied to the feedback force in order to assess the sensitivity and stability requirement

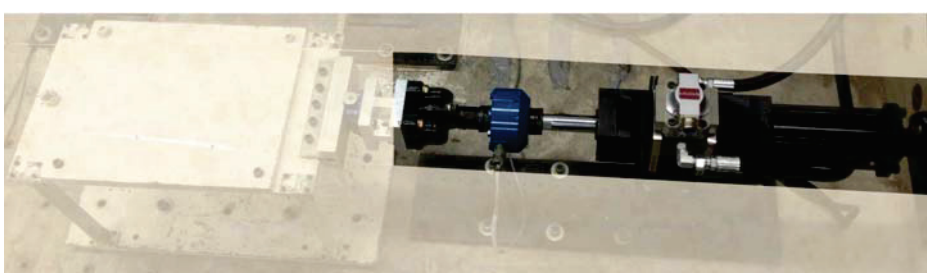

Fig. 2.12. Servo-hydraulic actuator as a common transfer system.

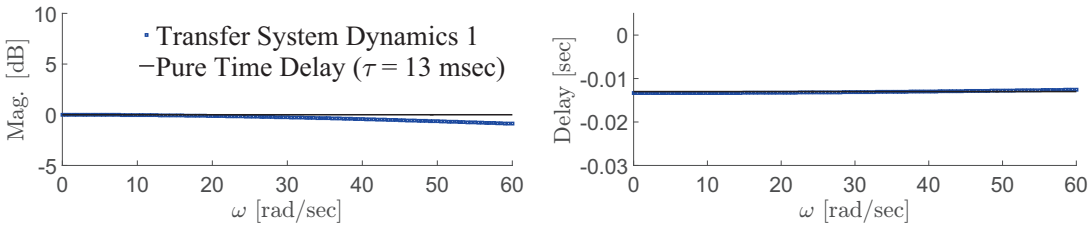

(a) Magnitude plot. (b) Phase plot.

Fig. 2.13. Frequency responses of hydraulic actuator and pure time delay.

of a partitioning choice subject to interface de-synchronization. The virtual framework is shown in Figure 2.14. For linear systems, Figure 2.14 can be mathematically represented as either a neutral or retarded delay differential equation. In order to obtain critical delay of a partitioning choice, the delay differential equation is analytically solved using a novel computationally inexpensive method. *Critical time delay* refers to the time delay associated with occurrence of a stability switch in Figure 2.14.

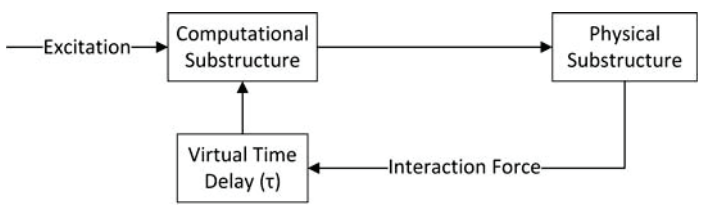

Fig. 2.14. Virtual framework for predictive indicators.

2.2 Single Degree of Freedom Linear System

Consider a linear single-degree-of-freedom (SDOF) reference structure subjected to a seismic excitation, as follows

$$M\ddot{x}(t) + C\dot{x}(t) + Kx = -M\ddot{x}_g(t) \tag{2.17}$$

where M, C, and K are the reference structure's mass, damping, stiffness, respectively. For a SDOF RTHS, the reference structure is partitioned into computational and

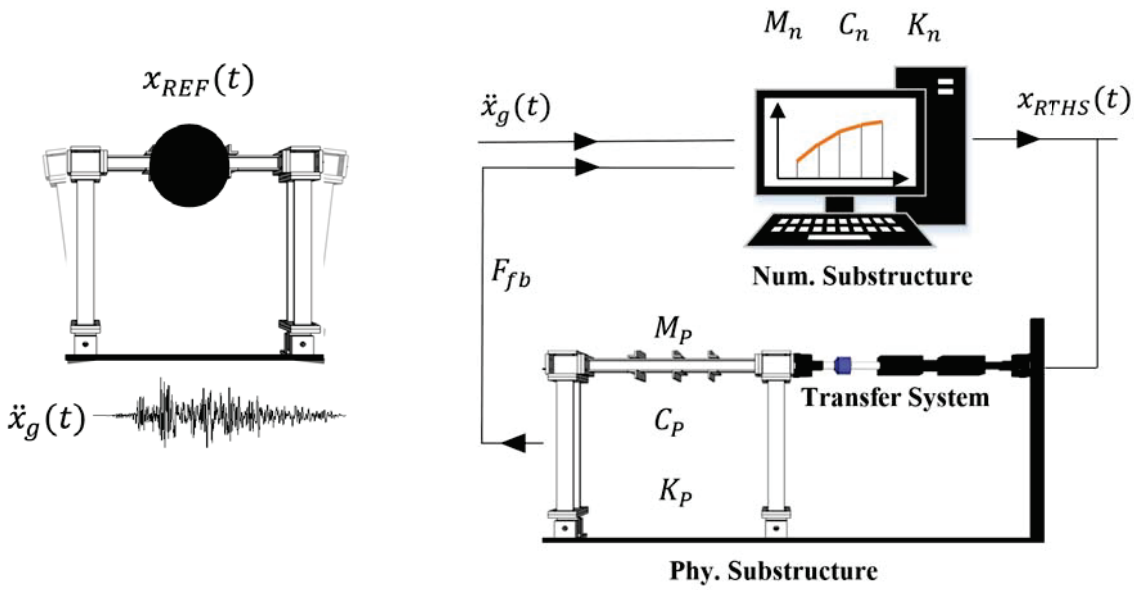

(a) Reference structure.

(b) Real-time hybrid simulation.

Fig. 2.15. Schematic diagram of a SDOF RTHS.

physical substructures, as shown in Figure 2.15. The governing equation of the SDOF RTHS shown in Figure 2.15, is approximated as a delay differential equation of the form

$$M_n\ddot{x}(t) + C_n\dot{x}(t) + K_n x = -M\ddot{x}_g(t) - F_{fb}(t-\tau) \tag{2.18a}$$

$$F_{fb}(t) = M_p\ddot{x}(t) + C_p\dot{x}(t) + K_p x \tag{2.18b}$$

Equations (2.18a) and (2.18b) provide a basis for (i) investigating the impact of time delay on the modal characteristics of a SDOF RTHS, and (ii) establishing stability and performance metrics for effective RTHS implementation.

2.2.1 Stability Switch Criterion

To establish an RTHS stability switch criterion for linear SDOF RTHS systems, a general geometric stability switch criterion in delay differential equations is implemented. A more detailed discussion on the general geometric stability switch criterion is provided in [45,46]. To study the response of this RTHS system, Laplace transform is used in which $s \in \mathbb{C}$ is the Laplace variable.

$$\mathcal{L}[\ldots](s) = \int_{-\infty}^{\infty} \ldots e^{-st} \mathrm{d}t \tag{2.19}$$

The response of the reference structure, Equation (2.17), is given by

$$x_{REF}(s) = \frac{-M}{Ms^2 + Cs + K} \ddot{x}_g(s) \tag{2.20}$$

In the absence of a feedback time delay ($\tau = 0$), the response of the RTHS system in Figure 2.15 can be expressed as

$$x_{RTHS}(s) = \frac{-M}{M_n s^2 + C_n s + K_n} \ddot{x}_g(s) - \frac{M_p s^2 + C_p s + K_p}{M_n s^2 + C_n s + K_n} x_{RTHS}(s) \tag{2.21}$$

therefore,

$$\frac{Ms^2 + Cs + K}{M_n s^2 + C_n s + K_n} x_{RTHS}(s) = \frac{-M}{M_n s^2 + C_n s + K_n} \ddot{x}_g(s) \tag{2.22}$$

and

$$x_{RTHS}(s) = x_{REF}(s) = \frac{-M}{Ms^2 + Cs + K} \ddot{x}_g(s) \tag{2.23}$$

Thus, in the absence of feedback time delay, the response of an RTHS system is identical to the response of the reference structure. However, in the presence of feedback time delay, the response of the RTHS system is

$$x_{RTHS}(s) = \frac{-M}{(M_n s^2 + C_n s + K_n) + (M_p s^2 + C_p s + K_p) e^{-\tau s}} \ddot{x}_g(s) \tag{2.24}$$

and the resulting characteristic equation can be written as

$$\Gamma(\lambda, \tau) = (M_n \lambda^2 + C_n \lambda + K_n) + (M_p \lambda^2 + C_p \lambda + K_p) e^{-\tau \lambda} \tag{2.25}$$

where $\lambda \in \mathbb{C}$. Equation (2.25) can be expressed as

$$\Gamma(\lambda, \tau) = \Gamma_n(\lambda) + \Gamma_p(\lambda) e^{-\tau \lambda} \tag{2.26}$$

For a dynamic system to be asymptotically stable about its fixed points, all eigenvalues, which are the roots of the corresponding characteristic equation, must lie in the left half of the complex plane. Therefore, stability switching occurs when a root of the characteristic equation crosses the imaginary axis (i.e., $Re(\lambda_i) = 0$) as some parameters vary in the characteristic equation. If the partitioning parameters are chosen such that any root of the characteristic equation is in the right half of the complex plane, then that configuration will be unstable.

Without loss of generality, it is assumed that the reference structure ($\tau = 0$) is stable (i.e., the roots of $\Gamma(\lambda, 0)$ in Equation (2.26) lie in the left half of the complex plane). Next, two new terms which are crucial in the theory of delay differential equations are introduced, (1) critical frequency ($\omega_{cr} = |\lambda_{cr}|$) which is the frequency at which a stability switch occurs, and (2) critical time delay (τ_{cr}) which is the time delay associated with the occurrence of a stability switch. In Equation (2.26), to obtain the critical frequency and critical time delay associated with Equation (2.26), one can simply replace λ, τ with $j\omega_{cr}$, τ_{cr} and equate $\Gamma(j\omega_{cr}, \tau_{cr})$ with 0, and express the characteristic equation as

$$-\frac{\Gamma_n(j\omega_{cr})}{\Gamma_p(j\omega_{cr})} = e^{-j\tau_{cr}\omega_{cr}} = e^{-j\Omega_{cr}} \tag{2.27}$$

where j is the imaginary unit number and Ω_{cr} is the product of the critical frequency and its corresponding critical time delay ($\Omega_{cr} = \tau_{cr}\omega_{cr}$). Equation (2.27) can be solved using the geometric construction presented in [47]. As Ω_{cr} increases from 0 to 2π, $e^{-j\Omega_{cr}}$ traces out a unit circle in the complex plane and the left hand side of the equation, which is called *the ratio curve*, traces out another curve. A stability switch occurs in the system when the unit circle intersects the ratio curve. The intersection can occur multiple times, meaning that the system is stable within a particular range of time delay, then it will be unstable for a specific range of time delay, and then the system may gain its stability back as the time delay increases, see Figure 2.16. However, in RTHS, the first occurrence of instability is considered meaningful. Using

Equations (2.25), (2.26), and (2.27) the characteristic equation of a SDOF RTHS can be expressed as

$$\frac{-M_n{\omega_{cr}}^2 + C_n\omega_{cr}j + K_n}{-M_p{\omega_{cr}}^2 + C_p\omega_{cr}j + K_p} = e^{-j\tau_{cr}\omega_{cr}} \tag{2.28}$$

Using Euler's formula (i.e., $e^{\cdots j} = \cos\ldots + j\sin\ldots$), Equation (2.28) can be written as

$$(-M_n{\omega_{cr}}^2 + C_n\omega_{cr}j + K_n)+(-M_p{\omega_{cr}}^2 + C_p\omega_{cr}j + K_p)(\cos(\tau_{cr}\omega_{cr})-j\sin(\tau_{cr}\omega_{cr})) = 0 \tag{2.29}$$

Separating the real and imaginary parts of Equation (2.29) yields the following system of equations

$$(K_p - M_p{\omega_{cr}}^2)\cos(\tau_{cr}\omega_{cr}) + C_p\omega_{cr}\sin(\tau_{cr}\omega_{cr}) = M_n{\omega_{cr}}^2 - K_n \tag{2.30a}$$

$$C_p\omega_{cr}\cos(\tau_{cr}\omega_{cr}) - (K_p - M_p{\omega_{cr}}^2)\sin(\tau_{cr}\omega_{cr}) = -C_n\omega_{cr} \tag{2.30b}$$

Dividing both sides of Equations (2.30a) and (2.30b) by M yields

$$\{(1-\gamma)\omega_n^2 - (1-\alpha)\omega_{cr}^2\}\cos(\tau_{cr}\omega_{cr}) + \{2(1-\beta)\omega_{cr}\zeta\omega_n)\}\sin(\tau_{cr}\omega_{cr}) = \alpha\omega_{cr}^2 - \gamma\omega_n^2 \tag{2.31a}$$

$$\{2(1-\beta)\omega_{cr}\zeta\omega_n)\}\cos(\tau_{cr}\omega_{cr}) - \{(1-\gamma)\omega_n^2 - (1-\alpha)\omega_{cr}^2)\}\sin(\tau_{cr}\omega_{cr}) = -2\omega_n\zeta\omega_{cr}\beta \tag{2.31b}$$

where $\{\alpha,\ \beta,\ \gamma\} = \{M_n/M,\ C_n/C,\ K_n/K\}$ are the partitioning parameters and ζ is damping ratio. Equations (2.31a) and (2.31b) are squared and added together to obtain a 4th order equation governing how the partitioning factors and the structural characteristics of the reference structure determine the critical frequency of the partitioned system (ω_{cr}),

$$(1-2\alpha){\omega_{cr}}^4 + {\omega_n}^2[4(1-2\beta)\zeta^2 - 2(1-\alpha-\gamma)]{\omega_{cr}}^2 + (1-2\gamma){\omega_n}^4 = 0 \tag{2.32}$$

Furthermore, Equation (2.32) is normalized with respect to ω_n and it becomes

$$(1-2\alpha){\phi_{cr}}^4 + [4(1-2\beta)\zeta^2 - 2(1-\alpha-\gamma)]{\phi_{cr}}^2 + (1-2\gamma) = 0 \tag{2.33}$$

where $\phi_{cr} = \omega_{cr}/\omega_n$ is the critical frequency ratio. Equation (2.33) may lead to 0, 1, or 2 meaningful critical frequencies (i.e., positive real values). The lowest of the

three is associated with the limit of an unconditionally stable RTHS system. After obtaining ϕ_{cr} from Equation (2.33), one can solve for the corresponding critical time delays using Equations (2.31a) and (2.31b).

$$\tau_{cr} = {\omega_{cr}}^{-1}[N\pi + \tan^{-1}(\frac{A}{B})] \tag{2.34a}$$

in which

$$A = [2(1-\beta)\omega_{cr}\zeta\omega_n)][\alpha{\omega_{cr}}^2 - \gamma{\omega_n}^2] + [(1-\gamma){\omega_n}^2 - (1-\alpha{\omega_{cr}}^2]2\omega_n\zeta\omega_{cr}\beta \tag{2.34b}$$

$$B = [(1-\gamma){\omega_n}^2 - (1-\alpha){\omega_{cr}}^2][\alpha{\omega_{cr}}^2 - \gamma{\omega_n}^2] - [2(1-\beta)\omega_{cr}\zeta\omega_n)]2\omega_n\zeta\omega_{cr}\beta \tag{2.34c}$$

where $N = 0, 1, 2, \ldots$ and making sure that Equations (2.31a) and (2.31b) are both achieved. Furthermore, Equation (2.34a) is normalized with respect to ω_n and it becomes

$$\Omega_{cr} = \tau_{cr}\omega_n = {\phi_{cr}}^{-1}[N\pi + \tan^{-1}(\frac{A}{B})] \tag{2.35a}$$

$$A{\omega_n}^{-4} = [2(1-\beta)\phi_{cr}\zeta)][\alpha{\phi_{cr}}^2 - \gamma] + [(1-\gamma) - (1-\alpha){\phi_{cr}}^2]2\zeta\phi_{cr}\beta \tag{2.35b}$$

$$B{\omega_n}^{-4} = [(1-\gamma) - (1-\alpha){\phi_{cr}}^2[\alpha{\phi_{cr}}^2 - \gamma] - [2(1-\beta)\phi_{cr}\zeta)]2\phi_{cr}\zeta\beta \tag{2.35c}$$

Thus, Equations (2.33) and (2.35a) can be used to find the stability characteristics of an RTHS system as a function of the partitioning parameters and the structural characteristics of the reference structure. However, it is recommended to first plot the RTHS stability diagram using Equations (2.33) and (2.35a), and then determine the stability characteristics of the RTHS system.

2.2.2 Stability Diagrams for a Linear SDOF RTHS

This section examines the impacts of the partitioning parameters and the structural characteristics of the reference structure on the stability of a linear partitioned system through the use of RTHS stability diagrams. Four sample partitioning cases are considered, see Table 2.1. In Figure 2.16, the stability diagrams associated with

Table 2.1.
Partitioning parameters of the nine cases examined.

	α factor	β factor	γ factor
Case I	$\in [0,1]$	0.4	0.9
Case II	0.9	0.6	$\in [0,1]$
Case III	$\in [0,1]$	0.6	0.1
Case IV	0.1	0.4	$\in [0,1]$

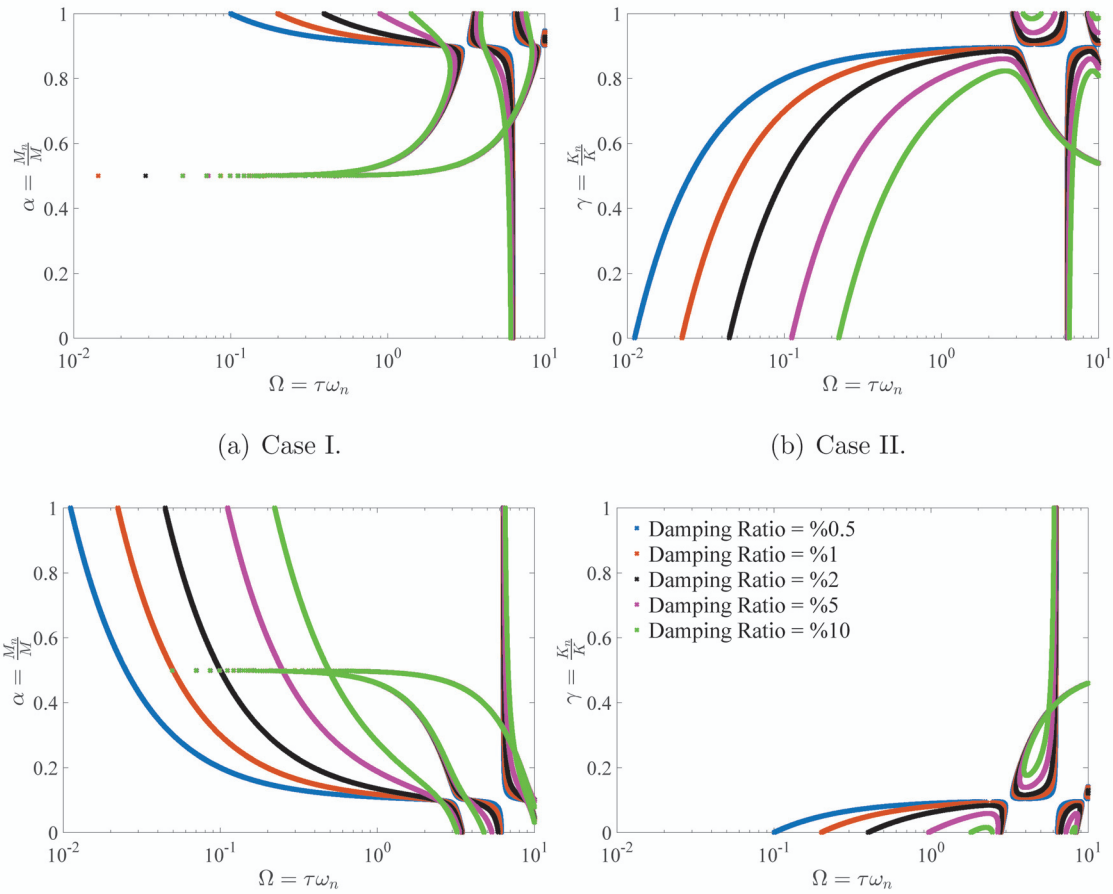

(a) Case I.

(b) Case II.

(c) Case III.

(d) Case IV.

Fig. 2.16. Normalized RTHS stability diagrams showing Ω_{cr}.

these sample cases, for five different reference damping ratios (a total of $4 \times 5 = 20$ reference systems) are examined.

Practically speaking, more realistic partitioning configurations are the ones where the majority of mass is modeled in the computational substructure (i.e., $\alpha \approx 1$) and the majority of stiffness is placed in the physical substructure (i.e., $\gamma \approx 0$). Therefore, the bottom portion of Figure 2.16(b) and the top portion of Figure 2.16(c) represent more realistic scenarios. As shown in Figure 2.16, the more realistic cases, where $\alpha \approx 1$ and $\gamma \approx 0$, are quite challenging configurations in terms of leading to small values of Ω_{cr}. Some important observations can be made from Figure 2.16.

- For a specific ζ, the area to the left of the first curve is considered a stable region in RTHS (i.e., $\Omega < \Omega_{cr}$).

- The critical time delay is inversely proportional to the natural frequency of the reference structure. Thus, higher modes of the reference structure are highly sensitive to time delays. Often for multi-degree-of-freedom systems, higher modes are suppressed with artificial damping in the computational substructure [8].

- In selecting the partitioning parameters, $\alpha \approx 0.5$ is not a good choice from stability and performance perspectives, see Figures 2.16(a) and 2.16(c).

- For a particular RTHS configuration, multiple Ω_{cr} exist. Clearly, a stability switch occurs in the system when the unit circle in Equation (2.27) intersects the ratio curve, and this can occur multiple times. Thus, the system is stable within a particular range of Ω, then it will be unstable for a specific range of Ω, and then the system will again be stable as Ω increases. Although the system may be stable at higher Ω, performance is likely to suffer. Therefore, it is recommended that to conduct an effective RTHS, users should consider just the first region of stability.

- As a rule of thumb, the value of critical time delay is closely related to $|\gamma - \alpha|$. Thus, larger value of $|\gamma - \alpha|$ usually leads to a relatively small critical time delay value.

- Critical time delay usually increases as the reference structure becomes more damped.

- Finally, if stability concerns lead to some changes in a partitioning setup, reducing $|\gamma - \alpha|$ and ω_n and/or increasing ζ are effective options.

2.2.3 Predictive Stability Indicator

Herein, the RTHS stability switch criterion is extended to establish a stability metric which indicates the global stability margin of a SDOF RTHS system with any partitioning choice. For a system with the characteristic equation of the form in Equation (2.26), a stability switch occurs when the unit circle intersects the ratio curve and the intersection can occur multiple times. However, to develop a stability indicator, the first occurrence of the instability is the most meaningful one. For a SDOF system of the form in Equations (2.18a) and (2.18b), the predictive stability indicator can be written as

$$PSI = \log_{10}(\frac{10^3 \times min[\Omega_{cr}]}{\omega_n}) = \log_{10}(min[\tau_{cr}(msec)]) \tag{2.36}$$

It should be noted that Equation (2.36) returns a meaningful value only for the first region of stability in the RTHS stability diagrams. Therefore, in Equation (2.36), $\min[\Omega_{cr}]$ is referred to the first stability switching value. As shown in Figure 2.17, PSI spans from $-\infty$ to $+\infty$ corresponding to the case on the verge of instability to the unconditionally stable case. To illustrate how the PSI values are obtained from the RTHS stability diagrams, Figures 2.18(a) and 2.18(b) illustrate the stability diagrams corresponding to configuration 1: $\{\alpha = 0.7, \beta = 0.4, \gamma = 0.9, \zeta = 0.1\}$ and configuration 2:$\{\alpha = 0.9, \beta = 0.6, \gamma = 0.7, \zeta = 0.05\}$.

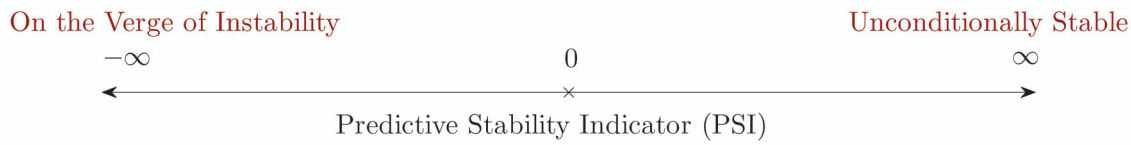

Fig. 2.17. Predictive stability indicator span.

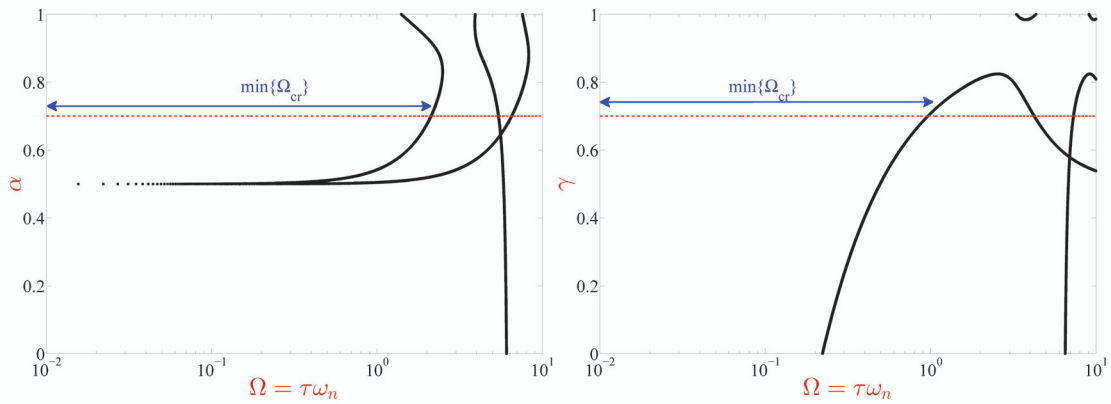

(a) (b)

Fig. 2.18. Obtaining PSI using RTHS stability diagrams: (a) Configuration 1: $\alpha = 0.7$, $\beta = 0.4$, $\gamma = 0.9$, $\zeta = 0.1$, (b) configuration 2: $\alpha = 0.9$, $\beta = 0.6$, $\gamma = 0.7$, $\zeta = 0.05$.

In Table 2.2, the PSI values associated with the two configurations shown in Figure 2.18 and three natural frequencies are listed. As listed in Table 2.2, configuration 1 with $\omega_n = 3\ rad/sec$ and configuration 2 with $\omega_n = 10\ rad/sec$ lead to the largest PSI value (i.e., the largest margin of stability) and the lowest PSI value (i.e., the smallest margin of stability), respectively. It should be noted that the use of PSI becomes even more significant in implementation of multi-degree-of-freedom RTHS (or geographically distributed RTHS) because higher modes of the structure are highly sensitive to time delays at the interface.

Table 2.2.
Predictive stability indicators for different configurations.

	$\omega_n(rad/sec)$	$\Omega_{cr}(rad)$	PSI ($\log(msec)$)
Configuration 1	3	2.123	6.56
Configuration 1	5	2.123	6.05
Configuration 1	10	2.123	5.36
Configuration 2	3	0.963	5.77
Configuration 2	5	0.963	5.26
Configuration 2	10	0.963	4.57

2.2.4 Unconditionally Stable Region

As noted earlier, Equation (2.33) may lead to 0, 1, or 2 meaningful critical frequency ratios. For case II and $\zeta = 5\%$, these three regions are shown in Figure 2.19.

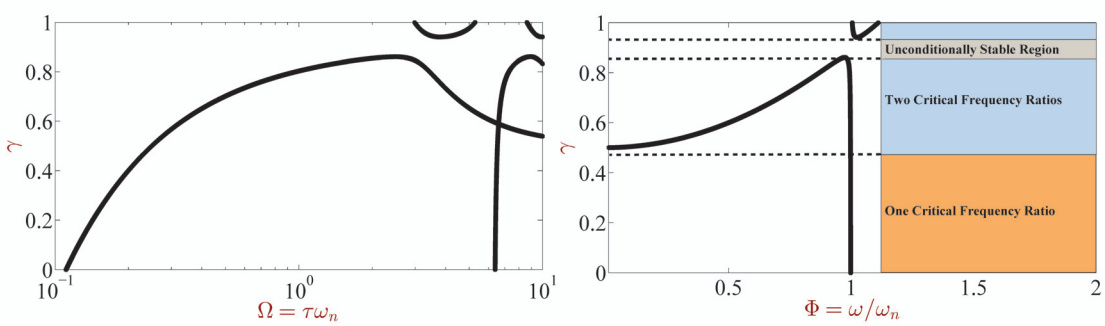

(a) Critical time delay. (b) Critical frequency ratio.

Fig. 2.19. Case II with $\zeta = 5\%$, (a) Normalized RTHS stability diagram showing Ω_{cr} vs. γ, (b) Plot of ϕ_{cr} vs. γ showing the three stability regions.

Using Equation (2.33), the required condition to have an unconditionally stable region is

$$(\gamma - \alpha) < 4\zeta^2(1 - 2\beta)[(1 - \alpha - \gamma) - (1 - 2\beta)\zeta^2] \tag{2.37}$$

Moreover, in terms of α and γ, the range of the unconditionally stable region, which occurs about $\gamma - \alpha = 0$, can be found using the following equation

$$(\gamma - \alpha)^2 + B(\gamma - \alpha) + C = 0 \tag{2.38}$$

where $B = 4(1 - 2\beta)\zeta^2$ and $C = -4\zeta^2(1 - 2\beta)(1 - 2\alpha - (1 - 2\beta)\zeta^2)$. Using Equation (2.38), the resulting unconditionally stable range associated with Case II about $\gamma - \alpha = 0$ and associated with various damping ratios can be obtained, see Figure 2.20. Thus, in certain RTHS configurations, there is a range about $\gamma - \alpha = 0$ in which

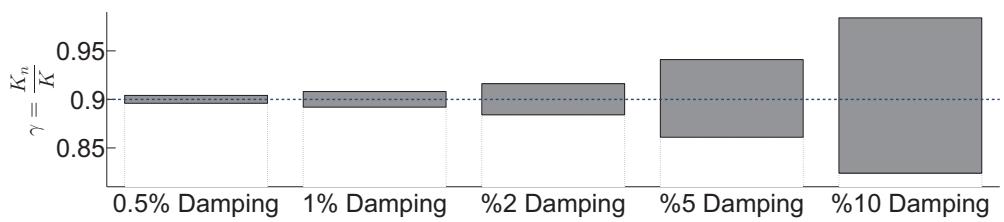

Fig. 2.20. Unconditionally stable range associated with case II for different damping ratios.

the system is unconditionally stable, and within that range, the critical time delay and PSI approaches ∞. Knowing the unconditionally stable region associated with a partitioning setup can be significant, especially when conducting geographically-distributed RTHS in which unpredictable time delay is a major challenge.

2.2.5 Minimum Stability Requirements

After obtaining the critical time delay using the RTHS stability diagrams or Equations (2.33) and (2.35a), one can identify the maximum permissible delay as the critical time delay. Therefore, if the interaction force signal has a time delay equal to or

greater than the critical time delay, the system will go unstable. Generally speaking, in SDOF RTHS, the time delay associated with the interaction force signal is

$$\tau_{F_{fb}} = \tau_{COMP} + \tau_{COMM} + \tau_{TS} \tag{2.39}$$

where τ_{COMP}, τ_{COMM}, and τ_{TS} are computational delay, communication delay, transfer system delay, respectively. Furthermore, if a ZOH digital-to-analog convertor is used, τ_{COMP} can be approximated by $(2f_s)^{-1}$ where f_s is the sampling frequency in Hz [48]. Assuming that τ_{COMM} is a known deterministic value, then, Equation (2.39) becomes

$$\tau_{F_{fb}} - \tau_{COMM} - (2f_s)^{-1} = \tau_{TS} \tag{2.40}$$

Therefore, with a given sampling frequency, the stability phase envelope which determines the minimum control requirements for the transfer system can be expressed as

$$e^{-j\omega(\tau_{cr} - \tau_{COMM} - (2f_s)^{-1})} = e^{-j\omega\tau_m} \tag{2.41}$$

where $\tau_m = \tau_{cr} - \tau_{COMM} - (2f_s)^{-1}$.

As shown in Figure 2.21, to conduct a stable SDOF RTHS, the phase plot of the transfer system control must lie above the stability phase envelope shown for a given value of τ_{cr}.

2.2.6 Weakly Nonlinear SDOF RTHS Systems

This section considers a physical substructure that is composed of weakly-nonlinear materials, wherein there is a nonlinearity between the materials' restoring forces and displacements, or composed of linear materials but loaded beyond the proportional limit. Let's examine how nonlinearity affects the overall stability of a SDOF RTHS system in the presence of feedback time delay. Consider a lightly-damped reference structure with the governing equation

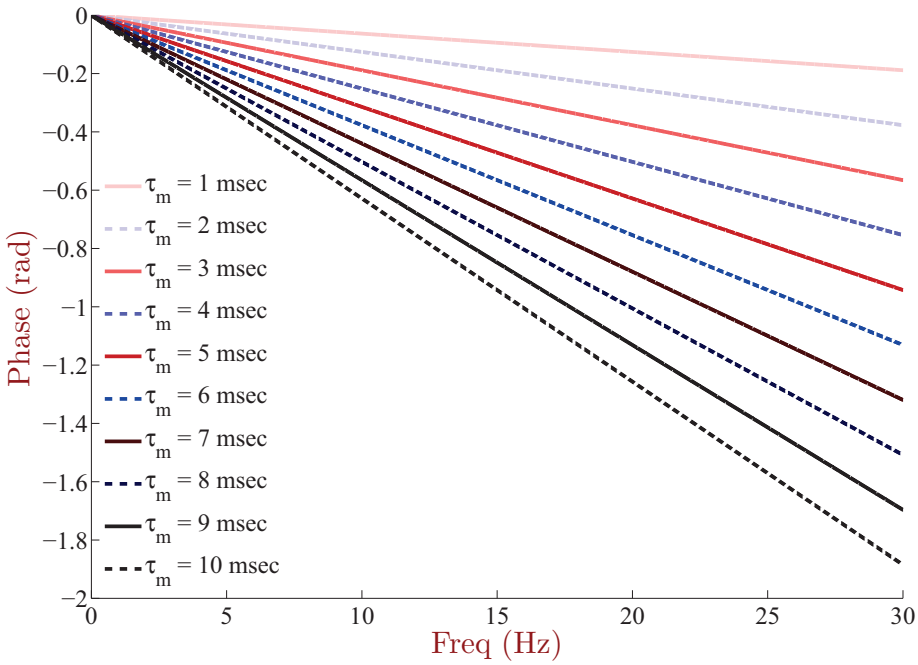

Fig. 2.21. Stability phase envelope to determine minimum control requirement.

$$M\ddot{x}(t) + C\dot{x}(t) + Kx(t) + \zeta R(x) = 0 \tag{2.42}$$

which is equivalent to

$$\ddot{x}(t) + 2\zeta\omega_n\dot{x}(t) + {\omega_n}^2 x(t) + \zeta M^{-1}R(x) = 0 \tag{2.43}$$

where $\zeta R(x)$ represents the weakly-nonlinear component of the restoring force. Weakly-nonlinear systems can be divided into two categories, (1) strain-hardening and (2) strain-softening. Figure 2.22 shows the qualitative behaviors of linear, strain-softening, and strain-hardening systems. In this work, it is assumed that these nonlinearities can be captured with cubic terms. Thus, Equation (2.43) becomes

$$\ddot{x}(t) + 2\zeta\omega_n\dot{x}(t) + {\omega_n}^2 x(t) + \zeta M^{-1}hx^3(t) = 0 \tag{2.44}$$

where $\{h < 0,\ h = 0,\ h > 0\}$ corresponds to {strain-softening, linear, strain-hardening} systems. Equation (2.44) can be partitioned into computational and physical substructures using the partitioning parameters, $\{\alpha, \beta, \gamma\} = \{M_n/M, C_n/C, K_n/K\}$,

$$\begin{aligned}&\{\alpha\ddot{x}(t) + 2\zeta\beta\omega_n\dot{x}(t) + \gamma{\omega_n}^2x(t)\}\\&+\{(1-\alpha)\ddot{x}(t) + 2\zeta(1-\beta)\omega_n\dot{x}(t) + (1-\gamma){\omega_n}^2x(t) + \zeta M^{-1}hx^3(t)\} = 0\end{aligned} \tag{2.45}$$

where in the presence of feedback delay, Equation (2.45) becomes

$$\begin{aligned}&\{\alpha\ddot{x}(t) + 2\zeta\beta\omega_n\dot{x}(t) + \gamma{\omega_n}^2x(t)\}\\&+\{(1-\alpha)\ddot{x}(t-\tau) + 2\zeta(1-\beta)\omega_n\dot{x}(t-\tau) + (1-\gamma){\omega_n}^2x(t-\tau)\}\\&+\{\zeta M^{-1}hx^3(t-\tau)\} = 0\end{aligned} \tag{2.46}$$

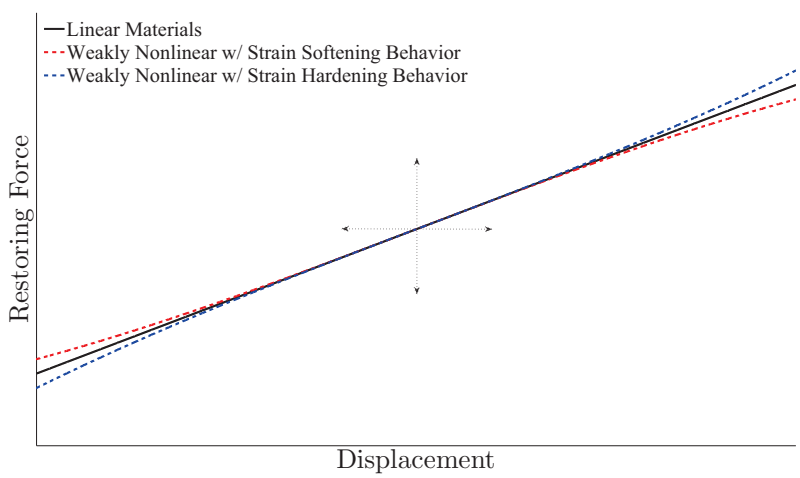

Fig. 2.22. Qualitative behavior of linear strain-softening, and strain-hardening materials.

For a SDOF RTHS system, it has been shown that the presence of a feedback time delay effectively adds energy into the system [2, 7, 49]. Figure 2.23 shows desired displacement against the restoring forces of linear and weakly-nonlinear systems associated with different time delays, where $\tau_1 < \tau_2 < \tau_3$. In each case, the additional energy added to the system is the enclosed area. Clearly, as the time delay becomes larger, the effective amount of added energy increases.

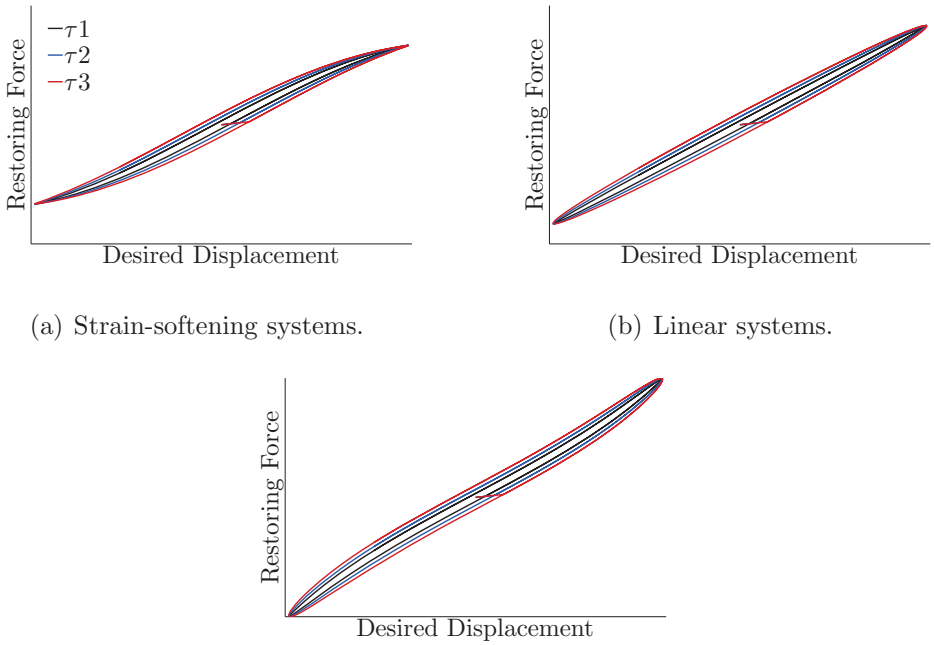

(a) Strain-softening systems.

(b) Linear systems.

(c) Strain-hardening systems.

Fig. 2.23. Additional energy due to time delay ($\tau_1 < \tau_2 < \tau_3$).

For RTHS, instability occurs when the additional energy becomes greater than the dissipated energy [49]. Using the stability switch criterion, the critical time delay associated with the linear system is obtained, and the qualitative effects of weak nonlinearity on the stability of the system can be understood by computing and comparing the enclosed areas shown in Figure 2.23.

Linear Systems

In Equation (2.46), linear systems correspond to systems with $h = 0$. Therefore, the enclosed area in Figure 2.23(b), can be computed as

$$A_L(\tau) = \int_{x(t_0)}^{x(t_1)} (1-\gamma)K[x(t) - x(t-\tau)]dx \tag{2.47a}$$

$$A_L(\tau) = \int_{t_0}^{t_1} (1-\gamma)K[x(t) - x(t-\tau)]\dot{x}(t)dt \tag{2.47b}$$

Strain-Softening Systems

In Equation (2.46), strain-softening systems correspond to systems with $h<0$. Therefore, the enclosed area in Figure 2.23(a) can be computed as

$$A_S(\tau) = \int_{x(t_0)}^{x(t_1)} \{(1-\gamma)K[x(t)-x(t-\tau)] + \zeta h[x^3(t)-x^3(t-\tau)]\}dx \tag{2.48a}$$

$$A_S(\tau) = \int_{t_0}^{t_1} [x(t)-x(t-\tau)]\{(1-\gamma)K + \zeta h[x^2(t)+x(t)x(t-\tau)+x^2(t-\tau)]\}\dot{x}(t)dt \tag{2.48b}$$

by applying the Tylor expansion on $[x(t)-x(t-\tau)]$ and truncating $o(\tau^2)$, $[x(t)-x(t-\tau)]$ can be approximated as $[\tau\dot{x}(t)]$, yielding

$$A_S(\tau) \approx \int_{t_0}^{t_1} (1-\gamma)K[x(t)-x(t-\tau)]\dot{x}(t)dt + \int_{t_0}^{t_1} \zeta h\tau[x^2(t)+x(t)x(t-\tau)+x^2(t-\tau)]\dot{x}^2(t)dt \tag{2.48c}$$

$$A_S(\tau) \approx A_L(\tau) + \Delta A_S(\tau) \tag{2.48d}$$

Knowing that $\forall x(t), \tau$ and $\zeta h\tau < 0 : \zeta h\tau[x^2(t)+x(t)x(t-\tau)+x^2(t-\tau)]\dot{x}^2(t) \leq 0$ yields

$$\Delta A_S(\tau) \leq 0 \tag{2.49a}$$

$$A_S(\tau) \leq A_L(\tau) \tag{2.49b}$$

Thus, the enclosed area in Figure 2.23(a) (i.e., the additional energy for strain-softening systems) is always smaller than the enclosed area in Figure 2.23(b) (i.e., the additional energy for linear systems).

Strain-Hardening Systems

In Equation (2.46), strain-hardening systems correspond to systems with $h>0$. Therefore, the enclosed area in Figure 2.23(c) can be computed as

$$A_H(\tau) = \int_{x(t_0)}^{x(t_1)} \{(1-\gamma)K[x(t)-x(t-\tau)] + \zeta h[x^3(t)-x^3(t-\tau)]\}dx \tag{2.50a}$$

$$A_H(\tau) = \int_{t_0}^{t_1} [x(t) - x(t-\tau)]\{(1-\gamma)K + \zeta h[x^2(t) + x(t)x(t-\tau) + x^2(t-\tau)]\}\dot{x}(t)dt$$

by applying the Tylor expansion on $[x(t) - x(t-\tau)]$ and truncating $o(\tau^2)$, $[x(t) - x(t-\tau)]$ can be approximated as $[\tau\dot{x}(t)]$, yielding

$$A_H(\tau) \approx \int_{t_0}^{t_1} (1-\gamma)K[x(t) - x(t-\tau)]\dot{x}(t)dt + \int_{t_0}^{t_1} \zeta h\tau[x^2(t) + x(t)x(t-\tau) + x^2(t-\tau)]\dot{x}^2(t)dt \tag{2.50b}$$

$$A_H(\tau) \approx A_L(\tau) + \Delta A_H(\tau) \tag{2.50c}$$

Knowing that $\forall x(t), \tau$ and $\zeta h\tau > 0 : \zeta h\tau[x^2(t) + x(t)x(t-\tau) + x^2(t-\tau)]\dot{x}^2(t) \geq 0$ yields

$$\Delta A_H(\tau) \geq 0 \tag{2.51a}$$

$$A_H(\tau) \geq A_L(\tau) \tag{2.51b}$$

Thus, the enclosed area in Figure 2.23(c) (i.e., the additional energy for strain-hardening systems) is always larger than the enclosed area in Figure 2.23(b) (i.e., the additional energy for linear systems). In Figure 2.24, for a given τ, $A_S(\tau), A_L(\tau)$, and $A_H(\tau)$ are compared, and clearly

$$A_H(\tau) \geq A_L(\tau) \geq A_S(\tau) \tag{2.52}$$

For weakly-nonlinear systems, the system can be linearized about its fixed point, and using the RTHS stability switch criterion, the critical time delay can be obtained. However, it should be noted that depending upon whether the system exhibits softening or hardening behavior, the obtained value is underestimated or overestimated, respectively. Therefore, for weakly-nonlinear systems with softening behavior, the obtained value is a conservative value. Furthermore, $A_L(\tau) - A_S(\tau)$ and $A_H(\tau) - A_L(\tau)$ are linearly proportional to $\zeta h\tau$. Thus, the level of nonlinearity and damping of the reference structure determine the level of overestimation or underestimation of the critical time delay value obtained using the RTHS stability switch criterion.

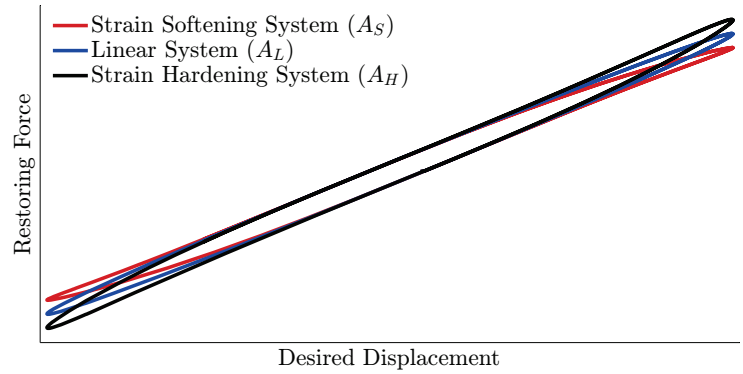

Fig. 2.24. Additional energy due to time delay in the restoring force.

2.2.7 Effective Damping

It has been shown that when a time delay is present in the system, the impact of that delay is similar to that of negative damping. The concept of effective damping was first applied to RTHS in [37, 50]. This interpretation of the impact of time delay has been used by several other researchers as well, [30,33,49]. For instance, Mosqueda, *et al.* [30] considered the following partitioning of a SDOF linear system

$$M\ddot{x}(t) + C\dot{x}(t) = -M\ddot{x}_g(t) - F_{fb}(t-\tau) \tag{2.53a}$$

$$F_{fb}(t) = Kx(t) \tag{2.53b}$$

To investigate the impact of time delay in this system, they compared the dynamics of the delay frequency response and the frequency response of the reference system and showed that this SDOF RTHS system can be approximated as

$$M\ddot{x}(t) + C'\dot{x}(t) + Kx = -M\ddot{x}_g(t) \tag{2.54}$$

where $C' = 2\zeta_{eff}\omega_n$ and ζ_{eff} is a function of damping ratio (ζ), natural frequency of the reference structure (ω_n), and time delay (τ). Mosqueda, *et al.* showed that ζ_{eff} becomes

$$\zeta_{eff} = \sqrt{\zeta^2 - \zeta\sin(\tau\omega_n) + \frac{(1-\cos(\tau\omega_n)))}{2}} \tag{2.55}$$

It should be noted that in the derivation of Equation (2.55), they assumed that the resonant peaks of the reference structure and the RTHS system occur at the same frequency. Equation (2.55) provides the effective damping corresponding to the particular partitioning configuration shown in Equations (2.53a) and (2.53b).

Here, the impact of time delay in a general partitioning configuration is considered by incorporating three partitioning parameters: $\alpha = M_n/M$, $\beta = C_n/C$, and $\gamma = K_n/K$. Consider the SDOF RTHS system, Equations (2.18a) and (2.18b), and divide them by M, they become

$$\begin{gathered}\{\alpha\ddot{x}(t) + 2\beta\zeta\omega_n\dot{x}(t) + \gamma{\omega_n}^2 x\} \\ +\{(1-\alpha)\ddot{x}(t) + 2(1-\beta)\zeta\omega_n\dot{x}(t) + (1-\gamma){\omega_n}^2 x\} = -\ddot{x}_g(t)\end{gathered} \tag{2.56}$$

Apply Fourier transform to Equation (2.56), the frequency response function of the partitioned system, $x(j\omega)$ becomes

$$x(j\omega) = \frac{-1}{{\omega_n}^2 C_N + {\omega_n}^2 C_P e^{-j\tau\omega}}\ddot{x}_g(j\omega) \tag{2.57}$$

where

$$C_N = -\alpha(\omega/\omega_n)^2 + j2\beta\zeta(\omega/\omega_n) + \gamma \tag{2.58a}$$

$$C_P = -(1-\alpha)(\omega/\omega_n)^2 + j2(1-\beta)\zeta(\omega/\omega_n) + (1-\gamma) \tag{2.58b}$$

Equation (2.57) can be normalized with respect to ω_n, as

$$\omega_n^2 x(j\omega) = \frac{-1}{C_N + C_P e^{-j\tau\omega}}\ddot{x}_g(j\omega) \tag{2.59}$$

Incorporating two new variables, $\phi = \omega/\omega_n$ and $\Omega = \tau\omega_n$, Equations (2.58a) and (2.58b) can be written as

$$C_N = -\alpha\phi^2 + j2\beta\zeta\phi + \gamma \tag{2.60a}$$

$$C_P = -(1-\alpha)\phi^2 + j2(1-\beta)\zeta\phi + (1-\gamma) \tag{2.60b}$$

Furthermore,

$$e^{-j\tau\omega} = e^{-j\Omega\phi} \tag{2.61}$$

and the normalized characteristic equation of the SDOF RTHS in Equation (2.56) becomes

$$\Gamma(\phi,\Omega) = \{(-\alpha\phi^2+\gamma)+((\alpha-1)\phi^2+(1-\gamma))\cos(\Omega\phi+(2\zeta(1-\beta)\phi)\sin(\Omega\phi))\} \\ +\{(2\zeta\beta\phi)+(2\zeta(1-\beta)\phi)\cos(\Omega\phi)+((1-\alpha)\phi^2-(1-\gamma))\sin(\Omega\phi)\}j \tag{2.62}$$

where the normalized characteristic equation of the reference structure can be expressed as

$$\Gamma(\phi) = -\phi^2 + j2\zeta\phi + 1 \tag{2.63}$$

By comparing the roots of Equation (2.62) and Equation (2.63), a SDOF system shown in Equation (2.56) can be approximated as

$$\ddot{x}(t) + 2\zeta_{eff}\omega_n\dot{x}(t) + {\omega_n}^2 x = -\ddot{x}_g(t) \tag{2.64}$$

where, the effective damping becomes

$$\zeta_{eff} = \sqrt{A_0 + A_1\zeta + A_2\zeta^2} \tag{2.65}$$

and

$$\begin{aligned} A_0 &= 0.5(\gamma-\alpha)^2(1-cos(\Omega)) \\ A_1 &= \sin(\Omega)(\gamma-\alpha) \\ A_2 &= 1+2\beta(1-\cos(\Omega))(\beta-1) \end{aligned} \tag{2.66}$$

It should be noted that in the derivation of Equation (2.64), the assumption is that the resonant peak in Equation (2.57) occurs in the close vicinity of ω_n meaning that the presence of delay in the feedback force signal does not affect the value of natural frequency (ω_n) significantly.

2.2.8 Predictive Performance Indicator

In this section, the frequency response function of error in SDOF partitioned systems due to time delay is used to establish a new pre-experiment performance metric. The frequency response function of the reference structure in Equation (2.17) can be expressed as

$$x_{REF}(j\omega) = \frac{-\ddot{x}_g(j\omega)}{-\omega^2 + 2j\zeta\omega_n\omega + {\omega_n}^2} \tag{2.67}$$

Equation (2.67) can be normalized with respect to ω_n as follows

$$x_{REF}(j\phi) = \frac{-1}{{\omega_n}^2 C_R}\ddot{x}_g(j\phi) \tag{2.68}$$

where

$$C_R = -(\omega/\omega_n)^2 + 2j\zeta\omega/\omega_n + 1 = -\phi^2 + 2j\zeta\phi + 1 \tag{2.69}$$

From Equation (2.59), the normalized frequency response function of the SDOF partitioned system becomes

$$x_{DELAY}(j\phi, \Omega) = \frac{-1}{{\omega_n}^2[C_N + C_P e^{-j\Omega\phi}]}\ddot{x}_g(j\phi) \tag{2.70}$$

Here, it should be noted that in the absence of a feedback time delay, the frequency response of RTHS, $x_{DELAY}(j\phi, \Omega)$, and that of the reference structure, $x_{REF}(j\phi)$, are identical. For $\tau = 0$ ($\Omega = \tau\omega_n = 0$), $e^{j\Omega\phi}$ becomes 1. Therefore,

$$x_{REF}(j\phi) = x_{DELAY}(j\phi, 0) = \frac{-1}{{\omega_n}^2[C_N + C_P \times 1]}\ddot{x}_g(j\phi) = \frac{-1}{{\omega_n}^2 C_R}\ddot{x}_g(j\phi) \tag{2.71}$$

However, for $\tau \neq 0$, the frequency response function of the error due to the presence of time delay in the feedback force signal can be expressed as

$$H_{ERR}(\Omega, \phi) = \frac{x_{REF}(j\phi) - x_{DELAY}(j\phi, \Omega)}{\ddot{x}_g(j\phi)} = \frac{C_P(1 - e^{-j\Omega\phi})}{\omega_n^2 C_R(C_N + C_P e^{-j\Omega\phi})} \tag{2.72}$$

The autospectral density of the error is

$$S_{ERR}(\Omega, \phi) = S_g(\phi)|H_{ERR}(\Omega, \phi)|^2 = S_g(\phi)H_{ERR}(\Omega, \phi)H^*_{ERR}(\Omega, \phi) \tag{2.73}$$

where $\{\ldots\}^*$ and S_g represent the complex conjugate of $\{\ldots\}$ and autospectral density (or power spectral density) of the ground acceleration, respectively. It should be noted that S_g is frequency-dependent for earthquake histories and constant for white noise ground accelerations. The steady-state variance of the error is related to the autospectral density as follows

$$\sigma^2 = \lim_{r' \to \infty} \frac{1}{2\pi} \int_{-r'}^{r'} S_{ERR}(\omega)\, \mathrm{d}\omega \tag{2.74}$$

Thus, using Equations (2.73) and (2.74), the steady-state variance of the error presented in a stationary SDOF delayed system becomes

$$\sigma^2 = \lim_{r'\to\infty} \frac{1}{2\pi} \int_{-r'}^{r'} S_g |H_{ERR}|^2 \, \mathrm{d}\omega \; = \lim_{r'\to\infty} \frac{1}{2\pi\omega_n^4} \int_{-r'}^{r'} \omega_n^4 S_g |H_{ERR}|^2 \, \mathrm{d}\omega \tag{2.75}$$

With a change of variable, Equation (2.76) becomes

$$\sigma^2 = \lim_{r\to\infty} \frac{1}{2\pi\omega_n^3} \int_{-r}^{r} \omega_n^4 S_g |H_{ERR}|^2 \, \mathrm{d}\phi \tag{2.76}$$

Taking advantages of the symmetry of autospectral density and constant autospectral density of white noise ground acceleration input, a predictive performance indicator (PPI) is defined as

$$PPI = \lim_{r\to\infty} \frac{1}{\pi} \int_{0}^{r} \omega_n^4 |H_{ERR}|^2 \, \mathrm{d}\phi \; = \omega_n^3 \sigma^2 / S_g \tag{2.77}$$

Equation (2.77) indicates that the steady-state variance of the error can be found by computing the area under the normalized autospectral density function of the error. Usually, the peak of $|I_{ERR}|^2(\pi)^{-1}$ occurs at $\phi \approx 1$ which corresponds to $\omega \approx \omega_n$ and the frequency bandwidth of interest is the seismic frequency bandwidth and it is restricted to a low frequency bandwidth ($0 < \omega < \omega_s$). Therefore, as shown in Figure 2.25, for $r \approx \omega_s/\omega_n$, $\omega_n^3\sigma^2/S_g$ is approximated as

$$PPI = \frac{1}{\pi} \int_{0}^{r} \omega_n^4 |H_{ERR}|^2 \, \mathrm{d}\phi \; \approx \omega_n^3 \sigma^2 / S_g \tag{2.78}$$

To derive the PPI in Equation (2.77), delta-correlated white noise ground acceleration with a constant autospectral density (S_g) over the whole spectrum is chosen. However, it should be noted that, for any specific seismic history, a similar indicator can be produced using the following equation

$$PPI' = \frac{1}{2\pi} \frac{\int_0^{a\omega_n^{-1}} \omega_n^4 S_g(\phi) |H_{ERR}|^2 \, \mathrm{d}\phi}{\int_0^{a\omega_n^{-1}} S_g(\phi) \, \mathrm{d}\phi} \approx \omega_n^3 \sigma^2 / [\int_0^{a\omega_n^{-1}} S_g(\phi) \, \mathrm{d}\phi] \tag{2.79}$$

where S_g' is the frequency-dependent auto-spectral density of the seismic input and $[-a, a]$ is the corresponding seismic bandwidth.

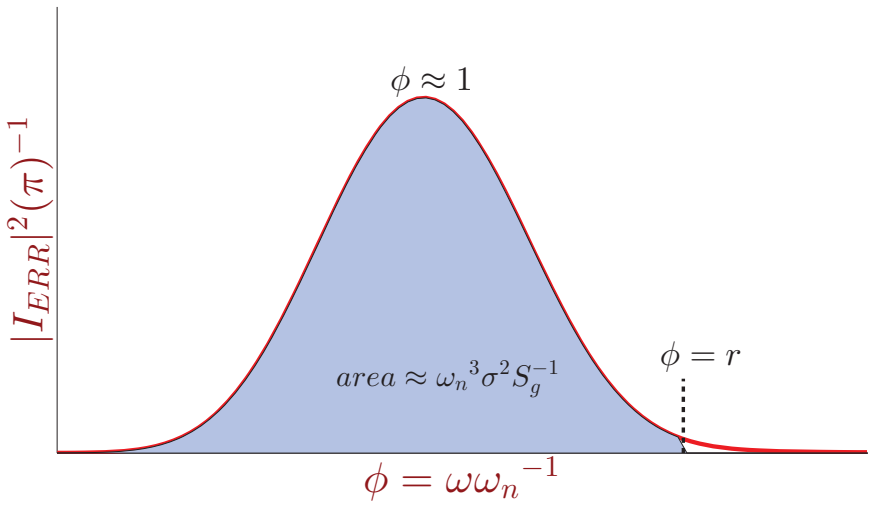

Fig. 2.25. PPI: area under the normalized autospectral density function.

2.2.9 Stability and Performance Diagrams for Linear SDOF RTHS

In this section, the impacts of partitioning choices, transfer system performance, and structural characteristics of the reference on the performance of a linear RTHS is investigated using PPI. Varying four different parameters (α, β, γ, and ζ), nine different partitioning cases, listed in Table 2.3, are considered and the corresponding PPI values are plotted in Figure 2.25. Furthermore, using the RTHS stability switch criterion, the stability diagrams associated with each partitioning case are plotted. It should be noted that a lower PPI indicates a less sensitive RTHS configuration to phase discrepancy at the interface, therefore, a more successful RTHS. This performance analysis is valid for the stable region that is the area to the left of the stability switch curve ($\Omega < \Omega_{cr}$).

Some important observations can be made from Figure 2.26.

- As a rule of thumb, the PPI is closely related to the value of $|\gamma - \alpha|$. For a specific transfer system performance, designing an experiment to have a smaller value of $|\gamma - \alpha|$ usually leads to a lower PPI and better performance.

Table 2.3.
Partitioning parameters of the nine cases examined.

	Case 1	Case 2	Case 3	Case 4	Case 5	Case 6	Case 7	Case 8	Case 9
α	$\in [0,1]$	0.8	0.95	$\in [0,1]$	0.8	0.8	$\in [0,1]$	0.8	$\in [0,1]$
β	0.5	0.5	0.5	0.5	0.5	$\in [0,1]$	0.5	0.5	0.5
γ	0.1	$\in [0,1]$	$\in [0,1]$	0.1	$\in [0,1]$	0.1	0.1	$\in [0,1]$	0.25
ζ	0.01	0.01	0.01	0.02	0.02	0.02	0.04	0.04	0.04

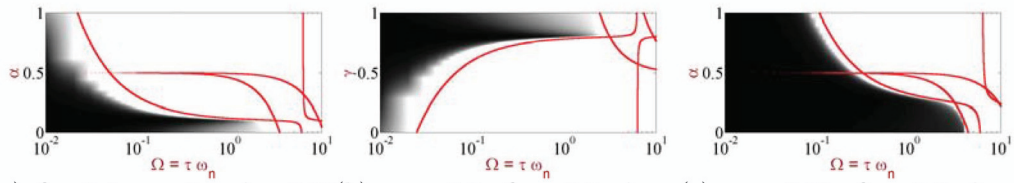

(a) $\beta = 0.5$, $\gamma = 0.1$, $\zeta = 0.01$ (b) $\alpha = 0.8$, $\beta = 0.5$, $\zeta = 0.01$ (c) $\alpha = 0.95$, $\beta = 0.5$, $\zeta = 0.01$

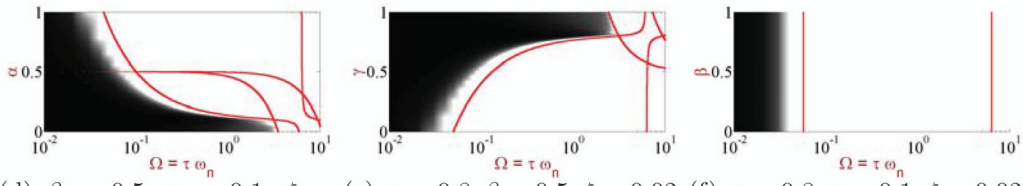

(d) $\beta = 0.5$, $\gamma = 0.1$, $\zeta = 0.02$ (e) $\alpha = 0.8, \beta = 0.5, \zeta = 0.02$ (f) $\alpha = 0.8, \gamma = 0.1, \zeta = 0.02$

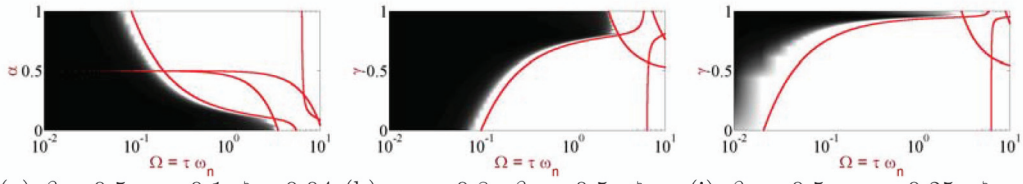

(g) $\beta = 0.5, \gamma = 0.1, \zeta = 0.04$ (h) $\alpha = 0.8$, $\beta = 0.5$, $\zeta = 0.04$ (i) $\beta = 0.5$, $\gamma = 0.25$, $\zeta = 0.04$

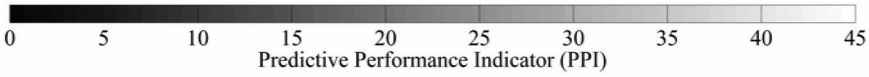

(j) scale = 0.32

Fig. 2.26. Performance and stability diagrams of the nine cases listed in Table 2.3.

- For a specific transfer system performance, a reference structure with a higher damping leads to a more successful simulation. To see the impact of the reference structure's damping (ζ), one can compare Figures 2.26(a), 2.26(d), and 2.26(g) or Figures 2.26(b), 2.26(e), and 2.26(h).

- The overall success of an RTHS is almost independent of how the reference structure's damping is partitioned (β factor) between the computational and physical substructures, see Figure 2.26(f).

- To achieve a better performance in conducting SDOF RTHS with a specific transfer system, decreasing $|\gamma - \alpha|$, ω_n and/or increasing ζ are effective options.

- To conduct a successful RTHS, the partitioning configuration needs to be sufficiently away from the stability switch curve.

- Generally speaking, conducting an RTHS with a small value of γ (i.e., more stiffness in the physical substructure) and a large value of α (i.e., more mass in the computational substructure) is the most challenging configuration, see Figures 2.26(a), 2.26(b), 2.26(c), and 2.26(f).

2.2.10 Illustrative Example: Virtual RTHS with Pure Time Delay

A simple way to conduct vRTHS is to lumpt the transfer system dynamics, communication and computational delays into a single time delay (τ). In this section, the results of 2000 realizations of vRTHS(s) with pure time delay are shown to verify that, (1) PPI is independent of the power of input ground acceleration and (2) PPI is a function of $\Omega = \tau\omega_n$ and independent of τ or ω_n. Furthermore, the impacts of $|\gamma - \alpha|$, ζ, and Ω, which are the most influential parameters on the PPI value, are investigated. In this study, eight different cases, listed in Table 2.4, are selected and each case is simulated in MATLAB using 125 different values for τ and two band-limited white noise inputs (with autospectral density of $S_g = 1\, m^2 sec^2$ and $S_g = 2\, m^2 sec^2$).

So, a total of 2000 vRTHS trials are conducted ($8 \times 2 \times 125$). In Figure 2.27, these eight cases are indicated on the performance diagrams.

Table 2.4.
Simulation case studies ($\alpha = 0.8$ and $\beta = 0.5$).

	γ	ζ	Ω	PPI		γ	ζ	Ω	PPI
Case 1	0.8	0.01	0.05	9.1×10^{-3}	Case 5	0.8	0.04	0.05	2.3×10^{-3}
Case 2	0.65	0.01	0.05	3.5×10^{0}	Case 6	0.65	0.04	0.05	3.4×10^{-2}
Case 3	0.8	0.01	0.1	3.6×10^{-2}	Case 7	0.8	0.04	0.1	9.1×10^{-3}
Case 4	0.65	0.01	0.1	5.1×10^{1}	Case 8	0.65	0.04	0.1	1.6×10^{-1}

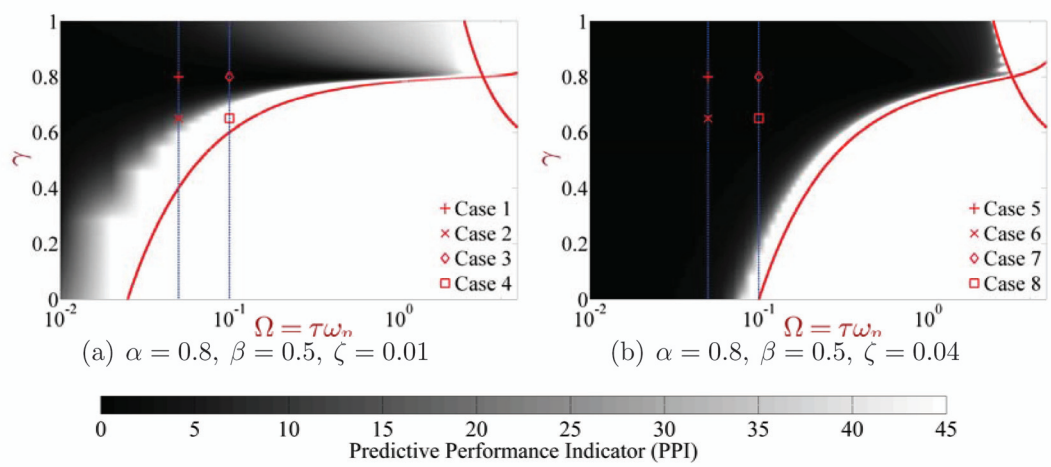

(a) $\alpha = 0.8$, $\beta = 0.5$, $\zeta = 0.01$ (b) $\alpha = 0.8$, $\beta = 0.5$, $\zeta = 0.04$

Fig. 2.27. Indication of vRTHS cases on the performance/stability diagrams.

In Figure 2.28, the $\omega_n^3 \sigma^2 / S_g$ values obtained from the vRTHS trials are compared with the corresponding PPI values using Equation (2.79). Each subfigure shows two sets of results corresponding to two input ground accelerations. Some important observations can be made from Figure 2.28.

- PPI is independent of the power of input ground acceleration. As one can see in Figures 2.28(a)-2.28(h), the PPI values are independents of which input ground acceleration is chosen.
- In each subfigure, the value of $\Omega = \tau\omega_n$ is constant, yet, τ and ω_n vary dependently, i.e., $\tau = \Omega\omega_n^{-1}$. The results indicate that PPI is a function of Ω and independent of τ or ω_n.
- A smaller values of $|\gamma - \alpha|$ and ω_n leads to a smaller PPI value which corresponds to a more successful RTHS.
- A larger value of ζ leads to a smaller PPI value which corresponds to a more successful RTHS.

2.2.11 Illustrative Example: Virtual RTHS with Transfer System Dynamics

In this section, to conduct a more realistic vRTHS, transfer system dynamics are considered to take into account the phase discrepancy at the interface. Therefore, two servo-hydraulic actuators were identified at the Intelligent Infrastructure System Laboratory (*IISL*) at Purdue University. The identified dynamics of the two servo-hydraulic actuators are,

$$TS_1 = \frac{x_{msd}(\omega)}{x_{cmd}(\omega)} = \frac{2.382 \times 10^9}{\omega^4 - j485.5\omega^3 - 1.317 \times 10^5\omega^2 + j3.182 \times 10^7\omega + 2.382 \times 10^9} \tag{2.80}$$

$$TS_2 = \frac{x_{msd}(\omega)}{x_{cmd}(\omega)} = \frac{4.520 \times 10^9}{\omega^4 - j577.1\omega^3 - 2.680 \times 10^5\omega^2 + j6.282 \times 10^7\omega + 4.930 \times 10^9} \tag{2.81}$$

and, the corresponding magnitude and phase plots are provided in Figures 2.29(a) and 2.29(b).

In this study, 198 vRTHS trials are conducted with the partitioning choices provided in Table 2.5. The input is a band-limited white noise with the Gaussian distribution (signal power = 1) and the natural frequency of the reference structure (ω_n)

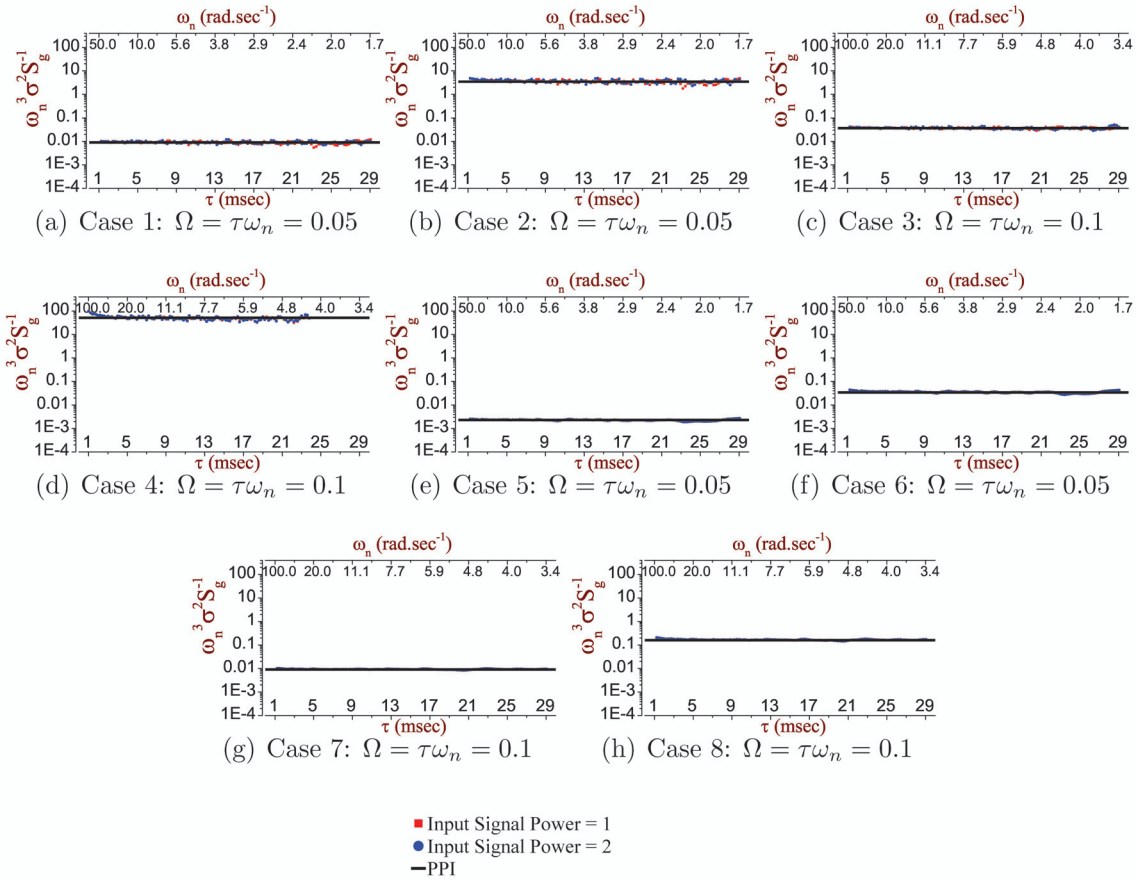

(a) Case 1: $\Omega = \tau\omega_n = 0.05$ (b) Case 2: $\Omega = \tau\omega_n = 0.05$ (c) Case 3: $\Omega = \tau\omega_n = 0.1$

(d) Case 4: $\Omega = \tau\omega_n = 0.1$ (e) Case 5: $\Omega = \tau\omega_n = 0.05$ (f) Case 6: $\Omega = \tau\omega_n = 0.05$

(g) Case 7: $\Omega = \tau\omega_n = 0.1$ (h) Case 8: $\Omega = \tau\omega_n = 0.1$

Fig. 2.28. Comparisons of simulated values of $\omega_n^3\sigma^2 S_g^{-1}$ with the corresponding PPI values associated with various partitioning choices.

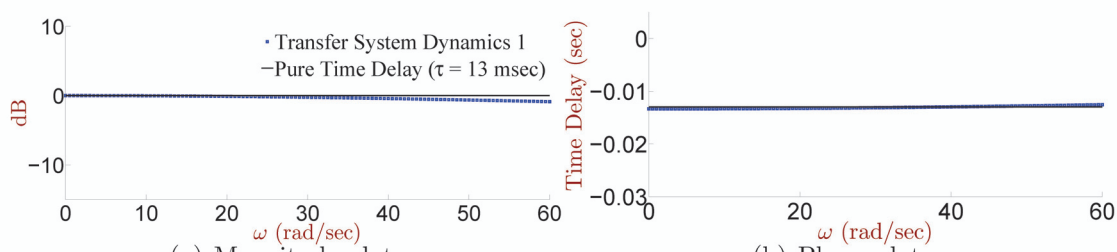

(a) Magnitude plot (b) Phase plot.

Fig. 2.29. Frequency responses of hydraulic actuator (TS_1) and pure time delay.

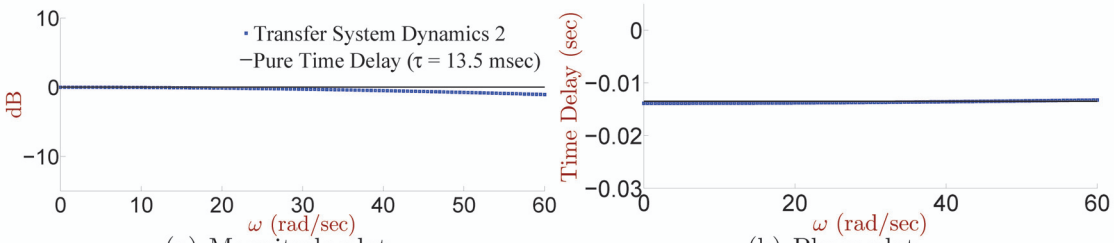

(a) Magnitude plot (b) Phase plot.

Fig. 2.30. Frequency responses of hydraulic actuator (TS_2) and pure time delay.

varies. In the first set, 99 vRTHS trials are conducted with the partitioning choice 1 and the transfer system 1 (TS_1). In the second set, 99 vRTHS trials are conducted with the partitioning choice 2 and the transfer system 2 (TS_2).

Table 2.5.
Partitioning choices.

Choice No.	α	β	γ	ζ	Computational Delay	Communication Delay
1	0.8	0.5	0.8	0.01	8192^{-1}	4096^{-1}
2	0.9	0.5	0.9	0.02	2048^{-1}	1024^{-1}

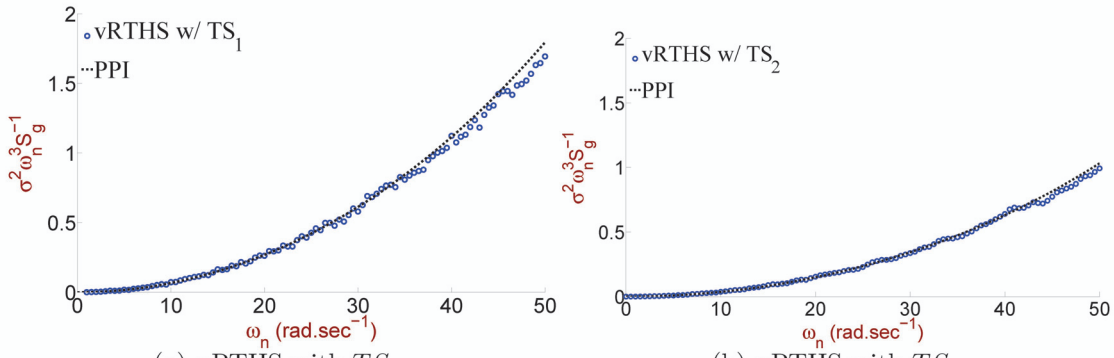

(a) vRTHS with TS_1 (b) vRTHS with TS_2

Fig. 2.31. Comparisons of $\sigma^2\omega_n^3 S_g^{-1}$ values obtained from vRTHS(s) with the corresponding PPI values.

In Figure 2.31, the $\sigma^2\omega_n^2/S_g$ values obtained from the vRTHS trials are compared with the corresponding PPI values. The comparisons show that PPI can be effectively used when transfer system dynamics, computational delays, and communication delays are all considered.

2.2.12 Illustrative Example: RTHS Case Study

In this section, the objective is to demonstrate the use of PSI and PPI as part of a systematic procedure to conduct a successful RTHS. The first step is to estimate the partitioning configurations. Then, the performance of transfer system, communication and computational delays are identified. The final step is to determine the stability and performance of the configuration either using stability/performance diagrams or directly computing the PSI and PPI values. For instance, in this case study (1) the performance of the transfer system (i.e., a servo hydraulic actuator) is relatively poor (see Figure 2.32), (2) the reference structure has a relatively large natural frequency ($\omega_n = 32.9\ \frac{rad}{sec}$) and it is lightly damped ($\zeta = 0.014$). Therefore, that $\Omega = \tau\omega_n$ is relatively large and ζ is relatively small makes this experiment quite challenging. In this experiment, the sampling frequency, computational delay, communication delay, and approximated transfer system delay are 4096 *Hz*, 0.12 *msec*, 0.24 *msec*, and 14.4 *msec*, respectively. Having assigned ζ and Ω, the only important parameter which can reduce the PPI value and enables a successful RTHS is $|\gamma - \alpha|$. Thus, the reference structure is partitioned as provided in Table 2.6. It should be noted that the natural frequency of the physical substructure is within the seismic bandwidth. The corresponding PPI value is 0.205 and by referring to the definition of the PPI value in Equation 2.79, the expected standard deviation of error for the system subject to a BLWN input with power spectral density of S_g is $0.0024\sqrt{S_g}$.

This partitioning choice minimizes the value of $|\gamma - \alpha|$ which maximizes the likelihood of conducting a successful RTHS experiment. In Figure 2.33(a), the RTHS case is indicated on the performance/stability diagram. Figure 2.33(a) shows that for the

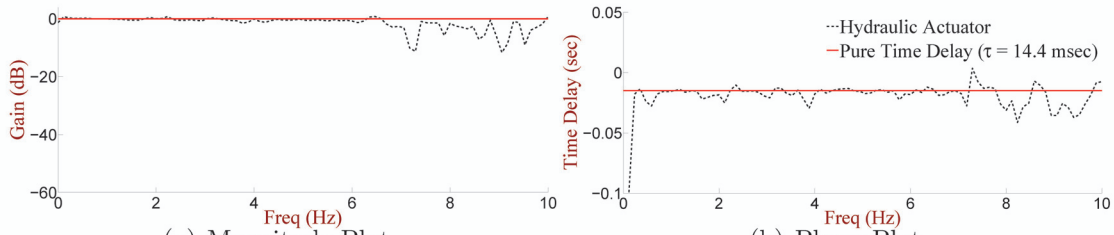

(a) Magnitude Plot (b) Phase Plot

Fig. 2.32. Frequency responses of hydraulic actuator and pure time delay.

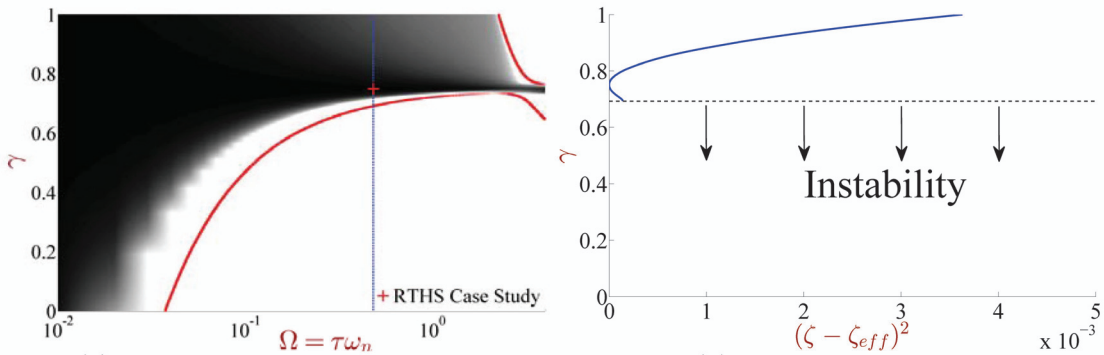

(a) RTHS Performance Diagram (b) Effective Damping

Fig. 2.33. Selection of a partitioning parameter (γ) using RTHS performance diagram and effective damping method.

specific values of α, β, ζ, and Ω, $\gamma = \alpha = 0.75$ is the best choice and it minimizes the PPI value. Furthermore, in Figure 2.33(b), γ is plotted versus $(\zeta - \zeta_{eff})^2$ in which

Table 2.6.
Reference and substructures.

	Reference	Physical	computational	Partitioning Parameter
M(kg)	98.4	24.6	73.8	$\alpha = 0.75$
C($N.s.m^{-1}$)	88.7	15.8	72.9	$\beta = 0.82$
K($N.m^{-1}$)	10.67×10^4	2.67×10^4	8.00×10^4	$\gamma = 0.75$

ζ_{eff} is obtained using Equation (2.65) and the damping of the reference structure (ζ) is 0.014. Figure 2.33(b) confirms that for the specified values of α, β, ζ, and Ω, $\gamma = \alpha = 0.75$ is the best partitioning choice (i.e., $\zeta_{eff} \approx \zeta$). With this configuration, even though τ is relatively large, RTHS can be effectively conducted with accurate results.

Using this partitioning choice, the experiment is conducted, see Figure 2.34, while the exciting input is the Chi-Chi earthquake with the peak ground acceleration (PGA) of 0.061 g. To verify the partitioning choices $\{\alpha, \beta, \gamma\}$, the reference structure is modeled and the model is verified in Figure 2.34. Figure 2.34 shows the comparison

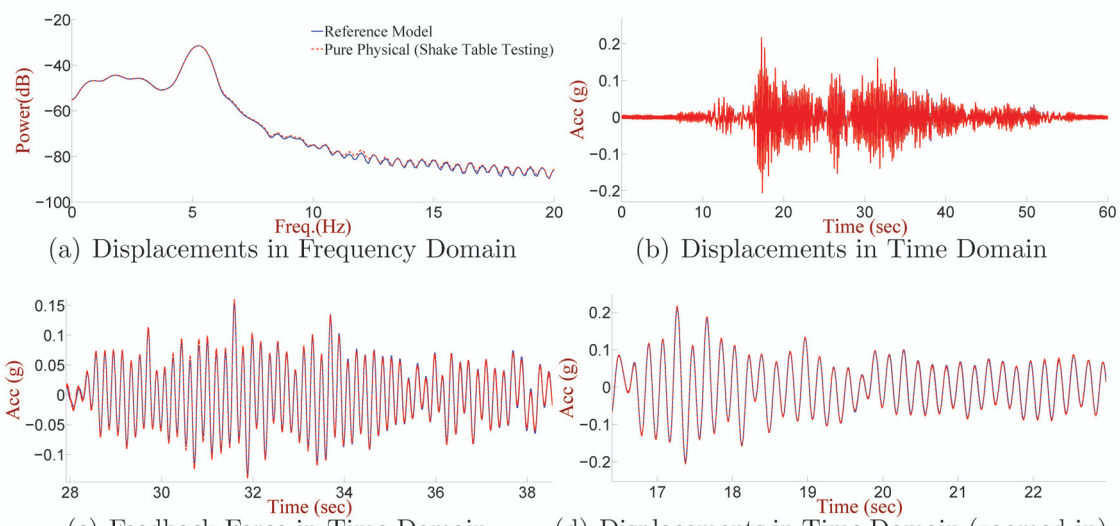

(a) Displacements in Frequency Domain (b) Displacements in Time Domain

(c) Feedback Force in Time Domain (d) Displacements in Time Domain (zoomed-in)

Fig. 2.34. Comparison of responses of the SDOF reference model with those of the pure physical (shake table) in frequency and time domains.

of responses corresponding to the shake table testing of the reference structure and the reference model. To quantify the associated modeling error, the following error indicator is employed.

$$NRMSE\% = \frac{RMS[(\ddot{x}_{SIM} - \ddot{x}_{PHY})]}{max(\ddot{x}_{PHY}) - min(\ddot{x}_{PHY})} \times 100 \tag{2.82}$$

The corresponding $NRMSE$ is 0.9%. The low $NRMSE$ along with an excellent match in the frequency domain (see Figure 2.35(a)) verify the reference model and,

consequently, the partitioning choices $\{\alpha, \beta, \gamma\}$. Next, an RTHS is conducted with the partitioning parameters listed in Table 2.6 and the results are shown in Figure 2.35.

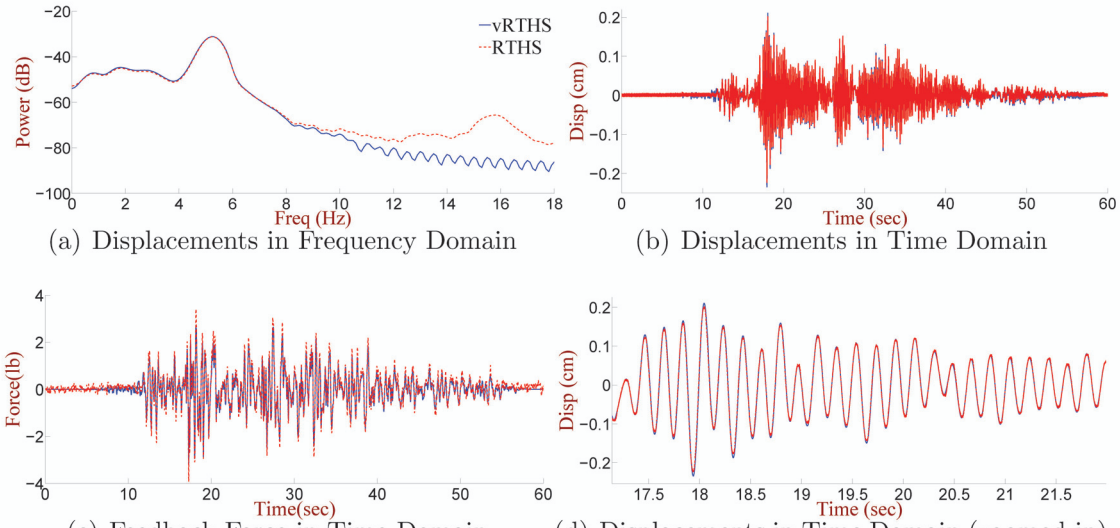

(a) Displacements in Frequency Domain (b) Displacements in Time Domain

(c) Feedback Force in Time Domain (d) Displacements in Time Domain (zoomed-in)

Fig. 2.35. Comparison of vRTHS and RTHS responses (relative displacements) of the single story structure in frequency and time domains.

In Figure 2.35, the RTHS results are compared with results from the reference model. To quantify the error, the following post-experiment indicator is employed.

$$NRMSE\% = \frac{RMS[(x_{SIM} - x_{RTHS})]}{max(x_{SIM}) - min(x_{SIM})} \times 100 \tag{2.83}$$

Using Equation (2.83) leads to an $NRMSE$ of 0.8%. Having a low $NRMSE$ value confirms that conducting an RTHS with a low PPI value leads to a successful RTHS despite being restricted to a poor transfer system performance, the reference structure being lightly damped, the reference structure having a relatively large natural frequency, and the natural frequency of the physical substructure being within the seismic bandwidth (CSI effect). Therefore, PPI can be used as an effective pre-experiment performance metric in conducting successful RTHS.

2.3 Multi Degree of Freedom Linear System

In this section, PSI is extended to any linear multi-degree-of-freedom system, irrespective of whether shake table(s) and/or hydraulic actuator(s) serve as the transfer system. Moreover, this section demonstrates how PSI can be used as an effective design tool in implementation of successful RTHS. The design of partitioning choice is a primary and fundamental step in the implementation of a successful and safe RTHS. Also, PSI sets the minimum transfer system performance. Based on PSI and available transfer system performance, prior to conducting an experiment, alternative partitioning choices can be classified, on the basis of system instability as: extremely sensitive, moderately sensitive, and slightly sensitive choices.

2.3.1 Stability Switch Criterion

In the current virtual framework, a time delay is applied to the feedback force (interaction force) in order to assess the sensitivity and stability requirement of an RTHS partitioning choice subject to the interface de-synchronization. The PSI framework is shown in Figure 2.36. For linear systems, Figure 2.36 can be mathematically represented as either a neutral or retarded delay differential equation. In order to obtain critical delay of a partitioning choice, the delay differential equation is analytically solved using a novel computationally inexpensive method. Critical time delay refers to the time delay associated with the occurrence of a stability switch in Figure 2.36.

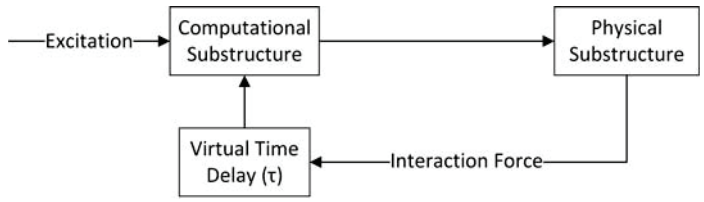

Fig. 2.36. Virtual framework for predictive indicators.

Transfer system is used to apply the interface conditions. Depending on how the emulated structure is partitioned into computational and physical substructures, hydraulic actuator(s) and/or shake table(s) are used as the transfer system. The general formulation for linear RTHS method and substructuring techniques are provided by Shao *et al.,* [40]. Herein, to demonstrate the preliminary PSI formulations (obtaining delay differential equations) for MDOF systems, two partitioning choices are selected using shake table and hydraulic actuators as transfer system. It should be mentioned that the PSI formulations also apply to any other partitioning choices in which hydraulic actuators and/or shake tables are used. Moreover, the PSI formulation can be used for more challenging RTHS cases in which stability is more critical such as multi-directional multi-actuator RTHS configurations, multi-rate RTHS (mrRTHS) or geographically distributed RTHS.

2.3.2 Case I: RTHS Using Shake Table

Here, a multi-story structure ($n + p$ stories) is partitioned into n stories as computational substructure and p stories as physical substructure shown in Figure 2.37. The computational substructure can be modeled as a shear model or a finite element model (as long as Equation 2.84 still applies). In this partitioning procedure, the top p stories are mounted on a shake table while the bottom n stories are computationally modeled on a real-time operating system. In this case, the shake table serves as the transfer system to meet the boundary conditions at interface. Some implementations of RTHS with similar partitioning approach can be found in [39, 40, 51, 52]. To assess the sensitivity of possible partitioning choices, the virtual PSI framework shown in Figure 2.36 is adopted. Thus the PSI equation of motion for the computational substructure is

$$M_n\ddot{X}_n + C_n\dot{X}_n + K_nX_n = F(x_g, \dot{x}_g) - F_p(\tau) \tag{2.84}$$

where M_n, C_n, K_n, $F(x_g, \dot{x}_g)$, τ and F_p are computational mass, damping, stiffness, input force, virtual time delay and interface force from the physical substructure,

respectively. In this section, all states are absolute (or total) values. Because for linear systems, stability is an internal system characteristic and independent of the input, without loss of generality, the ground motion force in Equation 2.84 is dropped. The equation of motion for the computational substructure becomes

$$M_n\ddot{X}_n + C_n\dot{X}_n + K_nX_n = -F_p(\tau) \tag{2.85}$$

For this type of partitioning choice, the interface force becomes

$$F_p = k_{n+1}(x_{n+1} - x_n) + c_{n+1}(\dot{x}_{n+1} - \dot{x}_n) \tag{2.86}$$

Equation 2.86 can be written in the state space form as follows

$$\begin{bmatrix} \dot{X}_n \\ \ddot{X}_n \end{bmatrix} = \overbrace{\begin{pmatrix} 0_{n\times n} & I_{n\times n} \\ -M_n^{-1}K_n & -M_n^{-1}C_n \end{pmatrix}}^{An} \overbrace{\begin{bmatrix} X_n \\ \dot{X}_n \end{bmatrix}}^{Yn} + \overbrace{\begin{pmatrix} 0_{n\times 1} \\ -M_n^{-1}R^T \end{pmatrix}}^{Bn} F_p(\tau) \tag{2.87}$$

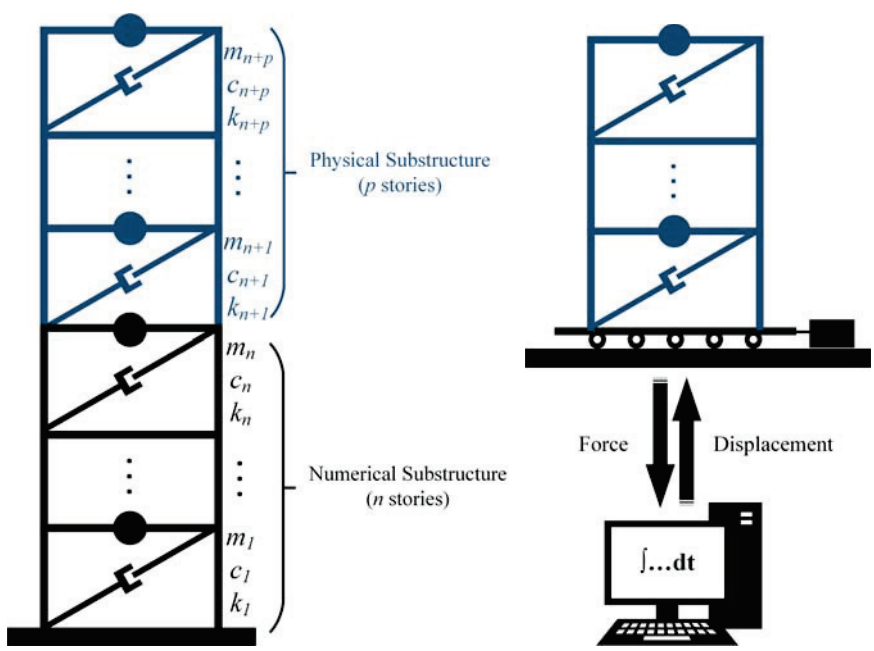

(a) Emulated structure.

(b) Real-time hybrid simulation.

Fig. 2.37. A typical real-time hybrid simulation using shake table as transfer system.

$$\overbrace{\begin{bmatrix} x_n \\ \dot{x}_n \end{bmatrix}}^{Yi} = \overbrace{\begin{pmatrix} R & 0_{1\times n} \\ 0_{1\times n} & R \end{pmatrix}}^{Cn} \begin{bmatrix} X_n \\ \dot{X}_n \end{bmatrix} \tag{2.88}$$

where R is interface vector $[0_{1\times n-1}1]^T$. The equation of motion for the physical substructure is

$$M_p\ddot{X}_p + C_p\dot{X}_p + K_pX_p = K_p\Gamma x_n + C_p\Gamma\dot{x}_n \tag{2.89}$$

Equation 2.89 can also be written in the state space form as follows

$$\begin{bmatrix} \dot{X}_p \\ \ddot{X}_p \end{bmatrix} = \overbrace{\begin{pmatrix} 0_{p\times p} & I_{p\times p} \\ -M_p^{-1}K_p & -M_p^{-1}C_p \end{pmatrix}}^{A_p} \overbrace{\begin{bmatrix} X_p \\ \dot{X}_p \end{bmatrix}}^{Y_p} + \overbrace{\begin{pmatrix} 0_{p\times 1} & 0_{p\times 1} \\ -M_p^{-1}K_p\Gamma & -M_p^{-1}C_p\Gamma \end{pmatrix}}^{B_p} \begin{bmatrix} x_n \\ \dot{x}_n \end{bmatrix} \tag{2.90}$$

$$F_p = \overbrace{\begin{pmatrix} k_{n+1} & 0_{1\times p-1} & k_{n+1} & 0_{1\times p-1} \end{pmatrix}}^{C_p} \begin{bmatrix} X_p \\ \dot{X}_p \end{bmatrix} + \overbrace{\begin{pmatrix} -k_{n+1} & -c_{n+1} \end{pmatrix}}^{D_p} \begin{bmatrix} x_n \\ \dot{x}_n \end{bmatrix} \tag{2.91}$$

Subject to virtual time-delay, Equation 2.91 becomes

$$F_p(\tau) = C_pY_p(\tau) + D_pY_i(\tau) \tag{2.92}$$

Using Equation 2.88, $F_p(\tau)$ can be written as

$$F_p(\tau) = C_pYp(\tau) + D_pC_nYn(\tau) \tag{2.93}$$

By substituting Equation 2.93 into Equation 2.87 and Equation 2.88 into Equation 2.90, respectively, dynamics of the computational and physical substructures can be expressed as

$$\dot{Y}_n = A_nY_n + B_nD_pC_nY_n(\tau) + B_nC_pY_p(\tau) \tag{2.94}$$

$$\dot{Y}_p = B_pC_nY_n + A_pY_p \tag{2.95}$$

Equations 2.94 and 2.95 can be expressed in the following *retarded delay differential equation* (RDDE) format

$$\begin{bmatrix} \dot{Y}_n \\ \dot{Y}_p \end{bmatrix} = \overbrace{\begin{pmatrix} A_n & 0_{n\times p} \\ B_pC_n & A_p \end{pmatrix}}^{A_0} \begin{bmatrix} Y_n \\ Y_p \end{bmatrix} + \overbrace{\begin{pmatrix} B_nD_pC_n & B_nC_p \\ 0_{n\times n} & 0_{n\times p} \end{pmatrix}}^{A_1} \begin{bmatrix} Y_n(\tau) \\ Y_p(\tau) \end{bmatrix} \tag{2.96}$$

2.3.3 Case II: RTHS Using Hydraulic Actuator

In this section, a multi-story structure (n stories) is divided into $n - m$ stories as computational substructure and m partitioned stories shown in Figure 2.38. The computational substructure can be modeled as shear model or finite element model (as long as Equation 2.97 still applies). In this partitioning procedure, the bottom m partitioned stories are physically constructed and attached to hydraulic actuators as transfer system while the computational substructure is being executed on a real-time operating system. Some implementations of RTHS with similar partitioning approach can be found in [53–57]. In this case, all states are relative values (relative to ground motion) and it is assumed that all the degrees of freedom has a non-zero computational mass. To assess the sensitivity of possible partitioning choices, the virtual PSI framework shown in Figure 2.36 is applied. The PSI equation of motion for the system shown in Figure 2.38 is

$$M_n\ddot{X} + C_n\dot{X} + K_nX = F(\ddot{x}_g) - F_p(\tau) \tag{2.97}$$

As mentioned earlier, because for linear systems, stability is an internal system characteristic and independent of the input, without loss of generality, the ground motion force in Equation 2.97 is dropped and it becomes

$$M_n\ddot{X} + C_n\dot{X} + K_nX = -F_p(\tau) \tag{2.98}$$

Equation 2.98 can also be written as

$$\begin{bmatrix} \dot{X} \\ \ddot{X} \end{bmatrix} = \begin{pmatrix} 0_{n\times n} & I_{n\times n} \\ -M_n^{-1}K_n & -M_n^{-1}C_n \end{pmatrix} \begin{bmatrix} X \\ \dot{X} \end{bmatrix} + \begin{pmatrix} 0_{n\times n} \\ -M_n^{-1} \end{pmatrix} F_p(\tau), \tag{2.99}$$

where F_p is

$$F_p = M_p\ddot{X} + C_p\dot{X} + K_pX \tag{2.100}$$

The interface force can also be expressed as

$$F_p = \begin{pmatrix} K_p & \rho C_p \end{pmatrix} \begin{bmatrix} X \\ \dot{X} \end{bmatrix} + \begin{pmatrix} (1-\rho)C_p & M_p \end{pmatrix} \begin{bmatrix} \dot{X} \\ \ddot{X} \end{bmatrix} \tag{2.101}$$

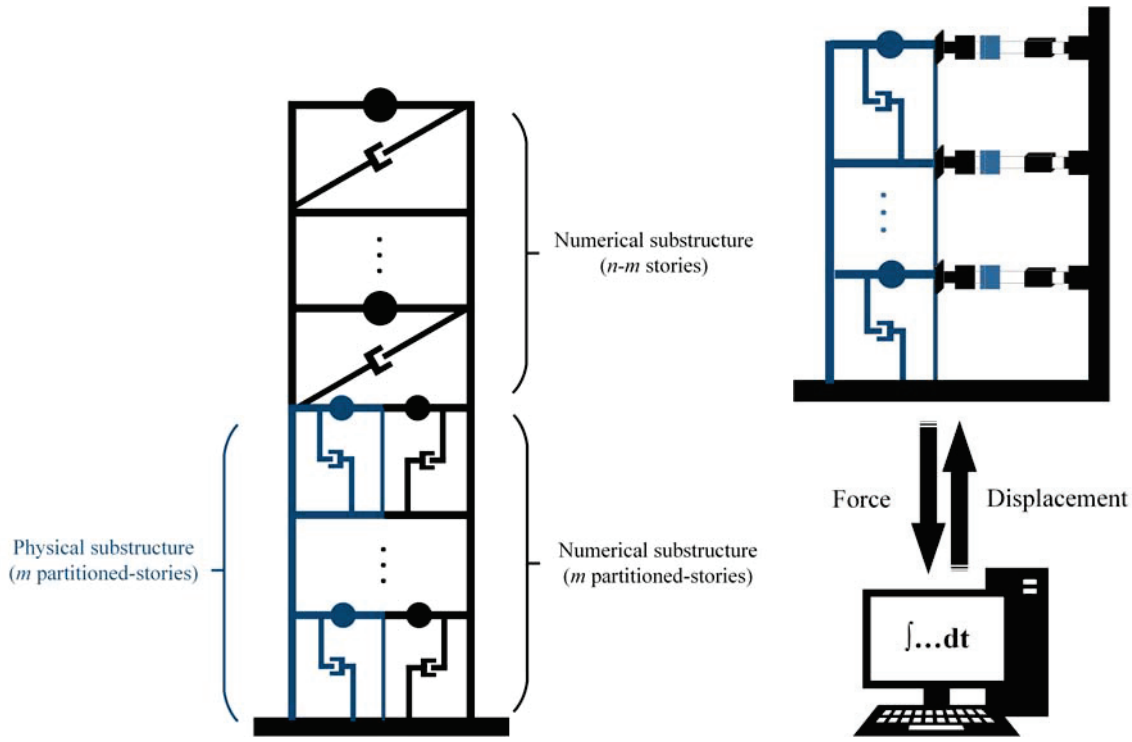

(a) Emulated structure.

(b) Real-time hybrid simulation.

Fig. 2.38. A typical real-time hybrid simulation using hydraulic actuator(s) as transfer system.

where ρ can take any value between 0 to 1. Substituting Equation 2.101 into Equation 2.99, it becomes

$$\begin{bmatrix} \dot{X} \\ \ddot{X} \end{bmatrix} = \begin{pmatrix} 0_{n\times n} & I_{n\times n} \\ -M_n^{-1}K_n & -M_n^{-1}C_n \end{pmatrix} \begin{bmatrix} X \\ \dot{X} \end{bmatrix} + \begin{pmatrix} 0_{n\times n} & 0_{n\times n} \\ -M_n^{-1}K_p & -\rho M_n^{-1}C_p \end{pmatrix} \begin{bmatrix} X(\tau) \\ \dot{X}(\tau) \end{bmatrix} + \begin{pmatrix} 0_{n\times n} & 0_{n\times n} \\ -M_n^{-1}(1-\rho)C_p & -M_n^{-1}M_p \end{pmatrix} \begin{bmatrix} \dot{X}(\tau) \\ \ddot{X}(\tau) \end{bmatrix} \quad (2.102)$$

Finally, Equation 2.102 can be rearranged and written in the following neutral delay differential equation (NDDE) format

$$\begin{bmatrix}\dot{X}\\ \ddot{X}\end{bmatrix}+\overbrace{\begin{pmatrix}0_{n\times n} & 0_{n\times n}\\ -M_n^{-1}(1-\rho)C_p & -M_n^{-1}M_p\end{pmatrix}}^{B}\begin{bmatrix}\dot{X}(\tau)\\ \ddot{X}(\tau)\end{bmatrix}=\overbrace{\begin{pmatrix}0_{n\times n} & I_{n\times n}\\ -M_n^{-1}K_n & -M_n^{-1}C_n\end{pmatrix}}^{A_0}\begin{bmatrix}X\\ \dot{X}\end{bmatrix}+$$
$$\overbrace{\begin{pmatrix}0_{n\times n} & 0_{n\times n}\\ -M_n^{-1}K_p & -\rho M_n^{-1}C_p\end{pmatrix}}^{A_1}\begin{bmatrix}X(\tau)\\ \dot{X}(\tau)\end{bmatrix} \quad (2.103)$$

Next, these delay differential equations need to be solved to obtain the associated critical time delay.

2.3.4 Critical Time Delay

In this section, a novel method is employed to solve the delay differential equations obtained in the previous section in a computationally efficient way. To derive PSI, the delay differential equation is converted to a generalized eigenvalue problem using a set of vectorization mappings. After obtaining the critical time delay for the neutral and retarded delay differential equations, the PSI value is computed to assess the sensitivity of the partitioning choice to interface de-synchronization.

First, it should be mentioned that RDDE (obtained for Case I) is a special case of NDDE in which the B matrix in Equation 2.104 becomes 0. Thus, without loss of generality, hereinafter, all the equations are based on the NDDE format. In general, a neutral delay differential equation takes the form of

$$\dot{X}(t)+B\dot{X}(t-\tau)=A_0X(t)+A_1X(t-\tau) \quad (2.104)$$

The characteristic equation of Equation 2.104 is

$$|s(I+Be^{-\tau s})-A_0-A_1e^{-\tau s}|=0 \quad (2.105)$$

where $|...|$ denotes the determinant, I refers to identity matrix and $s\in\mathbb{C}$. For a linear dynamic system to be asymptotically stable about its fixed points, all roots of the

characteristic equation (i.e., eigenvalues) must lie in the left half of the complex plane. Therefore, stability switching occurs when the rightmost eigenvalue goes from the left complex half-plane into the right complex half-plane by crossing the imaginary axis. So the appearance of an eigenvalue on the imaginary axis is the critical condition. Equation 2.105 can be rearranged as

$$|sI - A_0 + e^{-\tau s}(sB - A_1)| = 0 \tag{2.106}$$

Associated eigenvector (v) can be added to Equation 2.106

$$(sI - A_0)v = -e^{-\tau s}(sB - A_1)v, \tag{2.107}$$

conjugating and transposing Equation 2.107 yield

$$v^*(-sI - A_0^T) = -e^{\tau s}v^*(-sB^T - A_1^T) \tag{2.108}$$

Multiplying both sides of Equation 2.107 by minus Equation 2.108, it becomes

$$\overbrace{(sI - A_0)}^{O}\overbrace{vv^*}^{P}\overbrace{(sI + A_0^T)}^{Q} = (sB - A_1)vv^*(sB^T + A_1^T) \tag{2.109}$$

To solve Equation 2.109, the matrix method developed by Louisell [58] is employed. A brief overview of this matrix method is provided here. Let a vectorization operator $\xi : C^{n\times n} \longrightarrow C^{n^2}$ be defined as follows

$$\xi M = \begin{bmatrix} m_1^T \\ m_2^T \\ \cdots \\ m_n^T \end{bmatrix} \tag{2.110}$$

for any $M = \begin{bmatrix} m_1 \\ m_2 \\ \cdots \\ m_n \end{bmatrix}$. An important identity of this operator is used

$$\xi(OPQ) = (O \otimes Q^T)\xi P \tag{2.111}$$

where O, P, and $Q \in C^{n\times n}$ and $\otimes$ refers to the Kronecker product. Using Equation 2.111, Equation 2.109 becomes

$$[(sI - A_0) \otimes (sI + A_0) - (sB - A_1) \otimes (sB + A_1)]V = 0 \tag{2.112}$$

or simply

$$\Lambda(s)V = 0 \tag{2.113}$$

where V and $\Lambda(s)$ are ξvv^* and $(sI - A_0) \otimes (sI + A_0) - (sB - A_1) \otimes (sB + A_1)$. Next, consider the following two ordinary differential equations

$$\dot{X}(t) + B\dot{Y}(t) = A_0X(t) + A_1Y(t) \tag{2.114}$$

$$\dot{X}(t)B^T + \dot{Y}(t) = -X(t)A_1^T - Y(t)A_0^T \tag{2.115}$$

where A_0, A_1, B, X, and $Y \in C^{n\times n}$. Herein, two new operators E and F are defined by

$$E\begin{bmatrix} X \\ Y \end{bmatrix} = \begin{bmatrix} X + BY \\ XB^T + Y \end{bmatrix} \tag{2.116}$$

$$F\begin{bmatrix} X \\ Y \end{bmatrix} = \begin{bmatrix} A_0X + A_1Y \\ -XA_1^T - YA_0^T \end{bmatrix} \tag{2.117}$$

If $Z(t) = \begin{bmatrix} X \\ Y \end{bmatrix}$, then Equations 2.114 and 2.115 can be written in the matrix differential equation as

$$E\dot{Z}(t) = FZ(t) \tag{2.118}$$

Next, E and F are written in vector coordinates and the vectorization operator ξ to Z is applied

$$E_0 = \begin{bmatrix} I \otimes I & B \otimes I \\ I \otimes B & I \otimes I \end{bmatrix}, F_0 = \begin{bmatrix} A_0 \otimes I & A_1 \otimes I \\ -I \otimes A_1 & -I \otimes A_0 \end{bmatrix}, z = \xi Z = \begin{bmatrix} \xi X \\ \xi Y \end{bmatrix} = \begin{bmatrix} x \\ y \end{bmatrix} \tag{2.119}$$

Thus Equation 2.118 becomes

$$E_0\dot{z}(t) = F_0z(t) \tag{2.120}$$

and the corresponding characteristic equation becomes

$$(sE_0 - F_0)z = 0 \tag{2.121}$$

In the Laplace domain, Equations 2.114 and 2.115 become

$$(sI - A_0)X + (sB - A_1)Y = 0 \tag{2.122}$$

$$X(sB^T - A_1^T) + Y(sI + A_0^T)Y = 0 \tag{2.123}$$

Defining a new operator as $T = sE - F$

$$T \begin{bmatrix} X \\ Y \end{bmatrix} = \begin{bmatrix} (sI - A_0)X + (sB - A_1)Y \\ X(sB^T + A_1^T) + Y(sI + A_0^T) \end{bmatrix}, \tag{2.124}$$

Equations 2.122 and 2.123 become

$$T \begin{bmatrix} X \\ Y \end{bmatrix} = TZ = 0 \tag{2.125}$$

To understand the behavior of operator T, an attempt to solve Equation 2.126 is provided.

$$T \begin{bmatrix} X \\ Y \end{bmatrix} = \begin{bmatrix} X_0 \\ Y_0 \end{bmatrix} \tag{2.126}$$

By multiplying the upper equation by $sI + A_0^T$, and the lower on the left by $sB - A_1$, then subtracting, it becomes

$$(sI - A_0)X(sI + A_0^T) - (sB - A_1)X(sB^T + A_1^T) = X_0(sI + A_0^T) - (sB - A_1)Y_0 \tag{2.127}$$

Similarly, by multiplying the upper equation by $sB^T + A_1^T$, and the lower on the left by $sI - A_0$, then subtracting, it becomes

$$(sI - A_0)Y(sI + A_0^T) - (sB - A_1)Y(sB^T + A_1^T) = (sI - A_0)Y_0 - X0(sB^T - A_1^T) \tag{2.128}$$

Here, another operator T^+ is defined as

$$T^+ \begin{bmatrix} X \\ Y \end{bmatrix} = \begin{bmatrix} X(sI + A_0^T) - (sB - A_1)Y \\ -X(sB^T + A_1^T) + (sI - A_0)Y \end{bmatrix} \tag{2.129}$$

Applying both operators T^+ and T on $\begin{bmatrix} X \\ Y \end{bmatrix}$, it becomes

$$T^+T \begin{bmatrix} X \\ Y \end{bmatrix} = \begin{bmatrix} \lambda X \\ \lambda Y \end{bmatrix} \tag{2.130}$$

where

$$\lambda X = (sI - A_0)X(sI + A_0^T) - (sB - A_1)X(sB^T + A_1^T) \tag{2.131}$$

$$\lambda Y = (sI - A_0)Y(sI + A_0^T) - (sB - A_1)Y(sB^T + A_1^T) \tag{2.132}$$

Next, all the operators are vectorized using the vectorization operator ξ. Therefore, $T \begin{bmatrix} X \\ Y \end{bmatrix}$, $T^+ \begin{bmatrix} X \\ Y \end{bmatrix}$, λX and λY map to $K \begin{bmatrix} x \\ y \end{bmatrix}$, $K^+ \begin{bmatrix} x \\ y \end{bmatrix}$, Λx and Λy, accordingly, where

$$K = \begin{bmatrix} (sI - A_0) \otimes I & (sB - A_1) \otimes I \\ I \otimes (sB + A_1) & I \otimes (sI + A_0) \end{bmatrix} = sE_0 - F_0 \tag{2.133}$$

$$K^+ = \begin{bmatrix} I \otimes (sI + A_0) & -(sB - A_1) \otimes I \\ -I \otimes (sB + A_1) & (sI - A_0) \otimes I \end{bmatrix} \tag{2.134}$$

$$\Lambda(s) = (sI - A_0) \otimes (sI + A_0) - (sB - A_1) \otimes (sB + A_1) \tag{2.135}$$

Notice, in Equations 2.135 and 2.112, $\Lambda(s)$ is identical. Applying the vectorization operation (ξ) on Equation 2.130, it becomes

$$K^+K \begin{bmatrix} x \\ y \end{bmatrix} = \begin{bmatrix} \Lambda x \\ \Lambda y \end{bmatrix} = \begin{bmatrix} \Lambda & 0 \\ 0 & \Lambda \end{bmatrix} \begin{bmatrix} x \\ y \end{bmatrix} \tag{2.136}$$

which means

$$K^+K = \begin{bmatrix} \Lambda & 0 \\ 0 & \Lambda \end{bmatrix} \tag{2.137}$$

and therefore,

$$|K^+K| = \begin{vmatrix} \Lambda & 0 \\ 0 & \Lambda \end{vmatrix} = |\Lambda|^2 \tag{2.138}$$

In a lemma, Louisell proved that $|K| = |K^+|$, see [58], therefore

$$|K| = |\Lambda| \tag{2.139}$$

To obtain the solution to Equation 2.104, it is needed to solve Equation 2.112. The solution to Equation 2.112 is

$$|\Lambda| = 0 \tag{2.140}$$

Using Equations 2.133 and 2.139 yields

$$|\Lambda| = |K| = |sE_0 - F_0| = 0 \tag{2.141}$$

Notice, Equation 2.141 is a generalized eigenvalue problem which can be simply solved. To find the corresponding critical time delay(s), the method proposed by Marshal *et al.,* [59] is adopted. For the imaginary eigenvalues found from Equation 2.141 ($s = i\omega$), Equation 2.107 becomes singular

$$|(i\omega I - A_0) + e^{-\tau i\omega}(i\omega B - A_1)| = 0 \tag{2.142}$$

The solutions of Equation 2.142 are the solutions of the generalized eigenvalue of the pair matrix $A_0 - i\omega I$ and $i\omega B - A_1$ if and only if the magnitude of the eigenvalue solution is 1 as $|e^{\tau i\omega}| = 1$.

2.3.5 Predictive Stability Indicator

Designing an RTHS configuration becomes more meaningful considering the fact that designing a transfer system controller is inherently characterized by a balance between tracking accuracy (performance) and robustness (stability). To conduct an accurate RTHS, while system stability is reliably held, a researcher needs to know the sensitivity of the partitioning choice to the interface de-synchronization from stability and performance perspectives. In the PSI framework, by solving the neutral (or retarded) delay differential equations, researchers obtain a set of critical time delays. For a particular partitioning choice, the critical time delays correspond to the

time delays at which stability switch occurs in the virtual PSI framework. In order to develop a stability indicator, the first occurrence of a stability switch (from a stable system to an unstable system) is the most meaningful one. Thus, hereinafter, the critical time delay (τ_{cr}) refers to the smallest critical time delay obtained by solving the delay differential equation. The PSI value can be computed as

$$PSI = \log_{10}\left[\tau_{cr}(msec)\right] \tag{2.143}$$

Equation 2.143 maps $\tau_{cr} \in (0, \infty)$ to $PSI \in (-\infty, \infty)$. Figure 2.39 shows the relationship between critical time delay, predictive stability indicator and global stability for any partitioning choice. It should be noted that the proposed boundaries in Figure 2.39 are based on experience and the values may change based on transfer system controller design procedure and reasonableness of assumptions of transfer system linearity. It can be seen in Figure 2.39 that higher values of PSI refers to a partitioning choice with a greater stability margin.

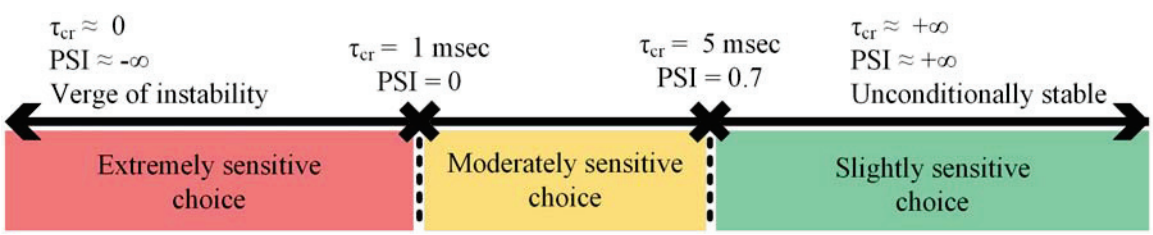

Fig. 2.39. Relationship between PSI, critical time delay and RTHS stability due to interface de-synchronization.

The proposed predictive stability indicator can be applied to more complicated systems, such as multi-directional multi-actuator RTHS, multi-rate RTHS, and distributed RTHS and piecewise linear (PL) dynamical systems. From a stability perspective, earlier in the chapter, it has been shown that linear RTHS is more susceptible to interface de-synchronization than a partitioning choice with strain-softening nonlinearities or energy dissipating systems in the physical substructure.

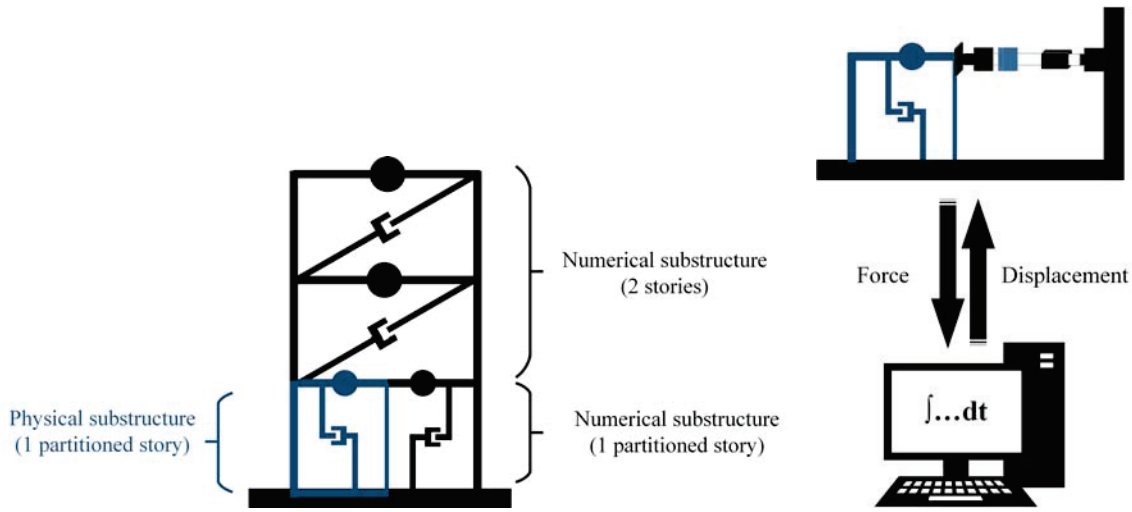

(a) Emulated structure. (b) Partitioned system.

Fig. 2.40. A typical real-time hybrid simulation using shake table as transfer system.

With the recent scientific and engineering advances that extend the connectivity of cyber-physical systems, distributed RTHS can optimize the use of distributed computational and experimental resources and leverage multiple computational and experimental resources. However, the existence of substantial deterministic and random communication delays poses stability challenges which can be effectively addressed by this stability framework.

2.3.6 Illustrative Example: MDOF RTHS with a Single Actuator

In the first illustrative example, a stability analysis of $2,500,000$ simulated RTHS cases is performed and the results are compared with the corresponding PSI values. Consider a linear three story shear building subjected to a one-dimensional seismic excitation partitioned as depicted in Figure 2.40. The physical substructure is a portion of the first story, and the remaining is the computational substructure.

In this example, to avoid redesigning a control/compensation system for each case study, the physical substructure remains unchanged: $M_p = 2,924$ *kg*, $C_p = 15.8$ *N.sec/cm*, $K_p = 13,895$ *N/cm*. However, to study various partitioning choices, the computational substructure changes for each simulated case. Mass, stiffness, and damping of the computational substructure are computed as follows

$$M_n = \begin{bmatrix} M_n^1 & 0 & 0 \\ 0 & M_n^2 & 0 \\ 0 & 0 & M_n^3 \end{bmatrix} \tag{2.144}$$

$$C_n = \begin{bmatrix} C_n^1 + C_n^2 & -C_n^2 & 0 \\ -C_n^2 & C_n^2 + C_n^3 & C_n^3 \\ 0 & -C_n^3 & C_n^3 \end{bmatrix} \tag{2.145}$$

$$K_n = \begin{bmatrix} K_n^1 + K_n^2 & -K_n^2 & 0 \\ -K_n^2 & K_n^2 + K_n^3 & K_n^3 \\ 0 & -K_n^3 & K_n^3 \end{bmatrix} \tag{2.146}$$

where, M_n^1 and K_n^1 are computed using partitioning parameters α_1 and γ_1

$$\alpha_1 = \frac{M_n^1}{M_n^1 + M_p}, \gamma_1 = \frac{K_n^1}{K_n^1 + K_p} \tag{2.147}$$

and

$$C_n^1 = C_p \tag{2.148}$$

Mass, damping, and stiffness of the second and third floors are assigned as

$$M_n^2 = M_n^3 = M_n^1 + M_p \tag{2.149}$$

$$C_n^2 = C_n^3 = C_n^1 + C_p \tag{2.150}$$

$$K_n^2 = K_n^3 = K_n^1 + K_p \tag{2.151}$$

For the simulated RTHS cases, a hydraulic actuator is modeled according to the block diagrams shown in Figures 2.6 and 2.8. The model parameters are selected using an identified actuator in [7] where $a_1 = 5.17 \times 10^5$ *kN/(m.sec)*, $a_2 = 7.77 \times 10^4$ kN/m,

and $a_3 = 21.52$ *1/sec*. In [7], Carrion and Spencer also modeled the associated servo-valve dynamics as a first order transfer function

$$G_s = \frac{k_p}{\tau s + 1}, \tag{2.152}$$

where $k_p = 4.6$ and $\tau = 3.32$ *msec* are proportional gain and servo-valve time constant, respectively. Figure 2.41 depicts the block diagram of the simulated RTHS cases. In the simulated RTHS cases, control-structure interaction is also modeled.

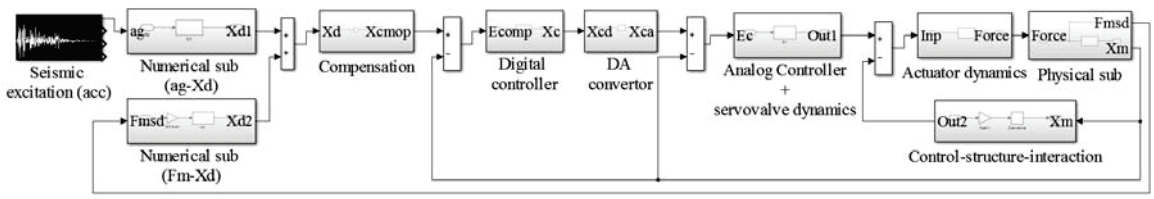

Fig. 2.41. Block diagram of simulated RTHS.

In Figure 2.42, the magnitude of frequency response functions of the physical substructure (force to displacement) and coupled actuator with the physical substructure (desired displacement to measured force) are demonstrated. This figure shows that because the physical substructure is lowly-damped (damping ratio: $\zeta = 1.24\%$), the actuator has a greatly limited ability to apply forces at the physical substructure's natural frequency.

Next, five different compensation/control systems with various levels of tracking performance are designed and stability of a total of $2,500,000$ (= 5 control systems$\times 500,000$ partitioning choices) simulated cases are determined and showed in Figure 2.43. Simulated RTHS results in Figure 2.43 are categorized in 6 different stability cases: (i) 5 controllers stable - 0 controller unstable ($0U/5S$); (ii) 4 controllers stable - 1 controller unstable ($1U/4S$); (ii) 3 controllers stable - 2 controllers unstable ($2U/3S$); (ii) 2 controllers stable - 3 controllers unstable ($3U/2S$); (ii) 1 controller stable - 4 controllers unstable ($4U/1S$); (ii) 0 controller stable - 5 controllers unstable ($5U/0S$).

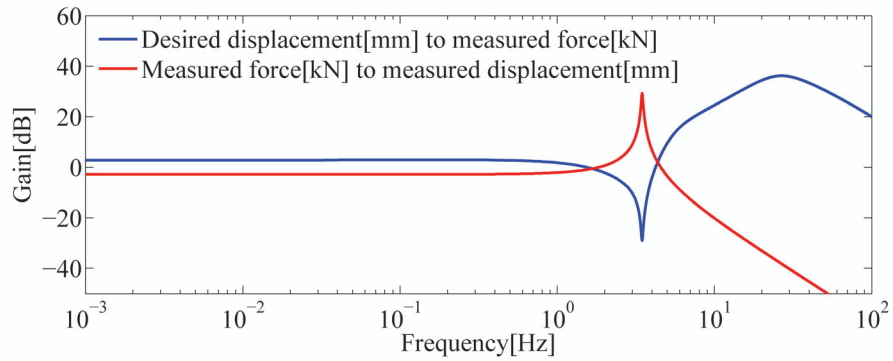

Fig. 2.42. Frequency response functions demonstrating control-structure-interaction in RTHS.

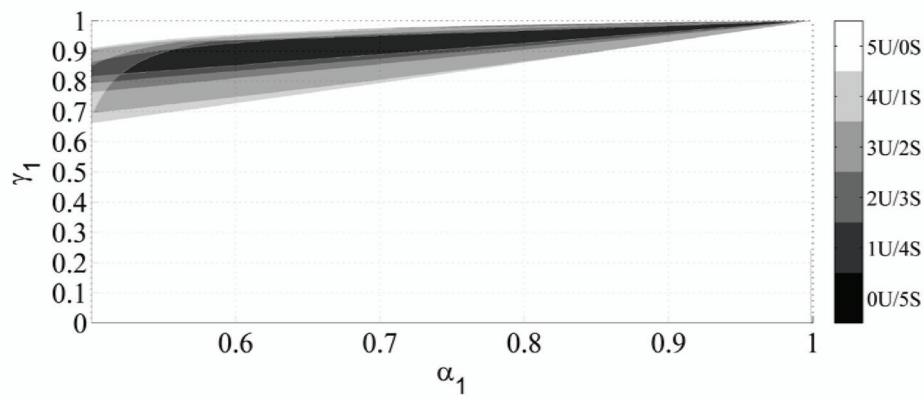

Fig. 2.43. Stability of simulated cases (α_1 and γ_1 are defined as: Equation 2.147).

In the next step, the PSI values associated with each partitioning choice are computed using Equation 2.143 and provided in Figure 2.44. By comparing Figures 2.43 and 2.44, it can be seen that the PSI plot is able to capture the essential results of the global stability in RTHS. In other words, prior to conducting an experiment, the PSI value provides a researcher with relative measures associated with the sensitivity of alternative partitioning choices to interface de-synchronization. This information (the PSI plot) is extremely valuable for the design and configuration of RTHS experiment.

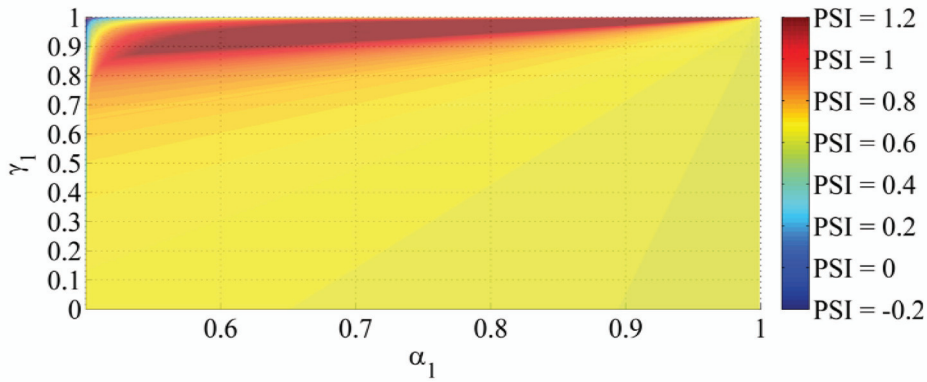

Fig. 2.44. Predictive stability indicator (α_1 and γ_1 are defined as: Equation 2.147).

2.3.7 Illustrative Example: MDOF RTHS with Multiple Actuators

As discussed earlier, currently RTHS is being implemented for complex MDOF systems in which control of multiple actuators is required. The multiple actuators are inherently coupled through the physical substructure. This phenomenon imposes certain challenges and considerations in transfer system control for implementing a successful test. Here, the objective is to evaluate the effectiveness of PSI for stability analysis of MDOF RTHS with multiple actuators while control-structure interaction is considered. In this case study, stability of $9,000,000$ simulated RTHS are determined and the results are compared with the PSI plot to evaluate how effectively PSI can capture the sensitivity of a partitioning choice to interface de-synchronization for MDOF RTHS with multiple actuators.

For this case study, the publicly available data in the NEEShub (NEES project ID: 648) for a three-story prototype building, which have been studied and identified in a NEESR project on performance based design using semi-active control, is used. This experimental study was implemented at the Real-Time Multi-Directional (RTMD) testing facility at Lehigh University. In this experiment, each floor was excited by a servo-hydraulic actuator. The first story used a hydraulic actuator model 200-100-1700 with a 2300 kN (501 $kips$) capacity and 500 mm (19.7 in) stroke while the second and third stories used a hydraulic actuator model 200-1000-1250 with a 1700 kN (382

kips) capacity and 500 *mm* (19.7 *in*) stroke. Figure 2.45 shows how the structure is partitioned into computational and physical substructures. The physical substructure is a concentrically-braced frame (CBF), and the computational substructure consists of a moment resisting frame (MRF) and the remaining components with seismic mass (i.e., lean-on column). Further details about the experiments conducted can be found in [60, 61].

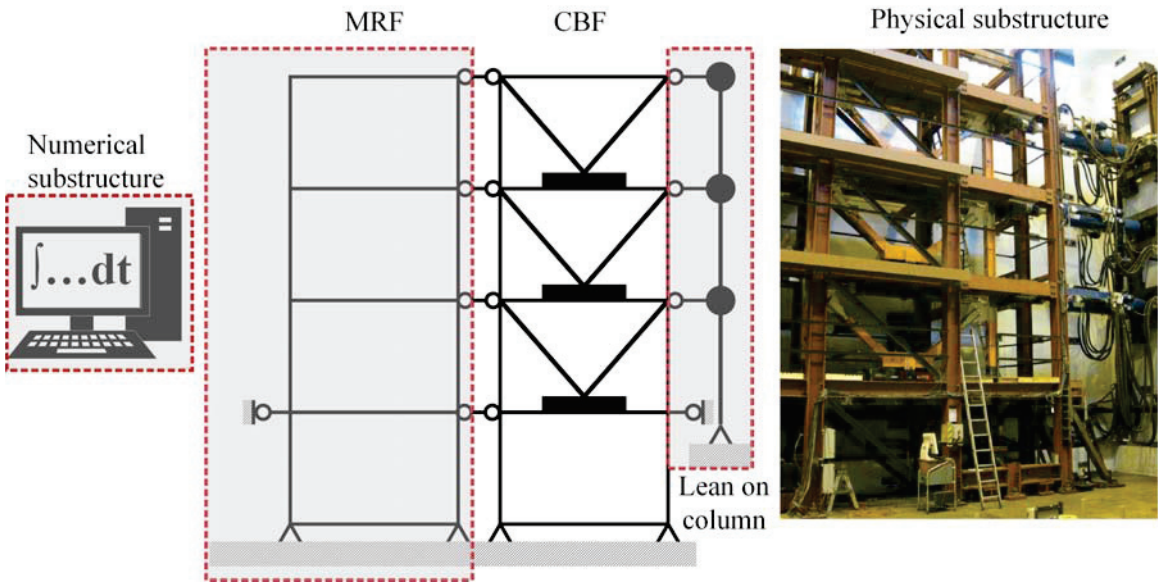

Fig. 2.45. Large scale multi-actuator RTHS (NEES project ID: 648).

Here, to avoid redesigning a control/compensation system for each case study, the physical substructure is identified and kept unchanged for all simulations.

$$M_p = \begin{bmatrix} 3.147 & 0 & 0 \\ 0 & 3.147 & 0 \\ 0 & 0 & 3.147 \end{bmatrix} \quad kN.sec^2/m \tag{2.153}$$

$$C_p = \begin{bmatrix} 74.21 & -32.73 & 4.29 \\ -32.73 & 59.87 & -23.20 \\ 4.29 & -23.20 & 26.10 \end{bmatrix} \quad kN.sec/m \tag{2.154}$$

$$K_p = \begin{bmatrix} 5.49 & -3.35 & 0.76 \\ -3.35 & 4.32 & -1.83 \\ 0.76 & -1.83 & 1.21 \end{bmatrix} \times 10^4 \quad kN/m \tag{2.155}$$

For the simulated RTHS cases, the hydraulic actuator model 200-100-1700 with a 2300 kN (501 $kips$) capacity and 500 mm (19.7 in) stroke is modeled according to the block diagrams shown in Figures 2.5 and 2.8. This model is later used to excite the three floors. The model's parameters are identified as $a_1 = 3.40 \times 10^6$ $kN/(m.sec)$, $a_2 = 2.52 \times 10^5$ kN/m, and $a_3 = 35.85$ *1/sec*. To validate the hydraulic actuator model, the experimental and simulated transfer functions (command displacement in m to measured force in kN) of the actuator attached to the first story of CBF are provided in Figure 2.46. This figure shows that because of the interaction between the physical substructure and the transfer system, the actuator has a limited ability to apply forces at the physical substructure's natural frequencies. Furthermore, the associated servo-valve dynamics is modeled as Equation 2.152 where $k_p = 2$ and $\tau = 7$ $msec$.

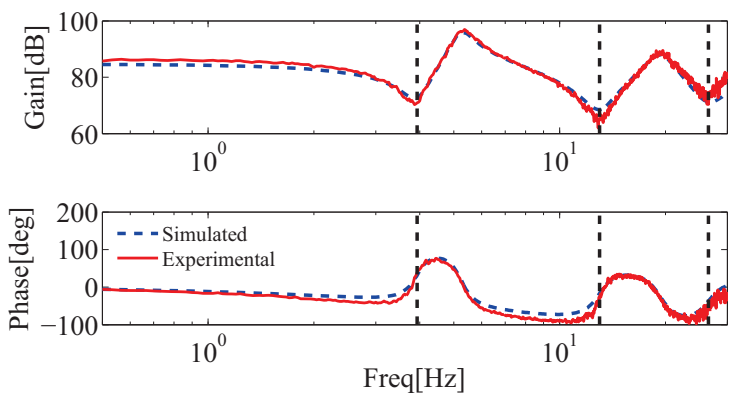

Fig. 2.46. Validation of the actuator model.

The original computational substructure is identified as

$$M_n = \begin{bmatrix} 98.9 & 0 & 0 \\ 0 & 98.9 & 0 \\ 0 & 0 & 70.8 \end{bmatrix} \quad kN.sec^2/m \tag{2.156}$$

$$C_n = \begin{bmatrix} 391.0 & -156.4 & 2.7 \\ -156.4 & 295.2 & -122.2 \\ 2.7 & -122.2 & 101.6 \end{bmatrix} \quad kN.sec/m \tag{2.157}$$

$$K_n = \begin{bmatrix} 1.17 & -0.73 & 0.16 \\ -0.73 & 0.89 & -0.34 \\ 0.16 & -0.34 & 0.20 \end{bmatrix} \times 10^5 \quad kN/m \tag{2.158}$$

which leads to $F_1 = 1.04 \;\; Hz$, $F_2 = 3.29 \;\; Hz$, $F_3 = 6.93 \;\; Hz$, $\zeta_1 = 2.71\%$, $\zeta_2 = 6.45\%$, and $\zeta_3 = 6.15\%$ where F_i and ζ_i are the ith natural frequency and damping ratio, respectively. To investigate the stability of various partitioning choices, three sets of simulations were performed: Case I in which the first mode's natural frequency and damping between $[0.52 - 1.56]$ Hz and $[0.54 - 3.25]\%$ while the second and third modes are kept unchanged; Case II in which the second mode's natural frequency and damping between $[1.65 - 4.94]$ Hz and $[1.29 - 7.74]\%$ while the first and third modes are kept unchanged; Case III in which the third mode's natural frequency and damping between $[3.46 - 10.39]$ Hz and $[1.23 - 7.38]\%$ while the first and second modes are kept unchanged. These varying parameters are provided in Table 2.7. It should be mentioned that in all the simulated cases, the modal mass and mode shapes remain unchanged.

To capture the stability trend, three different compensation/control systems with various levels of performance are designed. Thus, in total, stability of $9,000,000$ (= 3 control systems $\times 3$ variation cases $\times 1,000,000$ partitioning choices) simulated cases are determined. In Figures 2.47-2.49, simulated RTHS results are categorized in four different stability groups: (i) 3 controllers stable - 0 controller unstable ($0U/3S$); (ii) 2 controllers stable - 1 controller unstable ($1U/2S$); (ii) 1 controller stable - 2 controllers

Table 2.7.
Simulated case studies.

	F_1 (Hz)	F_2 (Hz)	F_3 (Hz)	ζ_1 (%)	ζ_2 (%)	ζ_3 (%)
Case I	[0.52 1.56]	3.29	6.93	[0.54 3.25]	6.45	6.15
Case II	1.04	[1.65 4.94]	6.93	2.71	[1.29 7.74]	6.15
Case III	1.04	3.29	[3.46 10.39]	2.71	6.45	[1.23 7.38]

unstable ($2U/1S$); (ii) 3 controllers stable - 0 controllers unstable ($3U/0S$). Next, the PSI plots corresponding to cases I-III are generated. Figures 2.47(a)-2.47(b) provide comparisons between the stability results of all the simulated cases and the predictive stability analysis based on the PSI values.

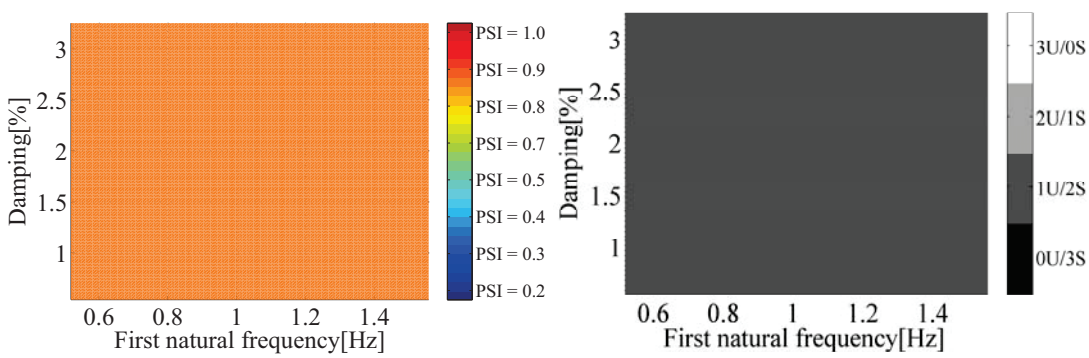

(a) Predictive stability indicator. (b) Stability of simulated cases.

Fig. 2.47. Sensitivity analysis of RTHS stability to the first mode of the computational substructure.

The x and y axes in Figures 2.47-2.49 correspond to variations in the natural frequency and damping of the computational substructure. Figures 2.47-2.49 show that there is significant agreement between the stability results and the PSI plots. Therefore, PSI plots are effective for designing a successful experiment. For this particular experiment, some observations can be made prior to conducting the experiment based

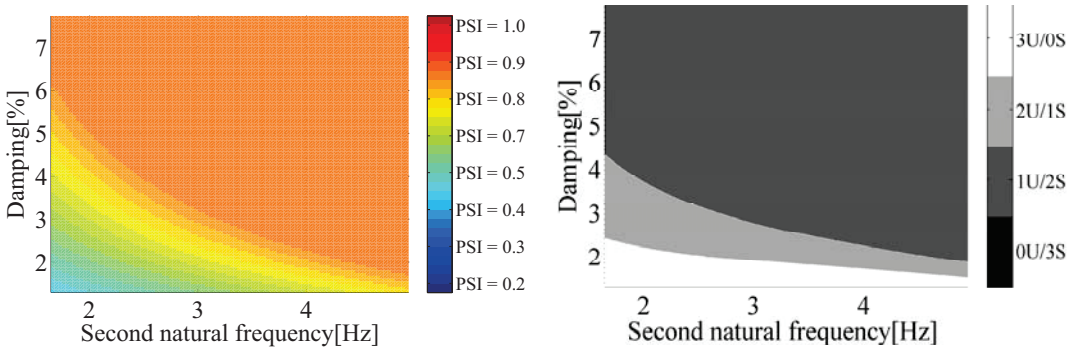

(a) Predictive stability indicator. (b) Stability of simulated cases.

Fig. 2.48. Sensitivity analysis of RTHS stability to the second mode of the computational substructure.

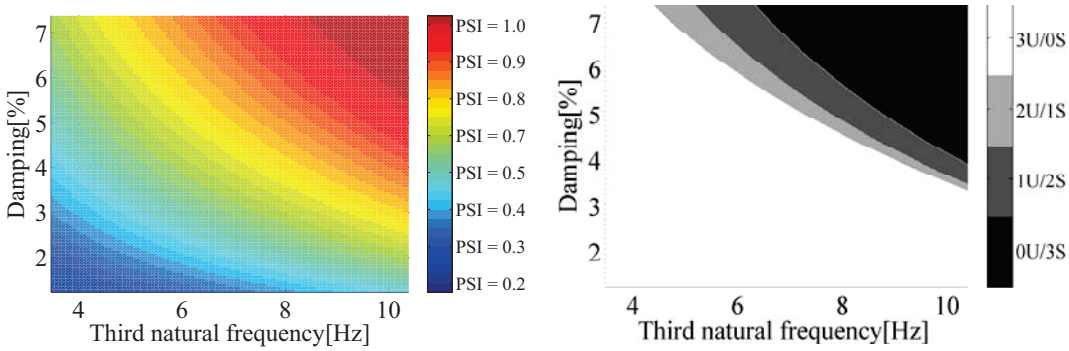

(a) Predictive stability indicator. (b) Stability of simulated cases.

Fig. 2.49. Sensitivity analysis of RTHS stability to the third mode of the computational substructure.

on the PSI plots. There are some partitioning choices in which an almost perfect controller is required for the system to hold its stability. These partitioning choices are not always clear to a researcher. For instance, it's more likely that a computational substructure with $F_3 = 5\ Hz$ and $\zeta_3 = 5\%$ causes instability than the same computational substructure with $F_3 = 10\ Hz$ and $\zeta_3 = 5\%$. Global stability is highly sensitive to the higher modes of the computational substructure and relatively insensitive to the lower modes of the computational substructure. However, an effective control

strategy might still be needed for certain partitioning choices. Adding damping in the computational substructure can always improve stability in the system.

2.3.8 Illustrative Example: MDOF RTHS with a Single Actuator

In this section, thirteen MDOF real-time hybrid simulations with different partitioning configurations are conducted. Herein, the reference structures are three-story linear shear structures. In all experiments, the first story is partitioned into computational and physical substructures while the second and third stories are pure computational. In this case study, four different computational substructures are considered, see Table 2.8.

Table 2.8.
Different computational substructures.

	Num. Sub. 1	Num. Sub. 2	Num. Sub. 3	Num. Sub. 4
$Mn_1(kg)$	30	294.7	30.0	36.8
$Mn_2(kg)$	50	319.3	54.6	61.4
$Mn_3(kg)$	50	319.3	54.6	61.4
$Cn_1(N.sec.m^{-1})$	280	800.0	800.0	500.0
$Cn_2(N.sec.m^{-1})$	300	812.2	812.2	512.2
$Cn_3(N.sec.m^{-1})$	300	812.2	812.2	512.2
$Kn_1(N.m^{-1})$	2.0×10^4	0.01×10^4	5.16×10^4	3.87×10^4
$Kn_2(N.m^{-1})$	1.5×10^4	2.00×10^4	7.73×10^4	6.44×10^4
$Kn_3(N.m^{-1})$	1.5×10^4	2.00×10^4	7.73×10^4	6.44×10^4

Different partitioning choices in the first floor can be better seen in Figure 2.50. where Mn_1, Cn_1, and Kn_1 refer to computational mass, damping, and stiffness in

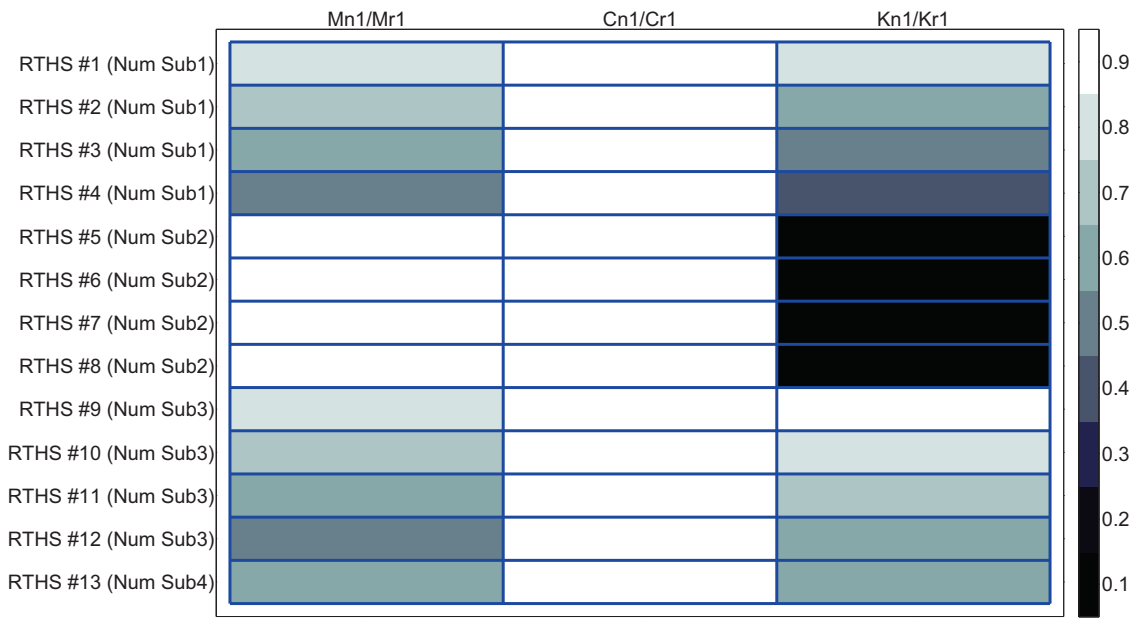

Fig. 2.50. Partitioning choices in the first floor (PSI values).

the first floor and Mr_1, Cr_1, and Kr_1 refer to the total (or reference) mass, damping and stiffness of the first floor.

Prior to implementation of the experiments, the predictive stability indicators are computed, see Figure 2.50. In the RTHS loop, to reject high-frequency force feedback noise, a low-pass finite-impulse-response filter ($\mathrm{F_{pass}} = 10\ Hz$, $\mathrm{F_{stop}} = 60\ Hz$, $\mathrm{A_{pass}} = 1\ dB$, and $\mathrm{A_{stop}} = 120\ dB$) is employed. Also, a PID controller with an inverse delay compensation is used to stabilize and compensate for the transfer system dynamics. Measuring/computing all the time delays/lags in the RTHS loop due to the filter, transfer system dynamics, communication and computation delays, the global time delay of the RTHS loop spans between 38 to 46 *msec*. Therefore, prior to implementation of RTHS tests, the predictive stability analysis indicates that R1, R9, R10, and R11 are unconditionally stable. More importantly, R13 is on the verge

of instability and it is very likely to become unstable during the test, see Tables 2.9 and 2.10.

Table 2.9.
Pick ground acceleration (El-Centro excitation) and the PSI values: R1-R7.

	R1	R2	R3	R4	R5	R6	R7
PGA(g)	0.068	0.068	0.068	0.068	0.027	0.027	0.027
$\tau_{cr}(msec)$	$+\infty$	149.9	124.7	115.9	166.1	94.3	77.3
PSI	$+\infty$	2.18	2.10	2.06	2.22	1.97	1.89

Table 2.10.
Pick ground acceleration (El-Centro excitation) and the PSI values: R8-R13.

	R8	R9	R10	R11	R12	R13
PGA(g)	0.027	0.137	0.137	0.137	0.137	0.017
$\tau_{cr}(msec)$	77.0	$+\infty$	$+\infty$	$+\infty$	86.0	45.3
PSI	1.89	$+\infty$	$+\infty$	$+\infty$	1.93	1.66

Next, all RTHS cases are implemented and the RTHS and vRTHS results are provided in Figures 2.51-2.54.

In this section, the experimental results demonstrated that by using PSI, researchers are able to successfully identify the unconditionally stable cases and, more importantly, the unstable cases. These case studies validate the effectiveness of PSI in conducting successful real-time hybrid simulations.

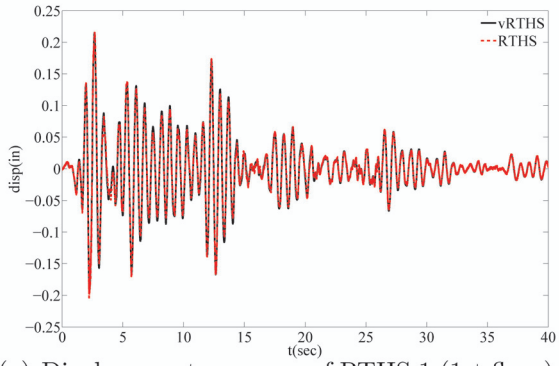

(a) Displacement response of RTHS 1 (1st floor).

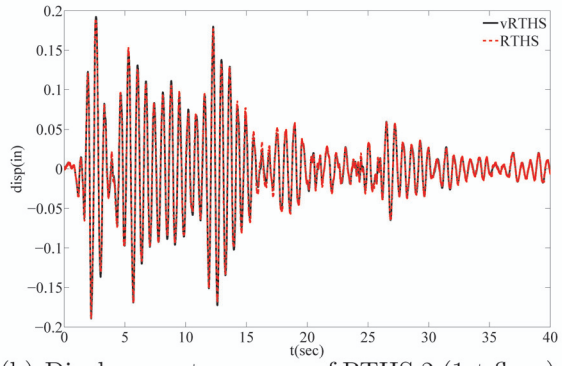

(b) Displacement response of RTHS 2 (1st floor).

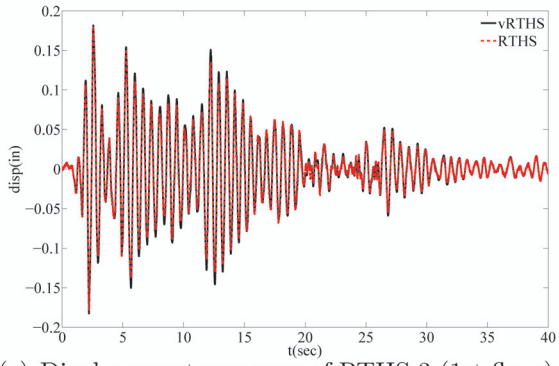

(c) Displacement response of RTHS 3 (1st floor).

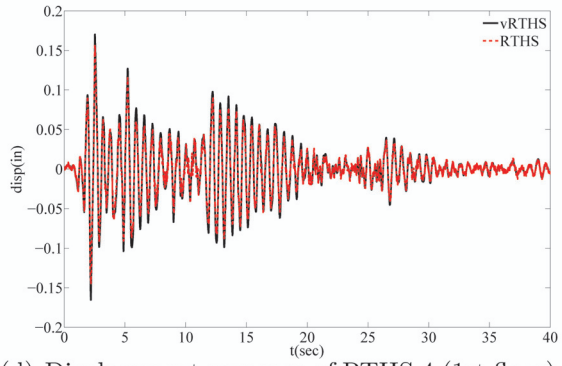

(d) Displacement response of RTHS 4 (1st floor).

Fig. 2.51. Comparisons of RTHS and vRTHS associated with the computational substructure 1.

2.4 Conclusions

In this chapter, the main objective was to demonstrate the effectiveness of using the predictive indicators in designing and configuring a successful experiment. The term partitioning choice (or configuration) refers to various choices of partitioning of a specific emulated structure into computational and physical substructures. In addition, for a specific emulated structure, designing an experiment referred to selection of a proper partitioning choice (of computational and physical substructures) and control strategy, subject to the existing transfer system limitations and interaction between the transfer system and the physical substructure.

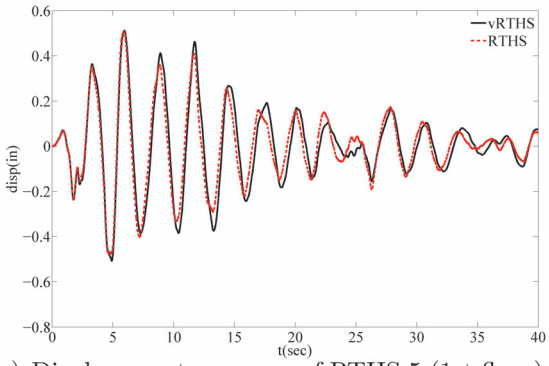

(a) Displacement response of RTHS 5 (1st floor).

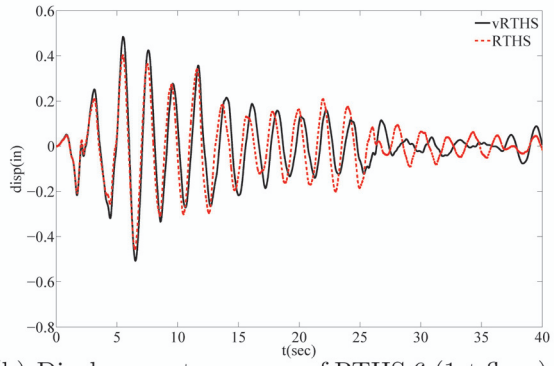

(b) Displacement response of RTHS 6 (1st floor).

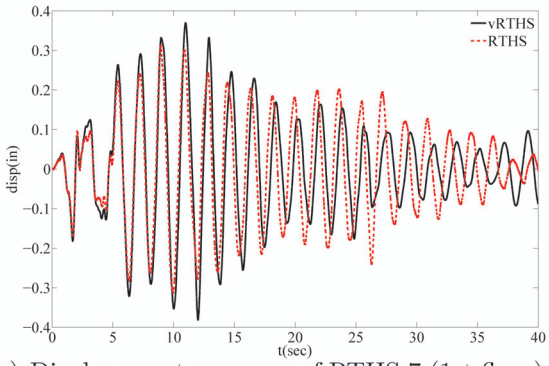

(c) Displacement response of RTHS 7 (1st floor).

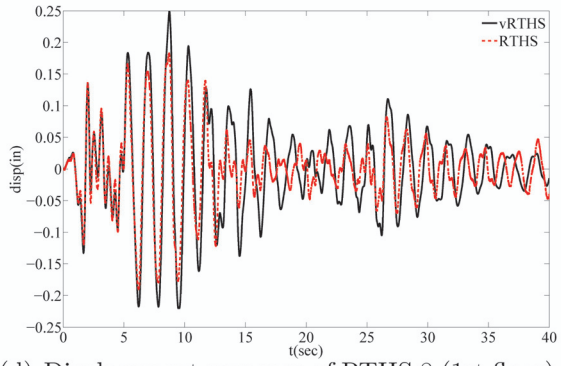

(d) Displacement response of RTHS 8 (1st floor).

Fig. 2.52. Comparisons of RTHS and vRTHS associated with the computational substructure 2.

Predictive indicators are obtained analytically and they are independent of the transfer system and controller dynamics, providing a relatively easy and useful method to examine many partitioning choices. Each partitioning choice has a different set of stability requirements. It is also important to point out that the set of stability requirements can become extremely narrow as the partitioning choice gets more complex. This fact explains why conducting a multi-dimensional complex RTHS is still an existing challenge for researchers. Thus, a set of stability and performance indicators are required to assist users configuring and designing a successful experiment.

An alternative method to PSI is stability analysis of various detailed components of RTHS including transfer system dynamics, transfer system controller and control-structure-interaction. In this alternative method, due to the presence of control-

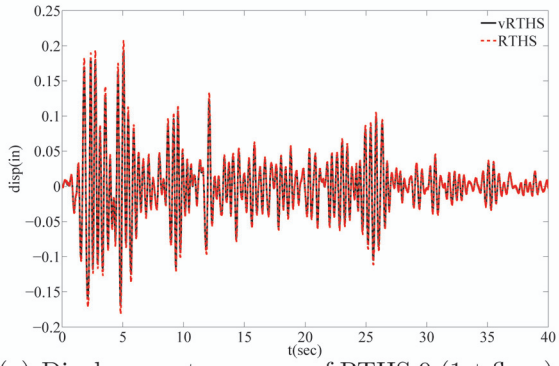

(a) Displacement response of RTHS 9 (1st floor).

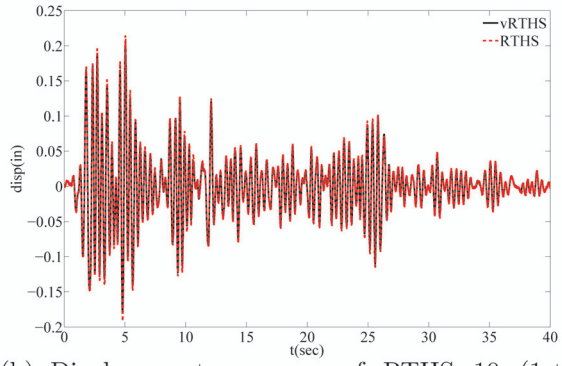

(b) Displacement response of RTHS 10 (1st floor).

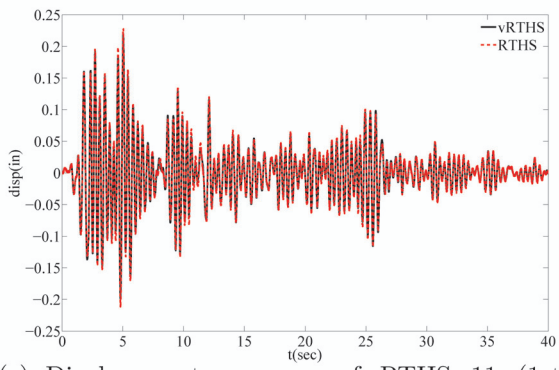

(c) Displacement response of RTHS 11 (1st floor).

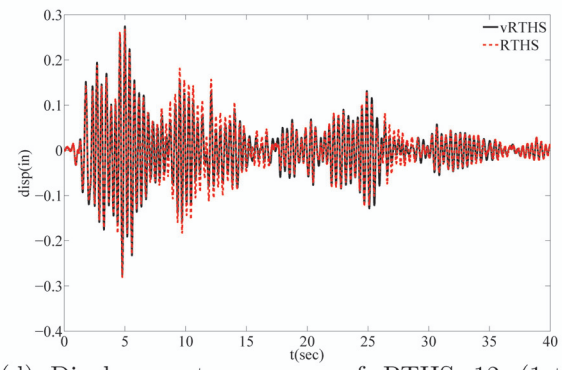

(d) Displacement response of RTHS 12 (1st floor).

Fig. 2.53. Comparisons of RTHS and vRTHS associated with the computational substructure 3.

structure-interaction, any change in the physical substructure (a new partitioning choice) yields change in transfer system performance which requires designing a new transfer system controller/compensation. To conduct stability (or performance) analysis of many partitioning choices, it is unfeasible to design a new transfer system controller every time a change is made in the physical substructure. However, since PSI is obtained analytically and it is independent of transfer system and controller dynamics, generating a PSI plot for many partitioning choices is easy, quick, and useful.

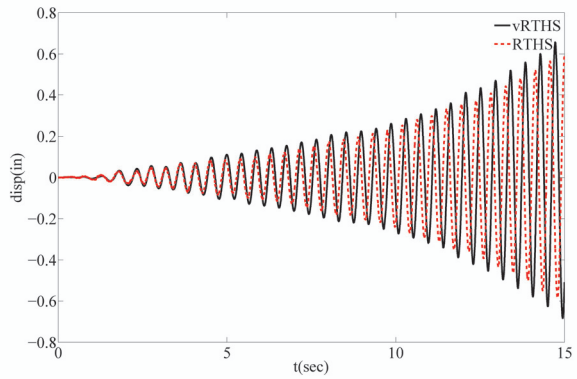

Fig. 2.54. Displacement responses of RTHS 13 (1st floor), comparison of RTHS and vRTHS responses associated with the computational substructure 4.

3. HYDRAULIC TRANSFER SYSTEM: IDENTIFICATION AND EXPERIMENTAL VERIFICATION

Hydraulic actuators have been extensively used in mechanical and structural systems by virtue of their large force-to-size ratios. They are capable of providing very large forces in a flexible manner. Compared to an electromagnetic actuator, the force limit of a hydraulic actuator can be an order of magnitude larger [42]. Thus, they have been used extensively for variety of mechanical engineering applications such as robotics [62, 63], hydraulic anti-lock braking systems [64, 65], vehicle motion simulator [66] and vibration control of automotive active suspensions [67]. Moreover, hydraulic actuators have been used for decades across many structural testing and earthquake engineering applications such as fatigue testing [68], seismic protection of structures [41, 69, 70], effective force testing [17, 71] and shake table testing [72, 73]. More recently, researchers have leveraged this experience to use hydraulic actuators for real-time hybrid simulation (RTHS). In the latter application, a servo-hydraulic actuator is also referred to as *hydraulic transfer system*.

Real-time hybrid simulation is a cyber-physical testing method used to examine the behavior and performance of structural systems under realistic conditions when rate-dependence plays a role. RTHS enables larger and more complex structural dynamic testing to be conducted than what would be affordable or even feasible in most individual structural testing laboratories. Here a structural system (i.e., reference structure) to be evaluated is partitioned into two substructures: computational substructure(s) containing reliable and accurate models of the majority of the reference structure, and physical substructure(s) comprising physical specimens of those parts of the reference structure that are unknown or otherwise difficult to model numeri-

cally. These substructures are coupled, and interact with each other, through transfer system executing the interface conditions.

Using hydraulic transfer systems, RTHS has been successfully executed to evaluate the performance of structures and to implement new structural control methods. For example, Christenson et al., evaluated the performance of magneto-rheological fluid dampers for seismic protection of civil structures using large-scale RTHS [44]. Mercan and Ricles investigated structures with full-scale elastomeric dampers using RTHS [74]. Also Friedman et al., used multiple hydraulic transfer systems to test a complex frame system, while they investigated the performance of an advanced control algorithm suitable for large scale magneto-rheological dampers [53]. A comprehensive survey of past RTHS in the US is provided in [75].

In RTHS, to enhance the ability of the transfer system to satisfy the interface conditions, researchers have developed several transfer system control/compensation techniques. Carrion and Spencer developed a model-based feedforward compensator for RTHS [7]. Chen et al., proposed an adaptive controller using an tracking indicator [76]. Gao et al., and Ou et al., developed and validated H_∞ loop shaping designs for hydraulic transfer systems in RTHS [33, 77]. Phillips et al., proposed a model-based feedforward control based on the backward difference method for hydraulic transfer system control [78].

In developing transfer system controllers and compensators for the hydraulic transfer system, the first step is identifying the transfer system attached to a physical specimen. Three approaches have been adopted by researchers :(1) simplification of the dynamics of the hydraulic transfer system to model as a pure time delay, (2) black-box identification of the dynamics of the hydraulic transfer system, and (3) parametric identification of the hydraulic transfer system based on a physical model. The first approach neglects the interaction between the hydraulic transfer system and physical specimen (see [41]) which may negatively impact the enforcement of necessary interface conditions. The second case may lead to suboptimal tracking performance in the case of extensive performance variations in the physical substructure

due to failure, complexity, and nonstationary behavior. The third approach, which is adopted herein, incorporates the dynamics of the hydraulic transfer system and its interaction with the physical substructure. Therefore, the latter approach is suitable for linear and nonlinear physical substructures with extensive behavioral variations.

In this chapter, a *plant* refers to a hydraulic transfer system coupled with a physical specimen. To model a hydraulic transfer system, the mechanical components include the servo-valve, hydraulic actuator and analog controller. Linear models are employed for the servo-valve and hydraulic actuator. To ensure generality, the physical specimen is presumed to be nonlinear, thus the plant becomes a nonlinear dynamical system. A system of differential equations governing the dynamics of the plant is derived. Then a simple technique is demonstrated to decouple and identify the parameters of the hydraulic transfer system. Next, the nonlinear dynamical model is transformed into controllable canonical form. This transformation of the nonlinear dynamical model is especially important when a nonlinear/linear digital controller needs to be designed and implemented to enhance the tracking performance of the transfer system. Finally, in a series of experiments, the controllable canonical model and identified parameters are validated.

3.1 Modeling and Formulation of Plant

This section discusses the impact of transfer system dynamics on implementation of RTHS. A new approach is proposed to identify the parameters of hydraulic transfer system. After identification of the parameters, the nonlinear model will be be transformed into a controllable canonical form in which the physical specimen is represented in a generalized nonlinear model.

3.1.1 Effect of Transfer System Dynamics in RTHS

For structural control purposes, Dyke et al. showed that hydraulic actuators have an implicit feedback interaction path that occurs due to the natural velocity feedback

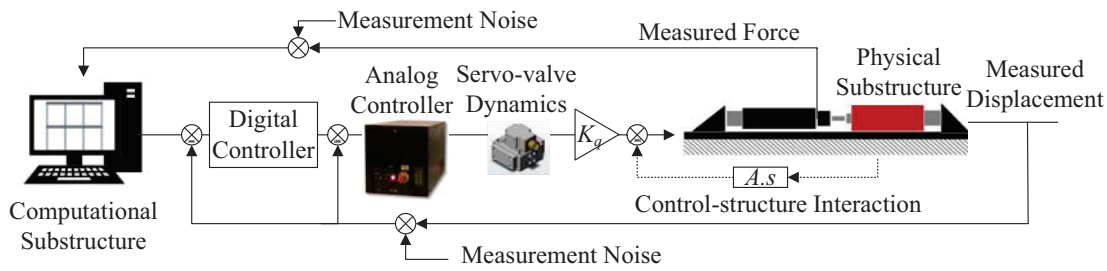

Fig. 3.1. Block diagram of a typical RTHS using a hydraulic transfer system.

of the actuator response (known as *control-structure interaction* or CSI) [41]. This interaction occurs for actuators configured for displacement, velocity, and/or force control. For such hydraulic transfer systems attached to a lightly damped structure, the ability of the actuator to apply forces at the structure natural frequencies is greatly limited.

In the execution of real-time hybrid simulation, the closed-loop plant enforces the interface conditions between the computational and physical substructures. In displacement control RTHS, an external command (command displacement) drives the transfer system attached to the physical substructure, see Figure 3.1. The transfer system and physical substructure are coupled through the feedback path that exists between the velocity of the transfer system and the command input to the actuator. Neglecting the dynamics of the transfer system generally results either in system instability or sub-optimal performance in control applications. In terms of implementing a successful RTHS test, the importance of considering the role of control-structure interaction is twofold: (1) to design an effective transfer system controller/compensator to enhance the performance and stability of the plant; and (2) to design a partitioning configuration with a suitable physical substructure in which the actuator's limited ability to apply forces at the natural frequencies of the physical substructure has minimal impact on the global response. Currently, RTHS is being extended to complex systems, such as single- and multi-degree-of-freedom nonlinear systems. In

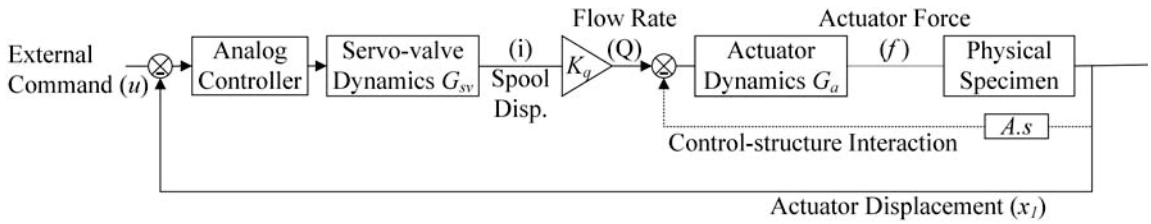

Fig. 3.2. Block diagram of a typical plant.

these cases, CSI imposes certain challenges and considerations in satisfying the interface conditions. A schematic block diagram representation of a typical plant is provided in Figure 3.2. Parametric identification and verification of the model shown in Figure 3.2, which accommodates linear and nonlinear physical substructures, can serve as a necessary building block for implementation of RTHS. In RTHS, the nonlinear plant developed and identified in this study will serve as the control plant for developing a model-based nonlinear transfer system controller/compensator.

3.1.2 Dynamics of the Plant

The main components of the plant are the servo-valve, hydraulic actuator, analog controller and physical specimen. For certain plants, researchers have developed and verified linear models to represent the first two components [42]. The third component, the analog controller, depends on what control method is being employed. In this study, a feedback analog controller is used to stabilize the plant. However, it should be noted that the techniques discussed in this study are equally applicable to a high sample rate digital servo-controller. The analog controller is a proportional-integral-derivative (PID) controller with displacement feedback which is commonly used for hydraulic actuators. However, throughout this study, to keep the mathematical equations relatively simple, the integral (I) and derivative (D) gains are set to zero. In this model, the physical specimen can be either linear or nonlinear.

To develop a physics-based model for the plant, DeSilva linearized the fluid flow rate in an actuator about the origin [42]. In this model, a natural velocity feedback path exists between the hydraulic actuator and the valve input. The coupling between the actuator dynamics and the physical specimen is shown in Figure 3.2 where $s \in \mathbb{C}$ denotes the Laplace variable. Figure 3.3 is obtained based on the linearized equation of hydraulic flow rate in a hydraulic actuator, which is

$$\dot{f} = \frac{2\beta}{V}(AK_q i - K_c f - A^2 \dot{x}_1) \tag{3.1}$$

where f, β, V, A, K_q, i, K_c, and x_1 are actuator force, bulk modulus of the fluid, half the volume of the hydraulic actuator, piston area, valve flow gain, valve input, leakage coefficient, and actuator displacement, respectively. These parameters are also described in Table 3.1. Equation 3.1 shows the dynamics of the force applied to physical specimen by the actuator. Clearly, Figure 3.3 and Equation 3.1 show that the dynamics of the physical specimen directly impact the characteristics of the plant. Moreover, when the physical specimen undergoes structural changes or is replaced by a new specimen, the overall dynamics of the plant changes through the natural velocity feedback path.

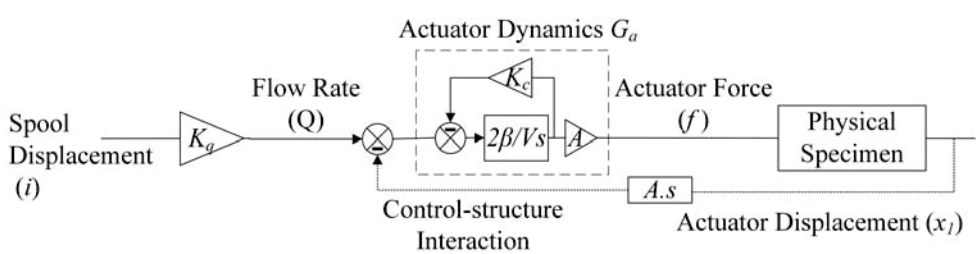

Fig. 3.3. Block diagram for an open-loop hydraulic actuator coupled with a physical specimen.

With a simple rearrangement of the block diagram in Figure 3.3, Figure 3.4a is obtained. In this representation, the actuator dynamics is written as

$$G_a = \frac{A}{\frac{V}{2\beta}s + K_c} \tag{3.2}$$

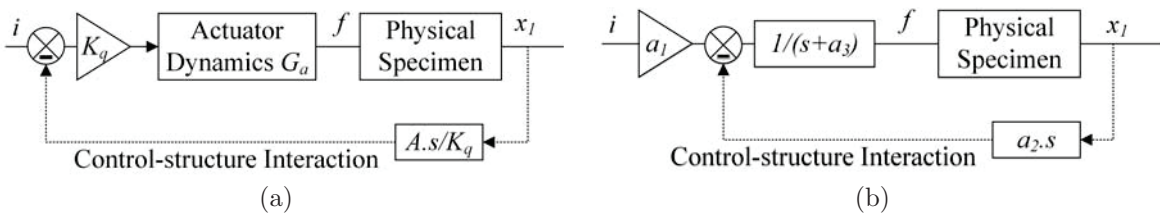

(a) (b)

Fig. 3.4. Equivalent block diagrams for the open-loop hydraulic actuator in Figure 3.3.

In this model, the underlying assumption is that the mass of piston is considered negligible in comparison to the mass of the physical specimen. Multiplying both sides by K_q, Equation 3.2 can be written as

$$K_q G_a = \frac{AK_q}{\frac{V}{2\beta}s + K_c} \tag{3.3}$$

Next, all the parameters are lumped into three new parameters [41]: a_1, a_2, and a_3,

$$a_1 = \frac{2\beta K_q A}{V}; \quad a_2 = \frac{2\beta A^2}{V}; \quad a_3 = \frac{2\beta K_c}{V} \tag{3.4}$$

and Equation 3.3 becomes

$$K_q G_a = \frac{\frac{a_1}{a_3}}{\frac{1}{a_3}s + 1} = \frac{a_1}{s + a_3} \tag{3.5}$$

With a simple rearrangement, it can be easily shown that Figures 3.3, 3.4a and 3.4b are dynamically equivalent.

Spool valves are commonly used in hydraulic transfer systems. This mechanical component regulates the fluid flow rate (Q) to the hydraulic actuator. To obtain an equivalent block diagram of the closed-loop plant in Figure 3.2, the servo-valve dynamics (G_{sv}: from analog controller command to spool displacement in servo-valve) is being modeled as a first order transfer function [7, 41, 79]. It should be noted that a first order model is a simplified representation of the dynamics of servo-valve. For instance, for a servo-valve with the operational frequency bandwidth of 0-60 Hz, this simplified model may be able to capture the essential dynamics of the servo-valve up

to ≈30 Hz. Further details on the dynamics of electro-hydraulic servo-valve can be found in [80, 81]. The first order model is

$$G_{sv}(s) = \frac{\gamma}{s + \beta_1} \tag{3.6}$$

where γ and $1/\beta_1$ denote a constant gain and servo-valve time constant, respectively. As noted before, to stabilize the plant, an analog PID controller is being used in which the integral (I) and derivative (D) gains are set to zero. The proportional (P) gain will intentionally be varied in different experiments. Here, the (P) gain and γ are lumped into a new parameter which is being defined as

$$\beta_0 = P\gamma \tag{3.7}$$

Note that β_0 holds a proportional linear relationship with the (P) gain. Also, to reduce the number of parameters for identification, a new dummy parameter is defined

$$r = a_1 i \tag{3.8}$$

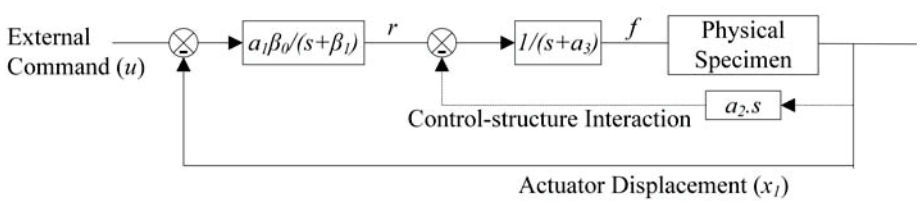

Fig. 3.5. Equivalent block diagram for the closed-loop plant.

Thus Figure 3.2 can be reduced to the dynamically equivalent form shown in Figure 3.5 which represents the dynamics from external command (u) to actuator displacement (x_1).

3.1.3 Identification of Hydraulic Transfer System Parameters

Assume a single-degree-of-freedom nonlinear physical specimen, expressed in the generalized form

$$x_3 = h(x_1, x_2) + f/m \tag{3.9}$$

where x_2 and x_3 denote $\dot{x}_1$ and $\ddot{x}_1$, respectively. The closed-loop dynamics in Figure 3.5 is written as a fourth order nonlinear system of differential equations

$$\begin{cases} \dot{x}_1 & = x_2 \\ \dot{x}_2 & = h(x_1, x_2) + f/m \\ \dot{f} & = -a_2 x_2 - a_3 f + r \\ \dot{r} & = -a_1 \beta_0 x_1 - \beta_1 r + a_1 \beta_0 u \end{cases} \tag{3.10}$$

where u denotes the external command to the plant. Incorporating the dummy parameter r, the closed-loop plant can be identified with four parameters: β_1, $a_1\beta_0$, a_2 and a_3. In Table 3.1, the parameters associated with the hydraulic transfer system are listed.

Table 3.1.
Hydraulic transfer system parameters.

Parameter	**Units**	**Component**	**Description**
P	mA/m	Analog Controller	Controller proportional gain
γ	$m/mA/sec$	Servo-valve	Servo-valve gain
$1/\beta_1$	sec	Servo-valve	Servo-valve time constant
K_q	$m^3/sec/m$	Servo-valve	Valve flow gain
i	m	Servo-valve	Spool displacement
A	m^2	Hydraulic actuator	Piston area
K_c	$m^3/sec/Pa$	Hydraulic actuator	Leakage coefficient of the actuator
V	m^3	Hydraulic actuator	Half the volume of the actuator
β	Pa	Hydraulic actuator	Effective bulk modulus of the fluid
Q	m^3/sec	Hydraulic actuator	Fluid flow rate into the actuator
x_1	m	Hydraulic actuator	Actuator displacement
f	N	Hydraulic actuator	Actuator force

Let's assume, the physical specimen is removed, the nonlinear system in Equation 3.10 can be simplified to a linear transfer function from external command (u) to actuator displacement (x_1)

$$G_{x_1,u} = \frac{n_0}{d_2 s^2 + d_1 s + d_0} \tag{3.11}$$

where $s \in \mathbb{C}$ is the Laplace variable, and

$$\begin{aligned} n_0 &= a_1 \beta_0 \\ d_2 &= a_2 \\ d_1 &= \beta_1 a_2 \\ d_0 &= a_1 \beta_0 \end{aligned} \tag{3.12}$$

Note that, the static gain of the transfer function in Equation 3.12 is unity. In case static gain is found to be a different value, that gain needs to be incorporated to modify the command displacement.

If the physical specimen is a linear spring, with a constant stiffness ($f = kx_1$), the nonlinear system of differential equations in Equation 3.10 becomes a linear system with the following transfer function from external command (u) to actuator displacement (x_1)

$$G_{x_1,u} = \frac{n_0}{d_2 s^2 + d_1 s + d_0} \tag{3.13}$$

where

$$\begin{aligned} n_0 &= a_1 \beta_0 \\ d_2 &= k + a_2 \\ d_1 &= a_3 k + \beta_1 k + \beta_1 a_2 \\ d_0 &= \beta_1 a_3 k + a_1 \beta_0 \end{aligned} \tag{3.14}$$

Finally, if the physical specimen is a linear single degree of freedom system of the form

$$x_3 = -[c/m]x_2 - [k/m]x_1 + f/m \tag{3.15}$$

The nonlinear system of differential equations in Equation 3.10) becomes a fourth order linear system, whose transfer function from external command (u) to actuator displacement (x_1) is given by

$$G_{x_1,u} = \frac{n_0}{d_4 s^4 + d_3 s^3 + d_2 s^2 + d_1 s + d_0} \tag{3.16}$$

where

$$\begin{aligned} n_0 &= a_1 \beta_0 \\ d_4 &= m \\ d_3 &= a_3 m + c + \beta_1 m \\ d_2 &= k + a_3 c + a_2 + \beta_1 a_3 m + \beta_1 c \\ d_1 &= a_3 k + \beta_1 k + \beta_1 a_3 c + \beta_1 a_2 \\ d_0 &= \beta_1 a_3 k + a_1 \beta_0 \end{aligned} \tag{3.17}$$

To identify the four parameters in Equation 3.10, the first case is the one in which the physical specimen is removed. In this case, β_1 and a dummy parameter R_1 is identified as follows

$$\begin{aligned} \beta_1 &= \frac{d_1}{d_2} \\ R_1 &= \frac{d_0}{d_2} = \frac{a_1 \beta_0}{a_2} \end{aligned} \tag{3.18}$$

The next step is to conduct a set of experiments in which the physical specimen is simply a linear spring. Using Equations 3.13 and 3.14, another two dummy parameters R_2 and R_3 are identified as follows

$$\begin{aligned} R_2 &= \frac{\beta_1 k}{d_0/n_0 - 1} = \frac{a_1 \beta_0}{a_3} \\ R_3 &= \frac{d_2/n_0 - 1/R_1}{k} = \frac{1}{a_1 \beta_0} \end{aligned} \tag{3.19}$$

To verify the identified results, different linear springs with various stiffnesses should be tested. Also, for a particular hydraulic transfer system, a sensitivity analysis is recommended to assess the sensitivity of these dummy parameters to the spring

stiffness. The results of this parameter sensitivity analysis determine the number of experiments required to confidently identify these dummy parameters.

Finally, after identifying the dummy parameters, $a_1\beta_0$, a_2 and a_3 are computed as follows

$$\begin{aligned} a_1\beta_0 &= \frac{1}{R_3} \\ a_2 &= \frac{1}{R_3 R_1} \\ a_3 &= \frac{1}{R_2 R_3} \end{aligned} \tag{3.20}$$

In this section, a simple method is demonstrated to identify β_1, $a_1\beta_0$, a_2, a_3. These parameters are required to construct the fourth order nonlinear system of differential equations in Equation 3.10.

3.1.4 Transforming the Plant Model into Controllable Canonical Form

In this section, the fourth order nonlinear system of differential equations in Equation 3.10 is reformulated to fit in a class of nonlinear systems of differential equations described by the *companion form* or *controllable canonical form*. This class of nonlinear systems of differential equations are important for control purposes. For completeness, this class of nonlinear systems is discussed in this section. Further detailed description is provided in [82].

A system is said to be in controllable canonical form if its dynamics can be represented by

$$x_1^{(n)} = f(\mathbf{X}) + b(\mathbf{X})u \tag{3.21}$$

where $\mathbf{X} = [x_1 \ \dot{x}_1 \ \cdots \ x_1^{(n-1)}]^T$ is the system state vector, x is the scalar state of interest, u is the scalar control input, $f(\mathbf{X})$ and $b(\mathbf{X})$ are nonlinear functions of the states. This system can be represented as

$$\begin{aligned} \dot{x}_1 &= x_2 \\ \dot{x}_2 &= x_3 \\ &\vdots \\ \dot{x}_n &= f(\mathbf{X}) + b(\mathbf{X})u \end{aligned} \tag{3.22}$$

For the nonlinear system in Equation 3.22, theoretically speaking, using the control input

$$u = \frac{1}{b(\mathbf{X})}[v - f(\mathbf{X})], \tag{3.23}$$

transforms the nonlinear system in Equation 3.22 into the following simple linear system of differential equations

$$\begin{aligned} \dot{x}_1 &= x_2 \\ \dot{x}_2 &= x_3 \\ &\vdots \\ \dot{x}_n &= v \end{aligned} \tag{3.24}$$

Thus, the coefficients of the control law

$$v = -k_0 x_1 - k_1 \dot{x}_1 - \cdots - k_{n-1} x_1^{(n-1)} \tag{3.25}$$

can be chosen so that the polynomial

$$p^n + k_{n-1} p^{n-1} + \cdots + k_0 = 0 \tag{3.26}$$

has all its roots strictly in the left-half of the complex plane. This leads the entire nonlinear system of differential equations to have exponentially stable dynamics. Moreover, in the case of tracking a desired signal, the tracking error ($e = x - x_d$) and the control law (v) can be chosen so that the entire nonlinear system behaves with exponentially convergent tracking.

To transform Equation 3.10 into the controllable canonical form, x_4 is defined as the first time derivative of x_3 in Equation 3.9

$$x_4 = \dot{x}_3 = \dot{h} + \dot{f}/m \tag{3.27}$$

using Equation 3.10, x_4 can also be written as

$$x_4 = \dot{x}_3 = \dot{h} + (-a_2 x_2 - a_3 f + r)/m \tag{3.28}$$

where

$$\dot{h} = \frac{\partial h}{\partial x_1}\frac{dx_1}{dt} + \frac{\partial h}{\partial x_2}\frac{dx_2}{dt} = \frac{\partial h}{\partial x_1}x_2 + \frac{\partial h}{\partial x_2}x_3 \tag{3.29}$$

Taking the time derivative of x_4, it becomes

$$\dot{x}_4 \;=\; \ddot{h} + (-a_2 x_3 - a_3 \dot{f} + \dot{r})/m, \tag{3.30}$$

where

$$\ddot{h} = \frac{\partial^2 h}{\partial {x_1}^2}x_2^2 + \frac{\partial^2 h}{\partial {x_2}^2}x_3^2 + 2\frac{\partial^2 h}{\partial x_1 \partial x_2}x_2 x_3 + \frac{\partial h}{\partial x_1}x_3 + \frac{\partial h}{\partial x_2}x_4 \tag{3.31}$$

Substituting $\dot{f}$ and $\dot{r}$ by their equivalent equations in Equation 3.10 yields

$$\dot{x}_4 \;=\; \ddot{h} + [-a_2 x_3 - a_3(-a_2 x_2 - a_3 f + r) + (-a_1\beta_0 x_1 - \beta_1 r + a_1\beta_0 u)]/m \tag{3.32}$$

Equating Equation 3.10 and Equation 3.27 and rearranging terms yields

$$r = (a_2 - m\frac{\partial h}{\partial x_1})x_2 - m\frac{\partial h}{\partial x_2}x_3 + m x_4 + a_3 f \tag{3.33}$$

Now in Equation 3.32, r can be replaced by Equation 3.33. Note that similar to r, f can also be found in terms of the system states. However, f is a meaningful measurable signal. Thus, f will remain as is in the new formulation of the nonlinear system of differential equations

$$\begin{cases} \dot{x}_1 & = x_2 \\ \dot{x}_2 & = x_3 \\ \dot{x}_3 & = x_4 \\ \dot{x}_4 & = -C_1 u + C_1 x_1 + C_2 x_2 + C_3 x_3 + C_4 x_4 + C_5 f + C_n \end{cases} \tag{3.34}$$

where

$$
\begin{aligned}
C_1 &= -a_1\beta_0/m \\
C_2 &= -\beta_1 a_2/m + \beta_1(\partial h/\partial x_1) + a_3(\partial h/\partial x_1) \\
C_3 &= \beta_1(\partial h/\partial x_2) + a_3(\partial h/\partial x_2) - a_2/m \\
C_4 &= -\beta_1 - a_3 \\
C_5 &= -\beta_1 a_3/m \\
C_n &= \ddot{h}
\end{aligned}
\tag{3.35}
$$

After transforming the dynamical model in Equation 3.10 into the controllable canonical form, the four parameters associated with the closed-loop hydraulic transfer system are required: β_1, $a_1\beta_0$, a_2 and a_3. Figure 3.6 summarizes all steps described in the preceding sections to acquire a nonlinear dynamical model for plants presented in controllable canonical form. In the following section, the proposed technique will be experimentally verified.

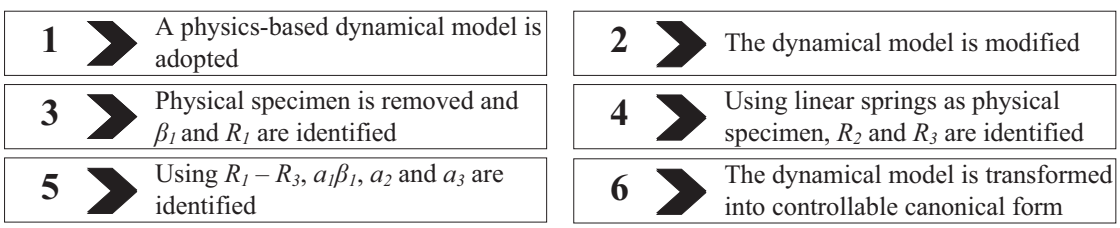

Fig. 3.6. Steps to obtain a nonlinear dynamical model for the plant in the controllable canonical form.

3.2 Illustrative Experimental Case Studies

In this section, the parameters associated with the plant are identified and experimentally verified. The impact of CSI is experimentally investigated. The hydraulic actuator employed in the experimental case studies is a double acting, double ended dynamic Shore Western's actuator with product number 910D-.77-6-4-1348. The pis-

ton area for this actuator is 2.387×10^{-4} m^2 and the actuator force capacity is 4.89 kN at 20.7 MPa pressure. A Schenck-Pegasus 162M servo-valve rated for 15 GPM at 20.7 MPa pressure is used to control the actuator. The servo-valve has a nominal operational frequency bandwidth of 0-60 Hz and is driven by the Shore Western Control System. The actuator is placed in a small-scale loading frame located in Intelligent Infrastructure System Laboratory, Purdue University. The actuator in the loading frame is equipped with an internal LVDT and is controlled by an SC6000 controller to provide the analog PID control loop. It should be noted that in all experiments the integral (I) and derivative (D) gains are set to zero to agree with the equations herein. The external command is applied using a high-performance Speedgoat/xPC (Speedgoat GmbH, 2011) real-time kernel. High-resolution, high-accuracy, 18-bit analog I/O boards are integrated into this digital control system that supports up to 32 differential simultaneous A/D channels and eight D/A channels.

3.2.1 Parametric Identification of Hydraulic Transfer System

To identify the parameters associated with the hydraulic transfer system, the first step is to remove the physical specimen and identify the dynamic performance of the isolated transfer system, see Figure 3.7. As discussed in the previous section, this system behaves dynamically like a second order transfer function, see Equation 3.11.

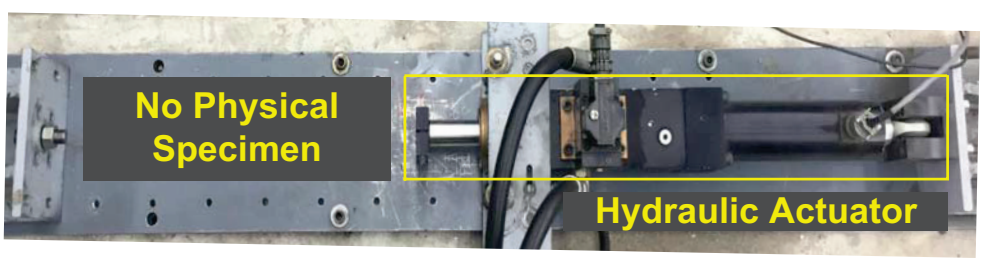

Fig. 3.7. Identification: hydraulic transfer system with no physical specimen.

Using the Transfer Function Estimation code (tfest) in MATLAB, the identified transfer function is identified as

$$G_{x_1,u} = \frac{3060}{s^2 + 267s + 3060} \tag{3.36}$$

Frequency response functions of the plant with no physical specimen and identified transfer function are shown in Figure 3.8.

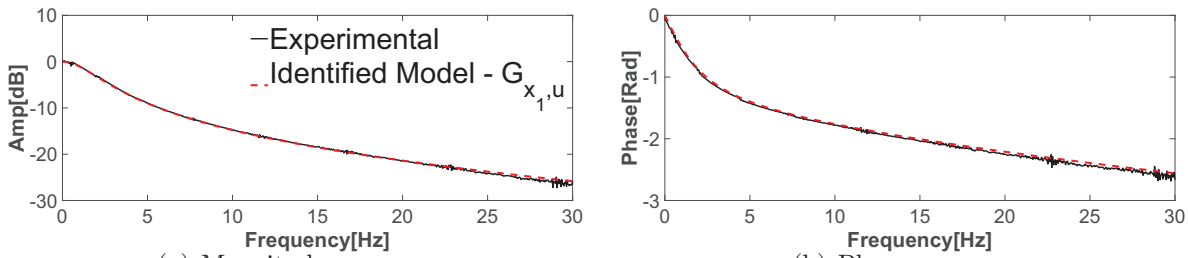

(a) Magnitude response (b) Phase response

Fig. 3.8. Plant with no physical specimen: experimental and identified frequency response functions, from external command to actuator displacement.

Figure 3.8 shows a good agreement between the experimental and identified frequency response functions, from external command to actuator displacement. Using Equation 3.36, for this hydraulic transfer system, β_1 and dummy parameter R_1 are identified as 267 $1/sec$ and 3060 $1/sec^2$, respectively. Figure 3.9 shows time domain results that further verify the identified transfer function for <0.5 Hz, ≈2.5 Hz, ≈18 Hz and ≈35 Hz excitations, respectively.

Next, two linear springs with known stiffness values are used as physical specimens: $k_1 = 116640\ N/m$ and $k_2 = 88540\ N/m$. As discussed in the previous section, the hydraulic transfer system coupled with a spring behaves dynamically like a second order transfer function in Equation 3.13. Experimental frequency response functions and identified transfer functions are obtained using the Transfer Function Estimation code (tfest) in MATLAB. The first system is identified as the following transfer function

$$G^{k_1}_{x_1,u} = \frac{2703}{s^2 + 263.4s + 3337} \tag{3.37}$$

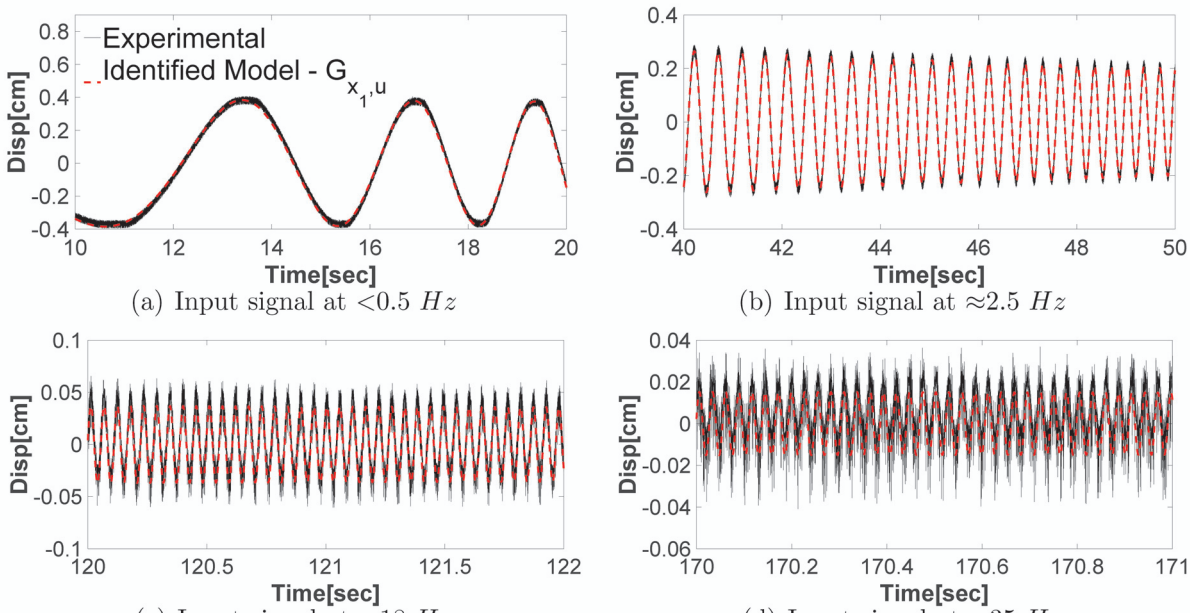

(a) Input signal at <0.5 Hz

(b) Input signal at ≈2.5 Hz

(c) Input signal at ≈18 Hz

(d) Input signal at ≈35 Hz

Fig. 3.9. No physical specimen: time domain comparison of the experimental and identified plant responses.

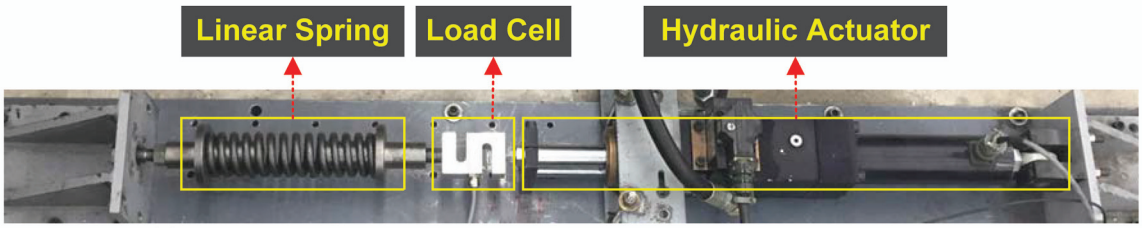

(a) Identification: hydraulic transfer system coupled with a linear spring.

(b) Linear spring: $k_1 = 116640\ N/m$

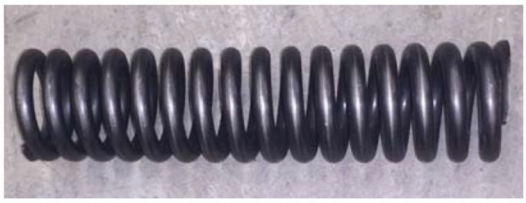

(c) Linear spring: $k_2 = 88540\ N/m$

Fig. 3.10. Hydraulic transfer system attached to a linear spring.

The frequency response functions of the actuator attached to the first spring and the identified transfer function, from external command to actuator displacement, are

shown in Figure 3.11. Also, Figure 3.12 demonstrates the time domain verification of the identified transfer function, for <0.5 Hz, ≈2.5 Hz, ≈18 Hz and ≈35 Hz excitations.

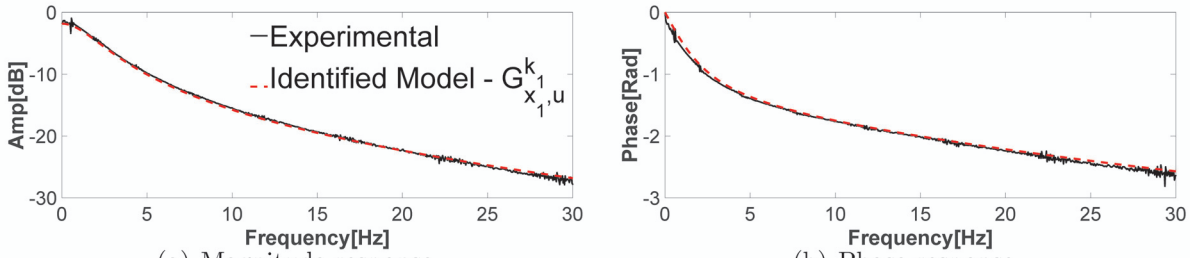

(a) Magnitude response (b) Phase response

Fig. 3.11. Hydraulic transfer system coupled with the linear spring k_1: experimental and identified frequency response functions, from external command to actuator displacement.

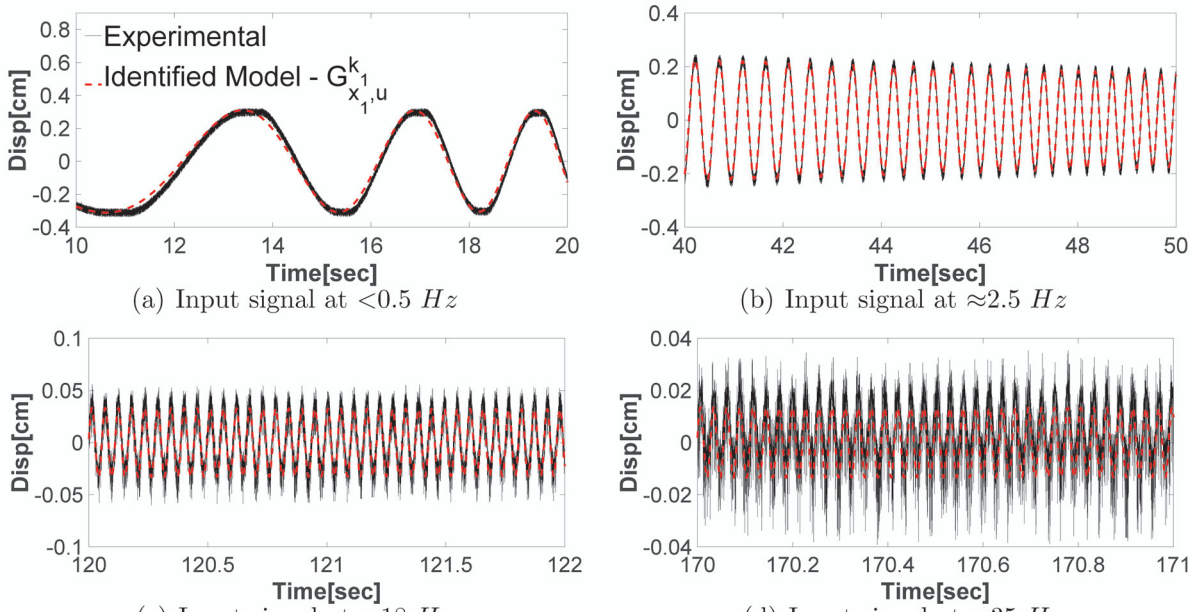

(a) Input signal at <0.5 Hz (b) Input signal at ≈2.5 Hz

(c) Input signal at ≈18 Hz (d) Input signal at ≈35 Hz

Fig. 3.12. Hydraulic transfer system coupled with the linear spring k_1: time domain comparison of the experimental and identified plant responses.

Using the Transfer Function Estimation code (tfest) in MATLAB, the second plant is also identified as the following transfer function

$$G^{k_2}_{x_1,u} = \frac{2714}{s^2 + 262.4s + 3073} \tag{3.38}$$

The frequency response functions of the hydraulic transfer system attached to the second spring and the identified transfer function are shown in Figure 3.13. In addi-

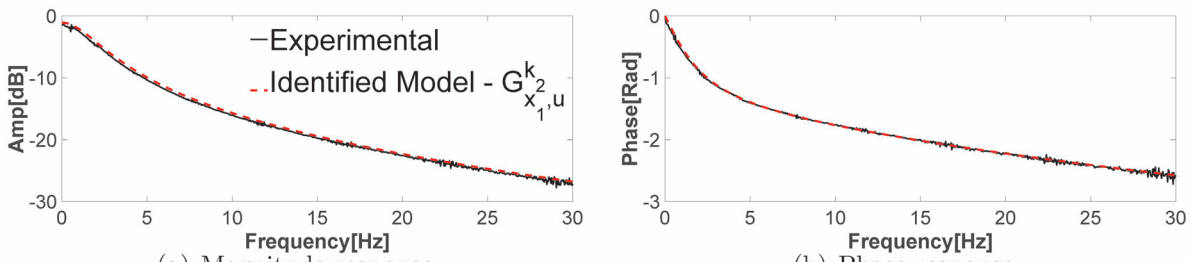

(a) Magnitude response (b) Phase response

Fig. 3.13. Hydraulic transfer system coupled with the linear spring k_2: experimental and identified frequency response functions, from external command to actuator displacement.

tion, Figure 3.14 demonstrates the time domain verification of the identified transfer function for <0.5 Hz, ≈2.5 Hz, ≈18 Hz and ≈35 Hz excitations.

The frequency and time domain comparisons show good agreement between the experimental system and identified model responses, thus, R_2^{k1} and R_3^{k1} associated with the first spring and R_2^{k2} and R_3^{k2} associated with the second spring are computed. Figure 3.15 shows the frequency domain comparison of the hydraulic transfer system attached to different physical specimens (i.e., no physical specimen, linear spring: k_1 = 116640 N/m and linear spring: k_2 = 88540 N/m): (a) experimental responses and (b) identified model responses.

After identifying β_1 and the dummy parameter R_1 (in the case with no physical specimen) and the dummy parameters R_2 and R_3 (in the case with linear springs), computations to get the remaining parameters $a_1\beta_0$, a_2 and a_3 are straightforward using Equation 3.20. The identified parameters are $\beta_1 = 267\ 1/sec$, $a_1\beta_0 = 2.412 \times 10^9\ m.Pa/sec^2$, $a_2^{k1} = 8.83 \times 10^5\ m.Pa$, $a_2^{k2} = 6.95 \times 10^5\ m.Pa$, $a_3^{k1} = 20.35\ 1/sec$

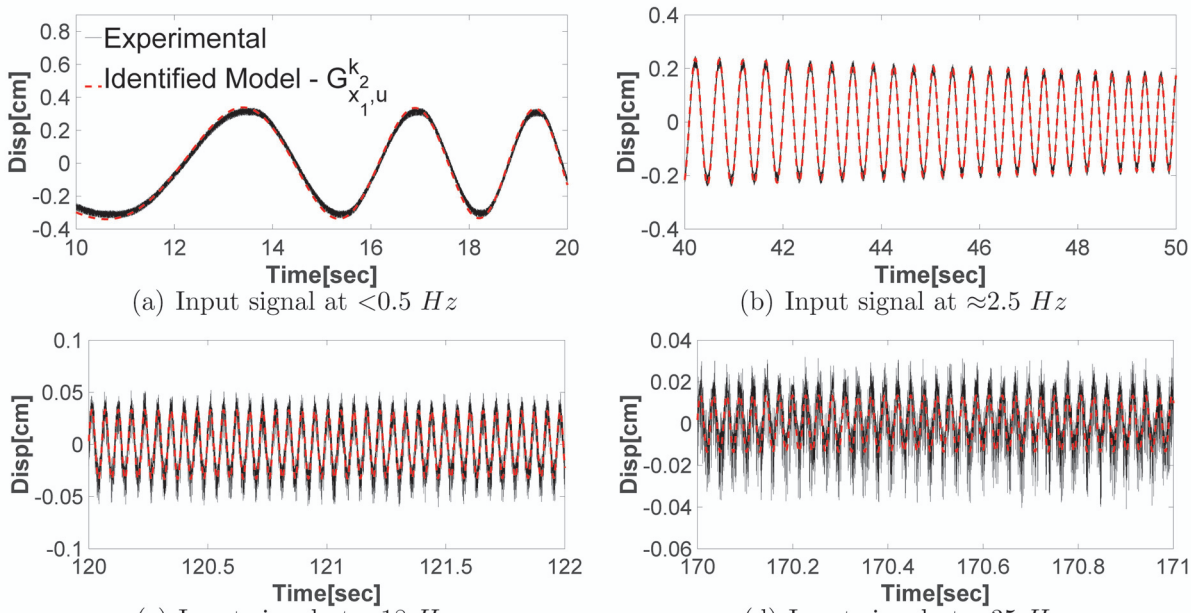

(a) Input signal at <0.5 Hz (b) Input signal at ≈2.5 Hz

(c) Input signal at ≈18 Hz (d) Input signal at ≈35 Hz

Fig. 3.14. Hydraulic transfer system coupled with the linear spring k_2: time domain comparison of the experimental and identified plant responses.

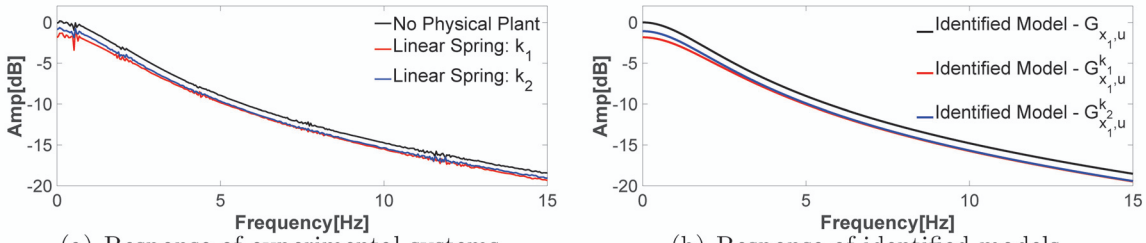

(a) Response of experimental systems. (b) Response of identified models.

Fig. 3.15. Frequency domain comparison of the hydraulic transfer system coupled with different physical specimens.

and $a_3^{k2} = 11.89\ 1/sec$. Thus, to identify a_2 and a_3 for the verification section, the mean values are computed as $a_2 = 7.881 \times 10^5\ m.Pa$ and $a_3 = 16.118\ 1/sec$.

In this section the parameters associated with the hydraulic transfer system are identified as $\beta 1$, $a_1\beta_0$, a_2 and a_3. With these parameters, a general nonlinear physical plant of the form

$$x_3 = h(x_1, x_2) + f/m \tag{3.39}$$

coupled with the hydraulic transfer system can be represented in controllable canonical form (Equation 3.34) where C_1-C_5 and C_n are defined in Equation 3.35. In the next section, the impact of coupling between the physical specimen and hydraulic transfer system will be investigated. In addition, the identified parameters will be experimentally verified.

The piston mass is assumed to be negligible in this technique because the force generated by the springs is quite large in comparison to the inertial force of the piston. In addition, the stiffness of spring should be such that the comparison between the plant with and without the spring (i.e., provided in Figure 3.15) would provide meaningful information. Excessively stiff or soft springs will lead to inaccurate parameter estimates due to the assumptions associated with the linearized model employed in this study.

3.2.2 Experimental Validation: Linear Physical Specimen

One of the motivations behind parametric identification of the hydraulic transfer system is to have a model which is still valid when the physical specimen and/or analog controller undergo changes. Ideally, after the parametric identification of the hydraulic transfer system, any change in the physical specimen (e.g., nonlinear structural behavior) or the controller can simply be accommodated without the need for re-identification of the plant. To demonstrate this feature and verify the identified parameters, four experiments are implemented. In these experiments, changes are made in the stiffness of the physical specimen (two choices: 129400 N/m and 84340 N/m) as well as the proportional (P) gain (two choices: 1 mA/m and 2 mA/m). These case studies are presented in Table 3.2. Note that the damping coefficient in Table 3.2 is

included to represent the energy dissipation mechanism within the physical specimen and between the physical specimen and actuator (e.g., friction).

Table 3.2.
Four experimental cases.

Case Study	**Mass** (kg)	**Damping** (N.s/m)	**Stiffness** (N/m)	**Proportional Gain** (P) gain
Exp1	3.8	5	129400	1
Exp2	3.8	5	129400	2
Exp3	3.8	5	84340	1
Exp4	3.8	5	84340	2

The next section experimentally investigates the natural coupling present between the hydraulic transfer system and the physical specimen (CSI) for Exp1-Exp4. It is worth mentioning that transforming the dynamical model into the controllable canonical form enables researchers to explain this phenomenon in a remarkably simple and straightforward way.

Control-structure-interaction

When a physical specimen is attached to a hydraulic transfer system, a coupling is present between the actuator and the specimen through a natural velocity feedback path [41]. Due to this phenomenon, for actuators attached to lightly damped physical specimen, the ability of the actuator to apply forces at the physical specimen natural frequencies (in case of linearity) is greatly limited. Thus, it is a relevant topic for RTHS researchers. Here, a simple way is presented to demonstrate the ability of a hydraulic transfer system to apply forces at the physical specimen natural frequencies using the nonlinear model in the controllable canonical form. The findings are experimentally verified.

In the case of a linear single-degree-of-freedom lumped parameter physical specimen of the form

$$\ddot{x}_1 = -kx_1/m - c\dot{x}_1/m + f/m \tag{3.40}$$

the system of differential equations in Equation 3.34 becomes

$$x_1^{(4)} = -C_1u + C_1x_1 + C_2x_1^{(1)} + C_3x_1^{(2)} + C_4x_1^{(3)} + C_5F \tag{3.41}$$

where $x_1^{(n)}$ denotes the nth derivative with respect to time. In the Laplace domain, the physical specimen is presented as

$$X_1 = \frac{F}{ms^2 + cs + k} \tag{3.42}$$

and Equation 3.41 becomes

$$C_1U = (C_1 + C_2s + C_3s^2 + C_4s^3 - s^4)X_1 + C_5F \tag{3.43}$$

where U, X_1 and F denote external command, actuator displacement and actuator force in the Laplace domain, respectively. In Equation 3.43, substituting X_1 using Equation 3.42 yields

$$C_1U = [\frac{-s^4 + C_4s^3 + C_3s^2 + C_2s + C_1}{ms^2 + cs + k} + C_5]F \tag{3.44}$$

Equation 3.44 is rearranged into

$$G_{fu} = \frac{F}{U} = \frac{C_1(ms^2 + cs + k)}{-s^4 + C_4s^3 + (C_3 + kC_5)s^2 + (C_2 + cC_5)s + (C_1 + kC_5)} \tag{3.45}$$

Notice that unless pole/zero cancellation occurs, the poles of the physical specimen are zeros of the hydraulic transfer system when it is coupled with a linear physical specimen.

Comparisons of the experimental and simulated (Equation 3.45 using the identified parameters in Table 3.2 and Table 3.3) frequency response functions (from external command to actuator force) associated with Exp1-Exp2 are provided in Figure 3.16. In these two cases, the physical specimen natural frequency is identified as 29.4 Hz. Using the same manner as the previous case, comparisons of the experimental and

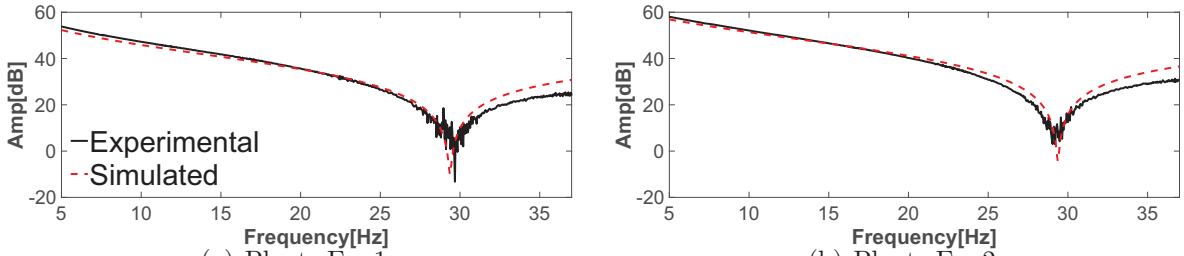

(a) Plant: Exp1 (b) Plant: Exp2

Fig. 3.16. Comparison of the simulated (Equation 3.45) and experimental frequency response functions: external command to actuator force (physical specimen natural frequency is identified as 29.4 Hz).

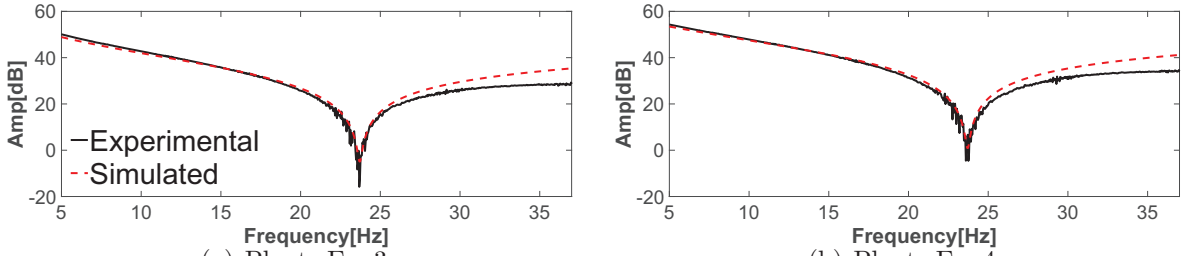

(a) Plant: Exp3 (b) Plant: Exp4

Fig. 3.17. Comparison of the simulated (Equation 3.45) and experimental frequency response functions: external command to actuator force (physical specimen natural frequency is identified as 23.7 Hz).

simulated frequency response functions (from external command to actuator force) associated with Exp3-Exp4 are provided in Figure 3.17. In these two cases, the physical specimen natural frequency is identified as 23.7 Hz.

The next section presents experimental verification of the identified parameters as part of different plants (Exp1-Exp4) in which the plants and their associated simulations are subjected to a quadratic chirp signal.

Identified parameters

In this section, the following controllable canonical form is employed to model the hydraulic transfer system coupled with various physical specimens (i.e., Exp1-Exp4 in Table 3.2)

$$\begin{cases} \dot{x}_1 &= x_2 \\ \dot{x}_2 &= x_3 \\ \dot{x}_3 &= x_4 \\ \dot{x}_4 &= -C_1 u + C_1 x_1 + C_2 x_2 + C_3 x_3 + C_4 x_4 + C_5 F + C_n \end{cases} \tag{3.46}$$

where C_1-C_5, and C_n are identified in Section 3.2.1 and their corresponding values are provided in Table 3.3. Note that the values vary as the physical specimen changes. Clearly, in the case of a linear physical specimen, C_n (i.e., the nonlinear term) is dropped from Equation 3.46 and assumed to be negligible. The physical specimen parameters and proportional (P) gain associated with different experiments are provided in Table 3.2. Note that $a_1\beta_0$ holds a proportional linear relationship with the (P) gain: $\beta_0 = P\gamma$.

A typical experimental setup in which a hydraulic transfer system is attached to a linear single-degree-of-freedom system is shown in Figure 3.18. Four experiments are implemented. In these experiments, the varying parameters are the stiffness of physical specimen and the (P) gain, see Table 3.2. The external command is a quadratic chirp signal sweeping from 0.1 Hz to 35 Hz.

In the first and second experiments (Exp1 and Exp2), the natural frequency of the physical specimen is identified as 29.4 Hz, and the proportional (P) gains are set to 1 and 2, respectively. Time domain responses of the plants and their associated simulations (using Equation 3.46 and Table 3.3) are compared in Figure 3.19 and Figure 3.20, respectively. Similarly, in the third and fourth experiments (Exp3 and Exp4, see Table 3.2), the natural frequency of the physical specimen is identified as 23.7 Hz, and the proportional (P) gains are set to 1 and 2, respectively. Time

Table 3.3.
Identified parameters associated with the dynamical model in Equation 3.46.

Parameters	**Exp1**	**Exp2**	**Exp3**	**Exp4**
β_1 $[1/sec]$	267	267	267	267
$a_1\beta_0$ $[m.Pa/sec^2]$	2.412×10^9	4.823×10^9	2.412×10^9	4.823×10^9
a_2 $[m.Pa]$	7.881×10^5	7.881×10^5	7.881×10^5	7.881×10^5
a_3 $[1/sec]$	16.118	16.118	16.118	16.118
C_1 $[1/sec^4]$	-6.602×10^8	-1.320×10^9	-6.602×10^8	-1.320×10^9
C_2 $[1/sec^3]$	-2.097×10^7	-2.097×10^7	-3.373×10^7	-3.373×10^7
C_3 $[1/sec^3]$	-2.143×10^5	-2.143×10^5	-2.143×10^5	-2.143×10^5
C_4 $[1/sec]$	-283.118	-283.118	-283.118	-283.118
C_5 $[m/N/sec^4]$	-1.133×10^3	-1.133×10^3	-1.133×10^3	-1.133×10^3

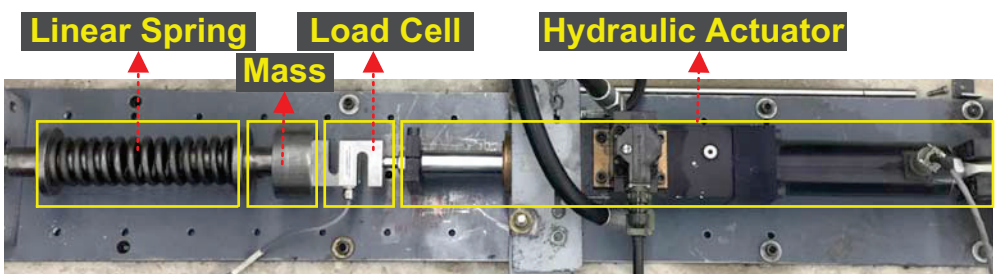

Fig. 3.18. Verification- hydraulic transfer system coupled with a linear single-degree-of-freedom specimen.

domain responses of the plants and their associated simulations (see Equation 3.46 and Table 3.3) are compared in Figure 3.21 and Figure 3.22, respectively.

Table 3.4.
Normalized error for experimental results.

	Exp1	**Exp2**	**Exp3**	**Exp4**
$NRMSE$	3.1%	2.8%	2.7%	2.8%
NAE	16.4%	12.6%	14.4%	12.9%

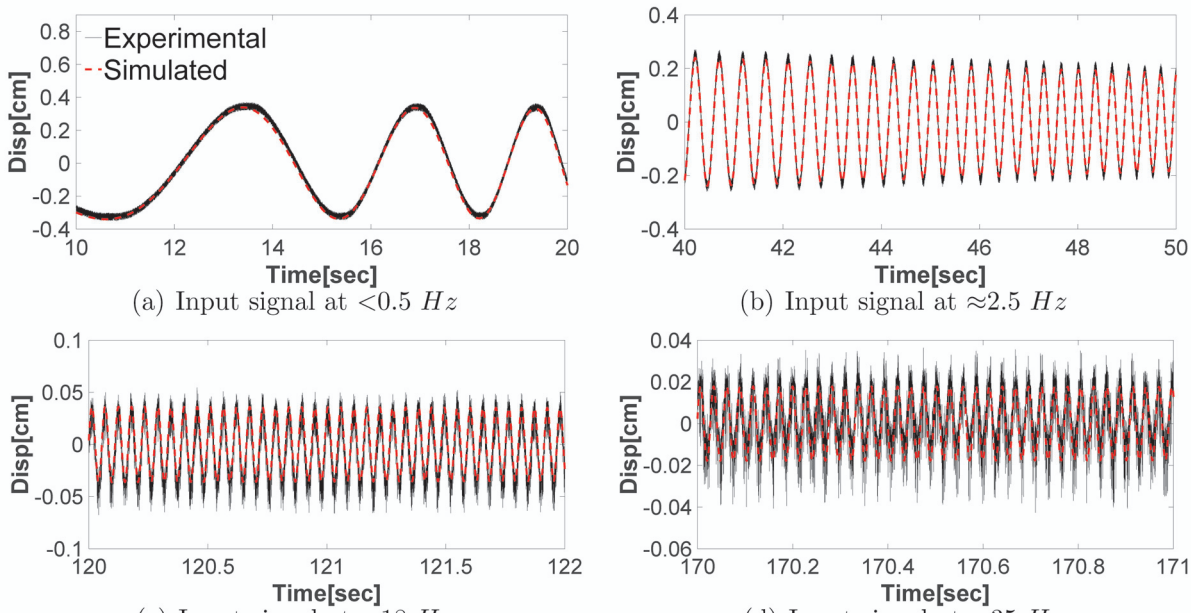

(a) Input signal at <0.5 Hz (b) Input signal at ≈2.5 Hz

(c) Input signal at ≈18 Hz (d) Input signal at ≈35 Hz

Fig. 3.19. Exp1: time domain comparison of the experimental and simulated plant responses.

The time domain comparisons show good agreement between the experimental and simulated responses, see Table 3.4. The normalized errors are computed as

$$NRMSE = \frac{\sqrt{\frac{1}{n-1}\sum_{i=1}^{n}[x_1^E(i\Delta t) - x_1^N(i\Delta t)]^2}}{max(|x_1^E|)} \times 100 \tag{3.47}$$

$$NAE = \frac{max(|x_1^E - x_1^N|)}{max(|x_1^E|)} \times 100 \tag{3.48}$$

where x_1^E and x_1^N are experimental and simulated actuator displacements and $NRMSE$ and NAE stand for normalized root mean square error and normalized absolute error, respectively. The results verify the adopted model and the identified parameters for the hydraulic transfer system.

Some important observations can be made from these results. As the proportional (P) gain increases, the hydraulic control system behaves slightly nonlinear (offset or drift) at high frequency vibrations. In the time domain comparisons, these drifts can be seen in Figures 3.20d and 3.22d. Based on the identified parameters, the servo-valve time constant is identified as 3.7 $msec$. In another study [83], the time

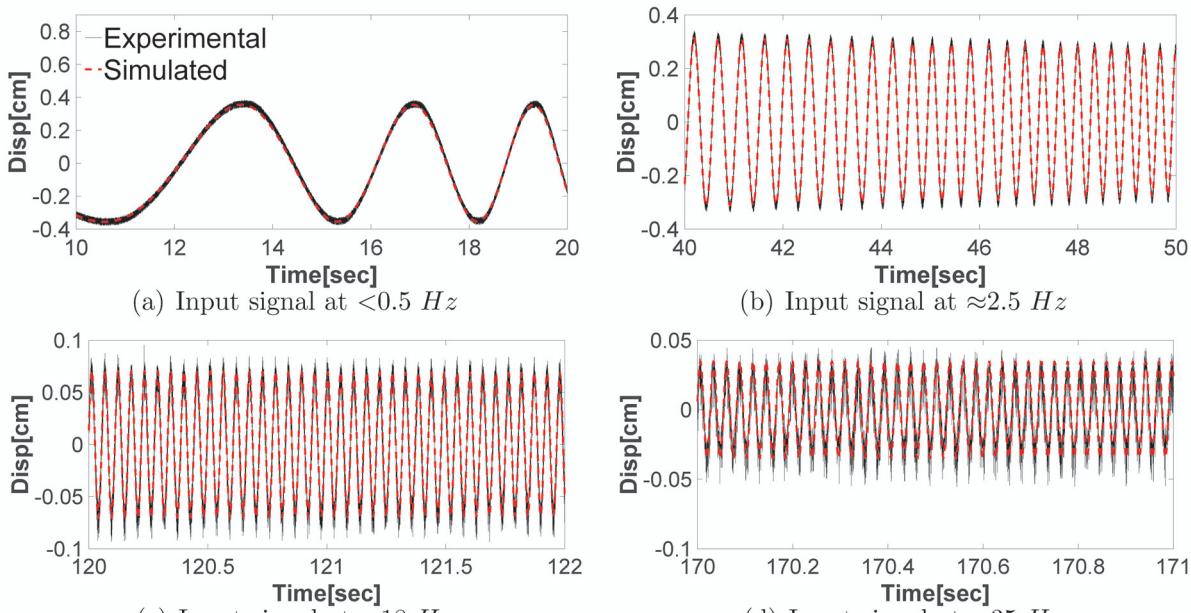

(a) Input signal at <0.5 Hz

(b) Input signal at ≈2.5 Hz

(c) Input signal at ≈18 Hz

(d) Input signal at ≈35 Hz

Fig. 3.20. Exp2: time domain comparison of the experimental and simulated plant responses.

constant associated with the same servo-valve was optimally identified as 3.6 $msec$ using genetic algorithms.

3.2.3 Experimental Validation: Nonlinear Physical Specimen

To validate the controllable canonical model for a hydraulic actuator coupled with a nonlinear physical specimen, a nonlinear device is designed and fabricated (see Figure 3.23). The nonlinear device is composed of a solid shaft that slides linearly into a hollow shaft, both of which are connected through two metallic coupons subjected to yielding. This specimen is designed to have certain features: (i) it exhibits nonlinear force-displacement profile; (ii) the force-displacement profile can easily be modeled using Equation 3.49; (iii) the force-displacement profile varies as functions of the initial condition of the specimen and the material used in the coupons (e.g., steel,

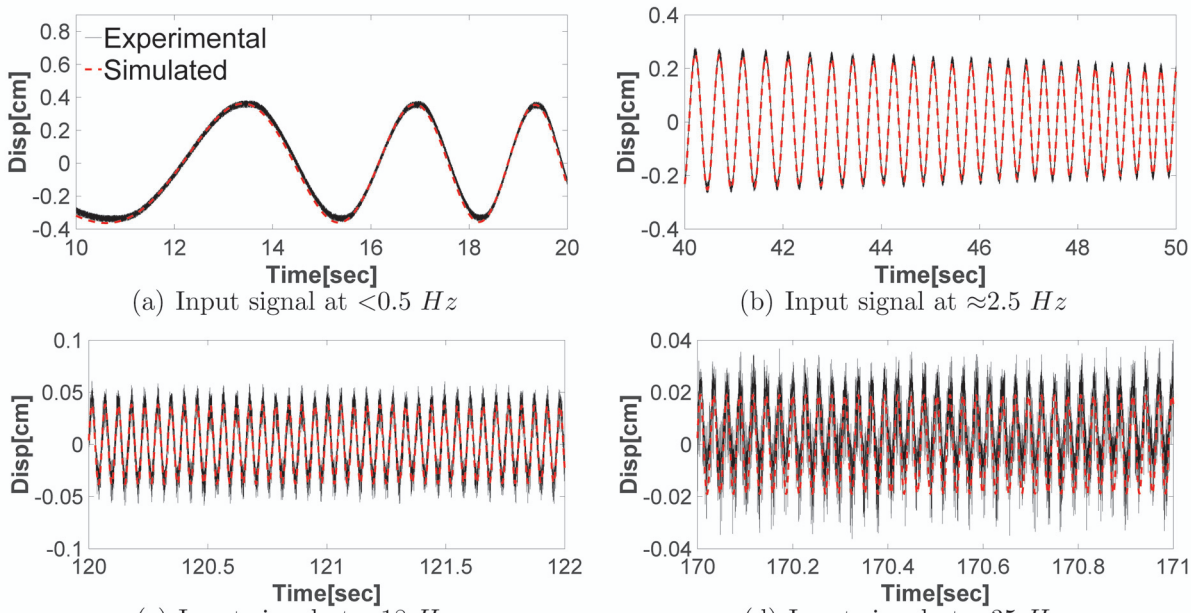

(a) Input signal at <0.5 Hz

(b) Input signal at ≈2.5 Hz

(c) Input signal at ≈18 Hz

(d) Input signal at ≈35 Hz

Fig. 3.21. Exp3: time domain comparison of the experimental and simulated plant responses.

aluminum, and brass); and (iv) after each experiment, the yielded part (the coupons) easily replaced.

The hydraulic actuator employed in the experimental case studies is a double acting, double ended dynamic Shore Western's actuator with product number 910D-.77-6-4-1348. The piston area for this actuator is 2.387×10^{-4} m^2 and the actuator force capacity is 4.89 kN at 20.7 MPa pressure. A Schenck-Pegasus 162M servo-valve rated for 15 GPM at 20.7 MPa pressure is used to control the actuator. The servo-valve has a nominal operational frequency bandwidth of 0-60 Hz and is driven by a Schenck-Pegasus 5910 digital controller. The actuator is placed in a small-scale loading frame located in Intelligent Infrastructure System Laboratory, Purdue University. The actuator in the loading frame is equipped with an internal LVDT and is controlled by an SC6000 controller to provide the analog PID control loop. It should be noted that in all experiments the integral (I) and derivative (D) gains are set to zero to agree with the equations herein. The external command is applied using a

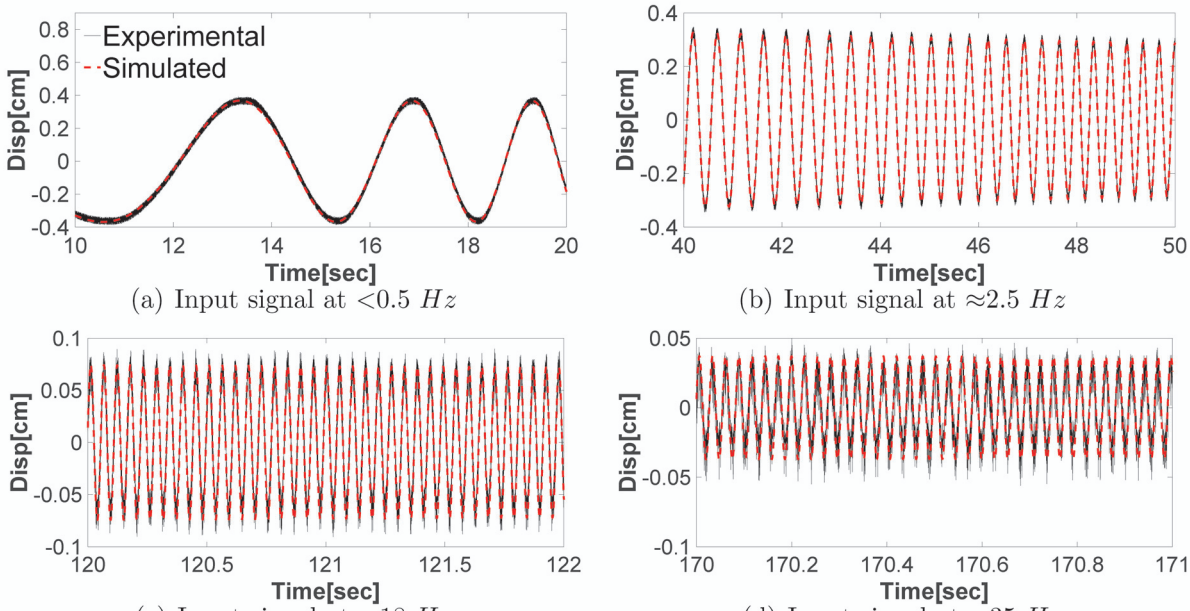

(a) Input signal at <0.5 Hz (b) Input signal at ≈2.5 Hz

(c) Input signal at ≈18 Hz (d) Input signal at ≈35 Hz

Fig. 3.22. Exp4: time domain comparison of the experimental and simulated plant responses.

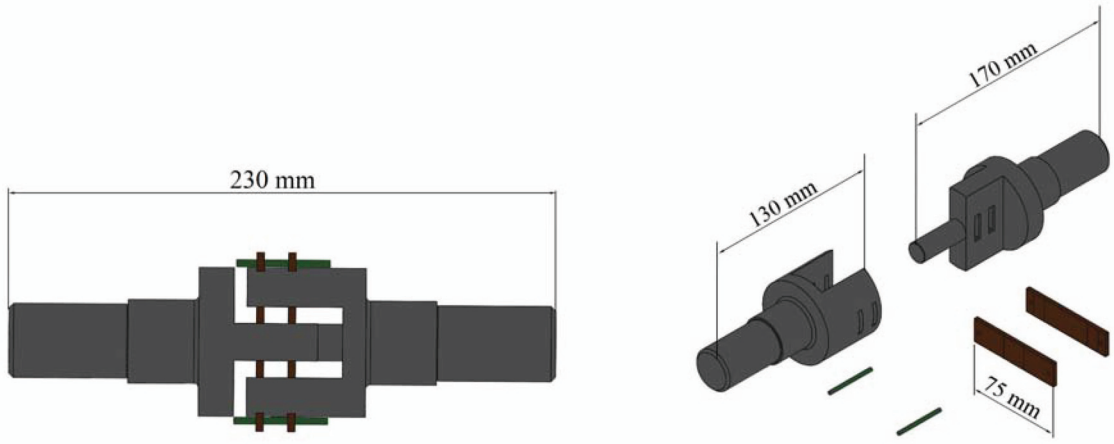

(a) Assembled View (b) Assembly View

Fig. 3.23. The nonlinear device designed and fabricated for the validation experiments.

high-performance Speedgoat/xPC (Speedgoat GmbH, 2011) real-time kernel. High-resolution, high-accuracy, 18-bit analog I/O boards are integrated into this digital

control system that supports up to 32 differential simultaneous A/D channels and eight D/A channels. The experimental setup showing the servo-hydraulic actuator coupled with the nonlinear physical specimen is provided in Figure 3.24.

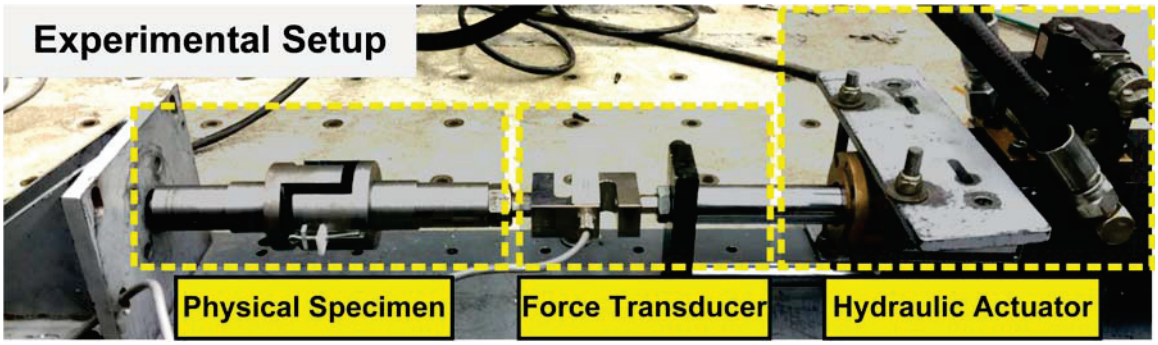

Fig. 3.24. The experimental setup: hydraulic actuator coupled with the physical specimen.

The first step is to identify the parameters associated with the servo-hydraulic actuator. In the previous section, the parameters associated with the hydraulic actuator are identified and these parameters will not vary as changes are made to the physical specimen. The identified parameters are provided in Table 3.5. Note that the only parameter in Table 3.5 that varies is $a_1\beta_0$ and it varies because it is linearly proportional to the (P) gain Equation 4.5. The proportional (P) gain will intentionally be varied in different experiments.

Table 3.5.
Identified parameters associated with the hydraulic actuator.

Parameters	**Values**
β_1 $[1/sec]$	267
$a_1\beta_0$ $[m.Pa/sec^2]$	$2.412 \times 10^9 \times P$
a_2 $[m.Pa]$	7.881×10^5
a_3 $[1/sec]$	16.118

Four experiments are conducted to systematically vary the behaviors of the physical specimen and validate the dynamical model. The proportional (P) gain and the initial condition of the physical specimen are varied to consider different nonlinear specimens. As mentioned previously, changes in the initial condition of the device generates different force-displacement profiles. The force generated by the device is estimated using the Nonlinear Least Square (Curve Fitting) Code in MATLAB as

$$f_n = m_n \ddot{x}_1 + h_n(x_1, \dot{x}_1) \tag{3.49}$$

where

$$h_n(x_1, \dot{x}_1) = c_n \dot{x}_1 + k_n^1 x_1 + k_n^2 x_1^2 + k_n^3 x_1^3 \tag{3.50}$$

Note that the restoring force is estimated as a general third order polynomial function which is asymmetric with respect to the initial point. In addition, Equation 3.49 can be simply rearranged in the form of Equation 3.1.

Table 3.6.
Four experimental cases.

Case Study	m_n (kg)	c_n (N.s/m)	k_n^1 (N/m)	k_n^2 (N/m^2)	k_n^3 (N/m^3)	P (mA/m)
Case 1	3	500	4.69×10^5	-7.52×10^6	2.44×10^{11}	2.0
Case 2	3	500	4.58×10^5	-3.86×10^8	2.35×10^{11}	2.5
Case 3	3	500	7.51×10^5	-5.88×10^8	2.34×10^{11}	3.0
Case 4	3	500	7.61×10^5	-5.78×10^8	2.18×10^{11}	3.5

The experimental and estimated (using Tables 3.5 - 3.6 and Equations 3.49 - 3.50) force-displacement profiles associated with Case 1 - Case 4 are shown in Figure 3.25.

For each case study, the input (external) command takes the form

$$u(t) = A \sin(2\pi f_u t) \tag{3.51}$$

and the servo-hydraulic actuator coupled with the nonlinear physical specimen is tested for $A = 6\ mm$ and f_u is set to either 1 Hz or 10 Hz. To quantify the modeling

error corresponding to the dynamical model and identified parameters in Table 3.3, the following normalized error is employed

$$NE = \frac{\sqrt{\frac{1}{N}\sum_{i=1}^{N}(x_i^p - x_i^e)}}{max(|x_i^e|)} \times 100 \tag{3.52}$$

where N, x_i^p and x_i^e correspond to total number of sample points, estimated displacement and experimental displacement, respectively.

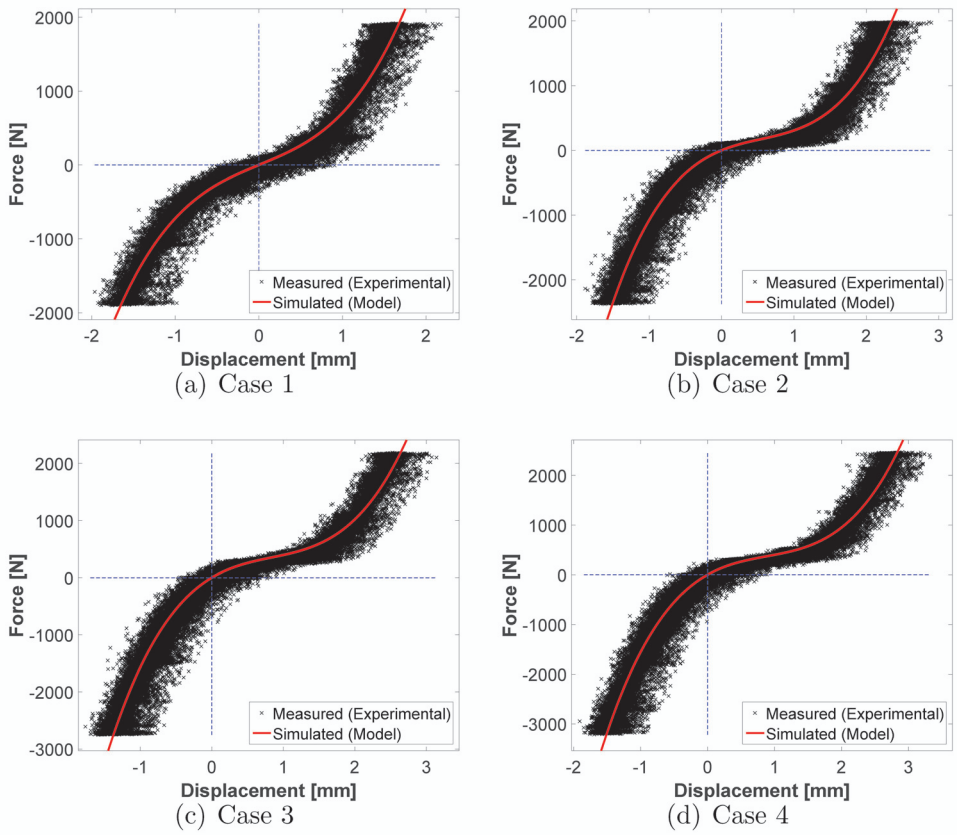

Fig. 3.25. Force-displacement profiles.

To demonstrate the accuracy of the dynamical model, Figures 3.26 to 3.29 compare the experimental and simulated responses where $u(t)$ is the input command. Figure 3.26 corresponds to Case Study 1 with the displacement-force profile shown in Figure 3.25(a) and the proportional (P) gain set to 2 mA/m. In Figure 3.26(a), the command frequency is $f_u = 1\ Hz$ and in Figure 3.26(c), the command frequency

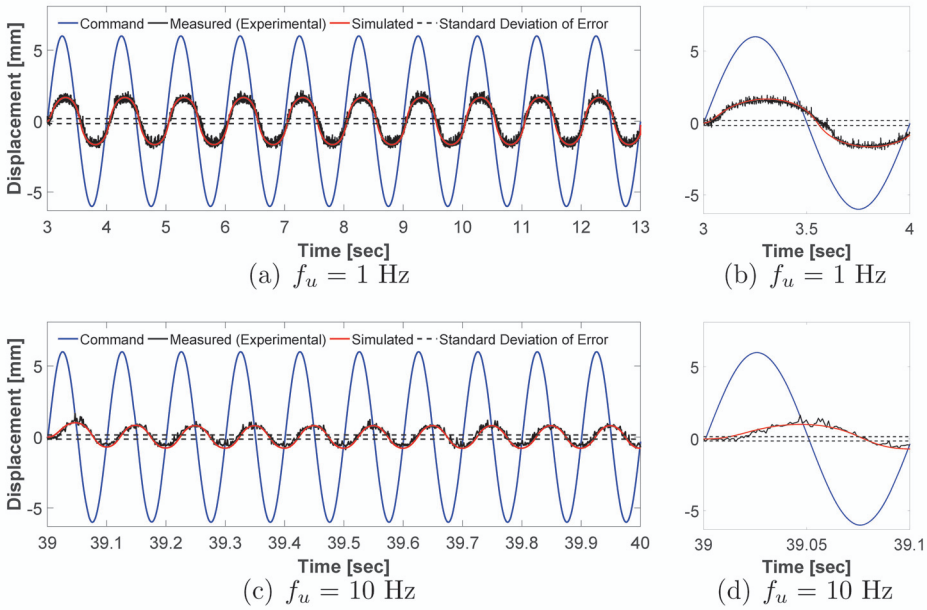

Fig. 3.26. Case Study 1: comparison of the experimental and simulated responses.

is $f_u = 10\ Hz$. The corresponding normalized errors for these two experiments are $NE = 7.97\%$ and $NE = 8.88\%$. Figure 3.27 corresponds to Case Study 2 with the displacement-force profile shown in Figure 3.25(b) and the proportional (P) gain set to 2.5 mA/m. Figure 3.28 refers to Case Study 3 with the displacement-force profile shown in Figure 3.25(b) and the proportional (P) gain set to 3 mA/m. In Figures 3.27(a) and 3.28(a), the frequency of command inputs is $f_u = 1\ Hz$; and in Figures 3.27(c) and 3.27(c), the frequency of command inputs is $f_u = 10\ Hz$. The normalized errors corresponding to Figures 3.27(a), 3.27(c), 3.28(a) and 3.28(c) are $NE = 7.01\%$, $NE = 9.54\%$, $NE = 6.89\%$ and $NE = 10.96\%$, respectively. Figures 3.29 corresponds to Case Study 4 with the displacement-force profile shown in Figure 3.25(d) and the proportional (P) gain is set to 3.5 mA/m. In Figure 3.29(a), the command frequency is $f_u = 1\ Hz$, and in Figure 3.29(c) the command frequency is $f_u = 10\ Hz$. The corresponding normalized errors for these two experiments are $NE = 6.39\%$ and $NE = 10.76\%$.

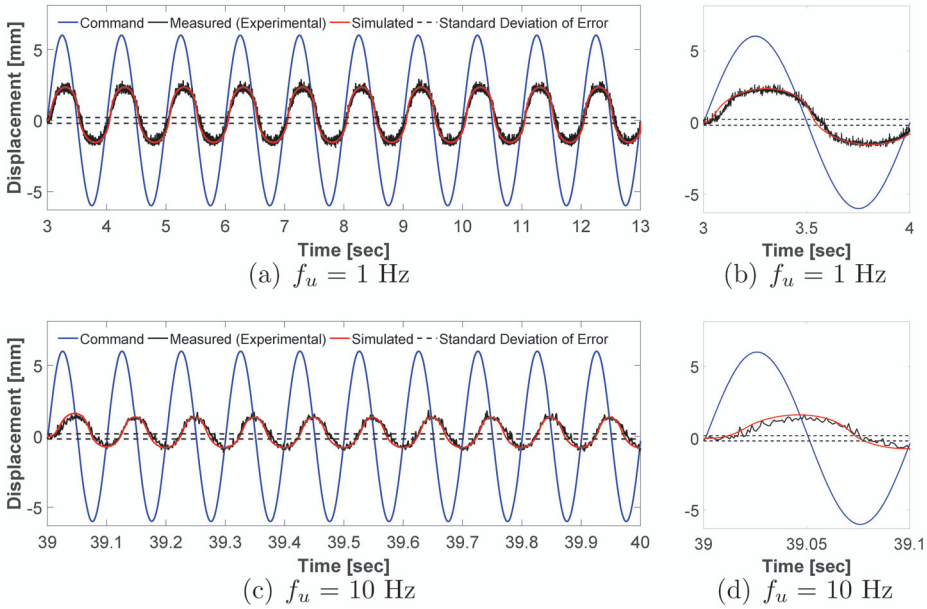

(a) $f_u = 1$ Hz (b) $f_u = 1$ Hz

(c) $f_u = 10$ Hz (d) $f_u = 10$ Hz

Fig. 3.27. Case Study 2: comparison of the experimental and simulated responses.

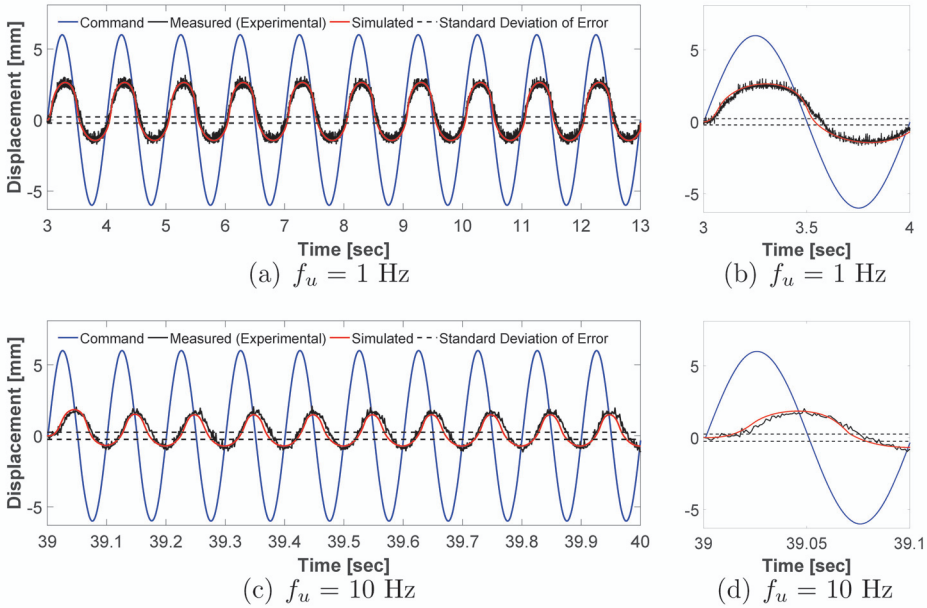

(a) $f_u = 1$ Hz (b) $f_u = 1$ Hz

(c) $f_u = 10$ Hz (d) $f_u = 10$ Hz

Fig. 3.28. Case Study 3: comparison of the experimental and simulated responses.

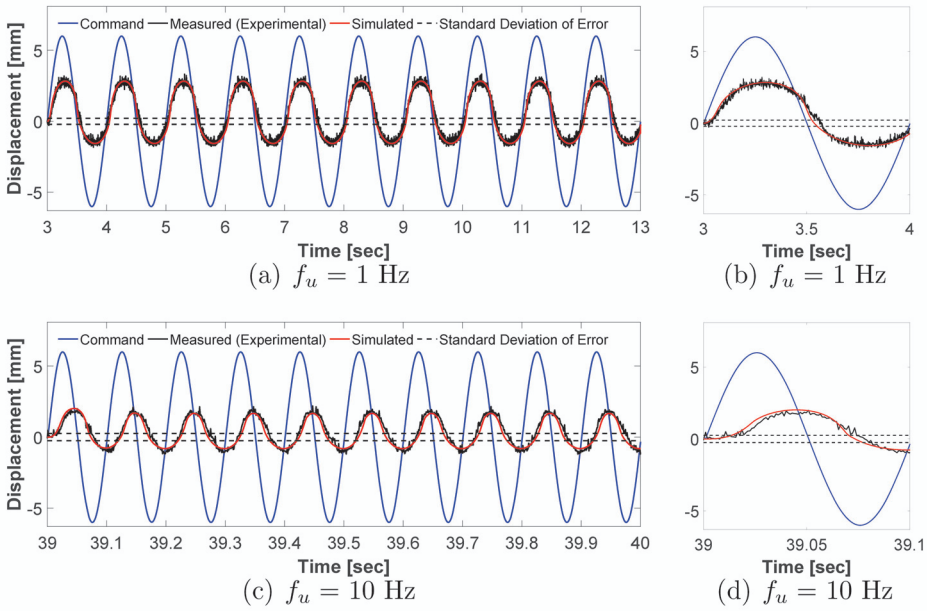

Fig. 3.29. Case Study 4: comparison of the experimental and simulated responses.

In addition to Cases 1 - 4, similar experiments with $f_u = 3\ Hz$, $f_u = 5\ Hz$ and $P = 6\ mA/m$ are conducted. The corresponding normalized errors are provided in Figure 3.30.

Herein, for a nonlinear physical specimen with different displacement-force profiles, time domain comparisons of experimental and simulated responses are provided in Figures 3.26 - 3.29. The time domain comparisons and the corresponding normalized errors in Figure 3.30 show good agreement between the experimental and simulated responses. It should be noted that almost 3% - 5% of the normalized errors in these experiments correspond to the measurement noise present in the LVDT reading.

For many experimental applications, highly-accurate displacement tracking of hydraulic actuator is required. For these applications, the controllable canonical dynamical model can serve as the control plant to design a nonlinear controller and enhance the performance and stability of the hydraulic actuator coupled with a nonlinear specimen.

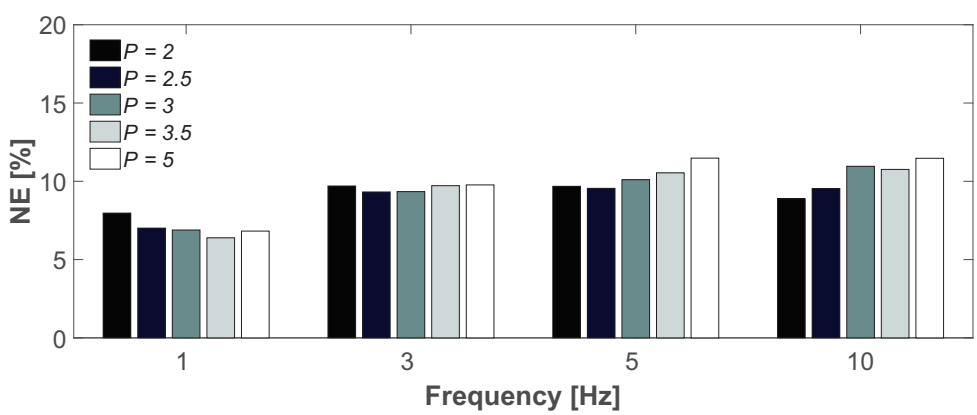

Fig. 3.30. Normalized errors associated with different experiments.

Figure 3.30 displays minimum modeling error for the proportional (P) gain = 1 mA/m. That the minimum modeling occurs at the (P) gain = 1 mA/m can be related to the range of validity/accuracy of the linear models adopted for the hydraulic actuator and the servo-valve. It should be mentioned that the parameters in Table 3.5

are identified while the (P) gain was set to 1 mA/m. One underlying assumption of these linear models is that when the servo-hydraulic actuator parameters (such as the proportional gain) and input command vary, the actuator behaves in a linear fashion. Thus, the slightly larger errors associated with different values of the proportional (P) gain can be related to the range of validity/accuracy of this assumption and within a reasonable range of operation, these errors can be incorporated into the dynamical model as parametric uncertainties.

3.3 Conclusions

In this chapter, a nonlinear dynamical model is developed for a hydraulic transfer system coupled with a linear/nonlinear physical specimen. The nonlinear dynamical model was transformed into the controllable canonical form. In addition, a technique was developed to identify the parameters associated with the dynamical model.

Controllability is a significant property of a control plant. Transforming the plant model into the controllable canonical dynamical model makes it appealing for displacement tracking. Adopting such model becomes especially important in two cases: (1) control-structure interaction dominates the dynamics of the coupled system and (2) hydraulic actuator is coupled with an unknown physical specimen. In such cases, after identifying the parameters associated with the servo-hydraulic actuator, parametric and non-parametric uncertainties are incorporated in the model due to uncertainties in the physical specimen. The controllable canonical model is formulated so that the measured forces applied to the physical specimen can be used as a feedback signal. Therefore, the measured force signal can be used as an additional piece of information by the control law for accurate displacement tracking of the plant with a high level of uncertainty.

A series of experiments have been conducted for linear and nonlinear physical specimens. In these experiments the natural coupling present between the hydraulic transfer system and the physical specimen have been investigated. Experimental and

simulated responses have been compared in time- and frequency domains to validate the dynamical model. Later, the controllable canonical dynamical model has been experimentally validated for a servo-hydraulic actuator coupled with a nonlinear physical specimen. For this purpose, a damage-controlled nonlinear device was designed and fabricated. The comparisons have shown good agreement between the experimental and simulated responses. Thus, this dynamical model can serve as the control plant for displacement tracking of hydraulic actuators coupled with linear/nonlinear physical specimens. Due to the formulation of the model, the actuator force applied to the physical specimen can be used as a feedback signal for accurate displacement tracking.

4. SELF-TUNING ROBUST CONTROL SYSTEM FOR REAL-TIME HYBRID SIMULATION WITH NONLINEAR PHYSICAL SUBSTRUCTURE

In earthquake engineering, researchers have developed structural design philosophies based on experimental results, computer simulations and observations from past incidents. Yet, there is an increasing demand to address increasingly difficult challenges (e.g., considering soil-structure interaction) as well as to exploit emerging opportunities (e.g., structural vibration control technologies).

In this chapter, *control plant* refers to the transfer system's components and the physical substructure. The plant to be controlled has parametric and non-parametric uncertainties. These uncertainties stem from: (1) modeling errors/approximations of the transfer system's components; (2) limited understanding of the physical substructure dynamics; and (3) unknown parametric variations in the physical substructure (such as structural yielding or internal resonance) while RTHS is being implemented.

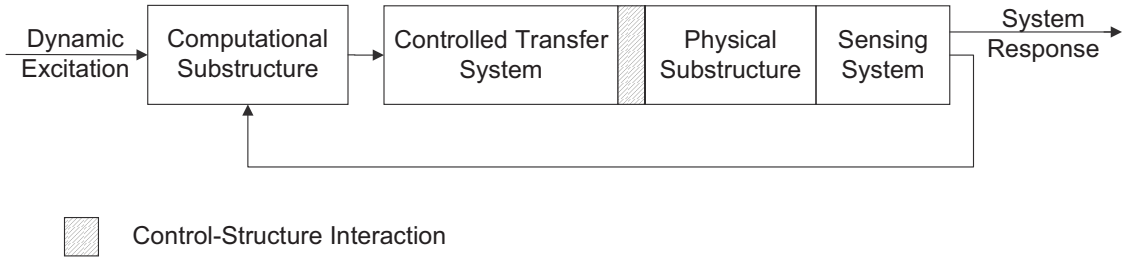

Fig. 4.1. Block diagram of a partitioned structural system for implementation of RTHS.

A number of researchers have investigated methods to minimize the uncertainties associated with the transfer system modeling [7, 41, 60, 83].

A fundamental step prior to adopting a control philosophy and designing a control law is realizing the existing constraints and making realistic assumptions about the control plant. In Chapter 3, it has been shown that transfer system and physical substructure are coupled through a natural velocity feedback path: *control-structure interaction*. Thus, the dynamics of the physical substructure directly impact the characteristics of the transfer system. During an implementation of RTHS, any change in the dynamic characteristics of the physical substructure (e.g., post yield behavior and dynamic destructive testing) impacts the dynamic behavior of the control plant. Another challenging, yet realistic, constraint in real-time hybrid simulation is the lack of/limited understanding about the physical substructure prior to implementation. However, to design an effective tracking control scheme, a nominal model for the control plant is required. Thus, for this control problem, any effective control strategy should accommodate the control-structure interaction, the dynamics of the control plant and associated parametric and non-parametric uncertainties. The key in modeling the control plant is to make some realistic assumptions within the operating range of RTHS, maintain the essential dynamics and discard insignificant ones.

In this tracking control problem, inaccuracies in the control plant model can be classified as *parametric* (or *structured*) and *non-parametric* (or *unstructured*) uncertainties. The former class of uncertainties refers to inaccuracies in the parameters already included in the nominal model, while the latter corresponds to inaccuracies in the structure of the nominal model (e.g., underestimation of the model order). Transfer system modeling error is usually dominated by non-parametric uncertainties while the physical substructure's uncertainties are more likely to be both parametric and non-parametric. Here, it should be noted that these assumptions are highly problem-dependent. The key point is that the control plant is subject to both parametric and non-parametric uncertainties.

To improve the performance of a transfer system in satisfying the interface conditions, researchers have recently developed several transfer system controllers. In an study, Stoten illustrates the challenge of advanced testing of systems via the principle of dynamic substructuring [84]. Ou et al. developed a linear robust integrated actuator control strategy which includes three control components: loop shaping feedback control based on $H\infty$ optimization, a linear-quadratic-estimation block for minimizing noise effect, and a feed-forward block that reduces small residual time delay [77]. In a numerical study, Moosavi et al. established a nonlinear state-space controller for hydraulic actuators under displacement control using state feedback linearization and transformation of the state variables [85]. Enokida et al. incorporated nonlinear signal-based control to design a transform system controller using the linearized model of the control plant [86].

To enable RTHS with control plants with high uncertainty and to enhance the achievable transfer system stability and performance, *Self-tuning Robust Control System* (*SRCSys*) is developed. The main objective of this control system is to rigorously enforce interface conditions between the computational and physical substructures. *SRCSys* consists of two complementary control layers. The first layer focuses on robustness and includes a nominal model for the control plant mainly aimed at dealing with non-parametric uncertainties. The second layer provides adaptation aimed at reducing parametric uncertainties through run-time, slow and controlled learning of the control plant based on measured performance. This unique integration of two distinct, yet complementary, control approaches is demonstrated to be an effective solution to this control problem due to the nature of uncertainties associated with the control plant.

4.1 Problem Statement

Hydraulic transfer systems have been widely employed in real time hybrid simulation as a transfer system by virtue of their large force-to-size ratios. Compared to an

electromagnetic actuator, the force limit of a hydraulic actuator can be an order of magnitude larger which makes it desirable for large scale testing [42]. To model the dynamics of a typical hydraulic transfer system, the fluid flow rate is often linearized about the origin. In this model by DeSilva, the interaction between the hydraulic actuator and the physical specimen is captured [42], see Figure 4.2 where $s \in \mathbb{C}$ denotes the Laplace variable. The actuator dynamics in Figure 4.2 is based on the linearized equation of hydraulic flow rate in an actuator which is

$$\dot{f} = \frac{2\beta}{V}(AK_q i - K_c F_A - A^2 x_2) \tag{4.1}$$

where F_A, β, V, A, K_q, i, K_c, x_1 and x_2 are actuator force, bulk modulus of the fluid, half the volume of hydraulic actuator, piston area, valve flow gain, valve input, leakage coefficient, and actuator displacement and velocity, respectively. Clearly, Figure 4.2 and Equation 4.1 demonstrate that the dynamics of the physical substructure directly impact the dynamics of the control plant. The actuator model parameters are lumped

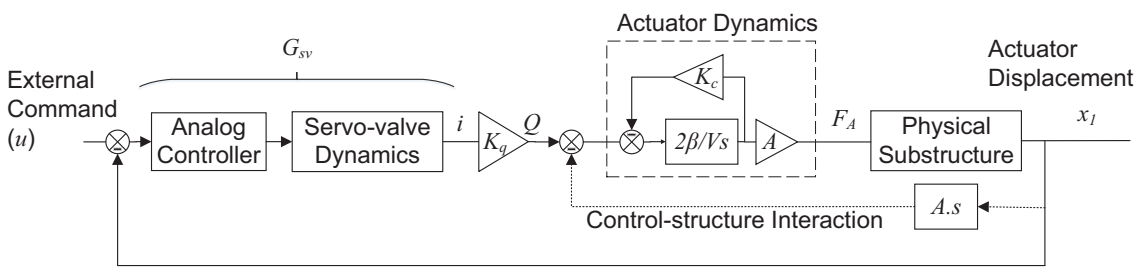

Fig. 4.2. Block diagram for the hydraulic control plant: transfer system and a physical substructure.

into three new variables a_1, a_2, and a_3 [41].

$$a_1 = \frac{2\beta K_q A}{V}; \quad a_2 = \frac{2\beta A^2}{V}; \quad a_3 = \frac{2\beta K_c}{V} \tag{4.2}$$

The analog controller (only a proportional gain) and servo-valve dynamics are modeled as a first-order transfer function

$$G_{sv} = \frac{\beta_0}{s + \beta_1} \tag{4.3}$$

Using these variables, Figure 4.3 is dynamically equivalent to Figure 4.2, see [25].

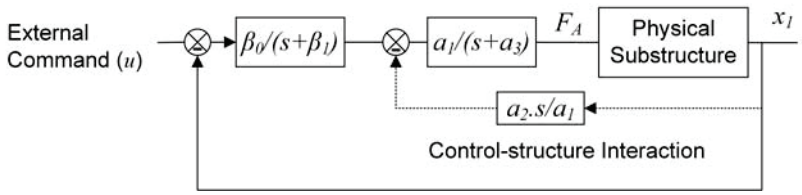

Fig. 4.3. Equivalent block diagram for the control plant.

To implement RTHS, a reference structure can be partitioned in many different ways depending on the nature and objective of the experiment. To meet the necessary interface conditions, the hydraulic actuator and the physical substructure are physically coupled through either a load frame/reaction wall or a shake table [87]. For instance, Figure 4.4a shows a nonlinear oscillator for vibration energy harvesting attached to a three-story structure while the entire structural system is subjected to ground excitation. Using the hydraulic control plant model in Figure 4.2, one possible way to partition the reference structure into computational and physical

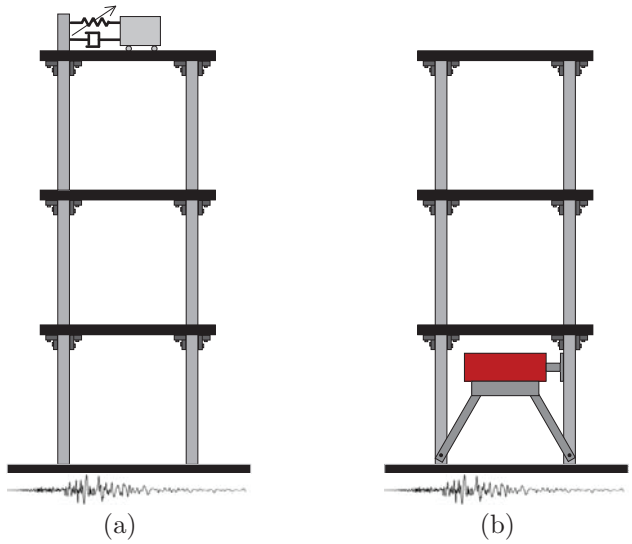

Fig. 4.4. A primary structural system attached to (a) nonlinear oscillator (b) magneto-rheological damper.

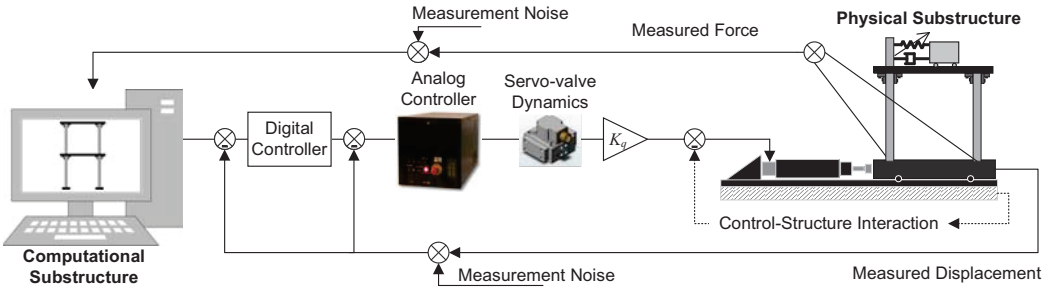

Fig. 4.5. Schematic diagram of real-time hybrid simulation for Figure 4.4a.

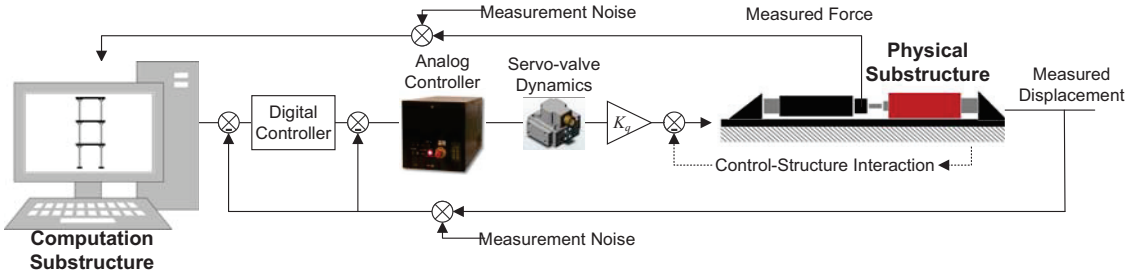

Fig. 4.6. Schematic diagram of real-time hybrid simulation for Figure 4.4b.

substructures is shown in Figure 4.5. In this configuration, the first two stories are included as the computational substructure and executed using a real-time operating platform. The top story and the nonlinear oscillator are mounted on a shake table driven by a controlled hydraulic actuator to enforce interface conditions. In another example, a magnetorheological damper (i.e., a semiactive control device) is attached to the first story of a three-story structure subject to ground excitation, see Figure 4.4b. Using the control plant model in Figure 4.2, one possible way to partition the reference structure into computational and physical substructures and implement a real-time hybrid simulation is shown in Figure 4.6.

For a physical substructure with a general form

$$x_3 = h(x_1, x_2) + \frac{F_A}{m} \tag{4.4}$$

Chapter 3 demonstrated an approach to construct a mathematical description of the control plant in controllable canonical form where x_1, x_2, x_3, f, m denote actuator displacement, velocity, acceleration, force and attached mass, respectively. The function h can be any differentiable nonlinear function. Note that Equation 4.4 is problem-dependent and may vary depending on the nature of the control plant. However, the methodology described in Chapter 3 can be easily adjusted according to the problem. Figure 4.3 is mathematically described using the nonlinear system of differential equations.

$$\begin{cases} \dot{x}_1 &= x_2 \\ \dot{x}_2 &= x_3 \\ \dot{x}_3 &= x_4 \\ \dot{x}_4 &= c_1x_1 + c_2x_2 + c_3x_3 + c_4x_4 + c_5F_A + c_6 + bu \end{cases} \tag{4.5}$$

where

$$\begin{aligned} c_1 &= -\frac{a_1\beta_0}{m} \\ c_2 &= -\frac{a_2\beta_1}{m} + \beta_1\frac{\partial h}{\partial x_1} + a_3\frac{\partial h}{\partial x_1} \\ c_3 &= \beta_1\frac{\partial h}{\partial x_2} + a_3\frac{\partial h}{\partial x_2} - \frac{a_2}{m} \\ c_4 &= -\beta_1 - a_3 \\ c_5 &= -\frac{a_3\beta_1}{m} \\ c_6 &= \ddot{h} \\ b &= \frac{a_1\beta_0}{m} \end{aligned} \tag{4.6}$$

The parameters in Equation 4.6 relate to physically meaningful parameters and are described in Equations 4.7-4.8 and Table 4.1.

$$\beta_0 = P\gamma, \tag{4.7}$$

$$\ddot{h} = \frac{\partial^2 h}{\partial {x_1}^2}x_2^2 + \frac{\partial^2 h}{\partial {x_2}^2}x_3^2 + 2\frac{\partial^2 h}{\partial x_1 \partial x_2}x_2x_3 + \frac{\partial h}{\partial x_1}x_3 + \frac{\partial h}{\partial x_2}x_4 \tag{4.8}$$

Using Equation 4.8 to redefine the parameters in Equation 4.6, it becomes

$$
\begin{aligned}
c_1 &= -\frac{a_1\beta_0}{m} \\
c_2 &= -\frac{a_2\beta_1}{m} + \beta_1\frac{\partial h}{\partial x_1} + a_3\frac{\partial h}{\partial x_1} \\
c_3 &= \beta_1\frac{\partial h}{\partial x_2} + a_3\frac{\partial h}{\partial x_2} - \frac{a_2}{m} + \frac{\partial h}{\partial x_1} \\
c_4 &= -\beta_1 - a_3 + \frac{\partial h}{\partial x_2} \\
c_5 &= -\frac{\beta_1 a_3}{m} \\
c_6 &= \frac{\partial^2 h}{\partial x_1^2}x_2^2 + \frac{\partial^2 h}{\partial x_2^2}x_3^2 + 2\frac{\partial^2 h}{\partial x_2 \partial x_1}x_2 x_3 \\
b &= \frac{a_1\beta_0}{m}
\end{aligned}
\tag{4.9}
$$

Based on the type of function h in Equation 4.4, the coefficients C_1-C_6 are subject to change. To ensure generality, in this study, Equation 4.5 is described as

$$
\begin{cases}
\dot{x}_1 &= x_2 \\
\dot{x}_2 &= x_3 \\
\dot{x}_3 &= x_4 \\
\dot{x}_4 &= f(X, F_A) + bu = \Lambda^T\Gamma + bu
\end{cases}
\tag{4.10}
$$

where Λ are vector of constant (or slowly changing) coefficients, and Γ is a vector of the nonlinear system states (e.g., $[x_1\ x_2\ x_3\ x_4\ f\ x_2^2\ x_3^2\ \ldots]^T$), respectively.

The general form in Equation 4.10 also allows for developing a nonlinear control system to other nonlinear (and of course linear) control plants (e.g., a shake table driven by servo-motor to simulate different ground motions). The only required condition is that the control plant must be mathematically described in this controllable canonical form. A single input plant is said to be in this controllable canonical form if its dynamics are represented in the form

$$
x^{(n)} = f(X) + b(X)u \tag{4.11}
$$

Table 4.1.
Hydraulic control system parameters.

Parameter	Units	Component	Description
P	mA/m	Analog Controller	Controller proportional gain
γ	$m/mA/sec$	Servo-valve	Servo-valve gain
$1/\beta_1$	sec	Servo-valve	Servo-valve time constant
K_q	$m^3/sec/m$	Servo-valve	Valve flow gain
i	m	Servo-valve	Spool displacement
A	m^2	Hydraulic actuator	Piston area
K_c	$m^3/sec/Pa$	Hydraulic actuator	Leakage coefficient of the actuator
V	m^3	Hydraulic actuator	Half of actuator volume
β	Pa	Hydraulic actuator	Effective bulk modulus of the fluid
Q	m^3/sec	Hydraulic actuator	Fluid flow rate into the actuator
x_1	m	Hydraulic actuator	Actuator displacement
f	N	Hydraulic actuator	Actuator force

where $X = [x\ \dot{x}\ \cdots\ x^{(n-1)}]^T$ is the system state vector, x is the scalar state of interest, u is the scalar control command, and $f(X)$ and $b(X)$ are nonlinear functions of the states. This system can also be represented as

$$\begin{aligned} \dot{x}_1 &= x_2 \\ \dot{x}_2 &= x_3 \\ &\vdots \\ \dot{x}_n &= f(X) + b(X)u \end{aligned} \tag{4.12}$$

4.2 Nonlinear Self-tuning Robust Transfer System Control Framework

To effectively meet the required interface conditions in the case of a nonlinear physical plant, a nonlinear control system is preferred if available. In the field of

nonlinear control, there is no general algorithm for designing a nonlinear controller which applies to any nonlinear plant. However, there is a rich collection of alternative and complementary design tools, each applicable to a specific class of nonlinear control problems. These design tools can be categorized under four classes of nonlinear control schemes [82, 88]:

- **Gain-scheduling:** In this class of controllers, researchers seek to apply the well-rounded and mature theory of linear control to nonlinear systems. This control philosophy is essentially based on selecting a number of operating points which span the operating range of the nonlinear system [82]. See [89].

- **Feedback linearization:** In this control philosophy, model of physical systems is transformed into an equivalent mathematical model in a linear form. Note that the linearized model is dynamically equivalent to the original system model [90].

- **Robust control:** In this controller design philosophy, a control law is designed based on the nominal model of physical systems as well as some characterization of the model uncertainties. This design philosophy has proven very effective in a wide range of practical linear/nonlinear control problems [82].

- **Adaptive control:** The basis of this control design approach is to reduce modeling uncertainties by making full use of the structural information of the physical system to be controlled and and an associated uncertainty model. Adaptation can be constructed to acquire better estimates of various unknown but constant or slowly changing parameters at run-time. Thus, the impact of model uncertainties is reduced or eliminated and a better steady-state tracking performance is achieved. See [90, 91].

4.2.1 Theoretical Background

The mathematical derivation of *SRCSys* is based on Barbalat's lemma and invariant set theory.

Barbalat's lemma addresses the sufficient mathematical requirement(s) for a function's derivative to converge to zero given that the function tends toward a finite limit. The proof and further detail on this lemma are provided in [82]. A brief overview of this lemma is discussed here. First, uniform continuity needs to be defined. A function $V(t)$ is continuous on $[0, \infty)$ if

$$\forall\, t_1 \geq 0,\ \forall\, R > 0,\ \exists\, \eta(R, t_1) > 0,\ \forall\, t \geq 0,\ |t - t_1| < \eta \Rightarrow |V(t) - V(t_1)| < R \tag{4.13}$$

$V(t)$ is considered to be uniformly continuous on $[0, \infty)$ if

$$\forall\, R > 0,\ \exists\, \eta(R) > 0,\ \forall\, t_1 \geq 0,\ \forall\, t \geq 0,\ |t - t_1| < \eta \Rightarrow |V(t) - V(t_1)| < R \tag{4.14}$$

A more convenient way to investigate the function's uniform continuity is through its derivative. A simple sufficient condition for a differentiable function to be uniformly continuous is that its derivative be bounded. Barbalat's lemma indicates that if the differentiable function $V(t)$ has a finite limit as $t \rightarrow \infty$, and if $\dot{V}$ is uniformly continuous, then $\dot{V} \rightarrow 0$ as $t \rightarrow \infty$. A straightforward mathematical interpretation of Barbalat's lemma for a energy-type function $V(t)$ is

$$\text{if} \left\{ \begin{array}{ll} V(t), & \text{is lower-bounded} \\ \dot{V}(t) \leq 0, & \text{always} \\ \ddot{V}(t), & \text{is bounded} \end{array} \right\}, \text{ then } \dot{V} \rightarrow 0 \text{ as } t \rightarrow \infty \tag{4.15}$$

Invariant set definition: For a dynamic system

$$\dot{X} = f(X(t)), \tag{4.16}$$

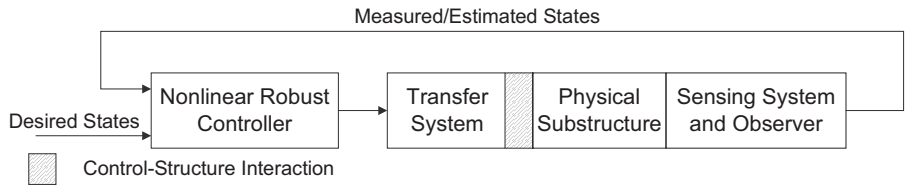

Fig. 4.7. Block diagram of the layer of robustness.

a set $\mathbf{M}$ is an invariant set if every trajectory in the system which starts from a point in $\mathbf{M}$ remains in the set as time goes to infinity [82, 90]. Mathematically, it can be interpreted as

$$X(t) \in \mathbf{M} \Rightarrow X(t) \in \mathbf{M}, \ \forall t \geq 0 \tag{4.17}$$

where $X \in \mathbb{R}^n$. Note that in literature, Equation 4.17 may be referred as a *positively invariant set*. Under that definition, an invariant set becomes a subset of Equation 4.17

$$X(t) \in \mathbf{M} \Rightarrow X(t) \in \mathbf{M}, \ \forall t \in \mathbb{R} \tag{4.18}$$

In this study, the former definition is adopted. Using Barbalat's lemma and the invariant set definition, the next two sections discuss the structure of the layers of robustness and adaptation.

4.2.2 Stability: Layer of Robustness

In this study, robustness refers to the system's sensitivity to parameters which are not explicitly considered in the nominal plant, such as parametric uncertainties, disturbances, measurement noise and unmodeled dynamics. In this layer, the main objective is to synthesize a nonlinear control law such that the overall dynamical system of this layer (see Figure 4.7) withstands the bounded unmodeled dynamics and uncertainties while tracking the desired trajectory (i.e., achieving the interface conditions).

For this purpose, sliding mode control (SMC) is employed in this layer as the control scheme. SMC allows for controlling nonlinear/linear physical plants subject to external disturbances and heavy model uncertainties. Also, SMC exhibits remarkable properties of accuracy, robustness, easy tuning and implementation [82]. SMC has three useful properties which will be fully exploited for this highly uncertain control problem. In this scheme, an nth order tracking problem is replaced by a 1st order stabilization problem. The closed-loop dynamic behavior of the controlled system may be designed and shaped by the particular choice of the sliding regime. The closed-loop response becomes insensitive to bounded uncertainties, such as parametric uncertainties, disturbances and unmodeled dynamics [82, 90].

In this control strategy, the tasks associated with the nth order nonlinear tracking problem are divided into two parts: (1) Reaching the Sliding Surface: A *compact tracking error measure* is defined. The compact tracking error measure creates a $n-1$ dimension hyperplane called the *sliding surface*. The sliding surface is designed to be an invariant set. Geometrically, in this part, the main objective is to ensure that under any initial condition, the sliding surface is reached in a finite time. The choice of sliding surface leads to a 1st order nonlinear stabilization problem. A control law is synthesized based on an energy-type function. Convergence of tracking error is investigated using Barbalat's lemma. (2) Sliding Surface Dynamics: Once the sliding surface is reached, tracking error slides toward zero governed by the dynamics of the sliding surface.

A detailed discussion on sliding mode control is provided in [82, 90]. Here, sliding mode control is applied to the physical plant in Equation 4.5, described as a general nonlinear dynamic system of the form

$$x^{(n)} = f(X, F_A) + b(X)u \tag{4.19}$$

where $X = [x \ \dot{x} \ \cdots \ x^{(n-1)}]^T$, the scalar x and F_A are the output of interest (e.g., actuator displacement) and another measurable state (e.g., actuator force), respectively. Note that the form of Equation 4.19 is consistent with the transfer system

tracking problem in Equations 4.11 and 4.12. The displacement tracking error in the variable x is defined as

$$e = x - x_d \tag{4.20}$$

where the scalar variable x_d is the desired tracking. The error in X is given by

$$E = X - X_d = [e \ \dot{e} \ \ldots \ e^{n-1}]^T \tag{4.21}$$

where $X_d = [x_d \ \dot{x}_d \ \cdots \ x_d^{(n-1)}]^T$. Equation 4.19 represents the necessary dynamics of the physical plant. However, the dynamics $f(X, F_A)$ and parameter b are unknown but estimated as $\hat{f}(X, F_A)$ and $\hat{b}$.

For now, let's assume

$$U = bu, \tag{4.22}$$

and first obtain the control command U. Later, the control command will be adjusted to accommodate the control gain and its associated uncertainty. Therefore, the true plant becomes

$$x^{(n)} = f(X, F_A) + U \tag{4.23}$$

where the nominal plant is

$$x^{(n)} = \hat{f}(X, F_A) + U \tag{4.24}$$

The estimation error on f is assumed to be bounded by some known time-varying function $F(X, t)$ where

$$|\hat{f} - f| \leq F(X, t) \tag{4.25}$$

Later, it will be shown that having a bounded uncertainty is a key factor in synthesizing an effective control law.

4.2.3 Discontinuous Control Law

This section discusses two main topics: (1) the control law that governs a trajectory to reach the sliding surface and (2) the governing dynamics on the sliding surface.

Part 1: Reaching the Sliding Surface: In this part, the nth order tracking problem in Equation 4.23 is replaced by a 1st order stabilization problem. Thus, $p(E,t)$ is defined as the compact tracking error measure

$$p(E,t) = (\frac{d}{dt} + \lambda)^{n-1} e \tag{4.26}$$

$p(E,t)$ can also be seen as a weighted sum of the state errors. For instance,

$$\begin{aligned} n = 2 &\Rightarrow p = \dot{e} + \lambda e \\ n = 3 &\Rightarrow p = \ddot{e} + 2\lambda\dot{e} + \lambda^2 e \\ n = 4 &\Rightarrow p = e^{(3)} + 3\lambda\ddot{e} + 3\lambda^2\dot{e} + \lambda^3 e \end{aligned} \tag{4.27}$$

$p(E,t) = 0$ is a linear differential equation whose stable equilibrium solution is $E = 0$. This stable equilibrium is precisely equivalent to achieving the desired tracking, or $X = X_d$.

Here, the 1st order stabilization problem is being constructed based on the compact tracking error measure. For the input U to appear, p needs to be differentiated only once. For instance, in the hydraulic physical plant tracking problem, n is 4, therefore $p = e^{(3)} + 3\lambda\ddot{e} + 3\lambda^2\dot{e} + \lambda^3 e$ and the 1st order differential equation becomes

$$\dot{p} = e^{(4)} + 3\lambda e^{(3)} + 3\lambda^2\ddot{e} + \lambda^3\dot{e} \tag{4.28}$$

Using Equation 4.20, it can also be written as

$$\dot{p} = x^{(4)} - x_d^{(4)} + 3\lambda e^{(3)} + 3\lambda^2\ddot{e} + \lambda^3\dot{e} \tag{4.29}$$

Defining the *reference* value of $x^{(4)}$ as $x_r^{(4)} = x_d^{(4)} - 3\lambda e^{(3)} - 3\lambda^2\ddot{e} - \lambda^3\dot{e}$, Equation 4.29 becomes

$$\dot{p} = f(X, F_A) - x_r^{(4)} + U \tag{4.30}$$

For the 1st order system in Equation 4.30, the objective is to find a control law such that reaching the sliding surface $p(E,t) = 0$ is achieved in a finite time. For this, Barbalat's lemma is employed and an appropriate energy-type function is chosen as follows

$$V = \frac{1}{2}p^2 \tag{4.31}$$

The *sliding regime* becomes

$$\dot{V} = \frac{1}{2}\frac{d}{dt}p^2 = \dot{p}p \leq -\eta|p| \tag{4.32}$$

where η is a strictly positive variable. The sliding regime can also be written as

$$\begin{cases} \dot{p} \leq -\eta & \text{for } p > 0 \\ \dot{p} \geq +\eta & \text{for } p < 0 \end{cases} \tag{4.33}$$

It is straightforward to show that $\ddot{V}$ is bounded. Considering the fact that $f(X, F_A)$ is unknown, the discontinuous control law

$$U = -\hat{f}(X, F_A) + x_r^{(4)} - K(X,t)\, sgn(p) \tag{4.34}$$

complies with the sliding regime in Equation 4.32. In Equation 4.34, $\hat{f}$ is the nominal plant and $sgn(p)$ is the signum function shown in Figure 4.8(a). Using a new notation

$$K(X,t) = F(X,t) + \eta \tag{4.35}$$

where $K(X,t)$ is a strictly positive scalar aimed at overpowering the bounded uncertainty $F(X,t)$ and ensuring that the trajectories are always pointing toward the sliding surface. Geometrically, the sliding regime and the choice of the control law result in the dynamics shown in Figure 4.8(b) where the trajectories off the surface $p(E,t) = 0$ are always pointing towards the sliding surface.

Part 2: Sliding Surface Dynamics: The goal of this part is to discuss the dynamics of trajectories once the sliding surface is achieved. Note that the sliding surface is an invariant set. The dynamics of the sliding surface are governed by the compact tracking error measure defined in Equation 4.26. Figure 4.9 provides a new perspective on Equation 4.26 demonstrating how bounds on the sliding variable $p(E,t)$ can be translated into bounds on the tracking error $e(t)$. The bounds can be mathematically described as

$$\forall\, t \;\geq\; 0,\; |p(t)| \;\leq\; \Phi \;\;\Rightarrow\;\; \forall\, t \;\leq\; 0,\; |e^{(i)}(t)| \;\geq\; \frac{(2L)^i \Phi}{L^{n-1}} \tag{4.36}$$

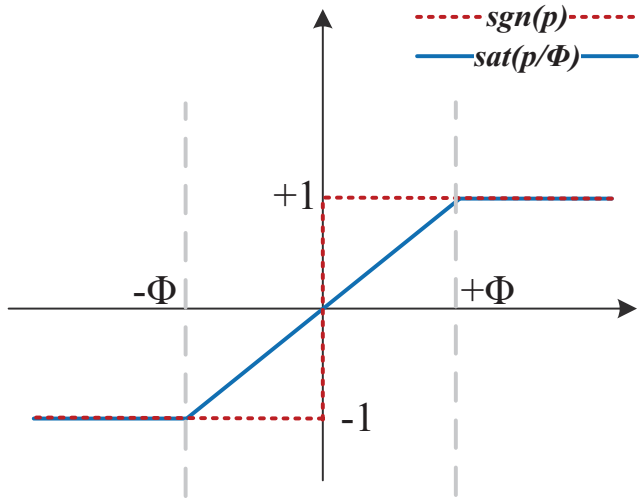

(a)

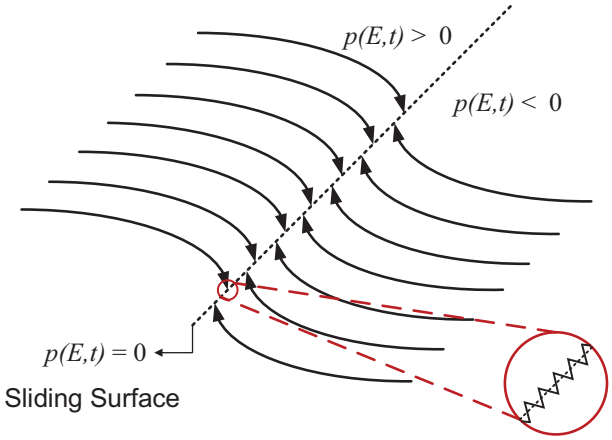

(b)

Fig. 4.8. (a) Control command interpolation within the boundary layer (b) sliding regime with the signum function.

where $i \in \{1,\ 2,\ \ldots,\ n-1\}$. Once the sliding surface is reached, the desired displacement will be achieved (i.e., $e = 0$) due to the stable dynamics of the sliding surface. Trajectories reach the desired trajectory following a path which depends merely on

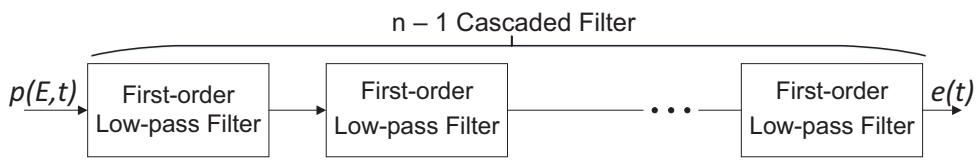

Fig. 4.9. Cascading first-order filters translating the sliding variable p to tracking error e.

the transient response of the linear $(n-1)^{th}$ order stable system in Figure 4.9. Using Equation 4.26, the dynamics of the sliding surface is given by

$$H_{ep}(s) = \frac{1}{(s+\lambda)^{n-1}} \tag{4.37}$$

where $s \in \mathbb{C}$ and $H_{ep}(s)$ denotes the Laplace variable and the transfer function from the compact tracking error measure to the tracking error, respectively. The inverse Laplace transform of $H_{ep}(s)$ reveals the tracking error path. For the 4th order nonlinear system in Equation 4.23, $H_{ep}(s)$ becomes

$$H_{ep}(s) = \frac{1}{(s+\lambda)^{3}} \tag{4.38}$$

For this system, once the sliding surface is reached at $t = t_0$, the tracking error path is given by

$$e(t) = e(t_0) \times [e^{-\lambda(t-t_0)} + \lambda(t-t_0)e^{-\lambda(t-t_0)} + \frac{1}{2}\lambda^2(t-t_0)^2 e^{-\lambda(t-t_0)}] \tag{4.39}$$

where $e(t_0)$ is the tracking error at $t = t_0$.

Implementation of the discontinuous control law in Equation 4.34 may result in some signal chattering (see Figure 4.8(b)) which may be undesirable in RTHS. Such signal chattering is due to the control law discontinuity as well as practical constraints of the hydraulic control unit such as digital-to-analog conversion, measurement noise, control command saturation, sensing system dynamics, and neglected time delays in the physical plant. This chattering may yield intense control command chattering and therefore, the control command may become practically unrealizable by the analog controller device. Thus, in the next section, an alternative control law will be discussed.

4.2.4 Continuous Control Law

To eliminate the chattering in the control command in Equation 4.34, the presence of the discontinuity resolved by smoothing out the control law and employing a time-varying *boundary layer* in the vicinity of the sliding surface. The boundary layer is described as

$$BL(t) = \{E, |p(E,t)| \leq \Phi(t)\} \tag{4.40}$$

where $2\Phi(t)$ is the boundary layer thickness and E is defined in Equation 4.21, see Figure 4.10. In the new control law, $sgn(p)$ is replaced by a continuous time-varying function $sat(\frac{p}{\Phi(t)})$, see Figure 4.8(a). Barbalat's lemma is then employed with an energy-type function as

$$V = \frac{1}{2}p^2 \tag{4.41}$$

To compensate for the replacement, the new sliding regime sets to

$$\dot{V} = \frac{1}{2}\frac{d}{dt}p^2 = \dot{p}p \leq (\dot{\Phi} - \eta)|p| \tag{4.42}$$

which is equivalent to

$$\begin{cases} \dot{p} - \dot{\Phi} \leq -\eta & \text{for } p > +\Phi \\ \dot{p} + \dot{\Phi} \geq +\eta & \text{for } p < -\Phi \end{cases} \tag{4.43}$$

Compared to Equation 4.33, the new sliding regime is adjusted to accommodate the fact that the thickness of the boundary layer varies over time. This adjustment ensures that the trajectories outside of the boundary layer are always pointing toward the boundary layer although the layer thickness varies in time. Similar as with the discontinuous control law, the new continuous control law becomes

$$U = -\hat{f}(X) + x_r^{(4)} - [K(X,t) - \dot{\Phi}]\, sat(\frac{p}{\Phi}) \tag{4.44}$$

which is in full compliance with the new sliding regime.

To verify the stability of the new system, the trajectories in Figure 4.10 are divided into two cases: those with $p(E,t)$ being outside of the boundary layer, and those with $p(E,t)$ being inside the boundary layer. In the former case, $sgn(p) = sat(\frac{p}{\Phi})$

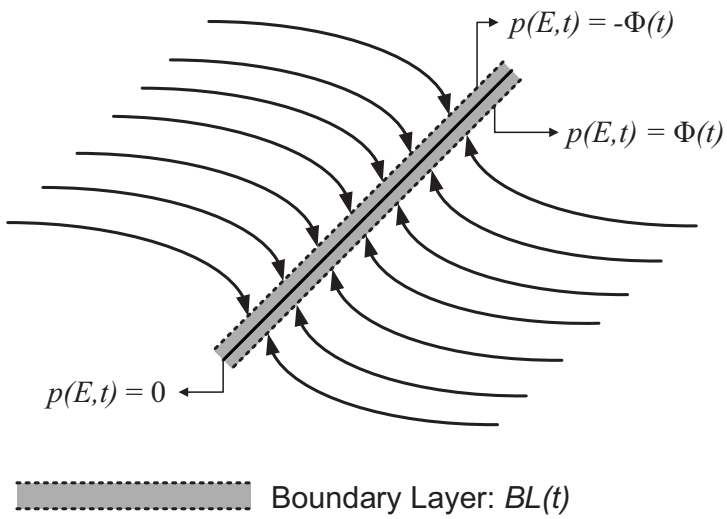

Fig. 4.10. The sliding regime with the time-varying saturation function.

(see Figure 4.8(a)), thus, there is no technical difference between the continuous and discontinuous control laws. In the latter case,

$$sat(\frac{p}{\Phi}) = \frac{p}{\Phi} \tag{4.45}$$

If the dynamics of the boundary layer thickness is chosen by,

$$\dot{\Phi} = -\lambda'\Phi + K \tag{4.46}$$

where λ' is strictly positive, the control law in Equation 4.44 becomes

$$U = -\hat{f}(X, F_A) + x_r^{(4)} - \frac{K(X,t) - \dot{\Phi}}{\Phi}p = -\hat{\Lambda}^T\Gamma + x_r^{(4)} - \frac{K(X,t) - \dot{\Phi}}{\Phi}p \tag{4.47}$$

Using Equation 4.46, this can be written as

$$U = -\hat{f}(X, F_A) + x_r^{(4)} - \lambda' p = -\hat{\Lambda}^T\Gamma + x_r^{(4)} - \lambda' p \tag{4.48}$$

If the real physical plant dynamics and control gain are known ($\hat{\Lambda}^T\Gamma = \Lambda^T\Gamma$ and $b = \hat{b}$), Equation 4.48 could be substituted in the plant and the plant becomes

$$x^{(4)} = f(X, F_A) + U = \Lambda^T\Gamma + U \tag{4.49}$$

and using Equation 4.29, Equation 4.49 becomes

$$x^{(4)} - x_r^{(4)} = \dot{p} = -\lambda' p \tag{4.50}$$

Equation 4.50 indicates an exponential convergence of the compact tracking error measure thus, guaranteeing the convergence of tracking error (see Figure 4.9 and Equation 4.36). However, in the absence of the real coefficients Λ, the nominal coefficients $\hat{\Lambda}$ and the bounded uncertainty are used to synthesize the control law. Using the best estimated coefficient vector, the dynamics associated with the compact tracking error measure become

$$x^{(4)} - x_r^{(4)} = \dot{p} = -\lambda' p + \tilde{l} x_r^{(4)} + \tilde{\Lambda}^T \Gamma \tag{4.51}$$

where $\tilde{l}$ and $\tilde{\Lambda}$ represent compensation for the unknown control gain b and error in the nominal dynamic model, respectively. Equation 4.51 can be viewed as a first-order low-pass filter where $\tilde{l} x_r^{(4)} + \tilde{\Lambda}^T \Gamma$ indicates estimation error. At this stage, the pole of this first-order low-pass filter $-\lambda'$ is strictly negative, see Figure 4.11. Combining

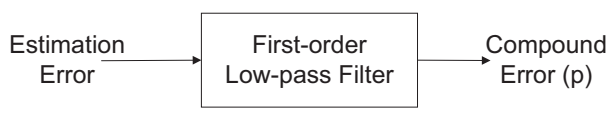

Fig. 4.11. First-order filter translating the estimation error to compact tracking error measure.

Figure 4.11 and Figure 4.9, the layer of robustness can be viewed from a new angle: n cascading first-order, low-pass filters, translating the estimation error to the tracking error. Figure 4.12 presents how the estimation error is translated to the tracking error through the layer of robustness.

4.2.5 Uncertainty Due to Control Gain

The control law in Equation 4.44 is designed for the plant in Equation 4.23. However, the plant in Equation 4.11 includes a control gain b. There are two different

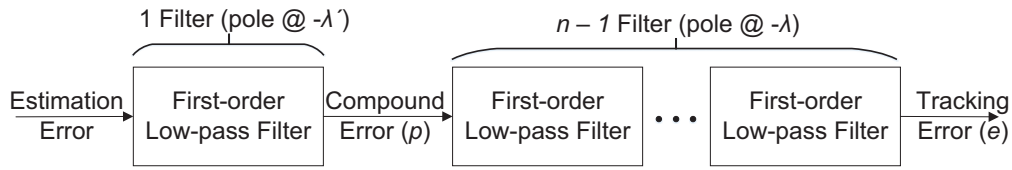

Fig. 4.12. The n cascading filters translating the estimation error to tracking error.

approaches to accommodate the uncertainty associated with the control gain in the control law [82, 90]. In this study, the one proposed in [82] is adopted. Let's assume b is bounded as follows

$$0 < |b_{min}| \leq |b| \leq |b_{max}| \tag{4.52}$$

The nominal value for b is taken as the geometric mean of b_{min} and b_{max}

$$\hat{b} = \frac{b_{min}}{|b_{min}|}(b_{min}b_{max})^{1/2} \tag{4.53}$$

Thus, $K(X,t)$ in Equation 4.44 is adjusted to

$$K(X,t) = \beta(F+\eta) + (\beta-1)|-\hat{f}(X) + x_r^{(4)}| \tag{4.54}$$

where $\beta = (b_{max}/b_{min})^{1/2} \geq 1$. Considering the control gain, the control law in Equation 4.44 is modified to

$$u = \hat{b}^{-1}\{-\hat{f}(X) + x_r^{(4)} - [K(X,t) - \dot{\Phi}]\, sat(\frac{p}{\Phi})\} \tag{4.55}$$

With this, designing a control law for the layer of robustness is completed. The control law accommodates the neglected dynamics, parametric uncertainties and disturbances associated with a physical plant as long as they are all bounded by $F(X,t)$.

4.2.6 A Discussion of the Layer of Robustness

Several points should be made: (i) An important design choice in this control layer is the control bandwidth (i.e., governed by λ and λ') in Equations 4.26 and 4.46. Although the tuning of this variable can be implemented experimentally. Some parameters impacting the choice of control bandwidth are: the lowest unmodeled dynamic pole of the physical plant, the largest unmodeled time-delay, and sampling

frequency [82]; (ii) Not only is this control framework robust with respect to parametric uncertainties captured in Equation 4.25, but it is also robust to unknown but bounded fast-varying coefficients or disturbances. The major reason behind this feature is the cascaded filters translating the estimation error (i.e., including fast-varying coefficients or disturbances) to tracking error; (iii) The p-trajectory, which is the variation of the compact tracking error measure with respect to time, reveals the overall tracking performance of the transfer system on a single plot; (iv) A plot of the boundary layer thickness ($\pm\phi$) and the compact tracking error measure p versus time conveys a significant amount of information about whether the nominal plant and corresponding estimation error are suitably chosen; and, (v) Figure 4.12 portrays how reducing the estimation error directly impacts the tracking performance convergence. Thus, the main objective of the layer of adaption is estimation error reduction, while the stability of the layer of robustness remains intact.

4.2.7 Accuracy: Layer of Adaptation

To use this approach for RTHS, there are parametric and non-parametric uncertainties associated with the physical plant to be controlled. Under certain conditions (mentioned in the preceding section), the high-frequency unmodeled dynamics in the hydraulic control system are being filtered out due to the adopted design choice of the layer of robustness, see Figure 4.12. However, unless parametric uncertainties are gradually reduced at run-time by an adaptation mechanism, they may cause tracking performance degradation. Thus, the main objective of the layer of accuracy is to withstand parametric uncertainties and/or parametric variations (such as yielding or internal resonance in the physical substructure) while tracking performance is consistently improving.

This section demonstrates how to synthesize an adaptation law in order to reduce the tracking error while the stability of the layer of robustness is maintained. This layer aims at consistently reducing the impact of parametric uncertainties asso-

ciated with constant (or slowly changing) coefficients in the nominal plant. Referring to Equation 4.51, all the constant (or slowly changing) coefficients to be estimated are lumped together and denoted as a new vector A. The best estimate of these coefficients at each instant of time is denoted as $\hat{A}$

$$\hat{A} = [\hat{l} \;\; \hat{\Lambda}^T] \tag{4.56}$$

and the corresponding error is

$$\tilde{A} = \hat{A} - A \tag{4.57}$$

Vector R denotes a combination of $x_r^{(4)}$ (i.e., the reference value of $x^{(4)}$) and the nonlinear system states, given by

$$R^T = [x_r^{(4)} \;\; \Gamma^T] \tag{4.58}$$

Therefore, Equation 4.51 can be written as

$$x^{(4)} - x_r^{(4)} = \dot{p} = -\lambda' p + \tilde{A}R \tag{4.59}$$

To synthesize the adaptation law using Barbalat's lemma, a new energy-type function is employed as follows

$$V(t) = \frac{1}{2}p^2 + \frac{1}{2}\tilde{A}N\tilde{A} \tag{4.60}$$

where M is a positive definite matrix. The first derivative of the function with respect to time becomes

$$\dot{V}(t) = \frac{dV(t)}{dt} = p\dot{p} + \tilde{A}N\dot{\tilde{A}} \tag{4.61}$$

Substituting Equation 4.59 into Equation 4.61 yields

$$\dot{V}(t) = \frac{dV(t)}{dt} = -\lambda' p^2 + \tilde{A}(N\dot{\tilde{A}} + Rp) \tag{4.62}$$

Since A includes only constant (or slowly changing) coefficients, thus

$$\dot{\tilde{A}} = \dot{\hat{A}} - \dot{A} = \dot{\hat{A}} \tag{4.63}$$

and Equation 4.62 becomes

$$\dot{V}(t) = \frac{dV(t)}{dt} = -\lambda' p^2 + \tilde{A}(N\dot{\hat{A}} + Rp) \tag{4.64}$$

To meet the convergence requirements associated with Barbalat's lemma, $\dot{V}(t)$ must be always less than or equal to 0. Knowing that λ' is chosen strictly positive, and setting

$$\tilde{A}(N\dot{\hat{A}} + Rp) = 0 \tag{4.65}$$

leads the energy-type function $V(t)$ to meet the requirements of Barbalat's lemma. The adaptation law for constant (or slowly changing) coefficients is synthesized based on Equation 4.65. Therefore, the adaptation law becomes

$$\dot{\hat{A}} = -N^{-1}Rp \tag{4.66}$$

Note that in the preceding section, to synthesize the control law, the estimation error on $f = \Lambda^T\Gamma$ is assumed to be bounded (Equation 4.25). However, the adaptation law in Equation 4.69 can result in unbounded parameter estimates in the presence of measurement noise, disturbances and unmatched uncertainties [92]. In an attempt to solve this problem, projection mapping is employed to condition the adaptation law so that only bounded parameter estimates are adopted in the adjustable model compensation. The projection mapping does not affect the nominal estimation capability of the adaptation law. All projection maps fall under two categories: *smooth* and *unsmooth*. Further details can be found in [91, 93, 94]. Herein, two projection maps are proposed: $P_1(\lambda_i)$, an unsmooth projection map and $P_2(\lambda_i)$, a smooth non-decreasing projection map. In these projection maps, λ_i corresponds to i^{th} element of vector $\hat{A}$. The unsmooth projection map can be described as

$$P_1(\lambda_i) = \begin{cases} \lambda_i & \text{for } \lambda_{i,min} \leq \lambda_i \leq \lambda_{i,max} \\ \lambda_{i,max} & \text{for } \lambda_i > \lambda_{i,max} \\ \lambda_{i,min} & \text{for } \lambda_i < \lambda_{i,min} \end{cases} \tag{4.67}$$

and the smooth projection mapping is given by

$$P_2(\lambda_i) = \begin{cases} \lambda_i & \text{for } \lambda^L_{i,min} \leq \lambda \leq \lambda^L_{i,max} \\ [2(\lambda_{i,max} - \lambda^L_{i,max})/\pi][\tan^{-1}(\alpha_1\lambda_i - \alpha_1\lambda^L_{i,max}) + \lambda^L_{i,max}] & \text{for } \lambda_i > \lambda^L_{i,max} \\ [2(\lambda_{i,min} - \lambda^L_{i,min})/\pi][\tan^{-1}(\alpha_2\lambda_i - \alpha_2\lambda^L_{i,min}) + \lambda^L_{i,min}] & \text{for } \lambda_i < \lambda^L_{i,min} \end{cases} \tag{4.68}$$

where α_1 can be tuned so that sufficient smoothness is achieved. Note that the projection upper and lower limits can be obtained based on the estimation error bounds in Equation 4.25. This projection mapping includes linear and nonlinear mapping ranges where $\lambda^L_{i,max}$ and $\lambda^L_{i,min}$ determine the boundaries.

Figure 4.13 depicts how an estimated value obtained from the adaptation law is translated using the projection maps $P_1(\lambda_i)$ and $P_2(\lambda_i)$. In the layer of adaptation, the nominal plant becomes

$$\hat{f} = P(\hat{\Lambda}^T)\Gamma \tag{4.69}$$

where P is a smooth or unsmooth projection mapping with prespecified upper and lower limits for each coefficient (i.e., *conditioned adaptation*), see Figure 4.13. Also, the evolution of these adaptive coefficients is governed by Equation 4.69.

This section demonstrated the use of Barbalat's lemma to synthesize the layer of adaptation in addition to the layer of robustness such that robust stability in the first layer remains intact. In this method, the design of control and adaptations laws are synthesized jointly through an energy-type function with reducing tracking error being the main objective.

4.3 Illustrative Example

4.3.1 Simulation: Design of SRCSys for a Nonlinear Plant

The objectives of this section are threefold: to simulate a set of typical challenges existing in execution of RTHS (see Figure 4.15) with highly uncertain nonlinear physical specimen; to illustrate the implementation of the proposed nonlinear self-tuning

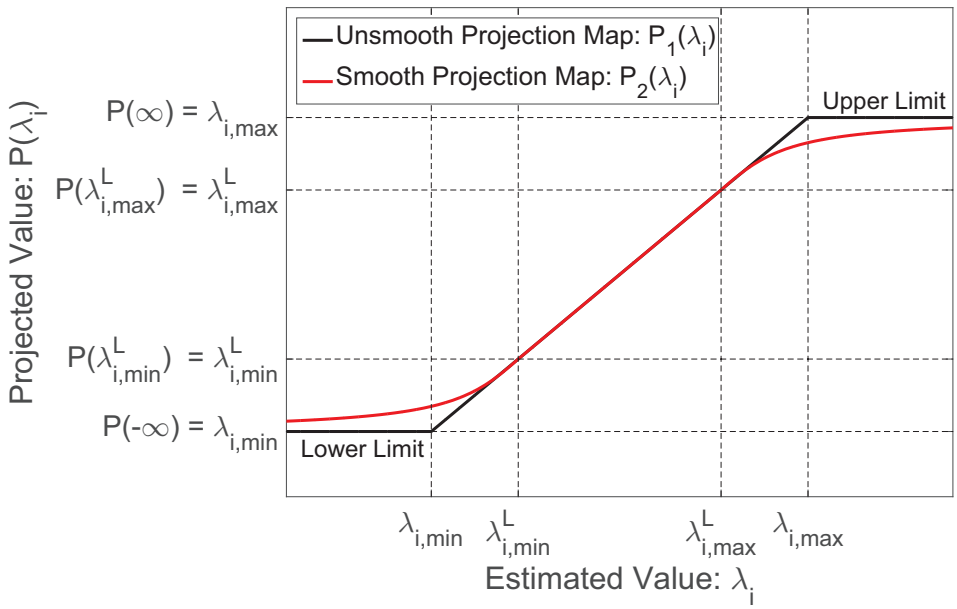

Fig. 4.13. Continuous projection of estimated parameters.

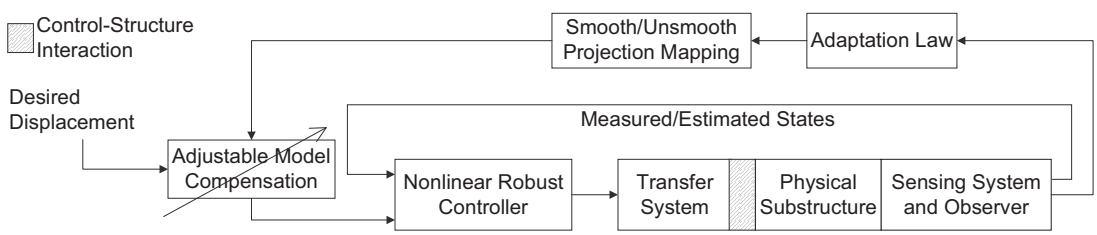

Fig. 4.14. Block diagram of nonlinear self-tuning robust control system.

robust control system; and, to evaluate the performance of the proposed control system in rejecting some major parametric and non-parametric uncertainties.

In this case study, the physical substructure is a steel frame equipped with a magnetorheological (MR) damper (see Figure 4.16). The MR damper is rate-dependent and time-varying as the damper command voltage varies with time. The frame's restoring force exhibits a hysteretic behavior. This hysteresis loop, in which the stiffness degrades significantly, may represent a full-scale test to collapse. Thus, the physical substructure is rate-dependent, time-varying and amplitude-dependent.

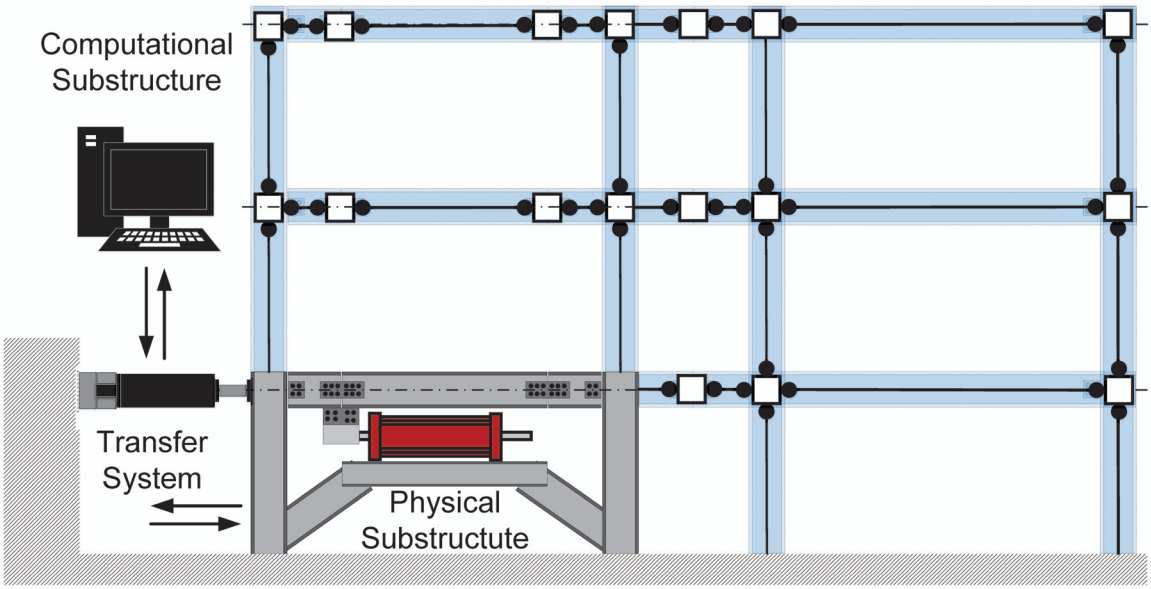

Fig. 4.15. Diagram of real-time hybrid simulation.

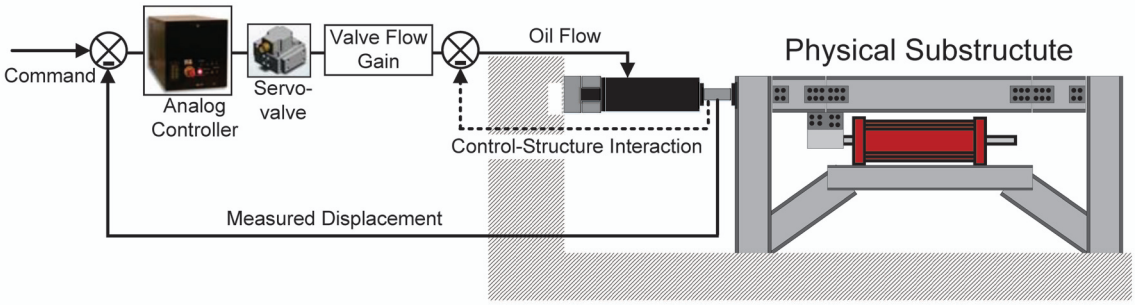

Fig. 4.16. Schematic diagram of the hydraulic control plant.

In this simulation, the true plant (which will be described in the next section) is subject to a desired tracking trajectory. However, to synthesize the control and adaptation laws, the actual dynamics of the true plant are assumed unknown. The essential dynamics of the true plant are captured in a reduced-order assumed plant (i.e., with non-parametric uncertainties). Here, the assumed plant is equivalent to the nominal plant in the previous section. Compared to the true plant, the reduced-order

assumed plant also suffers from parametric uncertainties. For a certain parameter μ, the corresponding parametric uncertainties are computed as follows

$$NE\ \% = \frac{|\mu_{true} - \mu_{assumed}|}{|\mu_{true}|} \times 100 \tag{4.70}$$

4.3.2 True Control Plant

The true control plant is composed of three subsystems: MR damper, steel frame and servo-hydraulic actuator. The dynamics of the MR damper are simulated using a phenomenological model proposed by Spencer et al., [95]. This mechanical model is shown in Figure 4.17. Later, this model was modified and verified for a large-scale 200 kN damper by Friedman [61]. To obtain the governing equation of this model,

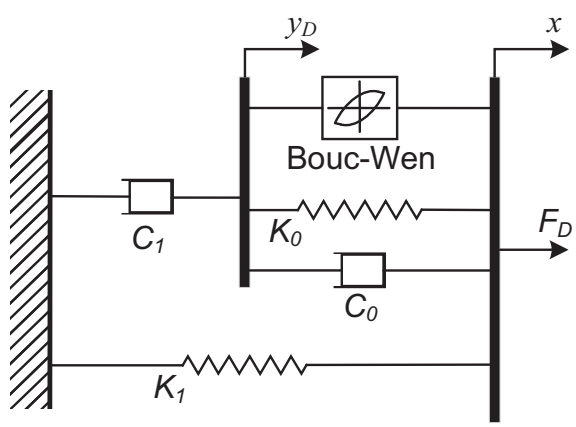

Fig. 4.17. Mechanical model of MR damper in the true plant.

in Figure 4.17, the forces on either side of the rigid bar are equivalent. Thus

$$C_1\dot{y}_D = \alpha z + K_0(x - y_D) + C_0(\dot{x} - \dot{y}_D) \tag{4.71}$$

where the time-varying variable z is governed by

$$\dot{z} = \gamma|\dot{x} - \dot{y}_D|z|z|^{n-1} - \beta(\dot{x} - \dot{y}_D)|z|^n + A(\dot{x} - \dot{y}_D) \tag{4.72}$$

Equation 4.71 is used to obtain $\dot{y}_D$, it becomes

$$\dot{y}_D = \frac{1}{(C_0 + C_1)}[\alpha z + C_0\dot{x} + K_0(x - y_D)] \tag{4.73}$$

From Figure 4.17, the total force of the MR damper can be written as

$$F_D = \alpha z + C_0(\dot{x} - \dot{y}_D) + K_0(x - y_D) + K_1(x - x_0) \tag{4.74}$$

The viscous damping constants (i.e., C_0 and C_1) vary with the voltage v. The following relations are proposed by Friedman [61]

$$\alpha = \alpha^a e^{(v(t)\alpha^b)} + \alpha^c e^{(v(t)\alpha^d)} \tag{4.75}$$

$$C_0 = C_0^a e^{(v(t)C_0^b)} + C_0^c e^{(v(t)C_0^d)} \tag{4.76}$$

$$C_1 = C_1^a + C_1^b v(t) \tag{4.77}$$

In this MR damper model, the amplifier dynamics and the inductance dynamics of large-scale MR dampers are considered. These relations are to take into account the existing dynamics between the voltage realized by the MR damper and the command voltage v_{cmd}. The amplifier dynamics are governed by [96]

$$I_{PWM}(s) = e^{-\tau s}\frac{p_n}{s + p_d} \tag{4.78}$$

The circuit dynamics of large-scale MR damper are modeled as

$$G_I(s) = \frac{1}{(L/R)s + 1} \tag{4.79}$$

Thus, the dynamics between the command voltage and the voltage realized by the MR damper become

$$\frac{v}{v_{cmd}} = I_{PWM}(s).G_I(s) \tag{4.80}$$

In this simulation, $v_{cmd}(t)$ is

$$v_{cmd}(t) = 1.5\sin(4\pi t) \tag{4.81}$$

The identified parameters for a 200 kN MR by Friedman [61] are provided in Table 4.2. Figure 4.18 shows the response of the MR damper model where the excitation signal

Table 4.2.
Parameters of Bouc-Wen model for 200 kN MR fluid damper in the true plant.

Parameter	**Value**	**Unit**	**Parameter**	**Value**	**Unit**
α^a	880.9	kN	C_1^a	100	$kN.sec/m$
α^b	0.0129	kN	C_1^b	28470	$kN.sec/m$
α^c	-865.3	kN	K_0	0.0559	kN/m
α^d	-1.003	kN	K_1	0.0641	kN/m
C_0^a	201.3	$kN.sec/m$	x_0	0.01	m
C_0^b	0.1229	$kN.sec/m$	β	4429.6	m^{-1}
C_0^c	-109	$kN.sec/m$	γ	4429.6	m^{-1}
C_0^d	-2.116	$kN.sec/m$	A	336.564	
τ	0.0006	sec	n	2	-
L	2	H	R	4.8	Ω
P_n	286.7	-	P_d	282.7	-

is a 1 Hz sinusoid with an amplitude of 0.0254 m for four voltage levels, 0 V, 0.5 V, 1.0 V, and 1.5 V. Two plots are shown, including the force versus displacement (clockwise progression) and force versus velocity (counter-clockwise progression).

The governing equation of the simulated steel frame in Figure 4.16 is

$$M\ddot{x} + C\dot{x} + R + F_D = F_A \tag{4.82}$$

where M, C, R, F_D and F_A corresponds to mass, damping coefficient, restoring force, MR damper force and applied force, respectively. In this study, the true mass and damping coefficient are 6.1 kN.sec^2/m and 32.73 kN.sec/m. The restoring force is governed by the hysteresis loop shown in Figure 4.21. The MR damper force F_D is governed by Equation 4.74.

To simulate the servo-hydraulic actuator, the model shown in Figure 4.3 with verified parameters associated with the hydraulic actuator model 200-100-1700 with a 2300 kN (501 $kips$) capacity and 500 mm (19.7 in) stroke are employed. These

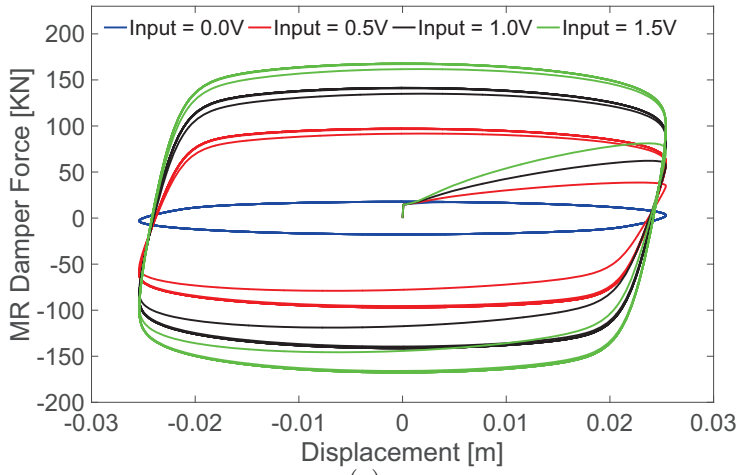

(a)

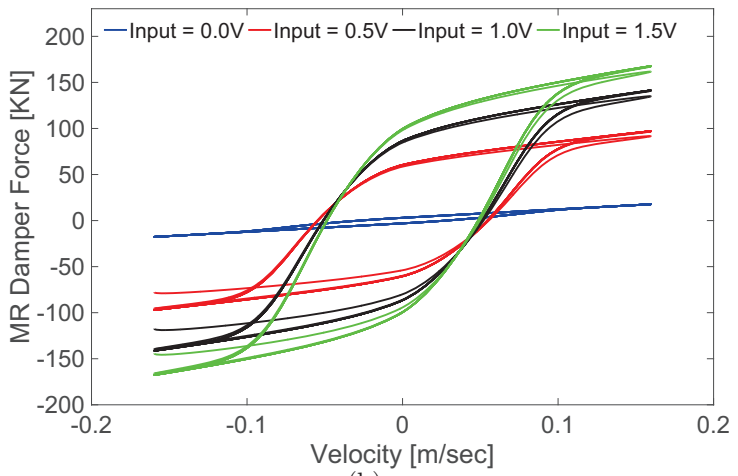

(b)

Fig. 4.18. 200 kN Bouc-Wen MR damper model response: (a) force vs displacement (b) force vs velocity.

parameters are provided in Table 4.3. The next section describes the reduced-order assumed plant. The assumed plant will be used to synthesize the control layers.

Table 4.3.
Parameters of servo-hydraulic actuator in the true control plant.

Parameter	Value	Unit
a_1	3.40×10^6	$kN/(m.sec)$
a_2	2.52×10^5	kN/m
a_3	35.85	sec^{-1}
β_0	285.71	sec^{-1}
β_1	142.86	sec^{-1}

4.3.3 Assumed Control Plant

Here, the dynamics of the MR damper is reduced to a simple arctangent model (see Figure 4.19) in which the MR damper force is governed by

$$\hat{F}_D = A_n \tan^{-1}(n_0\dot{x}) + C_n\dot{x} \tag{4.83}$$

where

$$A_n = d_1 + (d_2|v| + d_3|v|^3)^{1/3} \tag{4.84}$$

$$C_n = r_1 + (r_2|v| + r_3|v|^3)^{1/3} \tag{4.85}$$

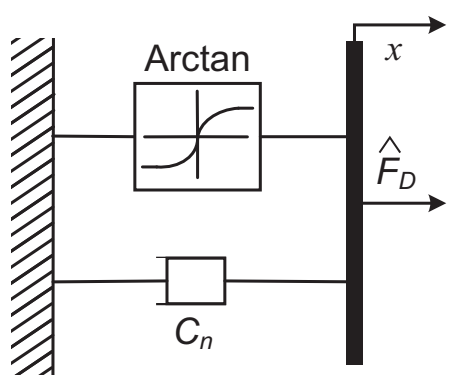

Fig. 4.19. Mechanical model of MR damper in the assumed plant.

Table 4.4.
Parameters of arctan model for 200 kN MR fluid damper in the assumed plant.

Parameter	**Value**	**Parameter**	**Value**
d_1	2.2	r_1	92
d_2	2.16×10^5	r_2	1.58×10^6
d_3	7.38×10^4	r_3	2.40×10^5
n_0	100		

The parameters for the 200 kN MR damper are provided in Table 4.4. Also, in this MR damper model, the PWM amplifier dynamics and the inductance dynamics of large-scale MR dampers are ignored. Therefore, the voltage realized by the MR damper is identical to the command voltage.

$$v = v_{cmd} \tag{4.86}$$

Figure 4.20 shows the response of this MR damper model where the excitation signal is a 1 Hz sinusoid with an amplitude of 0.0254 m for four voltage levels, 0 V, 0.5 V, 1.0 V, and 1.5 V. Two plots are shown, including the force versus displacement (clockwise progression) and force versus velocity.

The governing equation of the assumed physical substructure is

$$\hat{M}\ddot{x} + \hat{C}\dot{x} + \hat{K}x + \hat{F}_D = F_A \tag{4.87}$$

where $\hat{M}$, $\hat{C}$, $\hat{K}$, $\hat{F}_D$ and F_A corresponds to assumed mass, damping coefficient, restoring force, MR damper force and applied force, respectively. The assumed mass, damping coefficient and stiffness are 7.32 $kN.sec^2/m$, 49.1 $kN.sec/m$ and 4449 kN/m, respectively. Compared to the true plant, the assumed mass and damping coefficient correspond to 20% and 50% normalized error. Figure 4.21 shows the difference in the restoring force of the true and assumed models (i.e., non-parametric error).

In the assumed plant, the servo-hydraulic actuator is also modeled as shown in Figure 4.3. The corresponding parameters in the assumed plant are provided in

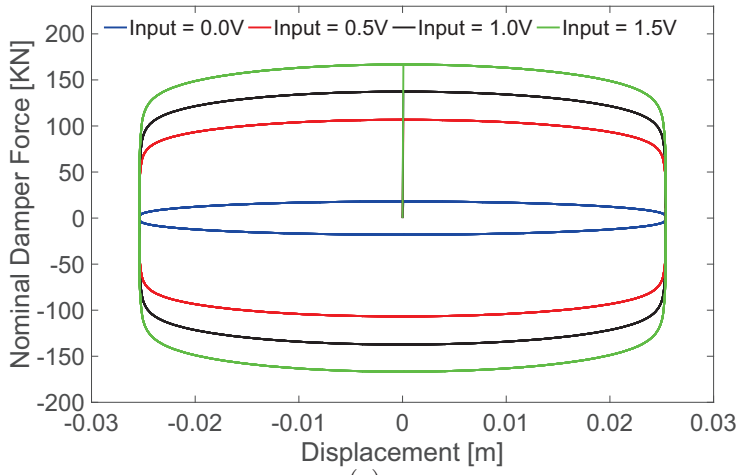

(a)

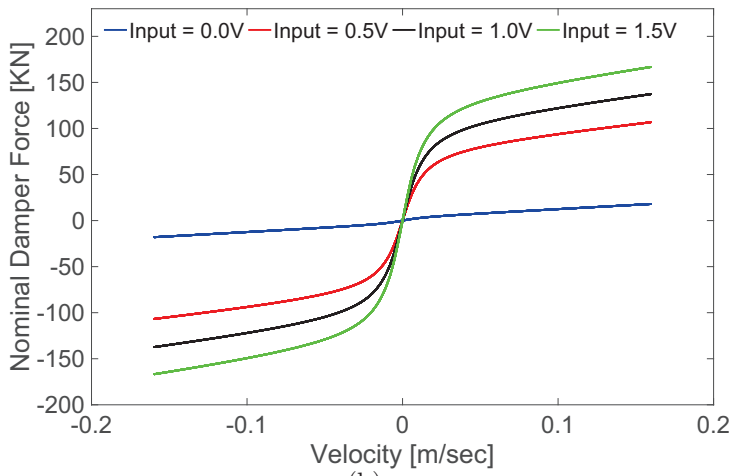

(b)

Fig. 4.20. 200 kN Arctan MR damper model response: (a) force vs displacement (b) force vs velocity.

Table 4.5. Compared to Table 4.3, parameters in the assumed model suffers from 30%-40% normalized error.

In the next section, the assumed plant is used to synthesize the control layers.

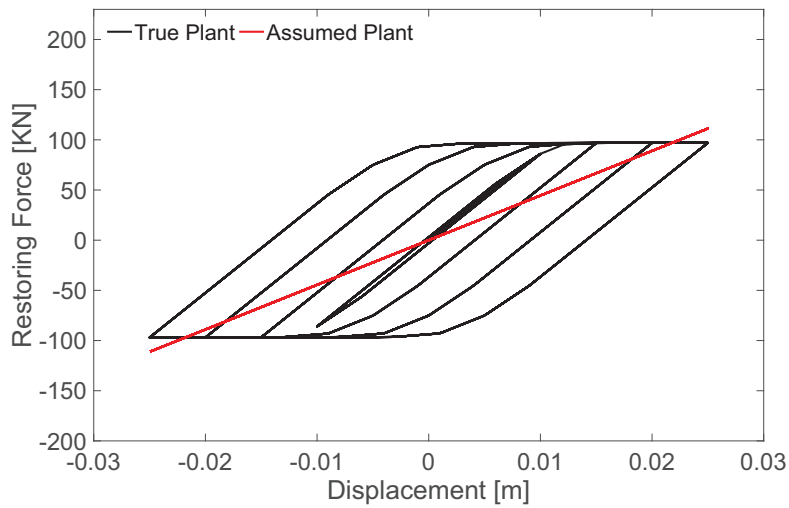

Fig. 4.21. Restoring forces in the steel frame models.

Table 4.5.
Parameters of servo-hydraulic actuator in the assumed plant.

Parameter	Value	Unit	Normalized Error
$\hat{a}_1$	4.42×10^6	$kN/(m.sec)$	30%
$\hat{a}_2$	1.76×10^5	kN/m	30%
$\hat{a}_3$	50.19	sec^{-1}	40%
$\hat{\beta}_0$	400	sec^{-1}	40%
$\hat{\beta}_1$	200	sec^{-1}	40%

4.3.4 Design of SRCSys

To synthesize the control layers, some rearrangements are needed to describe the assumed plant in controllable canonical form. The assumed physical substructure in Equation 4.87 is written as

$$\ddot{x} = h(x, \dot{x}) + \frac{F_A}{M} \tag{4.88}$$

where

$$h = -\frac{\hat{C}}{\hat{M}}\dot{x} - \frac{\hat{K}}{\hat{M}}x - \frac{\hat{1}}{\hat{M}}\hat{F}_D \tag{4.89}$$

The first and second partial derivatives of h are computed as

$$\begin{aligned}
h_1 &= \frac{\partial h}{\partial x_1} = \frac{-\hat{K}}{\hat{M}} & h_{22} &= \frac{\partial h}{\partial x_1} = \frac{2n^3 A_n \dot{x}}{\hat{M}(n^2\dot{x}^2+1)^2} \\
h_2 &= \frac{\partial h}{\partial x_2} = -\frac{\hat{C}+C_n}{\hat{M}} - \frac{nA_n}{\hat{M}(n^2\dot{x}^2+1)} & h_{12} &= \frac{\partial h}{\partial x_1} = 0 \\
h_{11} &= \frac{\partial^2 h}{\partial x_1} = 0
\end{aligned} \tag{4.90}$$

Using Equation 4.9, the assumed plant can be described in controllable canonical form as

$$\begin{cases}
\dot{x}_1 &= x_2 \\
\dot{x}_2 &= x_3 \\
\dot{x}_3 &= x_4 \\
\dot{x}_4 &= c_1x_1 + c_2x_2 + c_3x_3 + c_4x_4 + c_5 f + c_6 + bu
\end{cases} \tag{4.91}$$

where

$$\begin{aligned}
c_1 &= -\frac{\hat{a}_1\hat{\beta}_0}{\hat{M}} & c_5 &= -\frac{\hat{\beta}_1\hat{a}_3}{\hat{M}} \\
c_2 &= -\frac{\hat{\beta}_1\hat{a}_2}{\hat{M}} + (\hat{\beta}_1+\hat{a}_3)h_1 & c_6 &= h_{11}x_2^2 + h_{22}x_3^2 + 2h_{12}x_2x_3 \\
c_3 &= (\hat{\beta}_1+\hat{a}_3)h_2 - \frac{\hat{a}_2}{\hat{M}} + h_1 & b &= \frac{a_1\hat{\beta}_0}{\hat{M}} \\
c_4 &= -\hat{\beta}_1 - \hat{a}_3 + h_2
\end{aligned} \tag{4.92}$$

Using Equations 4.90-4.92, the assumed plant can be described as

$$x^{(4)} = \hat{\Lambda}^T\Gamma + bu \tag{4.93}$$

where $\hat{\Lambda} = [\hat{\lambda}_1 \cdots \hat{\lambda}_8]$ and $\Gamma = [\gamma_1 \cdots \gamma_8]$ are given by

$$\begin{aligned}
\hat{\lambda}_1 &= -\tfrac{\hat{a}_1\hat{\beta}_0}{\hat{M}} & \gamma_1 &= x_1 \\
\hat{\lambda}_2 &= -\tfrac{\hat{\beta}_1\hat{a}_2+(\hat{\beta}_1+\hat{a}_3)\hat{K}}{\hat{M}} & \gamma_2 &= x_2 \\
\hat{\lambda}_3 &= -\tfrac{(\hat{\beta}_1+\hat{a}_3)(\hat{C}+C_n)+\hat{a}_2+\hat{K}}{\hat{M}} & \gamma_3 &= x_3 \\
\hat{\lambda}_4 &= -(\hat{\beta}_1+\hat{a}_3) - \tfrac{\hat{C}+C_n}{\hat{M}} & \gamma_4 &= x_4 \\
\hat{\lambda}_5 &= -\tfrac{(\hat{\beta}_1+\hat{a}_3)A_n}{\hat{M}} & \gamma_5 &= \tfrac{n_0x_3}{n_0^2x_2^2+1} \\
\hat{\lambda}_6 &= -\tfrac{A_n}{\hat{M}} & \gamma_6 &= \tfrac{n_0x_4}{n_0^2x_2^2+1} \\
\hat{\lambda}_7 &= \tfrac{2A_n}{\hat{M}} & \gamma_7 &= \tfrac{n_0^3x_2x_3^2}{(n_0^2x_2^2+1)^2} \\
\hat{\lambda}_8 &= \tfrac{-\hat{\beta}_1\hat{a}_3}{\hat{M}} & \gamma_8 &= F_A
\end{aligned} \tag{4.94}$$

For this plant, the compact tracking error measure is

$$p = e^{(3)} + 3\lambda\ddot{e} + 3\lambda^2\dot{e} + \lambda^3 e \tag{4.95}$$

where λ is chosen to be 650 rad/sec. The dynamics of the boundary layer thickness Φ is governed by

$$\dot{\Phi} = -\lambda'\Phi + K \tag{4.96}$$

where λ' is set to be 700 rad/sec and K is defined in Equation 4.35. The bounded uncertainty F is chosen as

$$F = 0.6|\hat{\Lambda}^T\Gamma| \tag{4.97}$$

and η is 20. The control law is synthesized using Equation 4.55. Finally, the layer of adaptation is added to the layer of robustness. Here, the unsmooth projection

map in Equation 4.67 and the adaptation law in Equation 4.69 are employed. In the adaptation law, the following positive definite matrix is used.

$$N = \begin{pmatrix} 8.3^{-5} & 0 & 0 & 0 & 0 & 0 & 0 & 0 \\ 0 & 2.0^{-3} & 0 & 0 & 0 & 0 & 0 & 0 \\ 0 & 0 & 6.1^{0} & 0 & 0 & 0 & 0 & 0 \\ 0 & 0 & 0 & 7.1^{4} & 0 & 0 & 0 & 0 \\ 0 & 0 & 0 & 0 & 1.1^{2} & 0 & 0 & 0 \\ 0 & 0 & 0 & 0 & 0 & 2.9^{6} & 0 & 0 \\ 0 & 0 & 0 & 0 & 0 & 0 & 1.4^{8} & 0 \\ 0 & 0 & 0 & 0 & 0 & 0 & 0 & 1.5^{3} \end{pmatrix} \tag{4.98}$$

Here the design of *SRCSys* is completed. Now these design parameters can be used to synthesize the two control layers, see Figure 4.22. The next section presents

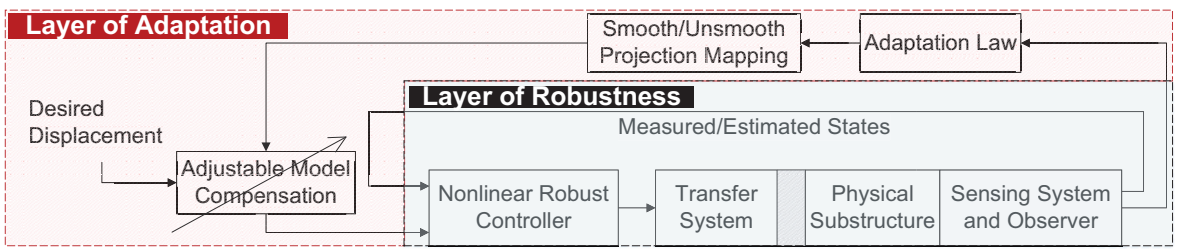

Fig. 4.22. Self-tuning robust control system: layer of robustness and layer of adaptation.

some results associated with two cases: (1) layer of robustness is activated while layer of adaptation is deactivated (i.e., w/o adaptation) and (2) layers of robustness and adaptation are both activated (i.e., w/ adaptation).

4.3.5 Simulation Results

To consider the bandwidth of interest in RTHS, the desired displacement is a harmonic signal

$$x_d = \sum_{i=1}^{3} a_i \sin(2\pi f_i t) \tag{4.99}$$

where $a_i \in \{0.007,\ 0.007,\ 0.007\}$ m and $f_i \in \{0.5,\ 6,\ 20\}$ Hz.

To evaluate the effectiveness of the proposed control system in the presence of parametric and non-parametric uncertainties, two major factors are considered: rate of convergence and steady-state accuracy. Figure 4.23 presents the rates of convergence associated with the two cases with and without the adaptation layer. The results show that the adaptation layer can effectively enhance the tracking performance. The normalized tracking error is computed as

$$NE(t)\ \% = \frac{x(t) - x_d(t)}{max(|x_d(t)|)} \times 100 \tag{4.100}$$

Figure 4.23 shows that due to the existence of parametric and non-parametric uncertainties, our initial understanding of the plant is limited and leads to a normalized tracking error of 40% in the beginning. However, the control law is designed so that the control command overcomes the uncertainties. Figure 4.24 presents the steady-state response of tracking for the two cases. The results show that, if properly synthesized, the adaptation layer also improves steady-state accuracy without jeopardizing the stability provided by the layer of robustness.

The p-trajectory (i.e., variation of the compact tracking error measure) quantifies the overall tracking performance of the transfer system in one measure. Figures 4.25b-c show the boundary layer thickness ($\pm\phi$) and the compact tracking error measure p versus time. This figure reveals a number of important points. It shows that at the starting time, the tracking error measure is trapped within the boundary layer which is one of the main objectives of this control system. It reveals the rate of convergence. Thus, this plot can be useful for tuning different control parameters (e.g., λ, λ' and N). Moreover, in this case the p-trajectory does not converge or exits the bounded

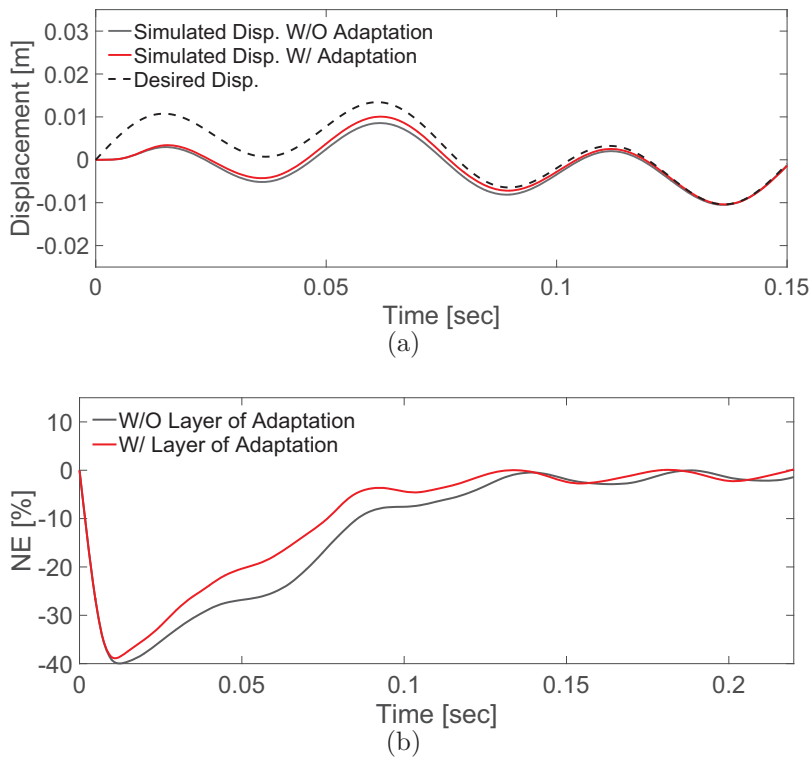

Fig. 4.23. Evaluating the transient response of displacement tracking with and without the adaptation layer: (a) displacement tracking (b) normalized tracking error.

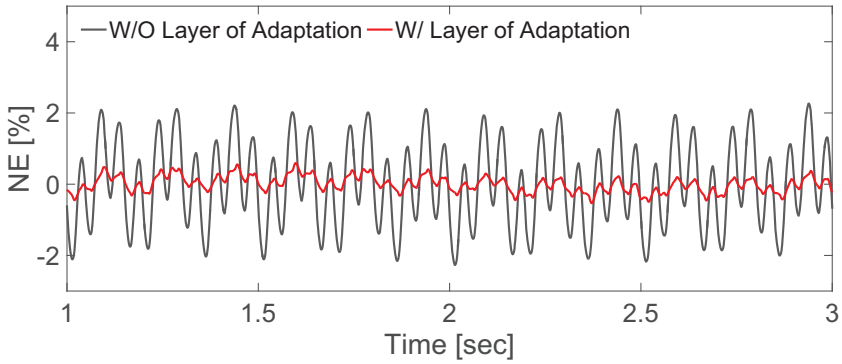

Fig. 4.24. Evaluating the steady-state response of displacement tracking with and without the adaptation layer.

region for a time-span. This behavior means that some assumptions such as the bounded uncertainty or the assumed plant are not suitable within that time-span.

Therefore, the tracking performance (and RTHS response when this control system is employed) associated with that time-span can be marked as unreliable. In the case of RTHS, this feature is important because the true plant and reference response are usually unknown.

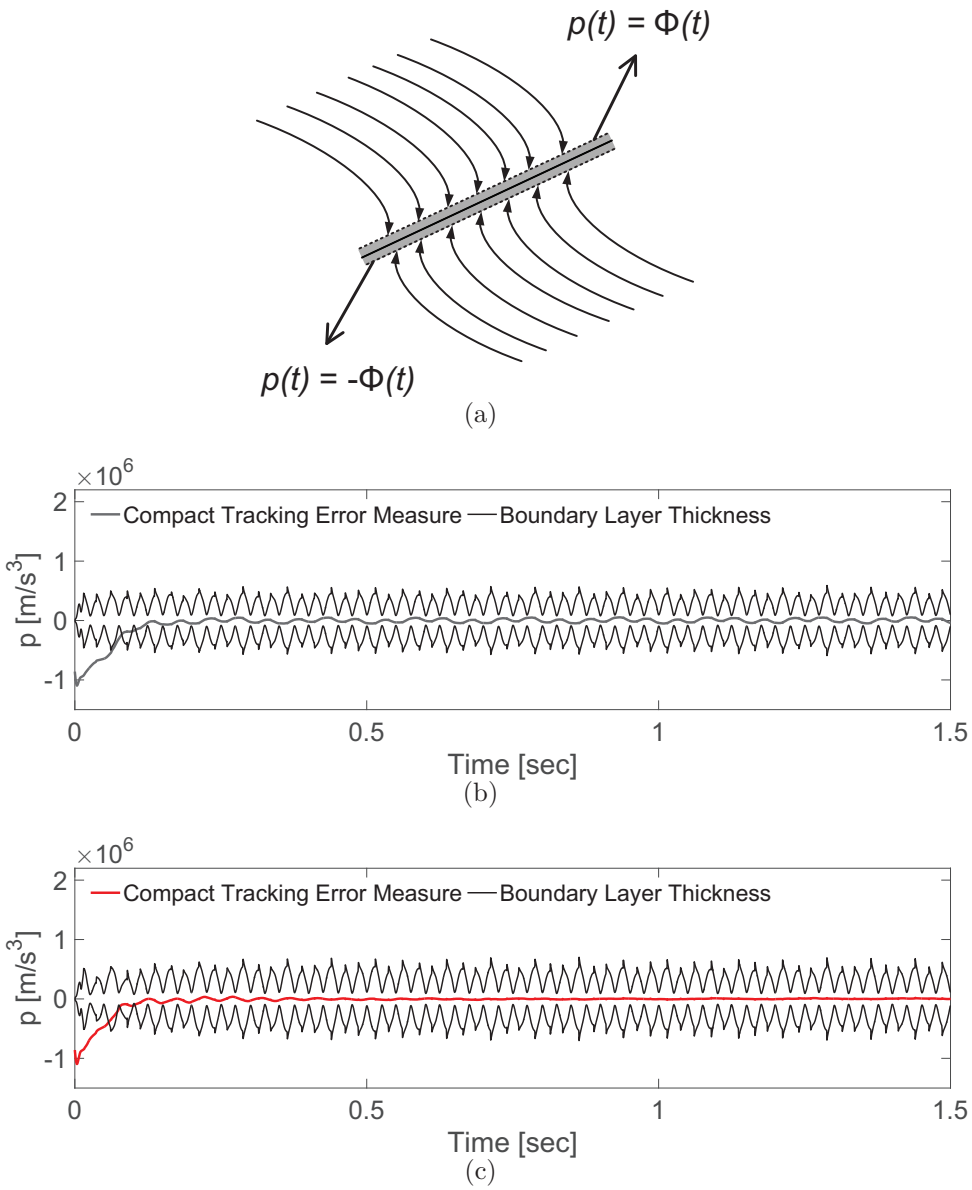

Fig. 4.25. Compact tracking error measure and boundary layer thickness trajectories: (a) boundary layer (b) w/o adaptation layer (c) w/ adaptation layer.

In the case with the adaptation layer, the coefficients in Equation 4.94 evolve over time to reduce the steady-state tracking error. This evolution is governed by Equation 4.69. Figure 4.26 shows the evolution of these coefficients over time. Note

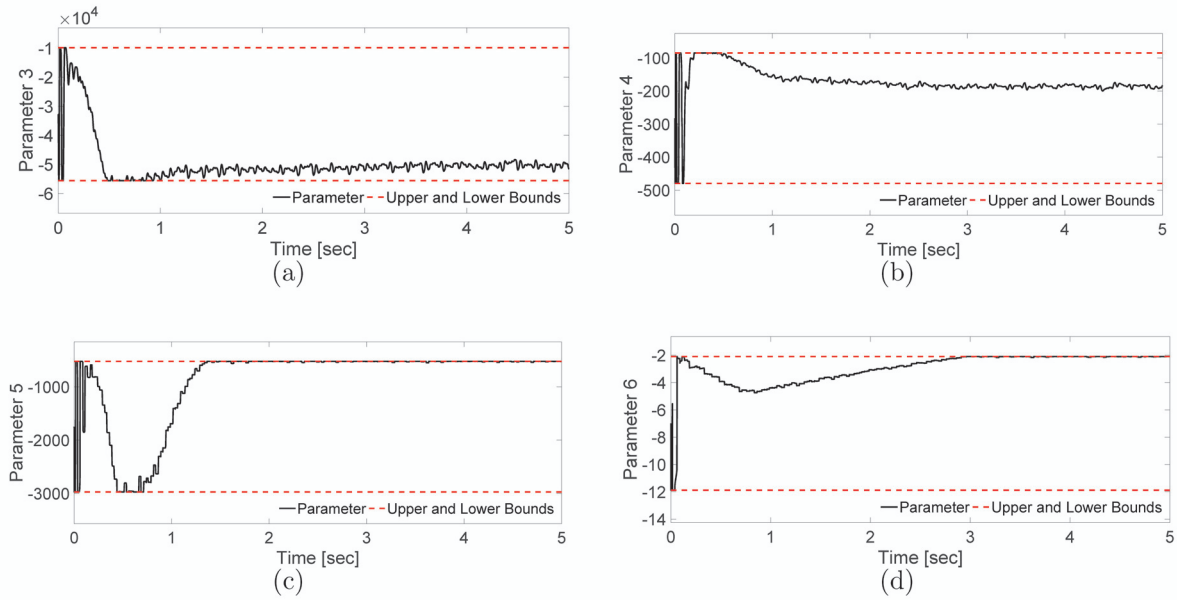

Fig. 4.26. Evolution of adaptive parameters subject to unsmooth projection map.

that in this study, the unsmooth projection map from Equation 4.67 is employed to ensure that the parameters remain within a specified region. Based on these varying parameters, control command is computed using Equation 4.55. For practical purposes, the control command signal is clipped to account for the existing control limitations.

In the execution of successful RTHS, effective implementation of transfer system tracking can be crucial. The main objective of the proposed nonlinear adaptive robust control system is to essentially negate the dynamics of (1) transfer system and (2) the interaction between physical substructure and transfer system. In this study, the physical substructure is rate-dependent, time-varying and amplitude-dependent and the assumed plant suffers from parametric and non-parametric uncertainties. To evaluate the performance of this control system, Figure 4.27 compares two cases: (a) the

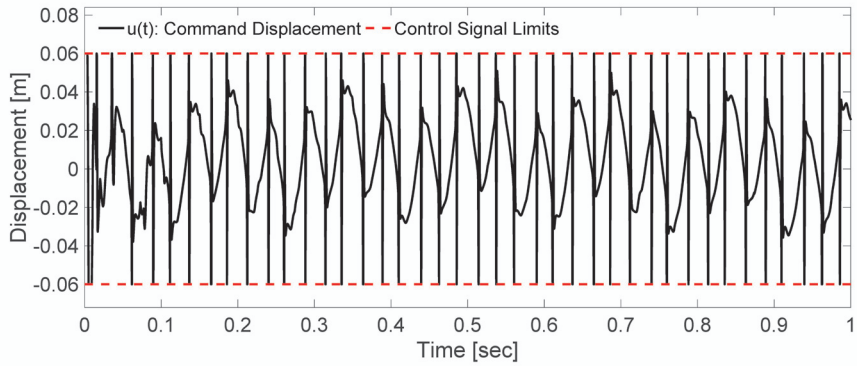

Fig. 4.27. Evolution of control command.

simulated case (physical substructure force versus simulated displacement/velocity) and (b) the ideal case in which transfer system and the interaction between the physical substructure and transfer system are ignored (physical substructure force versus desired displacement/velocity). In the latter case, the physical substructure in Figure 4.27 simply takes the desired boundary conditions (i.e., desired displacement, velocity and acceleration) as input and generates ideal force as output.

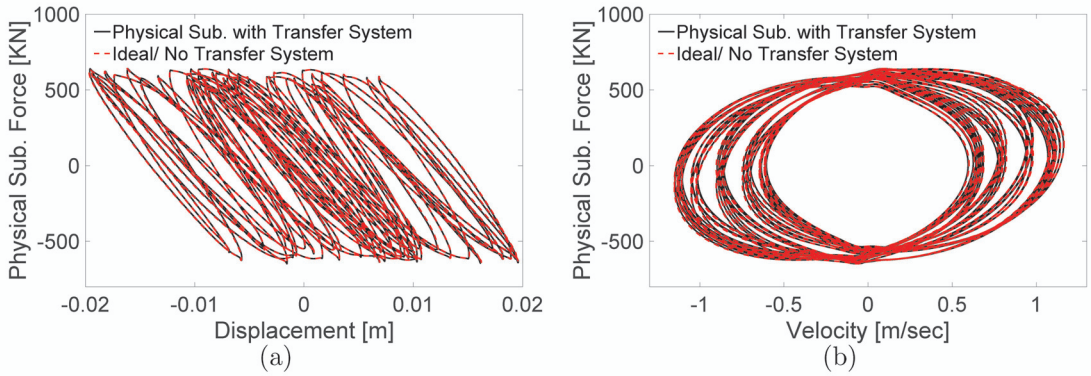

Fig. 4.28. Comparison of force generated in the realistic case w/ transfer system and the proposed control system and the ideal case: (a) physical substructure force versus displacement (b) physical substructure force versus velocity.

Figure 4.28 shows that even though limited understanding about the physical substructures and transfer system are available, *SRCSys* achieves good tracking.

4.3.6 Experimental: Trajectory Tracking w/ Failure in Physical Specimen

One of the primary objectives of developing *SRCSys*, as a multi-layer nonlinear control system, is to accommodate extensive performance variations in the physical specimen (physical substructure, in the case of RTHS) due to failure, complexity, and nonstationary behavior. Thus in this section, the performance and stability of *SRCSys* is investigated for a time-varying physical specimen in which the specimen yields and fails during the course of trajectory tracking experiment.

The specimen used in this experiment is the nonlinear device described earlier in Section 3.2.3, see Figure 3.23. As discussed in Section 3.2.3, this device exhibits nonlinear force-displacement profile and the device can be tested to yield and fail one or both the coupons. The hydraulic actuator employed in the experiment is the double acting, double ended fatigue-rated ShoreWestern actuator with product number 910D-.77-6-4-1348, described in Section 3.2.3. Figure 3.24 shows the experimental setup associated with the control plant. In the earlier chapter, the control plant is identified and the associated parameters are provided in Table 3.5. In this section, using the identified plant and the design procedure described in Section 4.3.4, a self-tuning robust controller is designed.

In this experiment, the desired trajectory is composed of two sinusoidal signals at 1 Hz and 10 Hz. To implement this experiment, approximately 85% force capacity of the hydraulic actuator is utilized which means that the dynamics of the control plant will change noticeably in the case of specimen failure. However, the controller is designed such that the failure in the specimen will not impact the trajectory tracking of the hydraulic actuator. Figure 4.29 shows trajectory tracking of the hydraulic actuator attached to the nonlinear device while both coupons fail at 2.78 *sec*. As it can be seen in Figure 4.29, at the instant of failure, the hydraulic actuator continues to track the desired trajectory. Further, in Figure 4.30, the actuator time-history is provided. Here, it can be seen that at the instant of failure, the actuator force drops

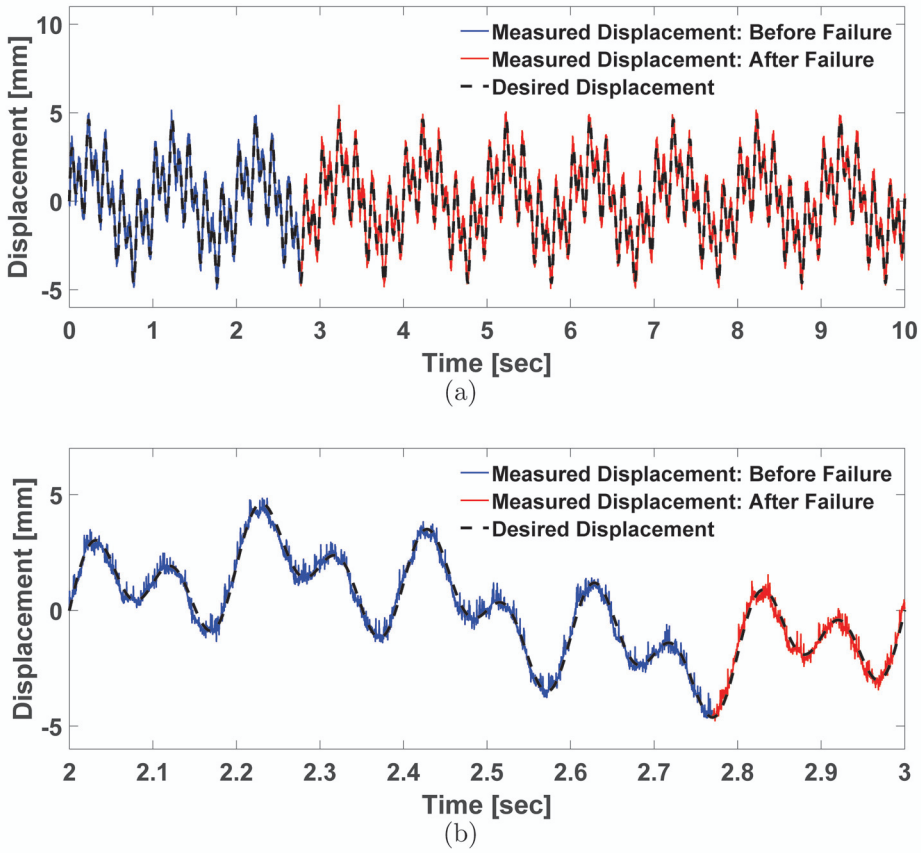

Fig. 4.29. Trajectory tracking with sudden change in the control plant: failure in the physical specimen.

from almost 4.3 kN to less than 0.5 kN. In addition, Figure 4.31 shows the force

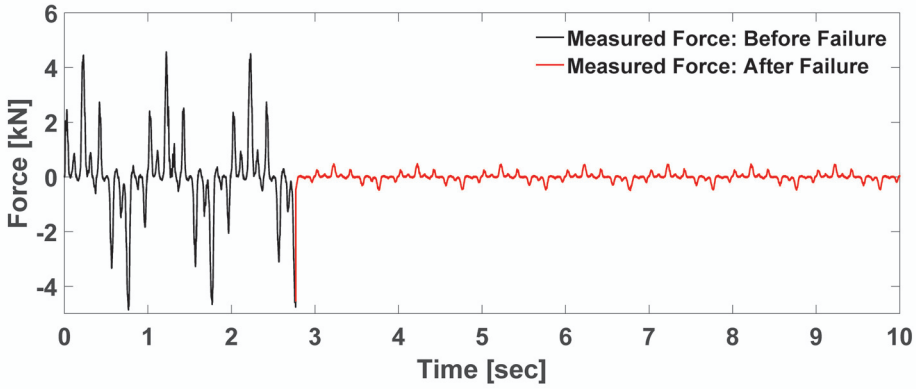

Fig. 4.30. Actuator force time-history before and after the failure.

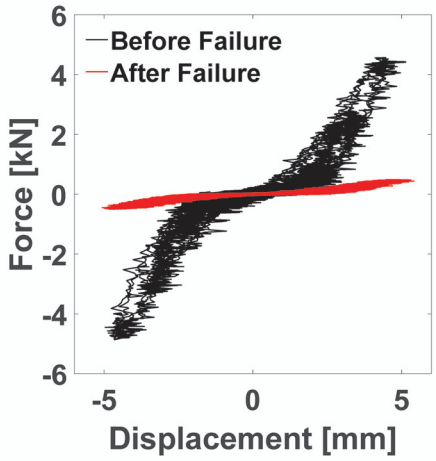

Fig. 4.31. Force-displacement profile before and after the failure.

profile associated with the physical specimen before and after the failure.

That *SRCSys* enables the implementation of high-precision trajectory tracking is significant in the case of RTHS. As discussed previously in this dissertation, ultimately, RTHS will be most useful when the physical substructure is quite general, for instance an unknown time-varying nonlinear system, or even including structural component failure. Thus, the transfer system controller should be designed robust with respect to significant uncertainties and/or changes in the dynamics of the control plant without sacrificing performance measures.

4.3.7 Experimental: Real-time Hybrid Simulation

In this section, the objective is validation of *SRCSys* from stability and performance perspectives using RTHS. For this reason, a moment resisting frame equipped with an MR damper, shown in Figure 4.32 is chosen as the reference structure.

The reference structure is further partitioned into the computational and physical substructures. The computational substructure in Figure 4.33 is modeled using an open-source real-time computational platform for RTHS of dynamically-excited steel frame structures: RT_Frame2D developed by [97]. The finite element model associated with the computational substructure is provided in Appendix A. RT_Frame2D

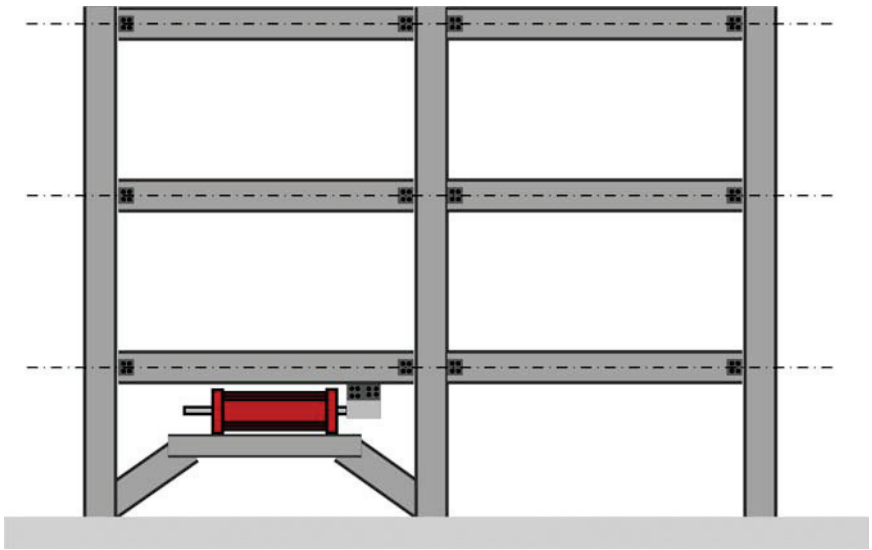

Fig. 4.32. Reference structure (unscaled).

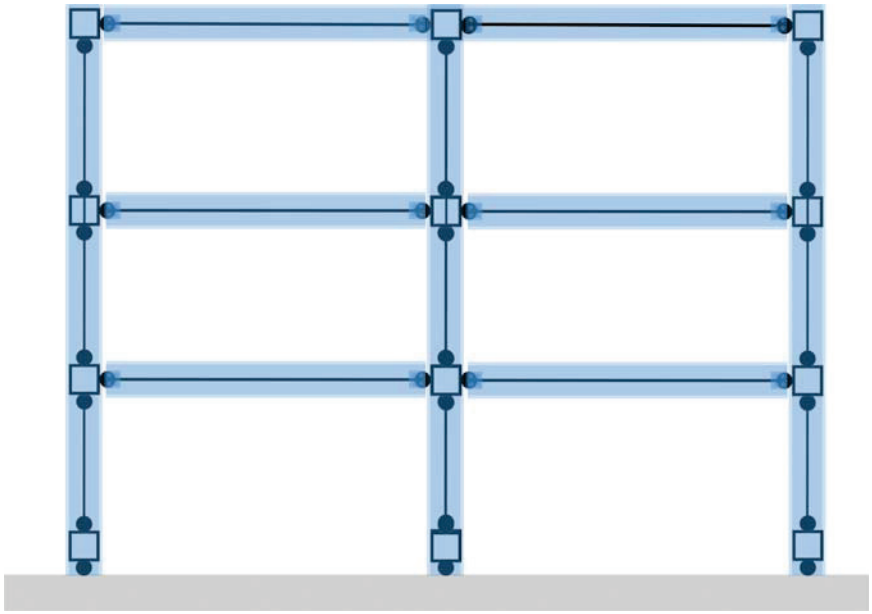

Fig. 4.33. Computational substructure (unscaled).

is executed as a MATLAB/embedded function. The embedded function supports efficient code generation to accelerate fixed point algorithm implementation for embedded systems [97].

Figure 4.34 shows the MR damper which serves as the physical substructure in this section. MR dampers can be used as passive or semi-active control devices to dissipate

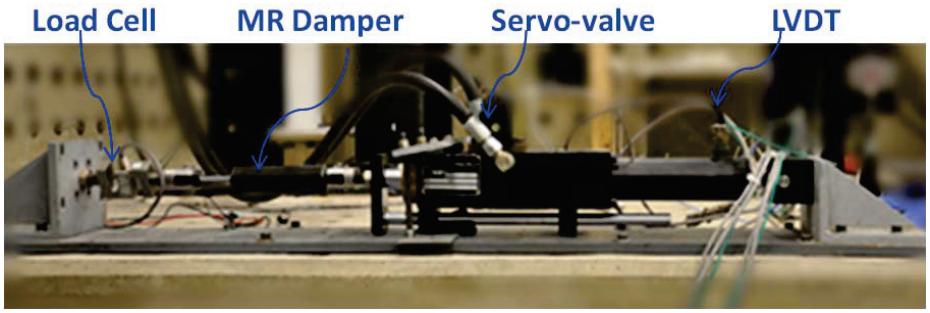

Fig. 4.34. Control plant: hydraulic actuator coupled with the physical substructure.

energy in dynamic systems. When a magnetic field is applied to the MR fluid, the magnetic particles connect and form chains, changing the MR fluid from a viscous controllable current driver is used to control the strength of the magnetic field applied to the MR fluid. The MR damper used as physical substructure (either passive on or off) is made by LORD (model #RD-1005-3). This MR damper is nominally capable of generating forces up to 2.5 kN when powered with an input current of 1 A. To power the MR damper, a voltage controllable current driver which generates current from 0 A to 3 A is used. The current driver is controlled using a high-performance Speedgoat/xPC (Speedgoat GmbH, 2011) real-time target machine. The hydraulic actuator used in these experiments is a double acting, double-ended fatigue-rated Shore Western actuator with product number 910D-.77-6-4-1348. The cross sectional area of this actuator is 0.37 in^2 and the nominal actuator's force capacity is 1.1 kip with 3000 psi supply pressure.

The dynamic behavior of this MR damper subject to different input voltages are investigated. Figure 4.35 shows the force time-history of the MR damper subject to various excitations. Figure 4.36 shows the corresponding force-displacement profiles. In addition, the rate-dependent behavior of this MR damper can be observed in the

force-velocity profiles provided in Figure 4.37. Clearly, Figures 4.35-4.37 show that this MR damper is a complex, nonlinear, and rate-dependent controllable device.

In implementation of the real-time hybrid simulations in this section, the robustness of *SRCSys* is exploited such that the *SRCSys* parameters remain unchanged while the dynamics of the MR damper (and consequently the control plant) changes. In these real-time hybrid simulations, the excitation used to determine the reference structure's responses is the EW component of the 1940 El Centro, shown in Figure 4.38. The ground excitation is scaled to 10% intensity to maintain the limitations corresponding to the maximum stroke of the MR damper.

Here, the results associated with different simulations are discussed. Figures 4.39-4.42 compare the first floor and third floor displacement time-histories of the frame (with no MR damper) with the one equipped with the MR damper, passive off (input voltage: 0 V), passive on (input voltage: 1 V), passive on (input voltage: 1.5 V), passive on (input voltage: 2 V), respectively.

Figure 4.43 compares the first floor and third floor displacement time-histories associated with all different cases. Figure 4.43 shows the effectiveness of the MR damper (as a passive energy dissipating device) as its resistance force changes in mitigating the earthquake-induced vibration of the reference structure. Figure 4.44 shows the corresponding force-displacement profiles generated with the MR damper for the passive off (input voltage: 0 V), passive on (input voltage: 1 V), passive on (input voltage: 1.5 V), passive on (input voltage: 2 V) cases.

In these simulations, *SRCSys* is employed as the hydraulic actuator controller to execute the interface conditions between the computational and physical substructures. As discussed earlier, the main objective of this section was to investigate the robustness of *SRCSys* as the control plant changes while the *SRCSys* parameters remain unchanged. Equation 4.100 is used to quantify error in executing interface conditions during the real-time hybrid simulations. The associated errors are provided in Table 4.6. In addition, tracking time-histories associated with the passive off and passive on cases are shown in Figures 4.45 and 4.46.

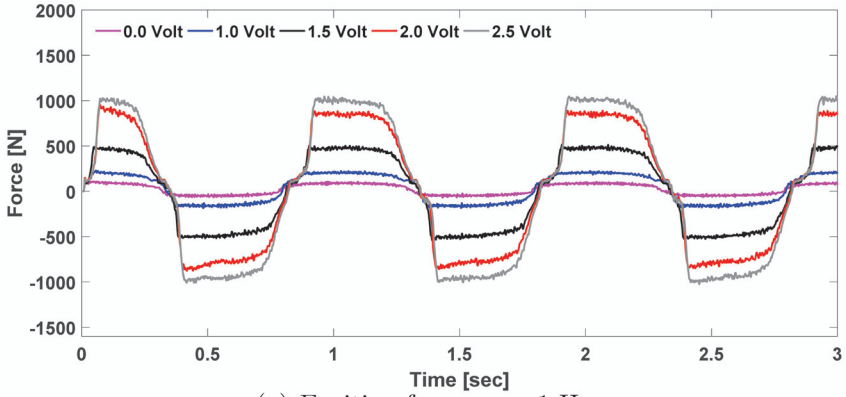

(a) Exciting frequency: 1 Hz.

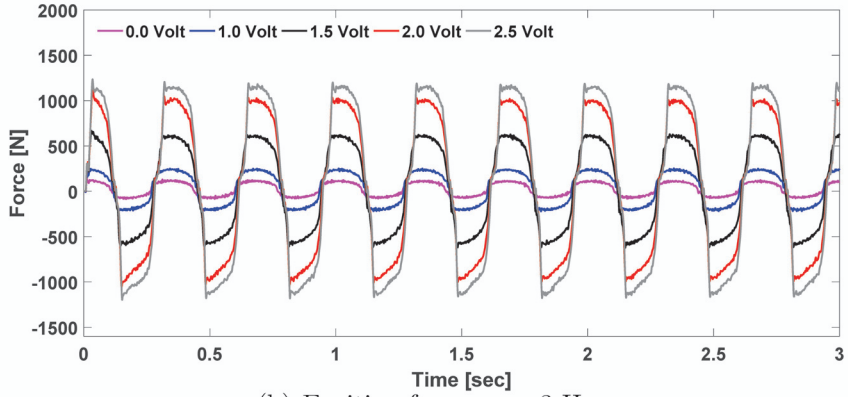

(b) Exciting frequency: 3 Hz.

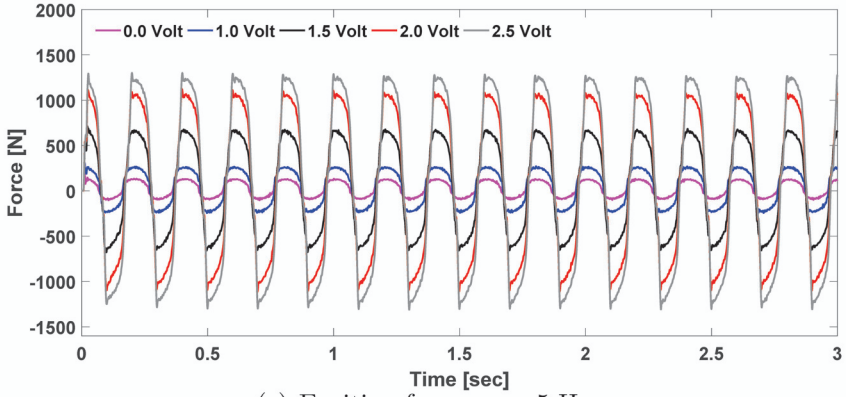

(c) Exciting frequency: 5 Hz.

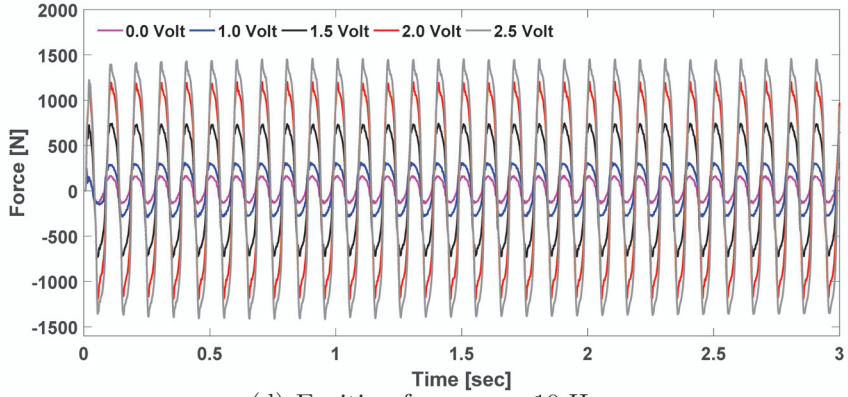

(d) Exciting frequency: 10 Hz.

Fig. 4.35. MR damper characterization behavior: force time-history.

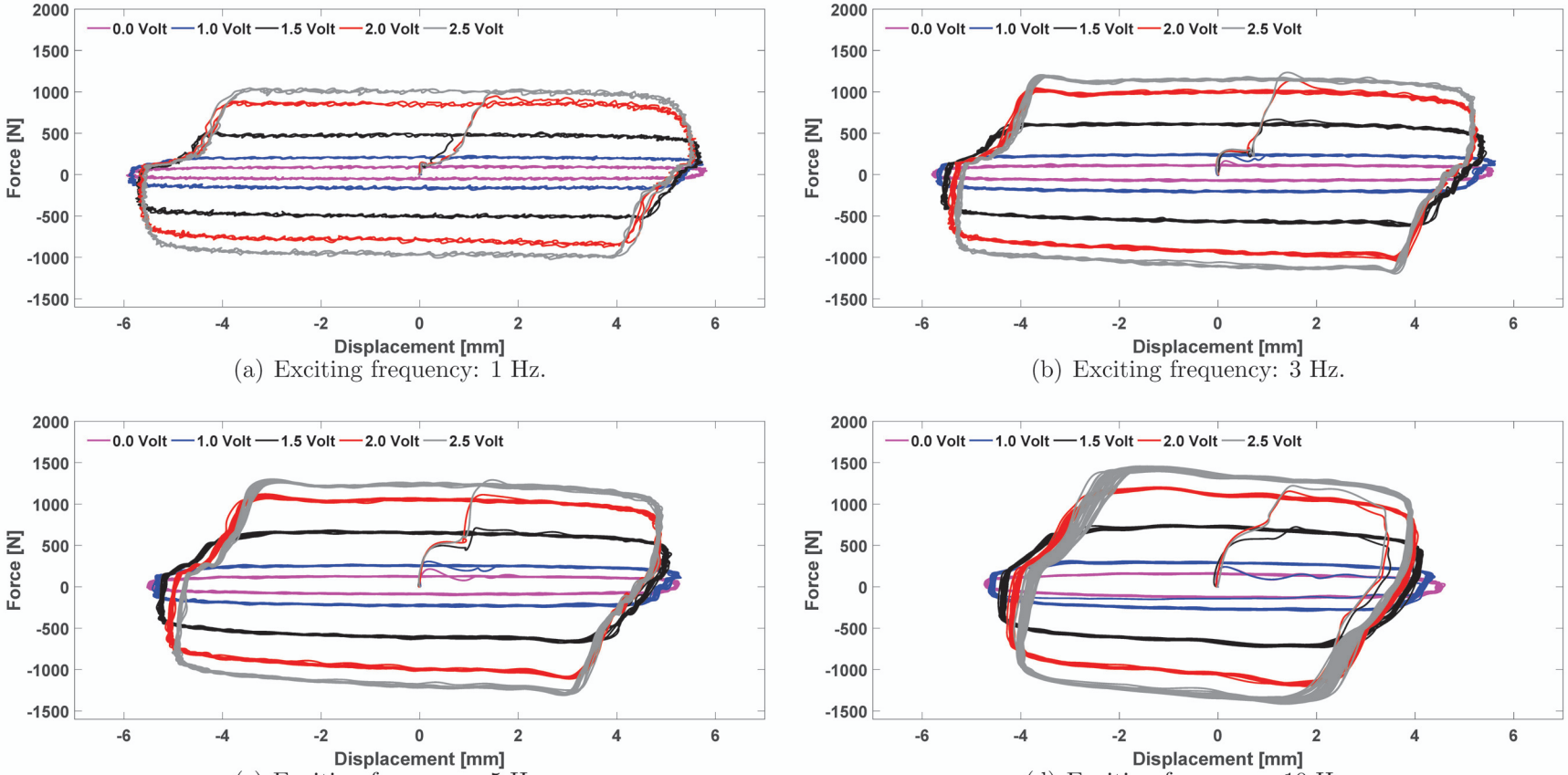

(a) Exciting frequency: 1 Hz.

(b) Exciting frequency: 3 Hz.

(c) Exciting frequency: 5 Hz.

(d) Exciting frequency: 10 Hz.

Fig. 4.36. MR damper characterization behavior: force-displacement profile.

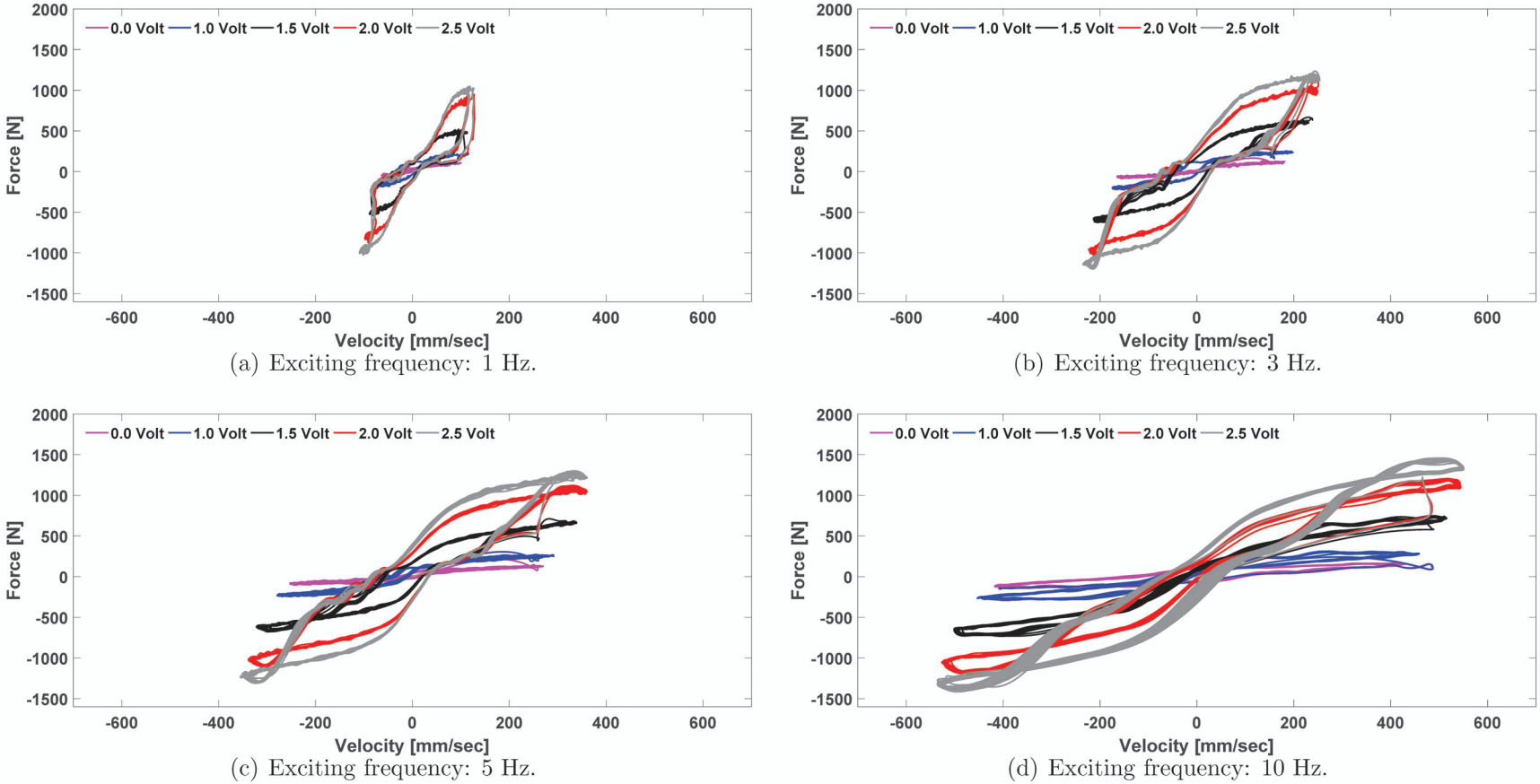

(a) Exciting frequency: 1 Hz.

(b) Exciting frequency: 3 Hz.

(c) Exciting frequency: 5 Hz.

(d) Exciting frequency: 10 Hz.

Fig. 4.37. MR damper characterization behavior: force-velocity profile.

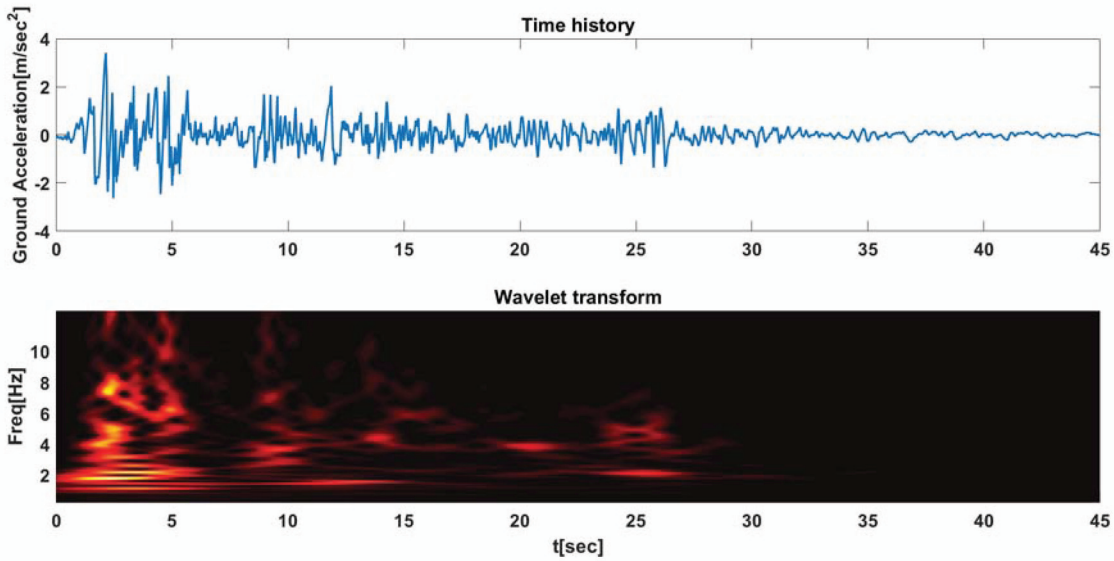

Fig. 4.38. El Centro ground excitation.

Clearly, the tracking performance provided in Table 4.6 and Figures 4.45 and 4.46 show that *SRCSys* is capable of accommodating extensive performance variations and uncertainties in the control plant. This feature can be effectively utilized in designing a high-precision robust transfer system controller while the physical substructure is quite general, for instance an unknown time-varying nonlinear system, or even including structural component failure during the course of RTHS.

Table 4.6.
Normalized error for desired displacement tracking.

	Passive off	**Passive on: 1** V	**Passive on: 1.5** V	**Passive on: 2** V
NE	0.17%	0.25%	0.28%	0.32%

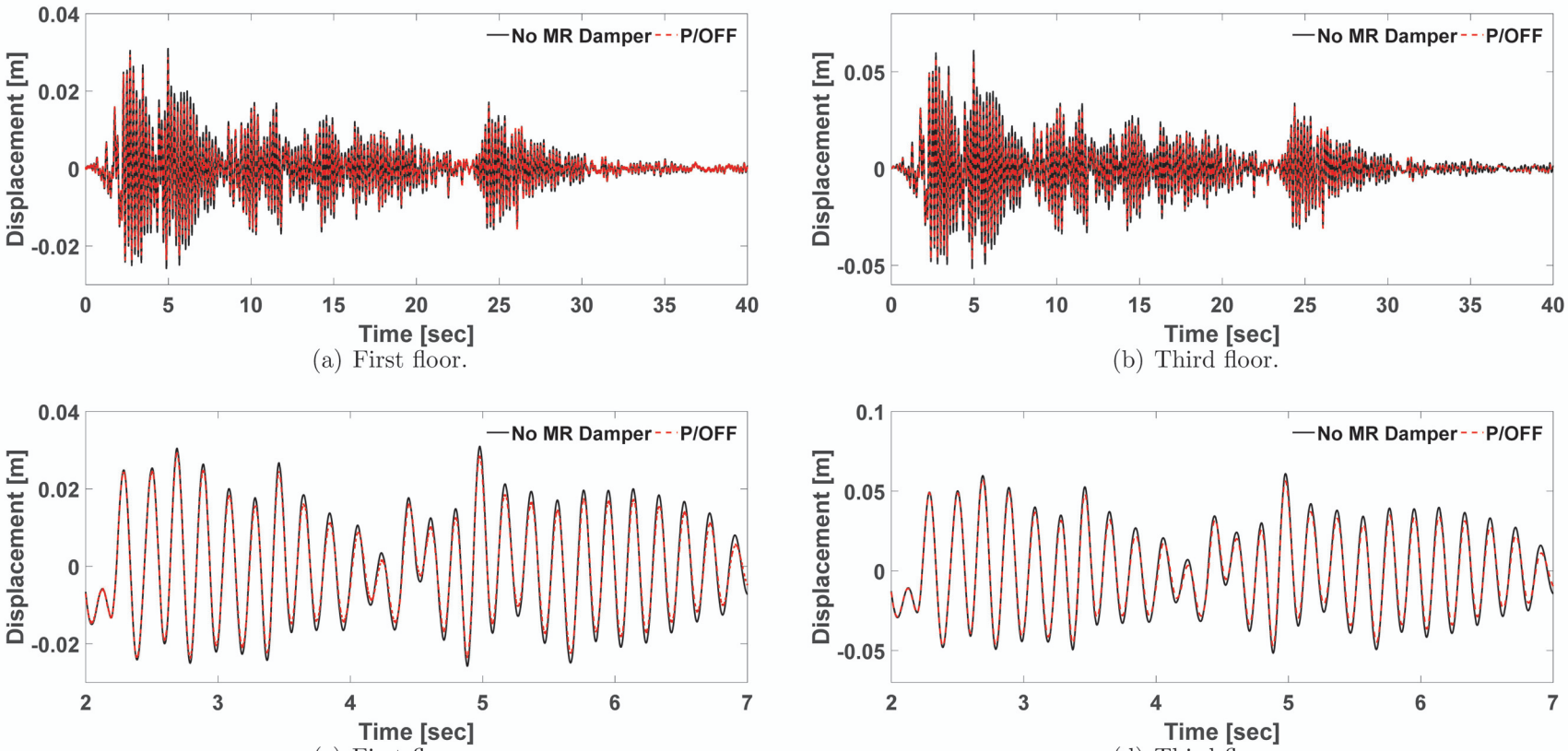

(a) First floor.

(b) Third floor.

(c) First floor.

(d) Third floor.

Fig. 4.39. Comparison of the uncontrolled and passively controlled (passive off) frame responses: first and third floor displacement responses.

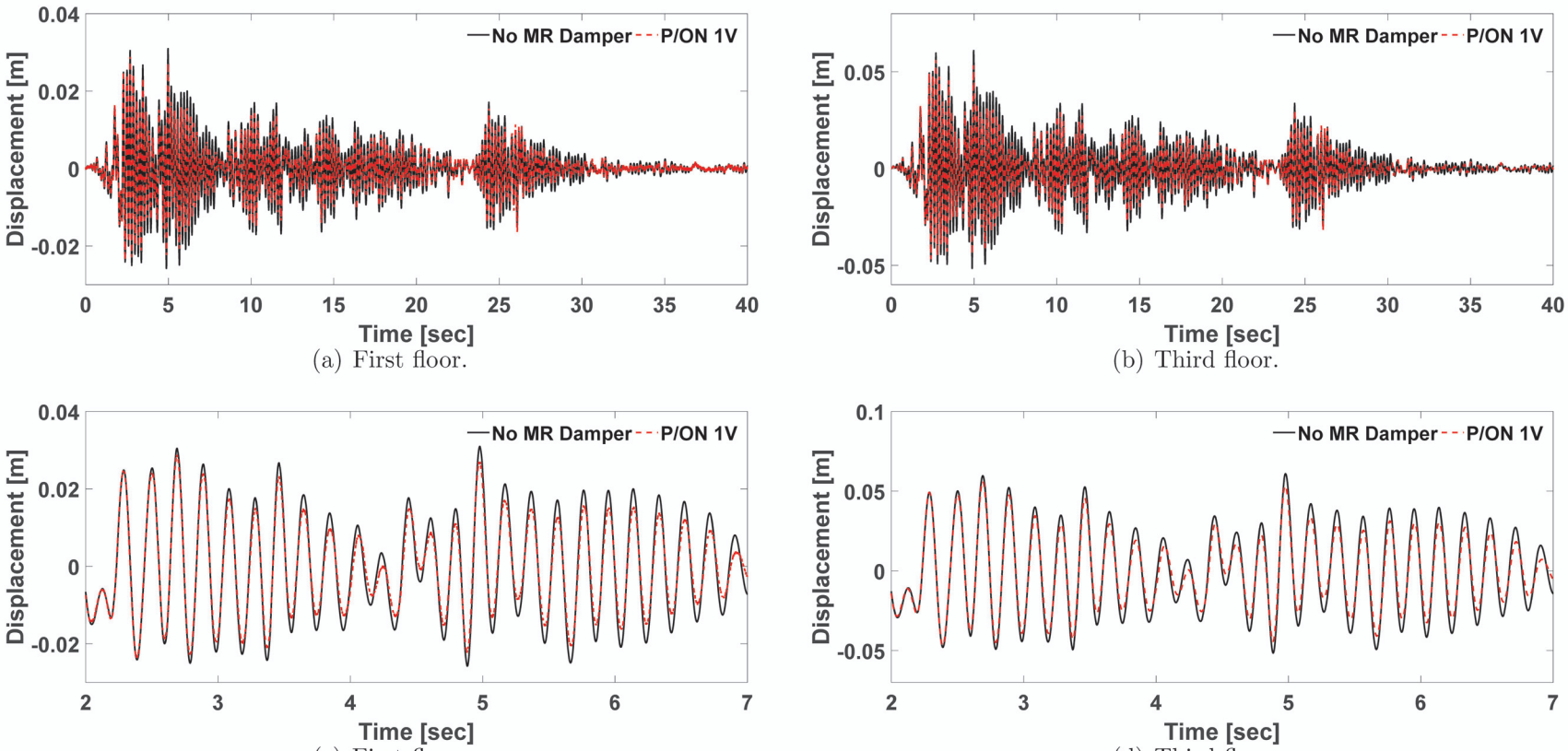

(a) First floor.

(b) Third floor.

(c) First floor.

(d) Third floor.

Fig. 4.40. Comparison of the uncontrolled and passively controlled (passive on, 1 V) frame responses: first and third floor displacement responses.

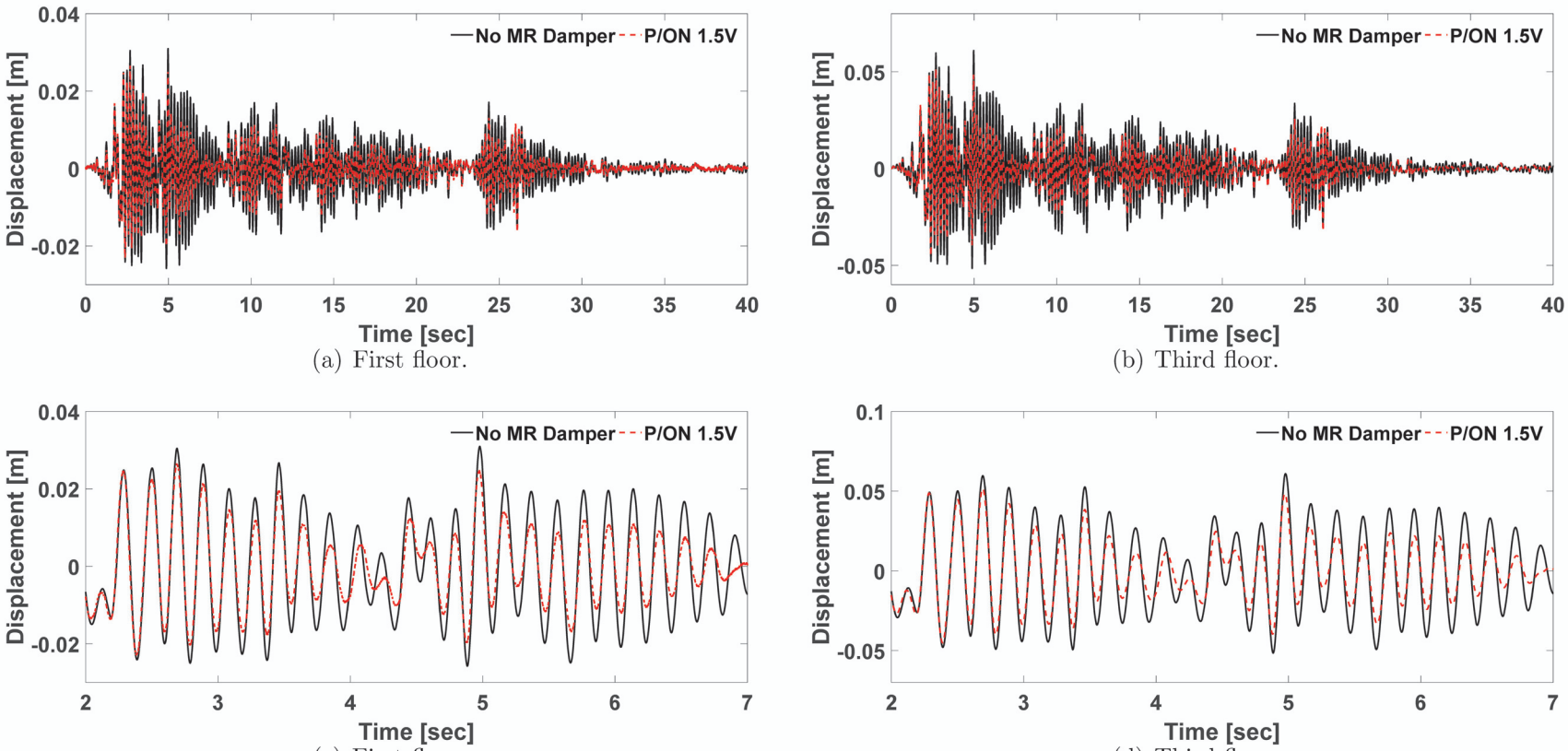

(a) First floor.

(b) Third floor.

(c) First floor.

(d) Third floor.

Fig. 4.41. Comparison of the uncontrolled and passively controlled (passive on, 1.5 V) frame responses: first and third floor displacement responses.

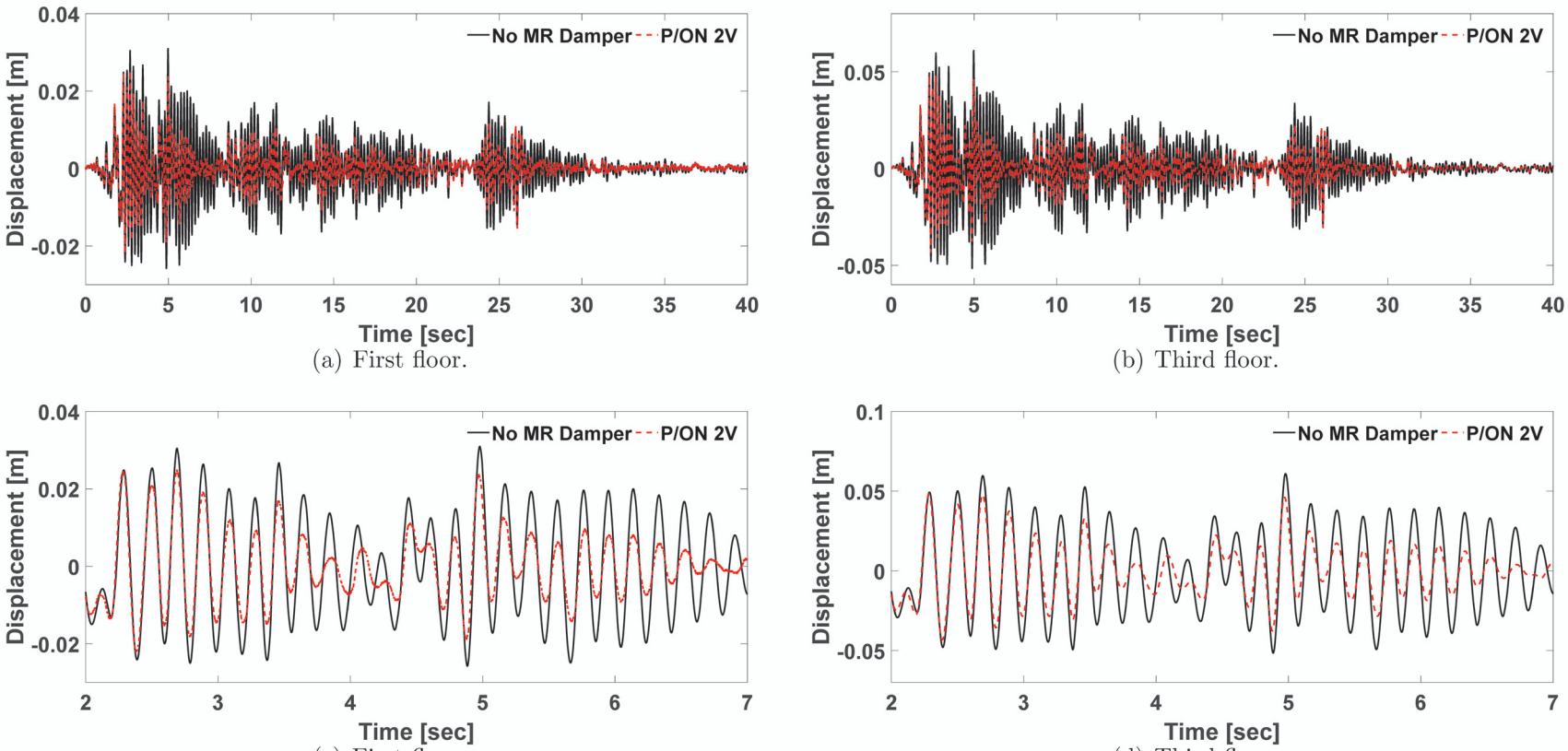

(a) First floor.

(b) Third floor.

(c) First floor.

(d) Third floor.

Fig. 4.42. Comparison of the uncontrolled and passively controlled (passive on, 2 V) frame responses: first and third floor displacement responses.

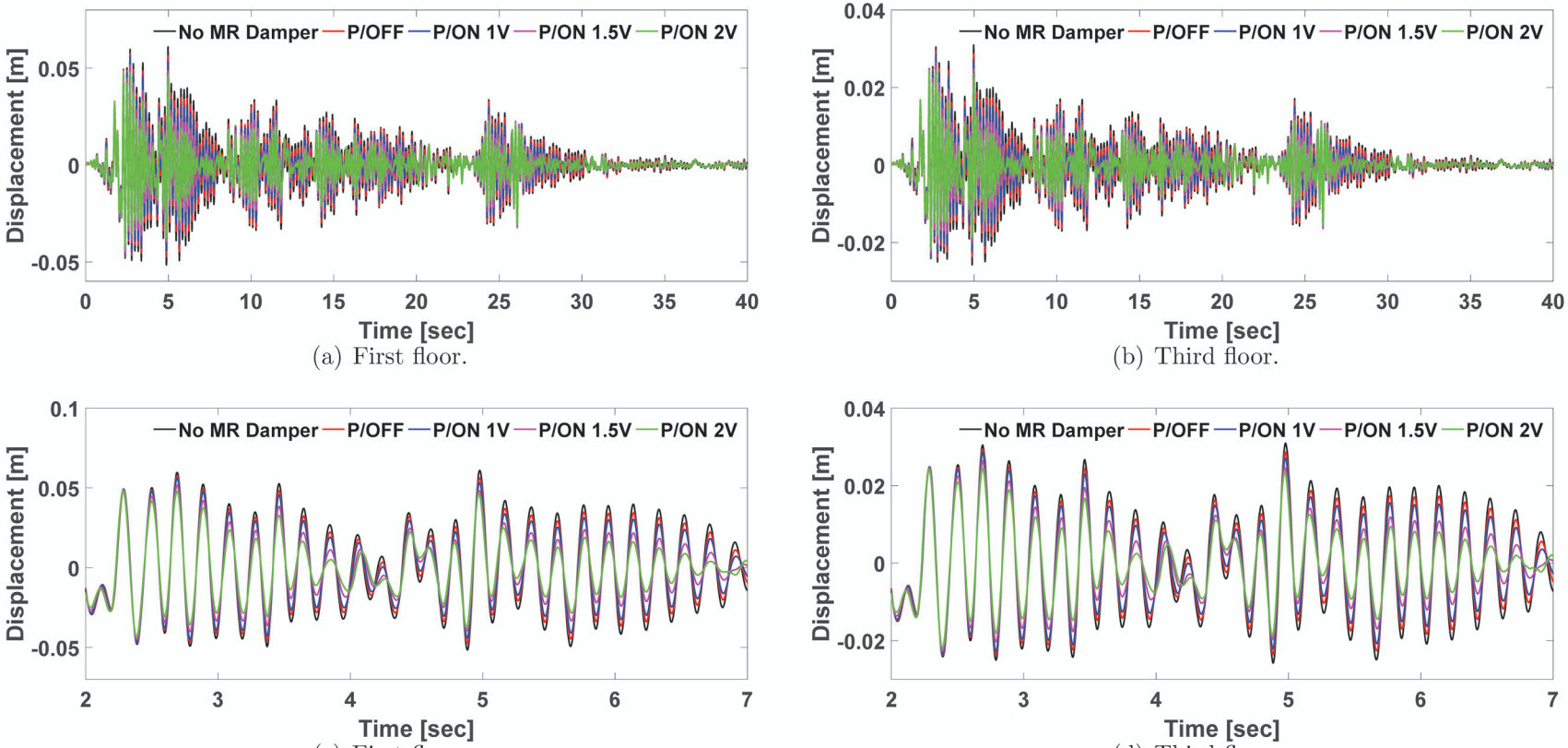

(a) First floor.

(b) Third floor.

(c) First floor.

(d) Third floor.

Fig. 4.43. Comparison of the uncontrolled and passively controlled (passive off and on) frame responses: first and third floor displacement responses.

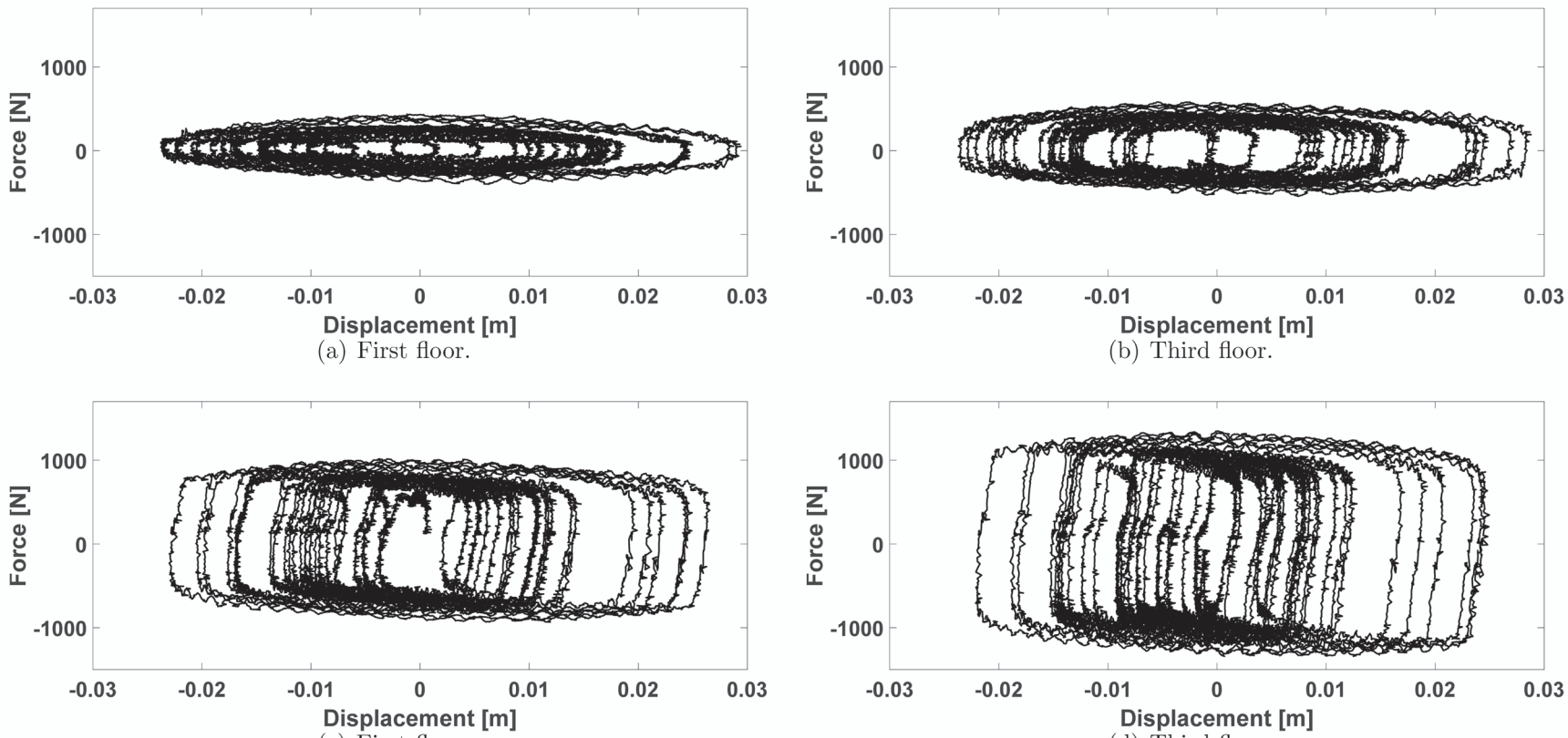

(a) First floor.

(b) Third floor.

(c) First floor.

(d) Third floor.

Fig. 4.44. MR damper force-displacement profiles associated with different input voltages.

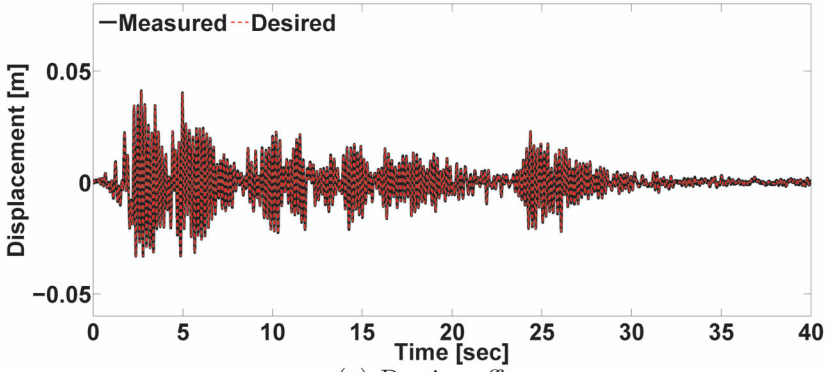

(a) Passive off.

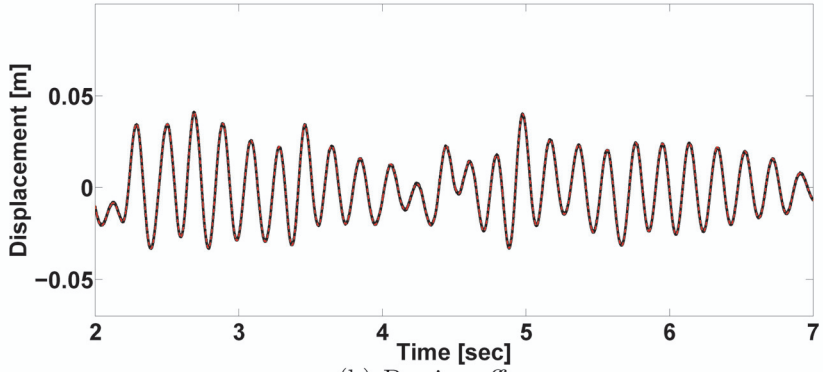

(b) Passive off.

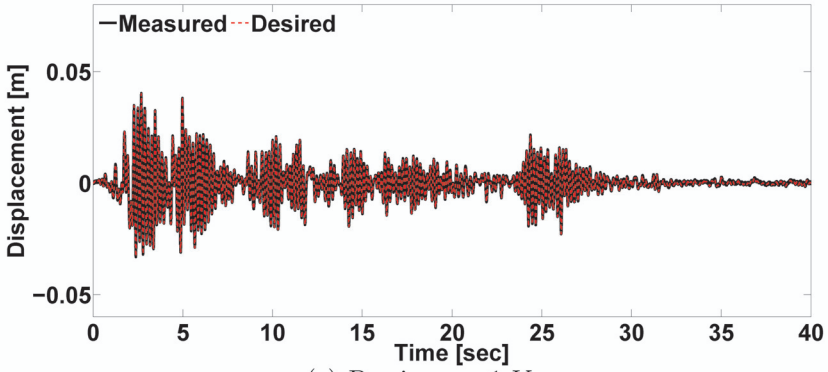

(c) Passive on: 1 V.

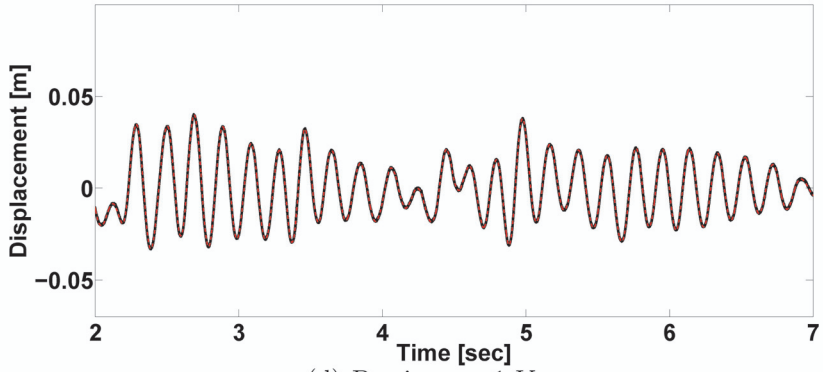

(d) Passive on: 1 V.

Fig. 4.45. Tracking performance during RTHS.

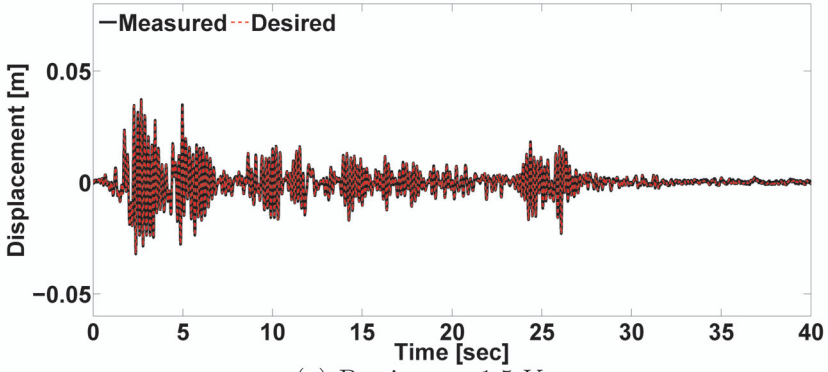

(a) Passive on: 1.5 V.

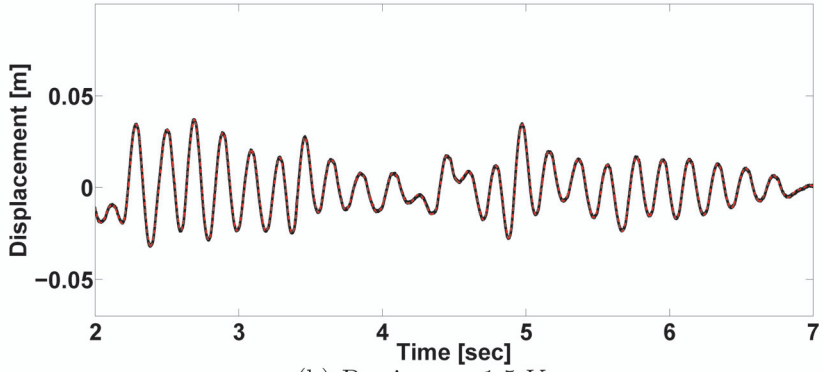

(b) Passive on: 1.5 V.

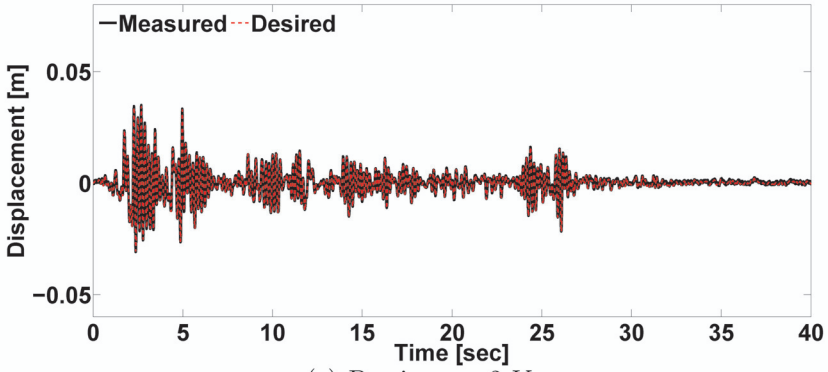

(c) Passive on: 2 V.

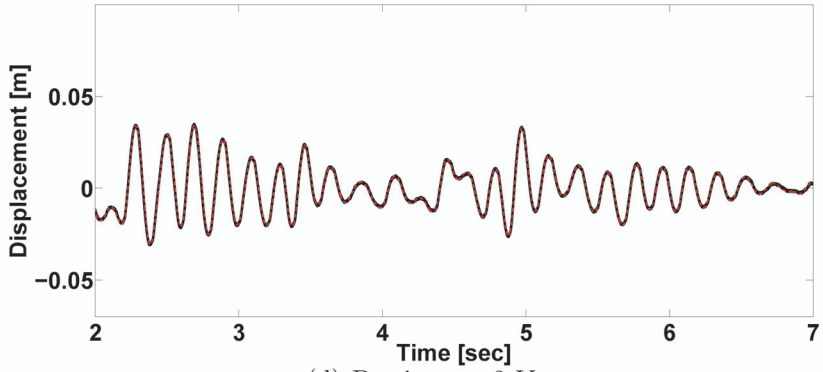

(d) Passive on: 2 V.

Fig. 4.46. Tracking performance during RTHS.

5. SUMMARY AND FUTURE WORK

5.1 Summary

Real-time hybrid simulation is an effective and versatile cyber-physical tool for the examination of complex structural systems with rate dependent behaviors. Although stability and accuracy challenges in getting started with using this mixed computation-testing method, a wide variety of testing can be performed realistically and at lower cost in many cases. In planning an RTHS, it is important to (i) establish clear goals and objectives; (ii) implement with those objectives in mind, and (iii) make decisions and trade-offs along the way. In other words, this dissertation addresses some fundamental questions a researcher should ask prior, during and after implementation of a successful RTHS:

- What options are avaiable in implementing this RTHS with respect to the goals of the experiment?
- From stability and accuracy perspectives, what will be the main challenges in each configuration?
- How well will the results represent reality in each case?
- What adjustments may alleviate the challenges? Or improve the accuracy or fidelity of the experiment?

Considering these questions, it is important to choose the right tools for the task. Based on the goals, the path forward, what tools will meet the needs of the test planned. This research provides a systematic approach to configure a safe, stable and accurate real-time hybrid simulation considering the significance of partitioning configuration, transfer system dynamics, and uncertainty (and nonlinearity) in the

physical substructure. This approach is an effective tool for configuring a successful execution of more challenging experiments.

In RTHS, the interface interaction between the substructures is measured by a sensing system and enforced by a transfer system. Sensing and transfer systems introduce de-synchronization at the interface, including frequency-independent time-delay (caused by communication delay, A/D conversion, and computation delay) and frequency-dependent time-lag (caused by transfer system dynamics and limitations). These added dynamics in the feedback loop can result in instabilities and losses in performance. In implementation of RTHS, stability and accuracy are mainly a function of five conditions,

- overall dynamics of the reference structure
- fidelity of the computational substructure
- integration scheme and time increment
- partitioning configuration
- execution of interface conditions

In Chapter 2, the impacts of condition (1): *overall dynamics of the reference structure* and condition (4): *partitioning configuration* on stability and accuracy of RTHS were discussed. The virtual time delay framework was developed in which the sensitivity of a partitioning choice to interface de-synchronization was studied independent of transfer system dynamics. That this virtual framework is independent of transfer system setup/equipment is a strong advantage of the technique. Later, predictive stability and performance indicators were developed for use with single degree-of-freedom linear and weakly nonlinear systems and multi degree-of-freedom linear systems. A novel matrix method was explained to convert the delay differential equation (i.e., the virtual time delay framework) to a generalized eigenvalue problem using a set of vectorization mappings, and then to analytically solve the delay differential equations in a computationally efficient way. These predictive indicators map

a configuration choice to a measure which can be associated with minimum control requirements for a successful execution and identify how realistic experimental results are in the absence of a reference response. Some advantages of this approach are:

- a detailed model of the components is not needed,
- it is independent of the equipment or controller designs, and
- it is useful for distributed and multi-rate testing.

Chapters 3 and 4 mainly discussed condition (5): *execution of interface conditions*. In Chapter 3, a nonlinear dynamical model for a hydraulic transfer system coupled with a linear/nonlinear physical specimen was developed. An identification technique to obtain the parameters associated with the dynamical model. The nonlinear dynamical model was further transformed into the controllable canonical form which gives a researcher an enormous advantage in terms of synthesizing an effective servo-hydraulic actuator controller, especially if the physical specimen behaves nonlinear. For successful implementation of RTHS, this dynamical model enables researchers to design an effective transfer system controller/compensator and to configure a partitioning configuration with suitable properties. Finally, a series of experiments were conducted to investigate the natural coupling present between the hydraulic transfer system and the physical specimen. For linear and nonlinear physical specimens, experimental and simulated responses were compared to validate the dynamical model.

In Chapter 4, the hydraulic control plant in the Chapter 3 is used to develop a high-precision multi-layer nonlinear control system (*Self-tuning Robust Control System*) which accommodates extensive performance variations and uncertainties in the physical substructure. *Self-tuning Robust Control System* consists of two layers: robustness and adaptation. The robustness layer will synthesize a nonlinear control law such that the closed-loop dynamics withstands the extensive parametric and non-parametric uncertainties. Sliding mode control is employed as the control scheme in this layer. Then the adaptation law reduces parametric uncertainties through

run-time, slow and controlled learning of the physical plant based on measured performance.

In Chapter 4, a nonlinear control system was developed for the physical plant (transfer system and physical substructure) using the dynamical model developed in Chapter 3. The dynamical model shows that lack of/limited understanding about the dynamics of the physical substructure (which is the case in RTHS) and change in the dynamic characteristics of the physical substructure during an experiment (e.g., post yield behavior and dynamic destructive testing) impose significant transfer system control challenges in RTHS. Thus, in this chapter, *Self-tuning Robust Control System* was developed which is a multi-layer nonlinear control system designed to accommodate extensive performance variations and uncertainties in the physical plant. The mathematical derivation of *SRCSys* is based on *Barbalats lemma* and *invariant set theory*. *Self-tuning Robust Control System* consists of two layers: robustness and adaptation. In the layer of robustness, sliding mode control was employed to synthesize a nonlinear control law such that the overall dynamical system of this layer withstands unmodeled dynamics and uncertainties while tracking the desired trajectory. In the second layer, the objective was to consistently improve tracking performance through run-time, slow and controlled learning of the physical plant.

5.2 Future Work

Real-time hybrid simulation has the potential to transform the design, optimization and validation of complex structural systems. RTHS promotes deeper investigations into ambiguity and uncertainty in such systems by isolating the more ambiguous section of the system in the physical substructure. Future efforts should be made toward examination of *complex nonlinear structural systems* by developing an adaptive robust RTHS platform for experimental design, optimization and validation of such systems. A complex nonlinear structural system is a nonlinear system consists of several interconnected subsystems. The emergent behavior of such systems cannot

be clearly understood when one considers only the subsystems. For example the behavior of targeted energy transfer (TET) systems, advanced monitoring and control systems, soil-structure interaction, and human-structure interaction cannot be really understood when the subsystems are examined in isolation.

This dissertation has addressed some challenges in implementation of a successful RTHS. A number of exciting research avenues still exist:

- The predictive indicators have already been applied to SDOF linear and weakly nonlinear systems and MDOF linear systems. These indicators should be extended to MDOF nonlinear systems.

- In the near future, RTHS will be implemented to evaluate the performance of complex MDOF nonlinear systems with rate dependent behaviors. For more complex experiments in this class, multiple actuators are required to enforce the boundary conditions at the interfaces. Thus, *SRCSys* should be extended to an integrated nonlinear multi-actuator control system.

- In a number of experimental studies, the predictive indicators should be used for more challenging RTHS cases in which stability is the critical concern, such as multi-rate RTHS or geographically distributed RTHS.

- In the case of using a high-fidelity finite element model in the computational substructure, the desired displacement at the interface usually contains high-frequency signals. Thus, for this case, tracking performance of *SRCSys* should be experimentally evaluated.

REFERENCES

REFERENCES

[1] S. J. Dyke, B. Stojadinovic, P. Arduino, M. Garlock, N. Luco, J. A. Ramirez, and S. Yim, "2020 Vision for Earthquake Engineering Research: Report on an OpenSpace Technology Workshop on the Future of Earthquake Engineering," vol. 20, no. 5, 2010. [Online]. Available: http://nees.org/resources/1636

[2] G. Mosqueda, B. Stojadinovic, and S. Mahin, "Implementation and Accuracy of Continuous Hybrid Simulation with Geographically Distributed Substructures," Tech. Rep. November, 2005. [Online]. Available: http://research.eerc.berkeley.edu/nees/Events/200604a–workshop-hybridsim/workshop-materials/HSW-EERCreport-Hybrid02.pdf

[3] A. Schellenberg and S. Mahin, "Integration of Hybrid Simulation within the General-purpose Computational Framework OpenSees," *Proc. of 100th Anniversary Earthquake Conference*, 2006.

[4] L. Dihoru and A. Bonzi, "Performance Requirements of Actuation Systems for Shaking Table and Pseudo-Dynamic Testing," *Deliverable D12.1, SERIES: Seismic Engineering Research Infrastructures for European Synergies.*, 2010.

[5] P. B. Shing, M. Nakashima, and O. S. Bursi, "Application of Psuedodynamic Test Method to Structural Research," *Earthquake Spectra*, vol. 12(1), pp. 29–56, 1996.

[6] M. Nakashima, H. Kato, and E. Takaoka, "Development of real-time pseudo dynamic testing," *Earthquake Engineering & Structural Dynamics*, vol. 21, no. 1, pp. 79–92, 1992.

[7] J. E. Carrion and B. F. Spencer, Jr., "Model-based Strategies for Real-time Hybrid Testing," NSEL-006, UIUC, Urbana-Champaign, Tech. Rep., 2007.

[8] P. B. Shing and S. A. Mahin, "Pseudodynamic Test Method for Seismic Performance Evaluation: Theory and Implementation," 1984.

[9] C. Chen, J. M. Ricles, T. L. Karavasilis, Y. Chae, and R. Sause, "Evaluation of a Real-time Hybrid Simulation System for Performance Evaluation of Structures with Rate Dependent Devices Subjected to Seismic Loading," *Engineering Structures*, vol. 35, pp. 71–82, feb 2012.

[10] S. A. Mahin and P. B. Shing, "Pseudodynamic Method for Seismic Testing," *Journal of Structural Engineering*, vol. 111, no. 7, pp. 1482–1503, jul 1985. [Online]. Available: http://ascelibrary.org/doi/10.1061/%28ASCE%290733-9445%281985%29111%3A7%281482%29

[11] D. J. Wagg and D. P. Stoten, "Substructuring of Dynamical Systems via the Adaptive Minimal Control Synthesis Algorithm," *Earthquake Engineering & Structural Dynamics*, vol. 30, no. 6, pp. 865–877, jun 2001.

[12] M. Hakuno, M. Shidawara, and T. Hara, "Dynamic destructive test of a cantilever beam, controlled by an analog-computer," *Trans. Japan Soc. Civil Eng.*, vol. 171, pp. 1–9, 1969.

[13] S. A. Mahin and M. E. Williams, "Computer Controlled Seismic Performance Testing," in *Second ASCE-EMD Specialty Conference on Dynamic Response of Structure*, Atlanta, GA, 1981.

[14] K. Takanashi and K. Ohi, "Earthquake response analysis of steel structures by rapid computer-actuator on-line system, A progress report, trial system, and dynamic response of steel beams." University of Tokyo, Tokyo, Japan, Tech. Rep., 1983.

[15] K. Takanashi and M. Nakashima, "Japanese Activities on OnLine Testing," *Journal of Engineering Mechanics*, vol. 113, no. 7, pp. 1014–1032, jul 1987.

[16] S. A. Mahin, P. B. Shing, C. R. Thewalt, and R. D. Hanson, "Pseudodynamic Test MethodCurrent Status and Future Directions," *Journal of Structural Engineering*, vol. 115, no. 8, pp. 2113–2128, aug 1989.

[17] J. Dimig, C. Shield, C. French, F. Bailey, and A. Clark, "Effective Force Testing: A Method of Seismic Simulation for Structural Testing," *Journal of Structural Engineering*, vol. 125, no. 9, pp. 1028–1037, sep 1999.

[18] B. Spencer, A. Elnashai, N. Nakata, H. Saliem, and G. Yang, "The MOST Experiment: Earthquake Engineering on the Grid," NEESgrid, Tech. Rep., 2004.

[19] S. J. Kim, R. Christenson, B. Phillips, and B. F. Spencer, Jr., "Geographically Distributed Real-Time Hybrid Simulation of MR Dampers for Seismic Hazard Mitigation," in *20th Analysis and Computation Specialty Conference*. Reston, VA: American Society of Civil Engineers, mar 2012, pp. 382–393. [Online]. Available: http://ascelibrary.org/doi/abs/10.1061/9780784412374.034

[20] A. Maghareh, S. Dyke, A. Prakash, and J. Rhoads, "Establishing a stability switch criterion for effective implementation of real-time hybrid simulation," *Smart Structures and Systems*, vol. 14, no. 6, 2014.

[21] A. Maghareh, S. Dyke, A. Prakash, and G. Bunting, "Establishing a predictive performance indicator for real-time hybrid simulation," *Earthquake Engineering and Structural Dynamics*, vol. 43, no. 15, 2014.

[22] A. Maghareh, F. Lin, S. J. Dyke, and A. Prakash, "Development of New Predictive Stability and Performance Metrics for Real-time Hybrid Simulation," 2014. [Online]. Available: https://nees.org/warehouse/project/1205/

[23] A. Maghareh, S. J. Dyke, and S. RabieniaHaratbar, "Use of predictive stability indicator in implementation of real-time hybrid simulations," in *Sixth World Conference on Structural Control and Monitoring (6th WCSCM)*, Barcelona, Spain, 2014.

[24] A. Maghareh, S. Dyke, S. Rabieniaharatbar, and A. Prakash, "Predictive stability indicator: a novel approach to configuring a real-time hybrid simulation," *Earthquake Engineering & Structural Dynamics*, vol. 46, no. 1, pp. 95–116, jan 2017.

[25] A. Maghareh, C. E. Silva, and S. J. Dyke, "Servo-hydraulic Actuator in Controllable Canonical Form: Identification and Experimental Validation," *Mechanical Systems and Signal Processing*, 2017.

[26] D. Ferry, A. Maghareh, G. Bunting, A. Prakash, K. Agrawal, C. Gill, C. Lu, and S. J. Dyke, "CyberMech: A Highly Parallel Concurrency Platform for Enhancing Performance of Real-time Hybrid Simulations, Engineering Structures," *Engineering Structures, (submitted January 2016)*.

[27] D. Ferry, J. Li, M. Mahadevan, K. Agrawal, C. D. Gill, and C. Lu, "A Real-Time Scheduling Service for Parallel Tasks," *IEEE Real-Time and Embedded Technology and Applications Symposium (RTAS'13)*, 2013.

[28] A. Maghareh, J. P. Waldbjørn, S. J. Dyke, A. Prakash, and A. I. Ozdagli, "Adaptive multi-rate interface: development and experimental verification for real-time hybrid simulation," *Earthquake Engineering & Structural Dynamics*, vol. 45, no. 9, pp. 1411–1425, jul 2016.

[29] A. P. Darby, M. S. Williams, and A. Blakeborough, "Stability and Delay Compensation for Real-Time Substructure Testing," *Journal of Engineering Mechanics*, vol. 128, no. 12, pp. 1276–1284, dec 2002.

[30] G. Mosqueda, B. Stojadinovic, and S. A. Mahin, "Real-Time Error Monitoring for Hybrid Simulation. Part I: Methodology and Experimental Verification," *Journal of Structural Engineering*, vol. 133, no. 8, pp. 1100–1108, aug 2007. [Online]. Available: http://ascelibrary.org/doi/abs/10.1061/(ASCE)0733-9445(2007)133:8(1100)

[31] G. Mosqueda, B. Stojadinovic, and S. Mahin, "Real-Time Error Monitoring for Hybrid Simulation. Part II: Structural Response Modification due to Errors," *Journal of Structural Engineering*, vol. 133, no. 8, pp. 1109–1117, 2007.

[32] C. Chen and J. M. Ricles, "Analysis of Actuator Delay Compensation Methods for Real-time Testing," *Engineering Structures*, vol. 31, no. 11, pp. 2643–2655, nov 2009.

[33] X. Gao, "Development of a Robust Framework for Real-Time Hybrid Simulation: from Dynamical System, Motion Control to Experimental Error Verification," 2012. [Online]. Available: http://nees.org/resources/5065

[34] C. Chen, J. Valdovinos, and H. Santiallno, "Reliability Assessment of Real-Time Hybrid Simulation Results for Seismic Hazard Mitigation," *Proc. of Structures Congress 2013*, pp. 2346–2357, apr 2013.

[35] A. Maghareh, S. J. Dyke, G. Ou, and Y. Qian, "Investigation of uncertainties associated with actuation modeling error and sensor noise on real time hybrid simulation performance," in *2013 International Conference on Computing, Networking and Communications, ICNC 2013*, 2013.

[36] J. Li, D. Ferry, K. Kieselbach, A. Saifullah, K. Agrawal, C. D. Gill, and C. Lu, "Practical Real-time Scheduling for Parallel Tasks from Theory to Platform," 2013. [Online]. Available: http://prt.cse.wustl.edu/

[37] T. Horiuchi, M. Inoue, T. Konno, and W. Yamagishi, "Development of a Real-time Hybrid Experimental System Using a Shaking Table (Proposal of Experimental Concept and Feasibility Study with Rigid Secondary System)," *JSME International*, vol. 42, no. 2, pp. 255–264, 1999.

[38] R. Christenson, S. Dyke, J. Zhang, G. Mosqueda, C. Chen, N. Nakata, P. Laplace, W. Song, Y. Chae, G. A. Marshall, G. Ou, C. Riascos, and C. Song, "Hybrid Simulation: A Discussion of Current Assessment Measures," NEEShub, Tech. Rep., 2014. [Online]. Available: https://nees.org/resources/13416

[39] N. Nakata, S. J. Dyke, J. Zhang, G. Mosqueda, X. Shao, H. Mahmoud, M. H. Head, M. E. Bletzinger, G. A. Marshall, G. Ou, and C. Song, "Hybrid Simulation Primer and Dictionary," NEEShub, Tech. Rep., 2014. [Online]. Available: https://nees.org/resources/7703

[40] X. Shao, A. M. Reinhorn, and M. V. Sivaselvan, "Real-Time Hybrid Simulation Using Shake Tables and Dynamic Actuators," *Journal of Structural Engineering*, vol. 137, no. 7, pp. 748–760, jul 2011. [Online]. Available: http://ascelibrary.org/doi/10.1061/%28ASCE%29ST.1943-541X.0000314

[41] S. J. Dyke, B. F. Spencer Jr., P. Quast, and M. K. Sain, "Role of Control-Structure Interaction in Protective System Design," *Journal of Engineering Mechanics*, vol. 121, no. 2, pp. 322–338, feb 1995.

[42] C. W. de Silva, *Control Sensors and Actuators*. Broken Sound Parkway, NW: Taylor & Francis Group, LLC, 2007.

[43] J. Zhao, C. French, C. Shield, and T. Posbergh, "Considerations for the Development of Real-time Dynamic Testing Using Servo-hydraulic Actuation," *Earthquake Engineering & Structural Dynamics*, vol. 32, no. 11, pp. 1773–1794, sep 2003.

[44] R. Christenson, Y. Z. Lin, A. Emmons, and B. Bass, "Large-Scale Experimental Verification of Semiactive Control through Real-Time Hybrid Simulation1," *Journal of Structural Engineering*, vol. 134, no. 4, pp. 522–534, apr 2008. [Online]. Available: http://ascelibrary.org/doi/pdf/10.1061/(ASCE)0733-9445(2008)134%3A4(522) http://ascelibrary.org/doi/abs/10.1061/%28ASCE%290733-9445%282008%29134%3A4%28522%29

[45] M. I. Wallace, J. Sieber, S. A. Neild, D. J. Wagg, and B. Krauskopf, "Stability Analysis of Real-time Dynamic Substructuring Using Delay Differential Equation Models," *Earthquake Engineering & Structural Dynamics*, vol. 34, no. 15, pp. 1817–1832, dec 2005.

[46] E. Beretta and Y. Kuang, "Geometric Stability Switch Criteria in Delay Differential Systems with Delay Dependent Parameters," *SIAM Journal on Mathematical Analysis*, vol. 33, no. 5, pp. 1144–1165, jan 2002.

[47] N. MacDonald, "Biological Delay Systems: Linear Stability Theory," 1989.

[48] K. J. Astrom and B. Wittenmark, "Computer-controlled Systems: Theory and Design," 1990.

[49] M. Ahmadizadeh, "Real-time Seismic Hybrid Simulation Procedures for Reliable Structural Performance Testing," 2007.

[50] T. Horiuchi, M. Nakagawa, M. Sugano, and T. Konno, "Development of a real-time hybrid experimental system with actuator delay compensation," *Proc. 11th World Conf. Earthquake Engineering*, 1996.

[51] A. Mueller, C. Griffith, X. Shao, and G. Enyart, "A Benchmark Testing System for Real-Time Hybrid Simulation Development," in *Structures Congress 2013*. Reston, VA: American Society of Civil Engineers, apr 2013, pp. 2370–2381. [Online]. Available: http://ascelibrary.org/doi/abs/10.1061/9780784412848.207

[52] J. A. Franco, R. M. Botelho, and R. E. Christenson, "Effective Control of a Six Degree of Freedom Shake Table," in *Dynamics of Coupled Structures*. Springer International Publishing, 2015, pp. 19–29. [Online]. Available: http://link.springer.com/10.1007/978-3-319-15209-7_3

[53] A. J. Friedman, S. J. Dyke, B. Phillips, R. Ahn, B. Dong, Y. Chae, N. Castaneda, Z. Jiang, J. Zhang, Y. Cha, A. I. Ozdagli, B. F. Spencer, J. Ricles, R. Christenson, A. Agrawal, and R. Sause, "Large-Scale Real-Time Hybrid Simulation for Evaluation of Advanced Damping System Performance," *Journal of Structural Engineering*, vol. 141, no. 6, p. 04014150, jun 2015.

[54] Y. Chae, J. M. Ricles, and R. Sause, "Real-time hybrid simulations of a 3-story steel frame building with magneto-rheological dampers subject to strong ground motions," in *Behaviour of Steel Structures in Seismic Areas: STESSA 2012*, F. Mazzolani and R. Herrera, Eds. CRC Press, Inc., 2012.

[55] B. Dong, R. Sause, and J. M. Ricles, "Accurate real-time hybrid earthquake simulations on large-scale MDOF steel structure with nonlinear viscous dampers," *Earthquake Engineering & Structural Dynamics*, vol. 44, no. 12, pp. 2035–2055, sep 2015. [Online]. Available: http://doi.wiley.com/10.1002/eqe.2572

[56] Y. Cha, A. K. Agrawal, A. Friedman, B. Phillips, R. Ahn, B. Dong, S. J. Dyke, B. F. Spencer, J. Ricles, and R. Christenson, "Performance Validations of Semiactive Controllers on Large-Scale Moment-Resisting Frame Equipped with 200-kN MR Damper Using Real-Time Hybrid Simulations," *Journal of Structural Engineering*, vol. 140, no. 10, p. 04014066, 2014. [Online]. Available: http://ascelibrary.org/doi/10.1061/%28ASCE%29ST.1943-541X.0000982

[57] B. M. Phillips and B. F. Spencer, "Model-Based Multiactuator Control for Real-Time Hybrid Simulation," *Journal of Engineering Mechanics*, vol. 139, no. 2, pp. 219–228, feb 2013.

[58] J. Louisell, "A matrix method for determining the imaginary axis eigenvalues of a delay system," *IEEE Transactions on Automatic Control*, vol. 46, no. 12, pp. 2008–2012, 2001.

[59] J. E. Marshall, H. Gorecki, A. Korytowski, and K. Walton, *Time-Delay Systems: Stability and Performance Criteria With Applications*. New York: Ellis Horwood, 1992.

[60] B. M. Phillips, "Model-based Feedforward-feedback Control for Real-time Hybrid Simulation of Large-scale Structures," Ph.D. dissertation, University of Illinois at Urbana-Champaign, 2012.

[61] A. J. Friedman, "Development and Experimental Validation of a New Control Strategy Considering Device Dynamics for Large-Scale MR Dampers using Real-Time Hybrid Simulation," Ph.D. dissertation, Purdue University, 2012.

[62] J. T. Kim, J. S. Cho, B. Y. Park, S. Park, and Y. Lee, "Experimental investigation on the design of leg for a hydraulic actuated quadruped robot," in *IEEE ISR 2013*. IEEE, oct 2013, pp. 1–5.

[63] J. W. Raade and H. Kazerooni, "Analysis and Design of a Novel Hydraulic Power Source for Mobile Robots," *IEEE Transactions on Automation Science and Engineering*, vol. 2, no. 3, pp. 226–232, jul 2005.

[64] C. Ahn, B. Kim, and M. Lee, "Modeling and control of an anti-lock brake and steering system for cooperative control on split-mu surfaces," *International Journal of Automotive Technology*, vol. 13, no. 4, pp. 571–581, jun 2012.

[65] M. Wu and M. Shih, "Simulated and experimental study of hydraulic anti-lock braking system using sliding-mode PWM control," *Mechatronics*, vol. 13, no. 4, pp. 331–351, may 2003.

[66] N. Mohajer, H. Abdi, K. Nelson, and S. Nahavandi, "Vehicle motion simulators, a key step towards road vehicle dynamics improvement," *Vehicle System Dynamics*, vol. 53, no. 8, pp. 1204–1226, aug 2015.

[67] W. Sun, H. Gao, and B. Yao, "Adaptive Robust Vibration Control of Full-Car Active Suspensions With Electrohydraulic Actuators," *IEEE Transactions on Control Systems Technology*, vol. 21, no. 6, pp. 2417–2422, nov 2013.

[68] A. C. Pickard, G. Sumner, G. P. Tilly, D. M. Waters, and D. Webber, *Full-Scale Fatigue Testing of Components and Structures*, K. Marsh, Ed. London: Butterworth & Co., 1988.

[69] M. D. Symans and M. C. Constantinou, "Semi-active control systems for seismic protection of structures: a state-of-the-art review," *Engineering Structures*, vol. 21, no. 6, pp. 469–487, jun 1999.

[70] L. M. Jansen and S. J. Dyke, "Semiactive Control Strategies for MR Dampers: Comparative Study," *Journal of Engineering Mechanics*, vol. 126, no. 8, pp. 795–803, aug 2000.

[71] N. Nakata, "Effective Force Testing Using a Robust Loop Shaping Controller," *Earthquake Engineering & Structural Dynamics*, vol. 42, no. 2, pp. 261–275, feb 2013.

[72] J. Kuehn, D. Epp, and W. N. Patten, "High-fidelity control of a seismic shake table," *Earthquake Engineering & Structural Dynamics*, vol. 28, no. 11, pp. 1235–1254, nov 1999.

[73] O. Ozcelik, J. P. Conte, and J. E. Luco, "Virtual Model of the UCSD-NEES High Performance Outdoor Shake Table," in *4th World Conference on Structural Control and Monitoring*, San Diego, USA, 2006.

[74] O. Mercan and J. M. Ricles, "Experimental Studies on Real-Time Testing of Structures with Elastomeric Dampers," *Journal of Structural Engineering*, vol. 135, no. 9, pp. 1124–1133, 2009.

[75] D. Gomez, S. J. Dyke, and A. Maghareh, "Enabling role of hybrid simulation in advancing earthquake engineering," *Journal of Smart Structures and Systems*, vol. 15, no. 3, pp. 913–929, 2015.

[76] C. Chen and J. M. Ricles, "Tracking Error-Based Servohydraulic Actuator Adaptive Compensation for Real-Time Hybrid Simulation," pp. 432–440, 2010.

[77] G. Ou, A. I. Ozdagli, S. J. Dyke, and B. Wu, "Robust integrated actuator control: experimental verification and real-time hybrid-simulation implementation," *Earthquake Engineering & Structural Dynamics*, vol. 44, no. 3, pp. 441–460, mar 2015.

[78] B. M. Phillips, S. Takada, B. F. Spencer, and Y. Fujino, "Feedforward actuator controller development using the backward-difference method for real-time hybrid simulation," *Smart Structures and Systems*, vol. 14, no. 6, pp. 1081–1103, 2014.

[79] H. E. Merritt, *Hydraulic Control Systems*. New York: John Wiley & Sons, 1967.

[80] D. H. Kim and T. Tsao, "A Linearized Electrohydraulic Servovalve Model for Valve Dynamics Sensitivity Analysis and Control System Design," *Journal of Dynamic Systems, Measurement, and Control*, vol. 122, no. 1, p. 179, 2000.

[81] A. Plummer, "Control techniques for structural testing: a review," *Proceedings of the Institution of Mechanical Engineers, Part I: Journal of Systems and Control Engineering*, vol. 221, no. 2, pp. 139–169, jan 2007.

[82] J. E. Slotine and W. Li, *Applied Nonlinear Control*. New Jersey: Pearson Education, 1991.

[83] Y. Qian, G. Ou, A. Maghareh, and S. J. Dyke, "Parametric identification of a servo-hydraulic actuator for real-time hybrid simulation," *Mechanical Systems and Signal Processing*, apr 2014. [Online]. Available: http://www.sciencedirect.com/science/article/pii/S0888327014000764

[84] D. P. Stoten, "A comparative study and unification of two methods for controlling dynamically substructured systems," *Earthquake Engineering & Structural Dynamics*, vol. 46, no. 2, pp. 317–339, feb 2017.

[85] H. Moosavi, R. Mirza Hessabi, and O. Mercan, "Numerical simulation and analysis of nonlinear state-space control design for hydraulic actuator control," *Structural Control and Health Monitoring*, vol. 22, no. 8, pp. 1068–1085, aug 2015. [Online]. Available: http://doi.wiley.com/10.1002/stc.1731

[86] R. Enokida, D. Stoten, and K. Kajiwara, "Application of the nonlinear substructuring control method to nonlinear 2-degree-of-freedom systems," *Journal of Physics: Conference Series*, vol. 744, p. 012039, sep 2016. [Online]. Available: http://stacks.iop.org/1742-6596/744/i=1/a=012039?key=crossref.0dddcb819403c3d1b6991075d8f7fcb4

[87] X. Shao, A. M. Reinhorn, and M. V. Sivaselvan, "Real-Time Hybrid Simulation Using Shake Tables and Dynamic Actuators," *Journal of Structural Engineering*, vol. 137, no. 7, pp. 748–760, jul 2011.

[88] A. Isidori, *Nonlinear Control Systems*, 3rd ed. New York: Springer, 2001.

[89] W. J. Rugh, "Analytical framework for gain scheduling," *IEEE Control Systems*, vol. 11, no. 1, pp. 79–84, jan 1991.

[90] H. K. Khalil, *Nonlinear systems*, 3rd ed. Saddle River, NJ: Prentice Hall, 2002.

[91] M. Krstic, I. Kanellakopoulos, and P. V. Kokotovic, *Nonlinear and Adaptive Control Design*, S. Haykin, Ed. New York: John Wiley and Sons, 1995.

[92] C. Rohrs, L. Valavani, M. Athans, and G. Stein, "Robustness of continuous-time adaptive control algorithms in the presence of unmodeled dynamics," *IEEE Transactions on Automatic Control*, vol. 30, no. 9, pp. 881–889, sep 1985.

[93] B. Yao and C. Jiang, "Advanced motion control: From classical PID to nonlinear adaptive robust control," in *2010 11th IEEE International Workshop on Advanced Motion Control (AMC)*. IEEE, mar 2010, pp. 815–829.

[94] G. C. Goodwin and D. Q. Mayne, "A parameter estimation perspective of continuous time model reference adaptive control," *Automatica*, vol. 23, no. 1, pp. 57–70, jan 1987.

[95] B. F. Spencer, S. J. Dyke, M. K. Sain, and J. D. Carlson, "Phenomenological Model for Magnetorheological Dampers," *Journal of Engineering Mechanics*, vol. 123, no. 3, pp. 230–238, mar 1997. [Online]. Available: http://ascelibrary.org/doi/10.1061/%28ASCE%290733-9399%281997%29123%3A3%28230%29

[96] Z. Jiang and R. Christenson, "A comparison of 200 kN magneto-rheological damper models for use in real-time hybrid simulation pretesting," p. 065011, 2011.

[97] N. E. Castaneda, "Development and Validation of a Real-Time Computational Framework for Hybrid Simulation of Dynamically-Excited Steel Frame Structures," Ph.D. dissertation, Purdue University, 2012.

APPENDICES

A. APPENDIX A

```
%-------------------------------------------------------------
Input File for RT-Frame2D
RT_F2D_input
Purdue University

Node = [
    0 0;
    0.762 0;
    2*0.762 0;
    0 0.635;
    0.762 0.635;
    2*0.762 0.635;
    0 0.635*2;
    0.762 0.635*2;
    2*0.762 0.635*2;
    0 0.635*3;
    0.762 0.635*3;
    2*0.762 0.635*3;
    ];
% --------------------------------------
% --- ELEMENT DEFINITION ---
% --------------------------------------

% -------------------------------
% Script to calculate element table based on number of stories and bays
% However a direct definition can be done by constructing a matrix as:
%     element_tbl=[Node0_a  Node0_b  I0  II0;
%                     .       .        .   . ;
%                     .       .        .   . ;
%                  Noden_a  Noden_b  In  IIn]
% -------------------------------

element_tbl = [
    1 4 1 1;
    2 5 1 1;
    3 6 1 1;
```

```
    4 7 1 1;
    5 8 1 1;
    6 9 1 1;
    7 10 1 1;
    8 11 1 1;
    9 12 1 1;
    4 5 2 1;
    5 6 2 1;
    7 8 2 1;
    8 9 2 1;
    10 11 2 1;
    11 12 2 1];


% ----------------------------------------------
% --- Define Linear-Elastic beam elements with
%     Linear/Nonlinear flexible connection Table
% --- Notes: ---
% 1. Connection Definition: connection_idx =
% [Number_of_connection K1 K2 K3 Teta1 Teta2];
% 2. Beam element that are selected to have flexible connections:
% connection_assig=[Number_of_beam connection_idx/tag_left_end
% connection_idx/tag_right_end];
% ----------------------------------------------

% Dummy definition of flexible connection definition
connection_idx=[1 1e8 1e2 1e1 0.0002 3*0.0004];
connection_assig=[0]; % When no element with flexible connections is included

% ----------------------------------------------
% --- Define Panel zone Table  ---
% --- Notes: ---
% 1. Two types: Linear with bidirectional tension/compression
% and shear distortion modes  - Rigid body
% 2. If panel zone is present: PZ_node =
%[Number_of_node a b thickness E v modeling_assumption
% = (1 for plane stress , 2 for plane strain)]
% ----------------------------------------------


Idx_Panel  = 0;
% Panel zone type: - 0: No panel zone, 1:Linear, 3:Rigid_Body
```

```
% Dummy definition of panel zone
% PZ_node=[8 .3 .5 7.62E-3 1.999E11 0.3 1;
%    10 .3 .5 7.62E-3 1.999E11 0.3 1;
%    ];

% -------------------------------------
% --- CONSTRAINTS DEFINITION ---
% -------------------------------------

% --------------------------
% --- Fixed Nodes ---
% --------------------------
%                       Fix: 1 , Free: 0
%              Node_no  Hor.  Vert.  Rot.

Fix_node = [    1       1     1     0 ;
                2       1     1     0 ;
                3       1     1     0 ];

% -----------------------------------
% --- Master - Slave Nodes ---
% -----------------------------------
%             Master  Dir  Num_slv  Slv_1  Slv_2  .....

slv_tbl = [ 4 1 2 5 6;
            7 1 2 8 9;
           10 1 2 11 12];

% -----------------------------
% --- Define Section Table ---
% -----------------------------
G = 79.3e9; %Pa
E = 200e9;
A1 = 0.00108;
A2 = 6.5024e-4;
I1 = 1.049e-6; %Column
I2 = 2.55e-7;

section_idx = [
% %Sec_no EI1 EI2 EI3 EA GA d1 d2 type_of_plasticity transverse_shear_factor
1 1.5*E*I1 1.5*E*I1 1.5*E*I1 1.5*E*A1 1.5*G*A1 0.5 1 1 0
2 1.5*E*I2 1.5*E*I2 1.5*E*I2 1.5*E*A2 1.5*G*A2 0.5 1 1 0
3 0.5*E*I1 0.5*E*I1 0.5*E*I1 0.5*E*A1 0.5*G*A1 0.5 1 1 0
```

```
4 0.5*E*I2 0.5*E*I2 0.5*E*I2 0.5*E*A2 0.5*G*A2 0.5 1 1 0];
% section_idx(:,3)=.025*section_idx(:,2);
% section_idx(:,4)=.025*section_idx(:,2);

% ----------------------
% --- MASS PARAMETERS
% --- Notes: ---
% 1. Lumped Mass assumption
% 2. Element_mass=[ Mass value associated to the correspoding element ]
% ----------------------
Mc = 0; %kg
Mb = 2000; %kg
Element_mass = [Mc;Mc;Mc;Mc;Mc;Mc;Mc;Mc;Mc;Mb-30;Mb;Mb;Mb;Mb;Mb];
rm_mult = 1e-6;

% ----------------------
% --- DAMPING PARAMETERS
% ----------------------
Damp_type  = 3;
% Damping Type: - 1:Mass, 2:Stiffness, 3:Rayleigh
zeta_cr    = 0.019;
% Critical Damping Ratio
h_max      = 0.01;
% Maximum Damping for Type 2
nCutOff    = 5;
% Number of mode for cutting off ( If Damping type == 3,
% then 0 indicates a direct definition of alpha and beta coefficients)
alpha_ray = 0.4977;
beta_ray  = 1.7186*10^-4;

% ---------------------------------------------
% --- TYME-HISTORY ANALYSIS PARAMETERS
% ---------------------------------------------
Idx_linear = 1; % Analysis type: - 1:Linear 0:Nonlinear
T_str   = 0.0; % Start time of the Analysis
T_end   = 60; % End time of the Analysis
dt_cal  = 1/4096; % Time Interval Delta_t
beta_val  = 1.0/4.0; % beta  value for Newmark-beta Method
gamma_val = 1.0/2.0; % gamma value for Newmark-beta Method

% ---------------------------------------------
% --- INPUT/OUTPUT DEFINITION
% ---------------------------------------------
```

```
% ------------------------------------------------
% --- File for loading control block parameters if existing
%  --- Notes: ---
% 1. Cnt_file = 'NAME OF FILE';
% 2. Cnt_file = 'NONE' if no file is available
% ------------------------------------------------
Cnt_file = 'NONE';

% ------------------------------------------------
% --- Observation Points for Evaluations: (y0) ---
% ------------------------------------------------
%  obs(i,1): No.
%  obs(i,2): Node number
%  obs(i,3): Direction (1, 2, or 3)
%  obs(i,4): Response (1, 2, or 3)
% ----------------------------------
obs = 0;
no =0;
for No_node=[1:12]
    for comp = 3:3
        no = no + 1;
        obs(no,1) = no;
        obs(no,2) = No_node;
        obs(no,3) = 1;       % Horizontal Component
        obs(no,4) = comp;    % Required Response
    end
end

% ---------------------------------------------
% --- Sensor Positions for feedback in the control force calculation: (y1)
% ---------------------------------------------
%  snr(i,1): No.
%  snr(i,2): Node number
%  snr(i,3): Direction (1, 2, or 3)
%  snr(i,4): Response (1, 2, or 3)
% ----------------------------------
snr = 0;
no =0;
for No_node=[5];
    for comp = 3:-1:1
        no = no + 1;
        snr(no,1) = no;
```

```
        snr(no,2) = No_node;
        snr(no,3) = 1;       % Horizontal Component
        snr(no,4) = comp;       % Required Response
    end
end
% ----------------------------------------
% --- Connection Points of control devices (y2) ---
% ----------------------------------------
%  cps(i,1): No.
%  cps(i,2): Node number
%  cps(i,3): Direction (1, 2, or 3)
%  cps(i,4): Response (1, 2, or 3)
% ----------------------------------
cps = 0;
no =0;
for No_node=[1,5];
    for comp = 2:2
        no = no + 1;
        cps(no,1) = no;
        cps(no,2) = No_node;
        cps(no,3) = 1;       % Horizontal Direction
        cps(no,4) = comp;       % Required Response
    end
end
% ----------------------------------------
% --- Location and direction of Control Forces: (f) ---
% ----------------------------------------
%  cf(i,1): No.
%  cf(i,2): Node number
%  cf(i,3): Direction (1, 2, or 3)
% ----------------------------------
ND = [5 1];
for i = 1:2
    cf(i,1) = i;
    cf(i,2) = ND(i);
    cf(i,3) = 1;
end
Num_cf = size(cf,1);
```